

# **DOCTORAL (PhD) THESIS**

ZOLTÁN TILL

University of Pannonia  
2020



University of Pannonia  
Institute of Chemical and Process Engineering

DOI:10.18136/PE.2020.763

Advanced Methods in the Design  
of Heterocatalytic Processes under Uncertainties

DOCTORAL (PhD) THESIS

Zoltán Till

Supervisors:

Dr. Tibor Chován, associate professor

Dr. Tamás Varga, associate professor

Doctoral School of Chemical Engineering and Material Sciences  
University of Pannonia  
2020



**Advanced Methods  
in the Design of Heterocatalytic Processes under Uncertainties**

Thesis for obtaining a PhD degree in the Doctoral School of Chemical  
Engineering and Material Sciences of the University of Pannonia

in the branch of Bio-, Environmental and Chemical Engineering Sciences

Written by Zoltán Till

Supervisors: Dr. Tibor Chován, Dr. Tamás Varga

propose acceptance (yes / no) .....  
.....  
(supervisors)

As a reviewer, I propose acceptance of the thesis:

Name of Reviewer: ..... yes / no  
.....  
(reviewer)

Name of Reviewer: ..... yes / no  
.....  
(reviewer)

The PhD-candidate has achieved .....% at the public discussion.

Veszprém, .....  
.....  
(Chair of Committee)

The grade of the PhD Diploma ..... (..... %)

Veszprém, .....  
.....  
(Chair of UDHC)



*“Beware of the man who works hard to learn something, learns it, and finds himself no wiser than before,” Bokonon tells us. “He is full of murderous resentment of people who are ignorant without having come by their ignorance the hard way.”*

(Kurt Vonnegut: Cat’s cradle)





## **Abstract**

### **Advanced Methods in the Design of Heterocatalytic Processes under Uncertainties**

All kinetic models are uncertain to some extent. Usually that is the case when many consecutive and competitive reactions occur in the system investigated. In such cases, determining individual reaction rates with high accuracy becomes ever less feasible. The kinetic parameter identification problem will be even more complicated if the reaction mixture contains an extensive range of individual species, and there are not enough resources (available analytical methods or time, which is also important in the engineering practice) available to measure the concentration of every component.

Nevertheless, engineers would even want to use uncertain kinetic models to size key pieces of equipment for the industrial implementation of the chemical process. And in order to counter the possible effects of uncertain parameters, these units tend to be oversized. Although this is viable, it would be economically more efficient if we had higher confidence in the kinetic parameters.

Consequently, this dissertation revolves around novel and improved methods to reduce uncertainties connected to reaction networks describing various heterocatalytic processes. Specifically, I authored new kinetic parameter identification methods, applied global sensitivity analysis and the concept of Factors Fixing to reduce the number of parameters to be identified from a series of measurements with a given level of detail, and mapped out the correlations between the formations of certain components that also reduces the number of independent reactions in the system.

Moreover, there are two case studies present in the second part of the dissertation that deal with the optimal design of heterocatalytic processes; the first one aims to answer the question of the optimal design itself, while the second one addresses the broader topic of design under uncertainties (including the uncertainties of reaction networks, or catalyst deactivation) and how we can take these into account when designing a reactor, aside from and possibly without much oversizing.



## Kivonat

### **Továbbfejlesztett módszerek heterogén katalitikus folyamatok bizonytalanságának csökkentésére**

Minden kinetikai modell valamilyen mértékű bizonytalansággal terhelt. Általában ez a helyzet áll fent akkor, ha nagyszámú konszekutív és kompetitív reakció játszódik le a vizsgált rendszerben. Ebben az esetben az egyes reakciók sebességének pontos meghatározása egyre kevésbé kivitelezhető. A kinetikai paraméterek identifikálásnak feladata még összetettebbé válik, ha a reakcióelegy sokkomponensű és ezzel egyidejűleg nem áll rendelkezésre elegendő erőforrás (analitikai módszer, illetve idő, mely szintén lényeges a mérnöki gyakorlatban) az elegyet alkotó összes komponens koncentrációjának meghatározására.

Mindezek ellenére a mérnöki munka során a bizonytalansággal terhelt kinetikai modellek is felhasználásra kerülnek fontos műveleti egységek méretezése, illetve az adott kémiai folyamat ipari mértékű implementálása során. A bizonytalan paraméterek lehetséges negatív hatásainak kiküszöbölése érdekében ezeket a műveleti egységeket általában túlméretezik. Bár ez járható út a tervezés során, gazdaságilag előnyösebb a kinetikai paraméterek megbízhatóságának növelése.

Ezt a felismerést követve dolgozatomban a heterokatalitikus folyamatokat leíró reakcióhálózatokat övező bizonytalanságok csökkentésére irányuló új és általam továbbfejlesztett módszereket mutatok be. Új módszereket dolgoztam ki a kinetikai paraméterek identifikálására, a globális érzékenységvizsgálat és paraméter rögzítés módszerét alkalmaztam az identifikálandó paraméterek számának csökkentésére adott részletességű mérési adatsorból, valamint feltártam az egyes komponensek képződése közötti korrelációkat, ezzel tovább csökkentve a meghatározandó paraméterek számát a vizsgált rendszerben.

Ezeken túlmenően a dolgozat második részében két esettanulmány kapott helyet, melyek a heterokatalitikus folyamatok optimális tervezésével foglalkoznak, melyek közül az első célja egy heterokatalitikus reaktor optimális tervezése, míg a második a bizonytalanság alapú tervezés tágabb témakörét érinti (ideértve a reakcióhálózatokat, vagy a katalizátor dezaktiválódását övező bizonytalanságokat), bemutatva, hogyan vehetőek ezek figyelembe a reaktor tervezés során, elkerülve a műveleti egység komolyabb túlméretezését.



## Auszug

### **Fortschrittliche Methoden bei der Entwicklung heterokatalytischer Prozesse unter Unsicherheiten**

Alle kinetischen Modelle sind bis zu einem gewissen Grad unsicher. In der Regel ist dies der Fall, wenn viele aufeinander folgende und konkurrierende Reaktionen im untersuchten System auftreten. In solchen Fällen wird die Bestimmung der Geschwindigkeiten der individuellen Reaktionen mit hoher Genauigkeit immer weniger durchführbar. Das Problem der kinetischen Parameteridentifikation wird noch komplizierter, wenn das Reaktionsgemisch ein umfangreiches Spektrum einzelner Arten enthält und es nicht genügend Ressourcen (verfügbare analytische Methoden oder Zeit, die auch in der Ingenieurpraxis wichtig ist) zur Messung der Konzentration jeder Komponente zur Verfügung stehen.

Dennoch werden sogar ungewisse kinetische Modelle zur Dimensionierung wichtiger Anlagen für die industrielle Umsetzung des chemischen Prozesses durch die Ingenieure verwendet. Und um den möglichen Auswirkungen unsicherer Parameter entgegenzuwirken, sind diese operativen Einheiten meist überdimensioniert. Obwohl dies lebensfähig bei der Planung ist, ist es wirtschaftlich effizienter, die Zuverlässigkeit der kinetischen Parameter zu erhöhen.

Folglich zeige ich in meiner Arbeit neuartige und verbesserte Methoden, um Unsicherheiten im Zusammenhang mit Reaktionsnetzen zu verringern, die verschiedene heterokatalytische Prozesse beschreiben. Insbesondere habe ich neue kinetische Parameter-Identifikationsmethoden, eine globale Sensitivitätsanalyse und das Konzept von Faktoren entwickelt, die die Anzahl der Parameter verringern, die aus einer Reihe von Messungen mit einem bestimmten Detailgrad identifiziert werden sollen. Ferner deckte ich die Korrelationen zwischen den Formationen bestimmter Komponenten auf, die auch die Anzahl unabhängiger Reaktionen im System reduzieren.

Außerdem gibt es zwei Fallstudien im zweiten Teil der Studie, die sich mit der optimalen Gestaltung heterokatalytischer Prozesse befassen. Die erste soll die Frage nach dem optimalen Design selbst beantworten, während die zweite das weiter gefasste Thema Planung unter Unsicherheiten (einschließlich der Unsicherheiten von Reaktionsnetzen oder Katalysatordeaktivierung) erörtert und aufzeigt, wie wir diese bei der Konstruktion eines Reaktors berücksichtigen können, ohne die operative Einheit erheblich zu überdimensionieren.



---

## Table of Contents

List of Notations.....	1
1 Introduction.....	7
2 Theoretical background.....	11
2.1 Heterocatalytic reactions.....	11
2.1.1 Plastic waste pyrolysis .....	12
2.1.2 Vacuum gas oil hydrocracking.....	14
2.1.3 Recycling HCl into chlorine via oxidation: the Deacon process ..	15
2.2 Discrete lumping .....	17
2.3 Uncertainties in reactor design.....	20
2.3.1 Optimal design criteria of a fixed-bed HCl oxidation reactor.....	21
2.3.2 Design of a VGO hydrocracking reactor under uncertainties .....	24
2.4 Reducing the uncertainties in lumped reaction networks .....	28
2.4.1 Ensuring observability .....	29
2.4.2 Application of Global Sensitivity Analysis (GSA).....	30
2.4.3 Accounting for correlations in the reaction network.....	32
2.4.4 Applying multiple algorithms for parameter identification .....	35
3 Reactor models.....	39
3.1 Dynamic model of a pyrolysis batch reactor system .....	39
3.1.1 Experimental setup.....	40
3.1.2 Reactor model .....	42
3.2 Steady-state plug flow reactor model for VGO hydrocracking .....	47
3.3 Extended model for VGO hydrocracking with H <sub>2</sub> consumption .....	49
3.4 Model of a steady-state single tube reactor for HCl oxidation .....	52
3.5 A few-step kinetic model for ethane pyrolysis (ETP).....	53
4 Kinetic identification of plastic waste pyrolysis on zeolite-based catalysts .	57
4.1 Identification strategy.....	57
4.2 Reliability of the identified kinetic parameters.....	62
4.3 Performance of the identified parameters .....	64
4.4 Comparing the various zeolite-based catalysts .....	68

---

4.5	Chapter summary.....	72
5	Identification and observability of lumped kinetic models .....	73
5.1	Identification strategies.....	73
5.2	Performance of the reaction network reduction algorithms .....	79
5.3	Observability of the reaction networks.....	84
5.4	Chapter summary.....	90
6	Reduction of lumped reaction networks using global sensitivity analysis ....	91
6.1	Choosing the right number of samples .....	91
6.2	Case study 1: thermo-catalytic pyrolysis.....	94
6.3	Case study 2: VGO hydrocracking.....	98
6.4	Comparison of GSA methods.....	102
6.5	Effectiveness and performance.....	103
6.6	Chapter summary.....	107
7	Structure of lumped reaction networks with correlating parameters.....	109
7.1	Revisiting the pyrolysis reactor network (P-N0-R10).....	109
7.2	First alternative reaction network (P-N1-R5).....	113
7.3	Second alternative reaction network (P-N2-R9) .....	117
7.4	Simplification of the experimental work .....	121
7.5	Chapter summary.....	123
8	Kinetic identification problems and different optimization algorithms .....	125
8.1	Investigated kinetic models .....	125
8.2	The optimization target.....	126
8.3	Identification methods .....	129
8.4	Reaching the optimization target .....	132
8.5	The importance of model reduction .....	135
8.6	Differences between the identified kinetic parameters.....	136
8.7	Chapter summary.....	138
9	Optimal temperature profile of a fixed-bed heterocatalytic reactor .....	139
9.1	The reactor design problem .....	140



---

9.2	Optimization strategy .....	141
9.3	Maximizing HCl conversion .....	141
9.4	Optimizing reactor temperature profile.....	143
9.5	Chapter summary .....	151
10	Uncertainties of lumped reaction networks in reactor design .....	153
10.1	Conventional design method.....	153
10.2	Stochastic design method .....	156
10.3	Conventional design results .....	158
10.4	Reactor sensitivity to uncertain parameters .....	160
10.5	Stochastic design results and comparison .....	162
10.6	Robustness of reactor design.....	163
10.7	Chapter summary .....	167
11	Final remarks and farewell.....	169
	Theses.....	173
	Publications related to theses .....	176
	Articles in international journals.....	176
	Articles in conference publications.....	177
	Conference abstracts .....	178
	Publications not related to theses .....	179
	Articles in international journals.....	179
	Articles in Hungarian journals .....	179
	Articles in conference publications.....	179
	Conference abstracts .....	179
	References .....	181
	Appendix .....	215
	List of Figures .....	259
	List of Tables.....	267
	Acknowledgement.....	273

---

## List of Notations

### Mathematical symbols

$a$	Catalyst Dilution Coefficient [-]
$A$	Cross-section [ $\text{m}^2$ ]
$c$	Concentration [ $\text{kg m}^{-3}$ ] or [ $\text{mol m}^{-3}$ ]
$c_p$	Specific Heat Capacity [ $\text{J kg}^{-1} \text{K}^{-1}$ ]
$d$	Diameter [ $\text{m}^2$ ]
$d_u$	Uncertainty Distance
$E_a$	Activation Energy [ $\text{J mol}^{-1}$ ]
$exs$	existence variable [-] (Eq. (5.2))
$f$	friction factor [-]
$F$	molar inflow rate [ $\text{kmol s}^{-1}$ ]
$k$	Reaction Rate Coefficient [varies]
$k_0$	Pre-exponential Factor [same as $k$ ]
$K$	Adsorption Equilibrium Constant [varies]
$l$	Length [m]
$\ell$	Dimensionless Length [-]
$L$	Kirchhoff Matrix of the Reaction System
$L_r$	Reactor Length [m]
$m_r$	Reactant Mass [kg]
$\dot{m}$	Mass Flow [ $\text{kg s}^{-1}$ ]
$M$	Molar Weight [ $\text{kg mol}^{-1}$ ]
$n$	Molar Mass [mol]
$N$	Number of Observations
$p$	Pressure [Pa]
$Q$	Adsorption Activation Energy [ $\text{kJ mol}^{-1}$ ]
$r$	Reaction Rate [ $\text{kg m}^{-3} \text{s}^{-1}$ ] or [ $\text{mol m}^{-3} \text{s}^{-1}$ ]
$r'$	Reaction Rate in Volume [ $\text{kg s}^{-1}$ ]
$R$	Gas Constant; $R = 8.314 \text{ J mol}^{-1} \text{K}^{-1}$
$R_c$	Component Source [ $\text{kg m}^{-3} \text{s}^{-1}$ ] or [ $\text{mol m}^{-3} \text{s}^{-1}$ ]
$R'_c$	Component Source in Volume [ $\text{kg s}^{-1}$ ]

## List of Notations

---

$Si$	Sensitivity index
$t$	Time [s]
$T$	Reactor Temperature [ $^{\circ}\text{C}$ ] or [K]
$ToS$	Catalyst Time-on-Stream [h]
$v$	Plug Flow Velocity [ $\text{m s}^{-1}$ ]
$\nu$	Dimensionless Velocity [ $\text{h}^{-1}$ ]
$V$	Volume [ $\text{m}^3$ ]
$\dot{V}$	Volume Flow [ $\text{m}^3 \text{s}^{-1}$ ]
$w$	weight fraction [-]
$x$	Mole Fraction [-]
$\underline{x}$	Search Variable Vector

### Greek letters

$\alpha$	Decay Coefficient of Catalyst Deactivation [ $\text{h}^{-1}$ ]
$\delta$	variation of the total molecular number in the reaction [-] (Eq. (2.2))
$\Delta_r H$	Heat of Reaction [ $\text{J kmol}^{-1}$ ]
$\varepsilon_{ref}$	Volume Ratio of the Catalyst and the Reference Phase [-] (Eq. (3.5))
$\varepsilon'$	Catalyst Volume Fraction [ $\text{m}_{cat}^3 \text{m}_{reactor}^{-3}$ ]
$\eta$	Catalyst Effectiveness Factor [-]
$\kappa$	Total Heat Transfer Coefficient [ $\text{W m}^{-2} \text{K}^{-1}$ ]
$\nu$	Stoichiometric Coefficient
$\rho$	Density [ $\text{kg m}^{-3}$ ]
$\varphi$	Catalyst Activity Coefficient (as a function of time) [-]

### Components

DME	Dimethyl Ether
HDPE	High-Density Polyethylene
LDPE	Low-Density Polyethylene
PE	Polyethylene
PP	Polypropylene
PVC	Polyvinyl Chloride

ZSM-5 Zeolite Socony Mobil-5; an aluminosilicate zeolite belonging to the pentasil family of zeolites. The additional leading chemical symbol in the abbreviation corresponds to the ion occupying the zeolite ion-exchange sites.

**Pseudocomponents**

C	Coke
D	Diesel
G	Gas
HN	Heavy Naptha
K	Kerosene
L+	Heavy Liquid
$L_i^+$	Heavy Isomer
$L_o^+$	Heavy Olefin
$L_p^+$	Heavy Paraffin
L-	Light Liquid
$L_i^-$	Light Isomer
$L_o^-$	Light Olefin
$L_p^-$	Light Paraffin
LN	Light Naptha
P	Polymer
P-	Cracked Polymer
VGO	Vacuum gas Oil

**Nonlinear Programming**

eSS	Enhanced Scatter Search
GA	Genetic Algorithm
LB	Lower Bound of Search variable
MINLP	Mixed-Integer Nonlinear Programming
NLP	Nonlinear Programming
NOMAD	Nonlinear Optimization with Mesh Adaptive Direct Search
PSwarm	Particle Swarm Pattern Search

UB Upper Bound of Search Variable

For non-frequently used algorithm abbreviations, refer to Table 8.4.

### Abbreviations

CDF	Cumulative Distribution Function
DAEM	Distributed Activation Energy Model
DTG	Differential Thermogravimetry
EET	Elementary Effects Test (Morris Method)
ELV	End-of-Life Vehicle
FAST	Fourier Amplitude Sensitivity Analysis
GC-MS	Gas Chromatography – Mass Spectrometry
GHSV	Gas Hourly Space Velocity [ $\text{h}^{-1}$ ]
GSA	Global Sensitivity Analysis
LHSV	Liquid Hourly Space Velocity [ $\text{h}^{-1}$ ]
MPC	Model Predictive Control
NMR	Nuclear Magnetic Resonance (Spectroscopy)
PAWN	Pianosi-Wagener Sensitivity Analysis
PDF	Probability Distribution Function
RMSE	Root Mean Squared Error
RS-HDMR	High Dimensional Model Representation with Random Sampling
STD	Standard Deviation
SAFE	Sensitivity Analysis for Everybody (Toolbox)
TBP	True Boiling Point
TGA	Thermogravimetric Analysis
VBSA	Variance Based Sensitivity Analysis

For identifiers of the different lumped reaction networks introduced in the thesis, refer to Table S1 in the Appendix.

### Subscripts

<i>act</i>	actual value
<i>B</i>	catalyst bed
<i>cal</i>	calculated
<i>cat</i>	catalyst

<i>comp</i>	component
<i>exp</i>	experimental
<i>g</i>	gas
<i>i</i>	$i^{\text{th}}$ reaction
<i>max</i>	maximum value
<i>min</i>	minimum value
<i>pt</i>	data point
<i>r</i>	reactor
<i>ref</i>	reference volume

**Superscripts**

<i>in</i>	inflow
<i>j</i>	$j^{\text{th}}$ reactor
<i>k</i>	$k^{\text{th}}$ catalyst layer (3.22)
<i>n</i>	normalized value
<i>net</i>	net amount
<i>out</i>	outflow





## 1 Introduction

A process model is a set of equations, and the necessary input data to solve those equations as well that allows us to describe the behavior of a chemical process system [1]. Needless to say, these two components have to be carefully balanced. We can cleverly set up a sophisticated model that would mimic the behavior of the system investigated as carefully as possible with high algorithmic efficiency; it would be all for nothing if we are not able to fetch the necessary quantity and quality of input data to validate it. Sometimes we have to get on with what we have. For example, interim measurements are usually not exactly detailed. They do not need to be in order to run the plant smoothly. With that in mind, we could say that simpler models have their own *raison d'être*. And if that is the case, there ought to be methods that exist to construct process models that are both simple and reliable, i.e., to reduce the uncertainties enveloping them.

After laying the necessary theoretical foundations, I will start with kinetic models, carefully examining the topic of how to represent a complex reaction mechanism with less (here I mean very few) reactions without actually losing the reliability of the kinetic model. For this topic, I have chosen examples of heterocatalytic processes in connection with sustainable development. For example, it is becoming increasingly urgent to do something with the tremendous amount of plastic waste that our civilization currently leaves behind. Among other things, we can utilize pyrolysis to recover valuable fuels and energy storage materials from this waste. On the other hand, the thermo-catalytic cracking of the feedstock polymer leads up to thousands of reactions that are quite a pain in the neck to follow individually. A similar example is the catalytic cracking of long hydrocarbons to produce fuels. The source material in this case can be vacuum gas oil in order to make better use of a barrel of crude oil, thus reducing excess emission; moreover, non-conventional feedstocks (like vegetable oils) can also be processed using such methods.

One of my main objectives is to construct reliable lumped reaction networks. By their very nature these models tend to have uncertain parameters. Considering that we replace thousands of chemical compounds and reactions with a few lumped ones, this is a plausible assumption. The uncertainty of the kinetic model

is not necessarily related to the model error. Strictly speaking, the latter represents the error between the output of the model and the modeled system. This can be reasonably low even in the case where the values of the model parameters cannot be identified with high certainty. In the specific case, this will mean that even if the difference between the experimental and calculated product composition is reasonably low, it will remain uncertain how many reactions form the lumped reaction network and what are the values of the corresponding kinetic parameters. Such a situation inevitably decreases our confidence in the kinetic model.

Therefore, I propose different methods in my thesis to reduce the emerging uncertainties. I account for observability and identifiability, correlations between the rates of parallel and consecutive reactions, or apply sensitivity analysis to eliminate the less significant reactions under the specific conditions. I also deal with the problem of the identification of the parameters of the reaction networks that usually involve the application of a nonlinear optimization program; nevertheless, I would like to show that this is also not an obvious step, associated with uncertainties that can be reduced.

The second major topic of my thesis work broadens the scope and discusses the uncertainty factors involved with the design of heterocatalytic processes themselves. The main objective here is to counter the effects of uncertainties in the design procedure, facilitating the applicability of the process model during reactor design and scale-up. On the one hand, I will carry on the knowledge acquired in constructing simplified reaction networks to describe complex processes, and using that as a starting point I would like to address other sources of uncertainties emerging during the design of a hydrocracking reactor, providing an integrated framework to induce robustness. Or, in other words, to fashion a reactor whose operation is the least susceptible to the changes of the possible uncertain parameters. On the other hand, moving away from the problem of simplified reaction networks, I will also investigate the design of a fixed-bed reactor for HCl oxidation using  $\text{CeO}_2\text{-CuO/Y}$  catalyst, showing that even such a system with only one reaction between four gaseous compounds could present a challenge of how the optimal reactor design can be defined. In addition to being a simpler reaction system, the choice of HCl oxidation to further investigate was

also motivated by sustainable development as this process is essential to close the production cycle of isocyanates. As the technology otherwise would involve manufacturing a high amount of chlorine from salt brine by consuming insane amounts of electricity, and the  $\text{Cl}_2$  in turn would end up as an HCl side product that should be somehow processed as well, this oxidation step turning HCl back to chlorine is essential to keep the production of isocyanates sustainable.

With the wide range of process examples, I would like to provide a convincing argument regarding the proposition of the application of the methods I developed to reduce the uncertainties emerging during the modeling of heterocatalytic processes, illustrating both their applicability and the advantages of their application.

This introduction, like any other, is already too long. Without stretching it any further, let us get into the merits!



## 2 Theoretical background

This thesis involves studying various heterocatalytic reactions, namely the catalytic oxidation of HCl into Cl<sub>2</sub> (the so-called Deacon process), vacuum gas oil (VGO) hydrocracking, and plastic waste pyrolysis (in case of the latter the exclusively thermal process is also part of the investigation; although this is not an essential consideration in the long run). I provide a brief introduction to these processes in Section 2.1.

Hydrocracking and pyrolysis are not single heterocatalytic reactions but rather involve so many individual reactions that it often becomes a thorn in one's side to model them individually. Fortunately, the well-proven lumping methods can come in handy here; I discuss the more common of these in Section 2.2.

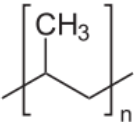
The application of discrete lumping is really straightforward; nevertheless, it involves some simplifications that can backfire if we apply it carelessly as the parameters of the reaction network become uncertain. And here comes the core of this thesis, namely how we can reduce the various uncertainties involving these lumped reaction networks. I will introduce various reduction methods in Section 2.4.

Before that, Section 2.3 deals with the heterocatalytic reactors themselves, involving the development of tools and methods to design such reactors, including the choice of the objective function for solving the model-based design problem and a case study on how to incorporate the effect of uncertain parameters (including the reaction kinetics) into the design problem as well.

### 2.1 Heterocatalytic reactions

A chemical reaction will be called heterocatalytic if the phase of the catalyst is different from the phase of the reactants or products. Heterocatalytic reactions are widely utilized in the chemical industry with some typical examples shown in Table 2.1. In most of these processes, the components flow through the reactor in gas and/or liquid phase while the catalyst is present as a solid (in the form of a fixed or fluidized bed or a structured arrangement (e.g., a mesh)). The main aim of my thesis is the model-based investigation of the said systems.

Table 2.1. Heterocatalytic reactions of industrial importance

Process	Alternate name	Reactants	Products	Catalyst
Ammonia synthesis	Haber-Bosch synthesis	$N_2, H_2$	$NH_3$	ferric oxides [2]
Formaldehyde production [3]	Formox process	$CH_3OH, O_2$	$CH_2O, H_2O$	ferric oxides / V
HCl oxidation	Deacon process	$HCl, O_2$	$Cl_2, H_2O$	$RuO_2$
Hydrocracking and hydrotreating [4]		Petroleum fractions, $H_2$	High-quality fuels	Zeolites [5]
Nitric acid production	Ostwald process	$NH_3, O_2$	$NO_2$	Pt-Rh [6]
Olefin polymerization	Ziegler-Natta polymerization	$C_3H_6$		$TiCl_3/MgCl_2$ [7]
Phosgene synthesis [8]		$CO, Cl_2$	$COCl_2$	activated carbon
Pyrolysis		varies	energy carrier materials	Zeolites [9], metal oxides [10]
Removal of nitrogen oxides		$NO_x, NH_3$	$N_2, H_2O$	$V_2O_5$ [11]
Sulphuric acid production [12]	Contact process	$SO_2, O_2$	$SO_3$	vanadium oxides
Syngas production [13]		$CH_4, H_2O$	$CO, H_2$	nickel

In particular, my thesis considers three areas, the thermo-catalytic pyrolysis of real plastic waste, the Deacon process, and vacuum gas oil hydrocracking. The following three subsections provide a bit more detailed introduction to these topics.

### 2.1.1 Plastic waste pyrolysis

The large amount of waste produced is one of the major downsides of economic and technical development. As such, adequate waste treatment plays a crucial role in making sustainable development goals a reality. Various methods aim to reduce the amount of waste going to landfills. These are part of the waste

management hierarchy that lays down priorities regarding which methods are generally more preferable than others. They are in order: prevention of generation, re-use, recycling, recovery, and only lastly, disposal [14]. In these terms, pyrolysis is a recovery technique among other cracking and energy recovery methods, categorized by Singh et al. [15]. The aim of pyrolysis is to recover various compounds, mainly hydrocarbons from the given feedstock; therefore, it is an effective tool in organic waste treatment. For example, biomass [16,17], polymer waste [18,19] or waste tires [20,21] can be treated and co-pyrolysis of these are also used extensively [22,23].

What makes pyrolysis an attractive method despite its relatively low ranking in waste management hierarchy that it is not only capable of energy recovery, but its products also have a possible use as valuable feedstock for the petrochemical sector and refinery. Olefin-rich gaseous pyrolysis products can be further processed by oligomerization to produce bio-gasoline [24]. C<sub>3</sub>–C<sub>5</sub> olefins obtained by pyrolysis or fluid catalytic cracking can be transformed into branched hydrocarbons with high octane number [25,26]. Pyrolysis oil can be blended with diesel oils to enhance its fuel properties [27], or it can be used as feedstock for hydrotreating in order for double bond saturation and heteroatom removal [28,29].

Using polymers as feedstock for pyrolysis could prove to be very important in handling the ever-growing amount of these not or slowly biodegradable materials [30]. Polyolefin materials, while certainly easier to be reused, do have their advantages when used as pyrolysis feedstock. Theoretically, the produced liquid oil has a much higher energy value than the energy consumed by the pyrolysis that makes the process energetically sustainable [31]. Moreover, polyolefins have negligible heteroatom content that is a significant advantage in fuel production. Catalytic pyrolysis of LDPE leads to the formation of a complex mixture of alkanes, alkenes, carbonyl group-containing compounds and aromatic compounds usable in the petrochemical industry [32]. Moreover, through advanced methods, a high percentage of monomer recovery can be achieved [33].

Product composition during pyrolysis can be significantly influenced by using different catalysts. In general, thermo-catalytic cracking results in higher quality products that need further processing to a lesser extent [30]. Marcilla et al. found

that the amount of gaseous products generated drastically increases when catalysts are employed compared to thermal pyrolysis. In addition, it was observed that while the coke:liquid:gas ratio remains roughly the same, the type of catalyst has an effect on the product composition of these fractions [34]. The presence of the catalyst also decreases the reaction time required for total cracking [35]. One major drawback of catalytic pyrolysis is that the catalyst is a subject for deactivation due to coke formation, while impurities of the polymer waste also contribute to this effect [36].

### 2.1.2 Vacuum gas oil hydrocracking

Hydrocracking is a chemical process during which complex molecules, e.g., long-chain hydrocarbons are broken down into more simple and lighter products, e.g., light hydrocarbons in the presence of hydrogen. Hydrocracking reactors have increasing significance in the petroleum industry to process heavy oils into cleaner fuels. Hydrocracking usually takes place at high pressures under catalytic conditions. Table 2.2 compares the processing of vacuum gas oil under various conditions [4].

Table 2.2. Hydrotreating and hydrocracking: ranges of H<sub>2</sub> partial pressure and conversion.

Process	H <sub>2</sub> partial pressure [barg]	Conversion [% (m/m)]
Hydrotreating	50 – 140	5 – 15
Mild hydrocracking	50 – 85	20 – 40
Once-Through Hydrocracking	100 – 140	60 – 90
Recycle Hydrocracking	100 – 140	80 – 99
Ebullated-bed hydrocracking	140	80 – 99

The application of hydrocracking makes the production of fuels from important nonconventional feedstocks, such as vacuum gas oil (VGO), various vegetable oils, or even waste cooking oil, possible with high quality [37]. These can also be co-processed or might be used in blends in different refinery technologies [38,39]. The importance of fuels from alternative feedstock has significantly increased



with the oil prices rising in the 2000s, and, although the market situation has since normalized, the so-called biofuels still have great importance. Beyond that, there are environmental as well as legal reasons, e.g., there is a mandatory target of a 20% share of energy from renewable sources in overall energy consumption in the European Union by 2020 [40]. When calculating this share, plant-derived motor fuels count as a renewable source, and most of that is consumed in conventional and renewable source blends.

Chemical kinetic modeling becomes increasingly difficult for complex processes such as the hydrocracking of VGO, where several thousands of individual species can be present, and between them, an even larger number of reactions can occur. While concentration measurement for individual components is a routine task nowadays and one can generate full reaction networks automatically, the identification of all kinetic parameters and the subsequent model reduction is usually not a viable method to find a solution. To address this problem, various lumping methods have been developed (see Section 2.2); I will investigate the applicability of these in Chapters 4-8.

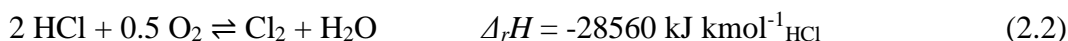
### 2.1.3 Recycling HCl into chlorine via oxidation: the Deacon process

Chlorine ( $\text{Cl}_2$ ) is a widely used reactant in the chemical industry. It is mostly produced via electrolysis of rock salt in the chloralkali process industrialized in the late 19<sup>th</sup> century [41]. The two main types of this process are the mercury cathode and the diaphragm cell technologies; the share of the first is decreasing due to the Minamata Convention on Mercury with a deadline for decommissioning these plants by 2025 [42]. Another factor needs to be taken into consideration is isocyanate production which mostly takes place according to Eq. (2.1) [43]:



The resulting byproduct HCl has to be processed or sold in the form of hydrochloric acid solution. One of the methods of processing HCl is to convert it into  $\text{Cl}_2$  and recycle it in the process (Eq. (2.2)). With this chlorine supply, it is possible to increase isocyanate production capacity while the volume of chlorine-based products (e.g., hydrochloric acid or PVC) remains the same, or considering

the same capacity, the mercury cathode electrolysis cells can be shut down without the necessity of replacing it by diaphragm cells.



Although this so-called Deacon process has been known for more than 140 years [44], its industrial application was long prevented by the lack of a suitable catalyst system. Deacon proposed the application of  $\text{CuCl}_2$  as a catalyst, but copper chloride starts evaporating above  $400^\circ\text{C}$ . This caused rapid catalyst deactivation as the operating temperature range was  $430\text{--}475^\circ\text{C}$  [45]. Shell Research B.V. introduced a  $\text{CuCl}_2\text{--KCl/SiO}_2$  catalyst on a commercial scale, but eventually, it was abandoned due to low conversion rates and serious corrosion problems [46]. The MT-Chlor process developed by Mitsui Chemicals uses  $\text{Cr}_2\text{O}_3/\text{SiO}_2$  as an apparently stable catalyst; nevertheless, there is significant chromium loss because of unstable intermediates forming under reaction conditions [47]. More recently, Sumitomo Chemicals presented its solution for HCl conversion in 1995 [48,49] using a fixed-bed tubular reactor system with a divided shell area using  $\text{TiO}_2$ -supported  $\text{RuO}_2$  as a catalyst [50]. Alternatively, Bayer Materialscience AG patented its own Ru-based Deacon catalyst with  $\text{SnO}_2$  support [51]. The difference besides the catalyst between the Sumitomo and Bayer processes is the reactor design, as the latter utilizes an adiabatic fixed-bed reactor cascade with a much simpler design in contrast to the robust but more complicated multitubular reactor with partitioning from shell side suggested by Sumitomo Chemicals [52].

Another sufficiently stable catalyst can be formed that is based on  $\text{CeO}_2$ , which is studied because of the rarity of ruthenium [53–55]. Cerium is the most abundant of rare earth minerals (unlike the name of the group, it is actually not considered a rare element), and it is a frequently used catalyst material in oxidation reactions [56–59]. While bulk  $\text{CeO}_2$  is a promising catalyst for HCl oxidation, a variety of support materials have also been studied for both technological and economic reasons. Moser et al. tested various supported  $\text{CeO}_2$  catalysts for gas-phase HCl oxidation, revealing that  $\text{CeO}_2/\text{ZrO}_2$  is a long-term stable and industrially relevant alternative of  $\text{RuO}_2$ , as the zirconia content reduced the apparent activation energy of the reaction considerably [60]. Further investigation of  $\text{CeO}_2/\text{ZrO}_2$  catalysts in

both HCl and HBr oxidation showed that a catalyst with a ceria-zirconia molar ratio of 1:3 has both higher activity and higher stability than bulk CeO<sub>2</sub> [61]. The disadvantage of using cerium dioxide as a catalyst is that the reaction takes place at higher temperatures than for RuO<sub>2</sub> [62]. Another approach is to develop and apply a stable Cu-based catalyst (as the “original” one is CuCl<sub>2</sub>) [63,64].

## 2.2 Discrete lumping

The lumping method most generally can be explained as a form of clustering, during which we take a complex chemical reaction network and replace two or more (or even hundreds) of chemical species with one pseudocomponent (aka. lump), thus greatly simplifying the chemical reaction network in question. We can do this multiple times, forming a lumped reaction network. There are two common methods for reaching this target [65]: a priori lumping, which is carried out based on empirical rules such as constraining the total number of species and/or reactions, and a posteriori lumping, where the detailed reaction network is generated first (although its parameters are not identified) and the component grouping is carried out based on the properties of the reaction network. The application of lumping methods in modeling complex reaction systems dates back to almost 50 years [66,67]. At first, it was classified as a problem related to the petroleum industry and was applied as an accessory tool, pointing out that some systems are only approximately lumpable.

By and large, there are four main approaches of modeling processes involving complex reaction networks, from simple to sophisticated: single reaction models, discrete lumping, continuous lumping and detailed kinetic mechanisms.

Single reaction models involve one power-law type equation in that the rate of conversion is expressed by a reaction rate coefficient and a function of conversion describing the type of the reaction [68,69]. Chandrasekaran et al. developed a kinetic model based on thermogravimetric analysis (TGA) results to determine and optimize pyrolysis process parameters (including the catalyst used in the reactor) that predicted the overall activation energy of the process on a given catalyst [70]. The apparent activation energy also indicates the difficulty of decomposing the polymer feedstock based on its composition [71]. A closely

related and more advanced approach is the Distributed Activation Energy Model (DAEM) that is also used for modeling the conversion of the feedstock, which consists of several different species, each having a contribution to the decomposition process described by a pseudo-nth-order rate equation, resulting in an activation energy distribution function [72]. Reaction enthalpy contributions can be taken into account as well, leading to detailed reactor simulations [73]. However, the application of single reaction models requires measuring the amount of remaining polymer in the reactor, and that were not available in the case investigated.

During discrete lumping, components are grouped together in such a way that one compound can only be part of one pseudocomponent. Using this method, we can form multiple component groups that in turn will form a lumped reaction network where each predefined group (lump) is treated as a single component. These models can handle multiple products in an explicit form with relative ease, while both parallel and consecutive reactions steps can be identified with different rates. The lumping approach is commonly used to give researchers a better understanding of experimental data [74,75] or to model industrial-scale processes [76,77]. A great deal of reported applications comes from the oil industry. A five-lump kinetic model for the hydrocracking of heavy oils under moderate conditions was proposed by Sánchez et al., which was capable of predicting component concentrations with an average absolute error of <5% at temperatures of 380–420 °C and liquid hourly space velocity (LHSV) values of 0.33-1.5 h<sup>-1</sup> [78]. The effect of pressure on the kinetics of hydrocracking can also be studied with the lumping approach [79]. An exhaustive review of heavy petroleum fraction hydrocracking, lumped reaction schemes, and kinetic data has been reported by Ancheyta et al. [80].

The process of catalytic upgrading of fuels, such as gasoline olefin content removal, can also be modeled with the lumping approach [81]. Wang et al. applied lumped kinetic simulation to optimize catalyst grading in shale oil hydrotreatment [82]. While the majority of publications involve quasi-homogeneous phase models, the lumped kinetic modeling approach is applicable for describing multiphase systems in detail as well [83,84]. A detailed, two-

dimensional, non-isothermal, heterogeneous model was established by Forghani et al., by applying two different reaction kinetic networks between four lumps that is also applicable for the scale-up of green diesel production [85]. Lumped kinetic models can also be used in the case of treating various oils from renewable sources, such as biomass tar cracking [86], catalytic cracking of vegetable oils [87,88], or waste cooking oil [89].

Moreover, this approach is not limited to the modeling of hydrocracking. Csukás et al. developed a dynamic simulation model for plastic waste pyrolysis in tubular reactors at laboratory and pilot-scale with 14 lumps collapsed into four measured groups. The vapor/liquid ratio along the reactor length was also determined [90]. An attempt was also made to incorporate a priori information into the determination of the reaction network, though there are several reaction mechanisms proposed in the literature that are not always based on the same considerations. One approach considers that products are mainly formed from the polymer feedstock directly, with interactions between the products to a degree [91,92]. Al-Salem et al. used such a mechanism that included the primary conversion of the feedstock into five different lumps with the further conversion of waxes to liquids and aromatics (also formed from the polymer) [93]. Another method is to use a more consecutive reaction scheme where lighter products can be formed from each heavier lump (e.g., gases can be formed from both polymer feedstock and liquid intermediates) [94,95]. In addition to that, Westerhout et al. suggested that PE and PP degrade randomly, producing a range of intermediates considered as a separate lump and the actual products are formed by further cracking in secondary (and ternary) steps [96]. In Section 3.1, I propose a similar mechanism that involves a cracked polymer intermediate.

There are some remarks that kinetic models using discrete lumps are so elementary that their results cannot be reproduced because the feedstock and product compositions are not recognized in-depth sufficiently [97,98]. On the other hand, with appropriate selection of the pseudocomponents considered in the model, it is possible to describe the behavior of the system in detail, e.g., to model catalyst deactivation [99]. Furthermore, there are some cases, e.g., interim measurements or preliminary experimental design procedures, where more

complex methods are not applicable simply because there are no detailed measurement data available.

In the case of continuous lumping, the reaction mixture is represented by a continuous function (such as a function of true boiling point (TBP)) that is then discretized in order to recover the concentration of the sought pseudo-components (defined by TBP range) [100,101]. The advantage of this approach is that any number of lumps can be defined and the reaction rate coefficient can be correlated to the normalized TBP, thus reducing the number parameters to be identified. The disadvantage is that some underlying ideas come directly from the field of hydrocracking (e.g., the form of the so-called yield distribution function); nevertheless, this method has found its way into the field of modeling other processes as well [102].

Lastly, it should be noted that methods based on detailed kinetic mechanisms are also applicable to model complex reaction systems. These involve a significantly higher number of species and reactions present that makes the identification of model parameters increasingly difficult. One of the possible solutions to this problem is to decompose the problem into smaller subtasks that can be solved sequentially [103]. This approach has been successfully applied to pyrolysis reactors previously [104]. Population balance models can also be used to determine the molecular weight distribution of a polymer during thermal degradation [105,106]. Still, more complex methods generally require more comprehensive measurement data and the acquisition of that is not always feasible.

### **2.3 Uncertainties in reactor design**

Any reactor design procedure should cover, including but not limited to, the following aspects [107]:

- stoichiometry of the reactions taking place in the reactor;
- physical and chemical properties of the reactants and products;
- reaction rates (preferably equation-based, as a function of concentrations, temperature, pressure, catalytic activity, among others);
- the heat of reaction and reaction equilibrium;

- catalyst activity and deactivation, reactivation or replacement of spent catalyst;
- phase equilibria, heat and mass transfer between phases;
- operational mode (batch, semi-batch or continuous);
- flow pattern;
- stability and controllability of the system;
- corrosion and safety hazards, environmental protection.

There is more or less uncertainty present in all of the above areas. For example, we can choose an idealized flow pattern to model our reactor; nevertheless, it would never be ideal because of the reactor geometry and turbulence (the only question is how large the difference will be) [108]. Additionally, in the case of a lumped reaction network, the uncertainties can be much more prominent and diverse. What is the exact stoichiometry of a lumped reaction? How can we calculate the heat of a lumped reaction? And, above all, which and how many lumped reactions will cover the process that takes place in the reactor to be designed? I will introduce various methods to handle the uncertainties of a lumped reaction network (more on that topic in Section 2.4); moreover, I would like to present two case studies in that I investigate possible methods to deal with the uncertainties in connection with reactor design as well. The first case study involves a standard reaction (heterocatalytic oxidation of HCl to Cl<sub>2</sub>) whereas the second considers a lumped reaction network for VGO hydrocracking.

### **2.3.1 Optimal design criteria of a fixed-bed HCl oxidation reactor**

As discussed in Section 2.1.1, HCl conversion is mildly exothermic and has a maximal conversion as a function of temperature [109]; furthermore, as catalysts are, in general, the process is sensitive to higher temperatures, thus maintaining an optimal temperature profile in the tubes of the fixed-bed reactor is essential. From the design viewpoint, we can influence the temperature of the reactor directly with cooling or indirectly by diluting the catalyst with an inert component, thus reducing the rate of the reaction.

Luyben investigated the effect of catalyst dilution in tubular reactors using dynamic simulations and stated that with diluting the catalyst the dynamic

controllability of the reactor improves significantly as it can handle lower heat transfer coefficients, and although the size of the reactor increases, this effect could easily justify the higher investment costs [110]. With catalyst dilution, it is also possible to create an axial activity profile in a tubular reactor. This technique has been long known and used successfully [111]. The primary benefit of this approach is the ability to mitigate the dynamic temperature rise caused by a fast exothermic reaction such as the oxychlorination of ethylene [112].

Nie et al. determined the optimal activity distribution using a model-based approach with nonlinear programming (NLP) for ortho-xylene oxidation. The objective function was the maximum of productivity; the addition of a second activity zone lead to a 26.4% increase, which was boosted by a further 6.6% with the addition of a third zone [113]. Moser et al. studied HBr oxidation to Br<sub>2</sub> (which is in many ways similar to the HCl oxidation reaction) and implemented staged catalyst beds to overcome the problem of evolving hotspots due to the more exothermic nature of the reaction. Notably, they suggested mixing of CeO<sub>2</sub>/ZrO<sub>2</sub> and RuO<sub>2</sub>/TiO<sub>2</sub> catalysts in one bed to benefit from the advantages of both catalyst systems [114]. At the inlet of the reactor tube, CeO<sub>2</sub>/ZrO<sub>2</sub> was used as its lower activity and higher stability counteract the hotspot formation due to the exothermic nature of the reaction, while further on full HBr conversion can be achieved on the RuO<sub>2</sub>/TiO<sub>2</sub> bed as it has a high catalyst activity.

A problem with the graded catalyst bed is that the activity decreases at different rates in each bed. This causes the reactor to become unbalanced over time. This effect has been observed for ruthenium-based catalysts [48]. To achieve constant operation, the reactor shell can be divided into multiple zones so that the temperature in each bed can be controlled individually. Consequently, the optimal design procedure of the reactor should take both catalyst dilution and zoned reactor cooling into consideration as well, as is the case in the work presented in Chapter 9.

There is a point of interest on how to exactly define the optimal reactor design. Conveniently, it can be associated with the minimum of an objective function that integrates the various design criteria into a single scalar value. Chemical reactor design optimization problems have been successfully solved for numerous



reaction systems. In these problems, the objective function generally was the maximization of the amount of the desired product(s). Shahrokhi and Baghmisheh investigated methanol synthesis in a fixed-bed reactor and optimized the reactor feed composition and shell temperature to maximize methanol conversion [115]. Cheong et al. reached the highest conversion and selectivity for 1,3-butadiene production in a dual fixed-bed reactor system with the systematic variation of inlet composition and reactor temperature [116]. Vakili and Eslamloueyan applied a more sophisticated objective function for dimethyl ether (DME) production consisting of DME molar flow rate and various penalty parameters dealing with reactor temperature, pressure, and minimal product flow rate [117]. The formation of hotspots is usually avoided by defining a constant temperature maximum. Investigations for methanol synthesis were carried out by Montebelli et al. including catalyst load, coolant temperature and tube diameter as well [118].

On the basis of the literature review, it can be stated that a fixed-bed reactor is generally optimized for maximum conversion (and, if relevant, selectivity) and that the temperature of the reactor is only taken into consideration by applying upper bound or nonlinear constraints to it. However, the reactor ought to be designed so as to prevent thermal runaway. For cooled tubes, if an inflection point appears before the maximum temperature in function of conversion, then runaway will occur [119]. There are numerous criteria for reactor stability (e.g., generalized sensitivity criterion by Morbidelli and Varma [120], identifying nonstable steady-states [121], or relating it to reactor measurement [122], among many others). These are not always sufficient to predict thermal runaway, as a low temperature gradient after the inflection point indicates that actual runaway is not observed in the reactor despite the criterion was fulfilled [123].

Suffice to say, temperature gradients are important because high values may lead to local overheating on a microscale because of insufficient cooling. Moreover, if the same conversion and selectivity can be achieved while temperature gradient remains low at the same time (so there are more hotspots in the reactor but hot-spot temperatures are lower), then thermal deactivation of the catalyst will significantly slower [124]. Consequently, in Chapter 9 I use different methods to smooth reactor temperature profile and calculate temperature gradients

while using them as an indicator to evaluate the performance of the various objective functions while placing a nonlinear constraint to the conversion value. This could be particularly useful because conversion maximum can be reached by various reactor designs that can be distinguished based on the temperature profiles.

### **2.3.2 Design of a VGO hydrocracking reactor under uncertainties**

Most hydrocrackers are trickle-bed reactors in that the mixture of the feed and hydrogen flows downward through multiple fixed catalyst beds; additionally, slurry-phase or ebullating bed units can also be encountered [4]. The general structure of a trickle-bed hydrocracking unit is as follows. The feedstock and a part of the hydrogen are introduced to the first stage at the top of the reactor unit, and after each step, additional hydrogen is added, partly to enhance conversion and partially to quench the mixture and cool it back as the overall hydrocracking process is considered exothermic [101]. Due to this dual role of the hydrogen, which initiates cooling in a shorter term and then a mid-term heating resulting from the increased conversion, the control of the hydrocracking unit is somewhat more challenging; therefore, more sophisticated control methods such as model predictive control (MPC) are more often realized here [125].

As a complex process involving thousands of reactions, hydrocracking is often modeled using the lumping methods. These methods are in fact applicable during model-based reactor design and optimization of the hydrocracking unit [76,126]. Bhutani et al. employed such an approach to investigate an industrial hydrocracking unit, finding different ways to optimize the reactor, e.g., decreasing hydrogen makeup, or increasing kerosene or diesel yields [127]. There were a high number of decision variables present in this case, including feed and recycle flow rates whose control is not always feasible. On the contrary, Zhou et al. only varied the flow rate of the makeup hydrogen and still improved diesel and kerosene yields [128].

Nevertheless, using a lumped reaction network in reactor design involves the necessity to deal with a wide variety of uncertainties. A useful tool for this purpose is sensitivity analysis. Celse et al. compared the local (one-at-a-time) and a global approach to study the effect of various inputs and found that the results of

these are qualitatively similar and both can be used to identify model inputs responsible for the uncertainty of the output; so one can focus their attention to these variables to increase robustness [129]. In the case of a lumped reaction network, sensitivity analysis has a relatively low computational demand, with the drawback that such models involve a great deal of simplification, resulting in a broader range of uncertainties. Whereas, in the case of a detailed model, it is worth constructing a surrogate model for sensitivity analysis purposes [130,131].

Lesser sensitivity index values can also be translated to a more robust design, i.e., a parameter may still vary within the same range, but its effect on the output reduces significantly [132]. Therefore; in order to characterize reactor robustness, one would take a list of uncertain parameters with a possible effect on the output, eliminate those that can be described with lower influence on the model uncertainty (i.e., those associated with lower indices), then assess robustness regarding the remaining parameters [133]. Another model-based robustness criterion states that the deviation of the objective function caused by the variance of the uncertain parameter has to be minimal [134]. This is essentially an optimization problem. Steimel and Engell formulated this objective function as a sum of two terms. The first included the design variables that would be fixed after the realization of the system, and the second term summarized the costs of different operating scenarios, including their probabilities related to the chance that a specific uncertain condition would be actually met [135].

As process models are always affected by uncertainties (whether we acknowledge that explicitly or not), the topic has been widely discussed in the literature. The explicit depiction of uncertain parameters transforms the conventional deterministic mathematical model into a stochastic one [136]. Stochastic programming models consider the variability of possibly uncertain parameters so that we can optimize the expected (average) performance of the model based on the likeliness of these uncertain events [137]. The stochastic approach is commonly used for plant modeling (i.e., the interaction between several units) [138,139] or to model supply chains [140,141]. On the other hand, it is less often applied in designing a single reactor unit, mainly because at first glance, there is not much uncertainty in a model. The concept does appear in the

literature, e.g., Calderón and Ancheyta determined the sensitivity of a hydrocracking reactor to several uncertain parameters [142]; nevertheless, there was no apparent feedback from the sensitivity study to the initial modeling process. Moreover, Alvarez-Majmutov and Chen used a stochastic modeling approach to account for the uncertainties regarding the reactor heat balance, while also comparing the results to that of the conventional methods [143]. This could be important as the reactor temperature has a high impact on process performance.

Reaction kinetics are usually not treated as uncertain parameters because in the case of conventional reactions, we have a strong theoretical basis on the reaction mechanism available. There are exceptions, especially when multiple side reactions are present. Mukkula and Engell studied the optimal operating conditions of a pilot-scale tube reactor with the assumption that there could be a mismatch between the assumed and actual reaction mechanism, providing a real-time optimization solution that could handle the discrepancy [144]. Whereas, in the case of lumped networks the corresponding kinetic parameters are essentially obtained as a result of a parameter fitting to the experimental data. Therefore, it is worth investigating, and it might be as well worth considering the model sensitivity to the kinetics during the reactor design work. Despite that, based on our literature review, the uncertainty of lumped reaction networks usually does not get enough emphasis. In Chapter 10, I investigate how the uncertainties of the lumped reaction network affect the reactor design and how one can straightforwardly account for that.

Yet another uncertain aspect of the hydrocracking reactor model, which is not inevitably recognized in full detail, is catalyst deactivation. The formation of coke and other carbonaceous deposits on the surface of the catalyst is one of the main drawbacks of residue hydrocracking. Due to their low volatility and strong adsorption properties, these components are retained on the surface of the catalyst, blocking (fouling) the active sites and thus deactivating the catalyst [145]. Mesoporous catalysts show higher resistance to fouling [146]; nevertheless, the phenomenon cannot be neglected during the reactor design. There is also a slower process present where the metal content of the feed and the adsorbed nitrogen compounds change the surface structure (called poisoning) [147]. Because of

catalyst deactivation, the temperature of the reactor must be increased in the long-term to compensate for the activity loss and to maintain conversion, resulting in higher operating costs [148].

There are many deactivation models available in the literature, the more elementary equations describe the deactivation process as a function of Time-on-Stream (*ToS*), whereas the complex models also include at least the concentration of the deactivating agent [149]. In the case of using a lumped reaction network, the latter is difficult to interpret as these molecules are not addressed separately. Therefore, catalyst deactivation is usually modeled by using an exponential decay function:

$$\varphi = \exp(-\alpha \cdot ToS) \quad (2.3)$$

The decay coefficient,  $\alpha$ , is not necessarily constant, e.g., it can be influenced by the temperature [150]. Consequently, the application of the decay function is a powerful method with industrial applications as well [151]. On the other hand, it does not take the intrinsic kinetics into account; hence, its parameters might be uncertain.

In Chapter 10, I investigate the effect of catalyst deactivation as a form of uncertainty as well. This way, we can eliminate the necessity of using computationally expensive dynamic models and simulations to account for deactivation. Moreover, we can investigate the effect of deactivation (which, as I said, can be an uncertain process) alongside with the effects of other possible uncertain parameters using a single modeling framework.

Finally, I will point out that the application of a stochastic design method is not automatically advantageous; rather, its usefulness depends on how flexibly we can operate the designed reactor system. In order to investigate that, I compare the performance of the hydrocracking reactor designed by applying the conventional and stochastic methods and quantified the extent to which the optimal reactor operation could be maintained when exposing it to changes in the uncertain parameters.

## 2.4 Reducing the uncertainties in lumped reaction networks

As mentioned earlier, the application of a lumped reaction network in reactor design is a source of uncertainty. Consequently, a large part of my thesis deals with the lattermost question, namely, how to construct a lumped reaction network that can be applied in the reactor design process with sufficient confidence. This could be imperative as the values of the various reactor design parameters can only be as reliable as the underlying kinetic model. Despite this, generally the kinetic identification step is separated more than it would be beneficial in the literature. There are numerous works dealing with the kinetic identification step [152–154], while one can also find papers abundantly on the topic of reactor modeling and design where reaction kinetics are considered as readily available without further consideration [155,156]; however, interactions in between are less frequently addressed, with some notable exceptions [157].

The first study in this thesis (Chapter 4) involves plastic waste pyrolysis and is based on the proper processing of the available measurement information. I will show that by following a well-defined order during the identification of the kinetic parameters of the same lumped reaction network on different catalysts, it becomes possible to compare the performance of these catalysts and to carry out the preliminary sizing of a pilot-scale reactor. The fundamentals of this research are in strong connection with the experimental setup; therefore, they are discussed in Section 3.1.

Furthermore, I would like to present four different methods associated with reducing the uncertainties in lumped reaction networks. The first method (Section 2.4.1) comes from control theory and is based on the general rule that a given system is identifiable only if all of its states are observable. Interpreting the kinetic parameters as state variables, we can define the observability of the reaction network. This method is commonly applied in studying reaction networks but, surprisingly enough, it is seldom used to assess lumped reaction networks.

The second method (Section 2.4.2) involves the application of global sensitivity analysis methods to determine the possible contribution of each reaction to the final product composition.

The third option (considered in Section 2.4.3) is to explicitly account for the correlation between the concentrations of the specified components. If certain conditions are met, these correlations can be strong enough to allow us to merge certain components, consequently reducing the size of the reaction network and the number of parameters to identify.

The last method (in Section 2.4.4), which can be easily combined with any previous one, is that by applying multiple nonlinear optimization programs to identify these kinetic parameters, one can reduce the uncertainties of the identification step itself and can obtain a better answer for the question whether the actual global minimum of the optimization problem was reached or not.

### **2.4.1 Ensuring observability**

In the case of chemical reaction networks, the objective of model reduction is to identify a reaction subsystem as sparse as possible for which the calculated concentration values still show reasonable agreement, compared to the full kinetic network. If the reaction network is dense, i.e., a large number of reactions are supposed to occur, there is an emerging possibility that the system becomes overspecified, which practically means that two or more identified kinetic parameter sets would become equivalent in the aspect that they would lead to the same composition profiles, shown later in Chapter 5.

In order to investigate how reliable the results based on a specific dataset are, the determination of the observability of the system can be useful. The concept of observability, i.e., whether the states of a system can be observed (and, consequently, estimated), comes from control theory, where Bayesian state estimators, most notably the Kalman filter and its variants, are widely used to predict the states of the system from model output and measurements using state-space models [158]. The system is called observable if the values of state variables can be determined within a finite time from the values of outputs [159,160]. State estimators can be effectively used to determine kinetic parameters from measured variables (such as concentrations or temperature) in an observable system [161,162]. They can be applied to study tubular reactors with unknown kinetics as well, although they require that the values of the measured states (such as concentrations) are available along the reactor [163].

Despite this, the theoretical observability and identifiability of lumped reaction kinetic networks are almost never studied; hence, the results obtained using lumped kinetic models are often not applicable, for example, for process intensification. Consequently, in Chapter 5 I will show (in case of vacuum gas oil hydrocracking) that the observability of a lumped reaction network is a good indicator to choose between reduced reaction networks associated with (more or less) the same model error, thus reducing the uncertainties associated with the reaction network.

### 2.4.2 Application of Global Sensitivity Analysis (GSA)

The application of sensitivity analysis in the investigation of complex models is a common practice. It can aid the decision of which model parameters need to be fitted in a complex model to get an unbiased parameter subset that can be used to calibrate the model effectively [164]. Elementary microkinetic networks, large-scale in nature, can be screened to identify inactive parts under certain operating conditions [165]. Local sensitivity analysis, where the derivative of a process target parameter is calculated within a distance of a base point (e.g., the normal operating point of the system investigated), is very effective in terms of computational demand but lacks the ability to explore the whole space of the input factors [166], that is, on the other hand, the aim of global sensitivity analysis (GSA) [167]. GSA has many applications; regarding kinetic models it is mainly used in the field of combustion (e.g. [168,169]), but it is seldom used for reducing kinetic networks directly.

When building a lumped kinetic model, both the number of pseudocomponents and the number of reactions between them need to be determined. In the examples presented in Chapter 6, the former is considered as a fixed value, coming from previous studies. The number of reactions to be included, however, needs to be further investigated. In theory, the more reactions we consider the more identifiable parameters our model has that allow us to get a better model fit, represented by a lower minimum value of the objective function. On the other hand, the identification of an arbitrary complex kinetic model from limited measurement information is not always reasonable. The complexity of the kinetic model should be in parity with the available information; otherwise, the model



becomes uncertain. Firstly, if the complexity of the model increases, the numerical challenge of finding the actual global minimum of the objective function will occur. Secondly, the number of possible parameter combinations that give similar objective function values rapidly increases, which means we will obtain completely different kinetic parameter sets that all provide reasonable model fit. In conclusion, our ability to determine the true values of the identified kinetic parameters diminishes with the increase of the number of reactions taken into consideration, thus making the reduction of these kinetic models desired.

I have investigated the possible application of five different GSA methods in reaction network reduction. The Elementary Effects Test (EET), or the Morris method, provides the so-called elementary effects of the search variables on the objective function by averaging its derivatives over the search space [170]. While it is a global method, the elementary effects are considered semi-quantitative, in other words, it can only be used to rank the model parameters relative to each other. It can be applied to kinetic parameter investigation [171,172], but it is seldom used in the case of lumped networks.

Fourier Amplitude Sensitivity Test (FAST), Variance Based Sensitivity Analysis (VBSA) and High Dimensional Model Representation with Random Sampling (RS-HDMR) all fall into the category of the so-called variance- or momentum-based methods [166]. They use the second central momentum of the model output distribution (in other words, its variance) for characterization. The sensitivity index of a parameter is a quantitative indicator that gives its contribution to the total variance of the objective function, also called the Sobol index [173]. FAST uses a multidimensional Fourier-transformation of the objective function to decompose its variance as a function of the input [174,175]. For RS-HDMR, the objective function is expressed as a finite hierarchical expansion in terms of the input variables, initially proposed by Russian mathematician I. M. Sobol' [176]. VBSA differs mainly on which estimators are used to compute the sensitivity indices: the VBSA method uses the approximation technique of Saltelli et al. [177], while in case of the RS-HDMR, the component functions are approximately represented by orthonormal polynomials whose coefficients can be used to calculate the partial variances [178]. There are

examples in the literature of using variance-based sensitivity analysis methods for studying hydrocracking [129] or pyrolysis [179,180], but it cannot be considered as a common practice in this field. Moreover, in the case of lumped kinetic networks, local methods are favored more often [181,182].

Lastly, the PAWN method, name derived from its authors, is a density-based sensitivity approach that uses the Cumulative Distribution Function (CDF) of the model output rather than its variance to compute sensitivity indices [183]. As it does not use a specific moment (such as the variance) to characterize the model output distribution, it can be applied regardless of its shape. Based on the review of the literature, it has not been applied in the case of kinetic studies previously.

In Chapter 6, I explore the application of global sensitivity analysis methods. The proposed algorithm is based on the concept of Factors Fixing [184]; specifically, I aim to identify model parameters that have no significant influence on the objective function. In other words, sufficient model fit is provided on a wide range of these parameters, which means that their true values cannot be identified from the available data. In theory, if we can eliminate these parameters from the model, the number of uncertain values can be reduced significantly while the model fit is almost preserved. This is further discussed in Sections 6.2 and 6.3. In this way, we can obtain a reduced kinetic model with a lesser number of uncertain parameters. I regard this investigation as a step towards constructing reliable lumped kinetic models with a gradually increasing number of species included, while keeping the uncertainties in the model as low as possible.

### **2.4.3 Accounting for correlations in the reaction network**

Because we talk about reaction networks, usually we have to estimate the kinetic parameters of a set of correlating reactions, e.g. if more light components are formed in hydrocracking, a lesser amount of heavier components will be produced, meaning that the corresponding reactions are also not independent from each other. There is one thing, though. This issue is seldom addressed in the literature. Therefore, the key idea is to merge the lumped components with the highest correlation in the reaction network, then calculate their concentrations based on this correlation.

While used extensively, the properties of lumped reaction networks are infrequently studied in the literature. In an early work on the lumping of complex reaction networks, it is stated that the core of the lumping process is that the species grouped together into a lump are strongly interacting on a shorter time-scale [185]; i.e. the lumping method is not directly connected to the physical properties of the components; rather, it is related to the reactions themselves. The lumping process is a tradeoff between model prediction and precision (i.e. explicitly depicting as many components as possible to characterize the reaction mixture (fuel)) and the capabilities of the analytical techniques (i.e. we would want to use uncomplicated and fast methods) [65]. Therefore, it often comes in handy to lump together what we can to arrive at a more elementary model and use algebraic expressions later to express the concentrations of multiple components on the longer time-scale that are all part of the same lump.

With this, we can also target what kind of measurement we need to follow a particular process. This could bear high significance. Even at a laboratory scale, the detailed composition of the reaction mixture is usually not often determined. There are some works in that the final product is analyzed using different methods, mainly gas chromatography. Calemma et al. applied GC-MS and  $^{13}\text{C}$  NMR to analyze hydrocracking products of Fischer-Tropsch waxes [186]. Elordi et al. used both online GC and GC-MS techniques to measure product yields during HDPE pyrolysis [187]. Djokic et al. combined two-dimensional gas chromatography with Fourier Transform-Ion Cyclotron Resonance Mass Spectrometry [188]. On the other hand, detailed interim measurement is much less often carried out. Onwudili et al. investigated the effect of residence time on product composition during polyethylene and polystyrene pyrolysis and observed a significant effect [189]. The longer residence time provided an opportunity for secondary reactions to occur; hence, the average molecular weight of the pyrolysis oil decreased and the amount of pyrolysis gas and char increased. It should be noted that the process was carried out in a pressurized batch reactor and the volatile products have not been withdrawn continuously.

The effect of residence time is more likely investigated in a tube reactor, e.g. in the work of Ying et al. and apparently the shorter the carbon chain gets, the lower

its reactivity becomes [190]. This indicates that if volatiles are continuously purged from the system, the importance of the secondary reactions will diminish. Zheng et al. also reached this conclusion, stating that the secondary reactions between the product lumps immediately stopped after quenching had been introduced [191]. This is also the reason behind that, in many cases, thermogravimetric analysis is enough to follow the process [192–194].

However, detailed intermediate and end-product analysis, if available, provides an excellent opportunity to identify specific correlations between the formations of different components. Hashimoto et al. identified such correlations in biomass pyrolysis between the rate parameters and solid residue yield and between lignin content and solid residue yield, indicating that these correlations can positively be used in the kinetic parameter estimation [195]. Detailed kinetic models utilize correlations between the reaction rate parameters to avoid the number of model parameters to be identified to be too high [196,197]. In the long run, exploring these correlations makes the parameter estimation of more complex reaction mechanisms from a more elementary set of measurement data possible. Both the correlations between kinetic parameters and the correlations between the amounts of products are worth to be explored. The former represents a direct reduction in the number of parameters to be identified, while the latter contributes to this indirectly as it gives an opportunity to consolidate the number of components that consequently comes with a smaller number of kinetic parameters to be determined. One might not consider this an advantage in itself, but it does give space to expand the reaction network in other dimensions, as shown in Chapter 7.

In most works, the authors deal with one single lumped reaction network. This is perfectly logical as the modeling requirements can be met using that particular network; on the other hand, there can be underlying alternatives and the reasoning behind the final choice is usually fairly implicit. Nevertheless, there are a number of such works available in the literature. Arabiourrutia et al. investigated tire pyrolysis in a conical spouted bed reactor and compared two similar lumped kinetic models, one involving a secondary reaction between the volatiles, the main aim of which was to improve the fit of the model to the experimental results. It is worth noting that the activation energy of the secondary reaction was the highest

that is consistent with the assumption that the reactivity of volatile components during pyrolysis is significantly lower [198]. Puron et al. developed a four-lump kinetic model for vacuum residue hydrocracking and varied the number of reactions between four and nine; the intention of the kinetic modeling here was to obtain the best fit to the experimental data, but also involving the analysis of possible reaction pathways [199]. Santos et al. did a comparative study of kinetic models that can be derived from DTG (differential thermogravimetry) curves for bagasse pyrolysis, showing that the main degradation steps are parallel in nature [200]. Trejo et al. varied also the number of pseudocomponents in the kinetic model for the hydrocracking of asphaltenes by separating the feedstock into easy-to-react asphaltenes and hard-to-react asphaltenes [201]. Félix and Ancheyta compared four lumped reaction networks for crude oil hydrocracking, highlighting that there can be reactions present in the networks that do not actually take place at given operating conditions [202].

Still, the possible correlations between the lumped components are rarely mapped out. And this is what our aim here; to vary the pseudocomponents included in the lumped reaction network and use the correlations identified by analyzing the experimental data to reach an optimal lumped reaction network in sense of capturing as many characteristics of the measurement as possible for a given number of reactions.

#### **2.4.4 Applying multiple algorithms for parameter identification**

In the case of any engineering-related optimization problem, it is vital to select the best-suited algorithm in order to reach such a solution that can be reasonably applied during process design, debottlenecking, or scale-up. For example, Gomez-Gonzalez et al. modeled adsorption and used three different stochastic optimization routines to fit the adsorption isotherm parameters, here, a particle swarm algorithm stood out, because unlike the other methods, it gave a feasible solution every time [203]. However, the range of choice is quite extensive. Li et al. employed the Genetic Algorithm (GA) to identify the kinetics of the pyrolysis of fiberboards [204]. They suggested that the high computational demand of GA can be effectively countered by providing a good initial guess for the parameters using Kissinger's method [205]; however, it is only applicable for

thermogravimetric analysis. Ghahraloud and Farsi also used a genetic algorithm to optimize the heterocatalytic process of methanol oxidation [206]. Kumar and Balasubramanian utilized Particle Swarm Optimization, followed by a gradient-based step by the Levenberg-Marquardt algorithm for kinetic parameter estimation in case of hydrocracking of heavier petroleum feedstock [207]. Such combinations of heuristic and conventional search methods are promising to eliminate the randomness in the solution.

Therefore, the question arises from time to time on how to find the best-suited algorithm to solve a particular problem. Unfortunately, in most works dealing with algorithm comparison, only benchmark problems are used instead of the ones related to chemical engineering. Rios and Sahinidis provided an extensive comparison of more than 20 derivative-free solvers on convex and non-convex test problems, reaching a similar conclusion that there is no solver exist that dominates all the others [208]. Though overall they found the performance of some commercial solvers (that are not considered in this work) outstanding, there is a handful of solvers available on the public domain that performed well (e.g., PSwarm). There are other, less-extensive comparisons in the literature dealing with test problems available [209,210]. These also indicated that there is no single best choice.

In case of kinetic identification problems (i.e., the particular scope of this work), it is much less common to use multiple algorithms on one problem, and it is even rarer to compare them; usually, only the results of the leading algorithm are accepted, such as in the case of the VGO hydrocracking study of Zhang et al. [211]. Nevertheless, such works can be found, e.g., Baker et al. analyzed four popular global optimization methods in estimating the parameters of the upper part of glycolysis, emphasizing that balance has to be found between success and computational time [212]. Another good benchmark of optimization methods for kinetic parameter identification is the work of Villaverde et al. [213]. It only considers a limited number of methods but also deals with the scaling of the search variables, investigating the possible advantages of logarithmic scaling, showing that it has its advantages in the case of local and global optimization as well.

The solution of non-convex optimization problems (such as the kinetic identification problems considered in this paper) is likely to be non-unique. In other words, a finite set of experimental data can be fitted with multiple sets of adjustable parameter values [214]. It is possible to reformulate it to a convex optimization problem that in turn would have a unique global optimum [215,216]; nevertheless, such methods are less commonly used in the engineering practice due to their complexity. Alternatively, the application of statistical tools can be an effective way to compare the similar solutions [217].

The key idea here is that instead of choosing one best algorithm, we can apply several different methods simultaneously to obtain valuable information regarding the nature of the solution of the kinetic parameter identification problems. Through two examples (a lumped kinetic model for vacuum gas oil hydrocracking and a few-step kinetic model for ethane pyrolysis), we highlight the several advantages of this approach. Firstly, model variance and total model error can be calculated. Secondly, the uncertainty of the model can be quantified. Thirdly, further experimental work can be targeted to reduce model uncertainty.





### 3 Reactor models

Each heterocatalytic reaction system introduced in Section 2.1 has a corresponding reaction and reactor model that I take as a basis in the subsequent chapters to identify kinetic parameters or to design a reactor that is optimal in some sense. These models are relatively simple, involving steady-state approximations and elementary flow models (ideally mixed tank and plug flow reactors). The simplifications are within reason as in case of parameter identification of nonlinear models the computational demand is relatively high that one would like to counter this way.

Keeping that in mind, I provide the governing equations for four different systems in Chapter 3.

1. Section 3.1 covers the dynamic model of a two-stage tank reactor in which the pyrolysis of real plastic waste was conducted. This is an original model I developed specifically to be able to provide further insight on the experimental work carried out at University of Pannonia.
2. Section 3.2 cites a tube reactor model for vacuum gas oil (VGO) hydrocracking [218,219]. I extend this model to involve hydrogen consumption explicitly in Section 3.3.
3. The model of a laboratory-scale fixed-bed tube reactor for conducting the Deacon process [220,221] is present in Section 3.4.
4. A few-step kinetic model for the pyrolysis of ethane is described in Section 3.5 [222,223].

The last process has not been introduced earlier as the focus in this case is not on the reaction system itself, but rather this model is used in Chapter 8 to compare the performance of various programs in case of kinetic parameter identification.

#### 3.1 Dynamic model of a pyrolysis batch reactor system

The investigation of the low-temperature pyrolysis of real plastic waste from end-of-life vehicles was conducted, and subsequently concluded at the MOL Department of Hydrocarbon and Coal Processing at the University of Pannonia. Special thanks are due to János Sója and Norbert Miskolczi for sharing the experimental results and for providing valuable insight about the measurement

data and the process overall. The elements of the experimental procedure are covered in Section 3.1.1. This is followed by the reactor model that I constructed and a method that I developed to effectively analyze the provided data using the model-based investigation method.

### 3.1.1 Experimental setup

I would like to present a brief summarization of the methods of the pyrolysis experiments that led to the acquisition of the data I used to model the process. For more information, refer to the detailed description by Miskolczi et al. [224]. Large, easy-to-remove plastic parts of end-of-life vehicles (ELV) were collected and then shredded in a laboratory miller. The average particle size was approximately 3 mm. The resulting raw material had a weight composition of 41% (m/m) HDPE, 42% (m/m) PP and 17% (m/m) LDPE, with an approximately 1.1% moisture content that was removed at 110 °C in a drying cabinet. The dry raw material had 5.2% ash content (mainly glass fiber from reinforced plastics), 0.4% volatiles and 94.4% combustible, according to proximate analysis. Further analysis showed that the average carbon and hydrogen content was 85.5% and 14.5%, respectively [225].

The experiment was carried out in a two-stage laboratory-scale reactor system shown in Figure 3.1. For each pyrolysis experiment, 50 g raw material was introduced in the first stage of the reactor (1) with 2.5 g zeolite-based catalyst (ZSM-5). The purpose of using a zeolite-based catalyst in the first reactor stage was to increase volatile yields and to modify their properties. Several different catalysts were studied, as shown in Table 3.1 (the leading chemical symbol in the abbreviation corresponds to the ion occupying the zeolite ion-exchange sites). The primary intention here was to study their effect on the product composition and apparent kinetics of the pyrolysis process. There are also experimental runs present in Table 3.1 where no catalyst was present (hereinafter referred to as thermal pyrolysis). The temperature of the first stage was maintained at 425/455/485 °C, measured at the bottom of the vessel in the melted plastic.

Table 3.1. List of catalysts used in the two reactors during different runs.

Number of experimental run	1 <sup>st</sup> reactor	2 <sup>nd</sup> reactor
1.	HZSM-5	Ni/Mo-Al <sub>2</sub> O <sub>3</sub>
2.	HZSM-5	none
3.	NiZSM-5	none
4.	CuZSM-5	Ni/Mo-Al <sub>2</sub> O <sub>3</sub>
5.	NiZSM-5	Ni/Mo-Al <sub>2</sub> O <sub>3</sub>
6.	FeZSM-5	Ni/Mo-Al <sub>2</sub> O <sub>3</sub>
7.	none	Ni/Mo-Al <sub>2</sub> O <sub>3</sub>
8.	none	none

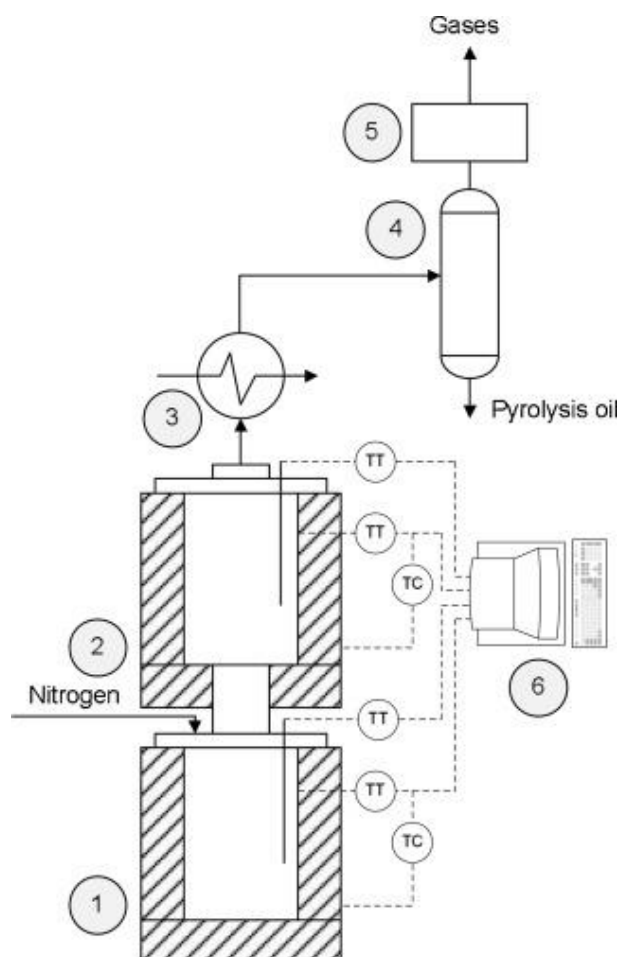


Figure 3.1. Pyrolysis process (1–1<sup>st</sup> reactor, 2–2<sup>nd</sup> reactor, 3 – heat exchanger, 4 – separator, 5 – gas flow meter, 6 – computer) [224].

As for the second stage (2), it contained a Raschig-ring package and 20 g alumina-supported Ni/Mo catalyst (the relatively large amount comes from its

reusability and the lower residence time of the reactants). The temperature of the second stage was maintained at 380 °C – that is controversially lower than of the first stage – as the foremost objective of the study mentioned above was to investigate the effect of Ni/Mo-Al<sub>2</sub>O<sub>3</sub> catalyst on the hydrogen production and aromatization. Here, the lower temperature was chosen to avoid coke deposition and excess gas formation. With that, it became possible to produce liquid fuels (more precisely, liquid products that can be further processed into fuels) as main products at low temperatures.

The process was carried out under nitrogen atmosphere at atmospheric pressure; the excess gas was continuously purged from the reactor by a 15 dm<sup>3</sup> h<sup>-1</sup> nitrogen flow. The outlet of the reactor was cooled down to 50 °C by a tube-in-tube water-cooled heat exchanger (3). The non-condensed gas was not subjected to a more in-depth analysis apart from measuring its flow rate (5); the liquid product, on the other hand, was sampled at constant time intervals and was analyzed by gas chromatography. Hence, the composition of the liquid product is known in great detail. Concentrations of components with carbon numbers ranging from six to 30 were determined separately for paraffins, olefins, and isomeric components. This makes the process modeling task challenging as we have to construct a kinetic model that can follow this many species accurately. On the other hand, the measured information is still sparse as neither the detailed composition of the feedstock is known nor its change was measured during the pyrolysis process experiments. At the end of the batch experiment, the remaining solid content in the two reactors was measured, reduced by the amount of catalysts used. The gas yield was calculated from the amount of initial polymer, pyrolysis oil produced and the remaining quantity of coke, the flow rate of the gas products was used to classify the integrity of the results using the mass balance.

### 3.1.2 Reactor model

In order to model the process described in the previous section, I developed a reaction network consisting of ten reactions between six lumps (Figure 3.2). The arrows representing the reactions were colored differently based on the reactants for the sake of better readability. I will introduce several modifications to this reaction network further along the way; therefore, the original version introduced

in this Section is identified as P-N0-R10. (Refer to Table S1 in the Appendix for all identifiers.) In the first step, plastic waste feedstock (P) decomposes, forming a cracked polymer intermediate (P-) with smaller molecular weight. The subsequent nine reactions follow a full-forward scheme in that a heavier pseudocomponent may decompose into any of the lighter ones (heavy liquid (L+), lighter liquid (L-), gas (G) and coke (C)). G and C are considered as end products, as the former has the smallest average molecular weight and the latter is a tailing product of the process.

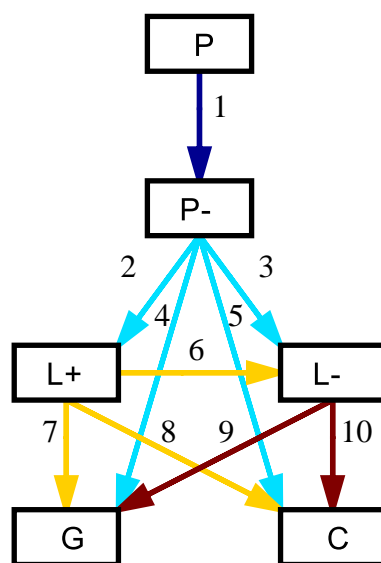


Figure 3.2. P-N0-R10 reaction network with ten reactions between six lumps.

Based on my literature survey, this can be considered a more general lumped model with an average number of pseudocomponents and a dense reaction network. It involves both parallel and consecutive reactions; in other words, alternative pathways were permitted. This leaves room for model reduction, an aspect further investigated in Chapter 6. The number of pseudocomponents in the model is determined by the detail of measurement data. Gas, coke and polymer intermediate is characterized by one pseudocomponent each as the compositions of these were not measured; polymer feedstock is also represented by one lump – this may be further separated to represent raw material composition better albeit this is not a common practice for lumped models, therefore was not applied in this case either. L+ and L- were defined based on the gas chromatography results using the average carbon number of identified components to define them (L+:

16–30, L–: 6–15). This gives room to refine the reaction network by increasing the number of pseudocomponents describing the liquid product composition (refer to Chapter 7 for more details). Aside from these lumps, nitrogen from reactor flush was modeled as an additional single component. P, P– and C were considered to be quasi-solid (steady phase) and the other pseudocomponents as gaseous. The mass transfer between the two phases was regarded as instantaneous, in other words, L+, L- and G are only present in the gas phase while P, P– and C form the steady phase.

The reactions were considered as pseudo-first-order mass-based ones. The rate of the  $i^{th}$  reaction in the  $j^{th}$  reactor is described as a function of the reactant mass concentration (Eq. (3.1)). For the mass concentration calculation, the weight of the given lump ( $m_r^j$ ) was divided by the volume of the appropriate phase ( $V_{ref,i}^j$ ): the volume of the steady phase for P and P– and the gas phase for L+ and L–. Temperature dependence of reaction rate coefficients was assumed to follow the Arrhenius-law (Eq. (3.2)).

$$r_i^j = k_i(T^j) \cdot \frac{m_r^j}{V_{ref,i}^j} \quad (3.1)$$

$$k_i = k_{0,i} \cdot \exp\left(\frac{-E_{a,i}}{RT^j}\right) \quad (3.2)$$

where  $k_{0,i}$  is the pre-exponential factor and  $E_{a,i}$  is the activation energy of the  $i^{th}$  reaction,  $R$  is the gas constant, and  $T^j$  is the absolute temperature of the  $j^{th}$  reactor.

Component sources were calculated from reaction rates and the stoichiometric matrix of the reaction network (Eq. (3.3)), the latter denoted in Table S2 in the Appendix. In order to maintain the mass balance, reaction rates were multiplied by the volume of the phase in which the reaction takes place (Eq. (3.4)). For thermo-catalytic pyrolysis, the volume ratio of the catalyst and the reference phase was also taken into consideration (Eq. (3.5)).

$$\underline{R}'^j = \underline{\nu} \cdot \underline{r}^j \quad (3.3)$$

$$r_i^j = V_{ref,i}^j \cdot \varepsilon_{ref,i}^j \cdot r_i^j \quad (3.4)$$

$$\varepsilon_{ref,i}^j = \frac{V_{cat}^j}{V_{ref,i}^j} \quad (3.5)$$

Given the low volume of the reactors and the low residence times of the components in the gas phase (approx. 2 minutes), the reactor system can be considered as ideally mixed, and the component mass balance equation for a component  $c$  in the  $j^{\text{th}}$  reactor is formalized as follows:

$$\frac{dm_c^j}{dt} = \dot{m}_c^{j,\text{in}} - \dot{m}_c^{j,\text{out}} + R_c^j \quad (3.6)$$

where  $m$  is the component mass,  $\dot{m}$  the component mass flow rate,  $t$  is the elapsed time and  $R_c$  is the component source. Flow rates of P, P- and C were assumed to be zero because of the immobility of the non-volatile components. In the case of the first reactor, there is no inflow except for the nitrogen flush. The inflow of the second reactor is equal to the outflow of the first reactor:

$$\dot{m}_c^{2,\text{in}} = \dot{m}_c^{1,\text{out}} \quad (3.7)$$

Outlet mass flow from the reactors is a cumulative effect from different phenomena (Eq. (3.8)). Firstly, component mass is increased in the reactor due to the continuous inflow. Secondly, components are formed and depleted in the reactor that results in a change in the average density. Lastly, the volume ratio of the steady and gas phases changes in the reactors; this also has an effect on the extent of the outflow.

$$\dot{m}_c^{j,\text{out}} = \left( \sum_k \frac{R_k^j}{M_k} + \sum_k \frac{\dot{m}_k^{j,\text{in}}}{M_k} + \frac{dn_g^j}{dt} \right) \cdot x_c^j \cdot M_c \quad (3.8)$$

where  $M$  is the molecular weight, and  $x$  is the molar weight fraction. At constant pressure and temperature values, the molar mass change of the gas phase  $\left(\frac{dn_g^j}{dt}\right)$  is a direct result of the alteration of the steady phase volume:

$$\frac{dn_g^j}{dt} = -\frac{p}{R \cdot T^j} \cdot \left[ \frac{d}{dt} \left( \frac{m_P^j}{\rho_P} \right) + \frac{d}{dt} \left( \frac{m_{P-}^j}{\rho_{P-}} \right) + \frac{d}{dt} \left( \frac{m_C^j}{\rho_C} \right) \right] \quad (3.9)$$

where  $p$  is the reactor pressure ( $p = 101325$  Pa), and  $\rho$  is the component density, calculated using Eq. (3.10). Individual component molecular weights and coefficients for calculating component densities are listed in Table S3 in the Appendix. Eq. (3.10) has a polynomial form, contrary to the hyperbolic function that can be derived from the ideal gas law. The reason behind this choice is the ambition to take the possible non-ideal behavior of the gas phase into

consideration. As the densities of most components present in the model depend linearly on the temperature between 425 °C and 485 °C, this choice is of little significance, and the actual densities can be calculated by using Eq. (3.10) with high accuracy.

$$\rho = aT^2 + bT + c \quad (3.10)$$

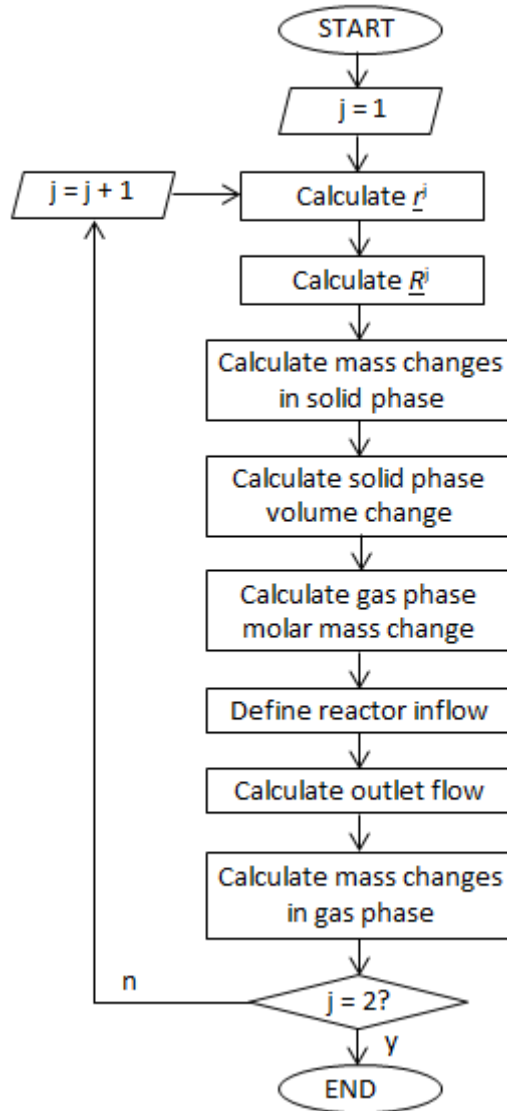


Figure 3.3. Sequential solution of the proposed reactor system model.

The governing differential equations for the two reactors were solved sequentially (Figure 3.3). At a given time step, first the component sources need to be calculated, then the component mass changes in the steady phase (this is possible because of the zero flow rates), followed by the gas phase molar mass change and the reactor outflow, and finally the component mass changes in the



gas phase can be determined. The reactor model was implemented in MATLAB 2017a; for solving the differential equations, the built-in solver ode15s, a variable-step, variable-order (VSVO) multistep solver was used [226,227].

### 3.2 Steady-state plug flow reactor model for VGO hydrocracking

A quasi-homogeneous phase plug flow model of a pilot-scale hydrocracking reactor operating under isothermal conditions and its parameters were reported earlier by Sadighi et al. [218,219]. Identified as VGO-N0-R15 (Table S1), this reaction network applies six lumped components, i.e., unconverted vacuum gas oil or residue (VGO), diesel (D), kerosene (K), heavy naphtha (HN), light naphtha (LN), and gas (G), as denoted in Figure 3.4. The reaction network consists of 15 reactions, including all pathways that might be encountered during that chemical decomposition.

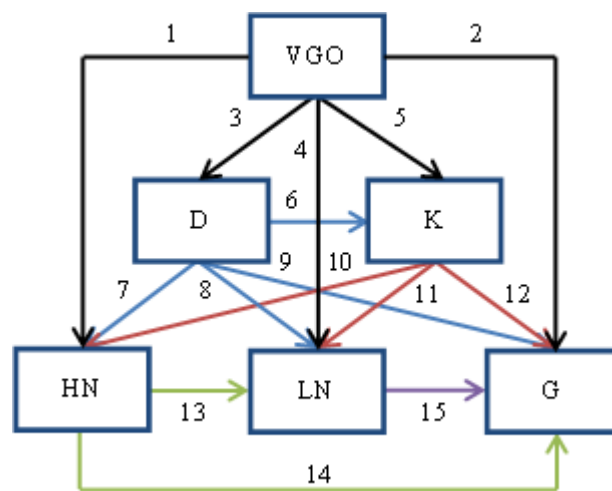


Figure 3.4. VGO-N0-R15 reaction network consisting of 6 component lumps and 15 lumped reactions, labeled in different colors based on reactants

The objective is to analyze the transitions between the lumped components; therefore, the reported experimental data under different conditions are applied here without any modifications. Assuming a steady-state operation and constant catalytic activity, the component mass balance equations of the system can be formalized as follows:

$$\frac{d(\underline{c} \cdot v(\bar{p}))}{d\ell} = \eta \cdot \varepsilon' \cdot \underline{\underline{L}} \cdot \underline{c} \quad (3.11)$$

where  $\ell$  is the dimensionless length of the reactor,  $\eta$  is the effectiveness factor of the heterocatalytic reactions, and  $\varepsilon'$  is the catalyst volume fraction. The values of  $\eta$  and  $\varepsilon'$  are 0.8 and 0.264, respectively; each of these values was taken from the data supplied in the original article. Since the catalyst suffers from deactivation during the hydrocracking of heavy distillates, this assumption is only valid for a limited time operation.  $\underline{c}$  is the component concentration column vector:

$$\underline{c} = [c_{VGO} \ c_D \ c_K \ c_{HN} \ c_{LN} \ c_G]^T \quad (3.12)$$

The actual space velocity ( $\nu$ ) is calculated from the LHSV, considering the density change along the reactor length (see Eq. (3.13) – (3.15)). LHSV values reported by Sadighi et al. were 0.5, 1, 1.5, and 2 h<sup>-1</sup> [218]. The average component density ( $\bar{\rho}$ ) is obtained using the individual component densities and molecular weights of the components in  $\underline{c}$ ; these are given in Table S4 in the Appendix.

$$\nu(\bar{\rho}) = LHSV \cdot \frac{\rho_{in}}{\rho_{act}} \quad (3.13)$$

$$\rho_{act} = \sum_{j=1}^6 (w_j \cdot \rho_j) \quad (3.14)$$

$$w_i = \frac{c_i \cdot \nu}{\sum_{j=1}^6 (c_j \cdot \nu)} \quad (3.15)$$

In Eq. (3.11),  $\underline{\underline{L}}$  is the Kirchhoff matrix of the reaction system [228]. For six components,  $\underline{\underline{L}}$  is a 6-by-6 square matrix, the diagonal elements of which represent the reaction rate coefficients, where the  $i^{th}$  component is consumed (hence, the negative sums in the main diagonal), while the off-diagonal elements contain the rate coefficients of the reactions where the  $i^{th}$  product is formed from the  $j^{th}$  reactant. Because of the mass conservation law,  $\underline{\underline{L}}$  is a column conservation matrix (i.e., the element summary for each column is zero).

$$\underline{\underline{L}} = a_{ij} = \begin{cases} -\sum_l k_{il} & \text{if } i = j \\ k_{ji} & \text{if } i \neq j \end{cases} \quad (3.16)$$

where  $k$  is the reaction rate coefficient. Each reaction is hypothesized to be a pseudo-first-order reaction with Arrhenius-type temperature dependence of the

rate coefficient (Eq. (3.2)). The steady-state reactor model was implemented and solved in MATLAB R2011b using the single-step, second-order solver based on a modified Rosenbrock formula called ode23s [226].

### 3.3 Extended model for VGO hydrocracking with H<sub>2</sub> consumption

The hydrocracking model introduced in Section 3.2 does not calculate with H<sub>2</sub> consumption explicitly. The authors of that model provided a method to estimate the overall amount of hydrogen required during the process [229], but it is more advantageous to tie H<sub>2</sub> consumption to the lumped reactions themselves. Hence, I modified the reactor model as follows. To begin with, the component mass balance from Eq. (3.11) can be more conveniently rewritten as

$$\frac{d\underline{c}}{dl} = \frac{1}{v(\underline{\rho})} \cdot \eta \cdot \varepsilon' \cdot \underline{R}_c \quad (3.17)$$

where  $\underline{c}$  is the component concentration vector,  $l$  is the reactor length,  $v$  is the linear flow velocity (depending on the component density,  $\rho$ ), and  $\underline{R}_c$  is the component source vector. In my thesis, I rely on the previous works of Sadighi et al. [218]; therefore, the hydrogen-to-oil ratio was maintained at 1780 Nm<sup>3</sup>/Sm<sup>3</sup> without further considerations. The reason behind this that the kinetic model used here comes from the experimental results obtained using such conditions [219].

The boundary condition of Eq. (3.17) can be calculated from the reactor inlet flow following Eq. (3.18):

$$\underline{c}_{l=0} = \frac{\frac{1}{\underline{M}} \circ \underline{\rho} \circ \dot{V}_{in}}{\sum_{i=1}^7 \dot{V}_{i,in}} \quad (3.18)$$

where  $\underline{M}$  is the molecular weight vector and  $\dot{V}_{in}$  is the volume inflow rate vector of the components; we can determine the latter from the LHSV value and the hydrogen-to-oil ratio. The flow velocity in the reactor ( $v(\underline{\rho})$ ) is dependent on the density of the quasi-homogeneous phase similarly as in Eq. (3.13) with the exception that now the inflow velocity,  $v_{in}$ , should be used as a base, which is itself determined by the inlet volume flow and the cross-section of the reactor. I chose the cross-section to size a pilot-scale fixed-bed tube reactor with a nominal vacuum gas oil load of 100 kg h<sup>-1</sup> at LHSV value of 0.5 h<sup>-1</sup>. The L/D value of the

system was fixed at 20 to facilitate the evolution of the plug flow pattern. The main reactor dimensions are given in Table 3.2.

Table 3.2. VGO hydrocracking reactor main dimensions.

Size parameter	Value
$V_r^{net}$ ( $V_{cat}$ )	0.1063 m <sup>3</sup>
$d_r$	0.19 m
$L_r$	3.78 m

The VGO-N0-R15 reaction network from Figure 3.4 is extended to annex H<sub>2</sub>, arriving to the hybrid reaction network VGO-N1-R5 considering both classic and lumped components (Figure 3.5). Here, only five reactions are noted, each colored differently. I eliminated the other ten using a reduction method discussed in Chapter 5 in order to increase its reliability in reactor design. Each of the five reactions involves hydrogen consumption. The numbers denote the molar ratios of hydrogen to each reactant in the lumped reactions that were estimated based on the molecular weights of the respective reactants and products appearing in that reaction. This might seem elementary; nevertheless, the resulting hydrogen consumption is in alignment with the measured ~5% (m/m) values (kg H<sub>2</sub> consumption / kg VGO converted) [229].

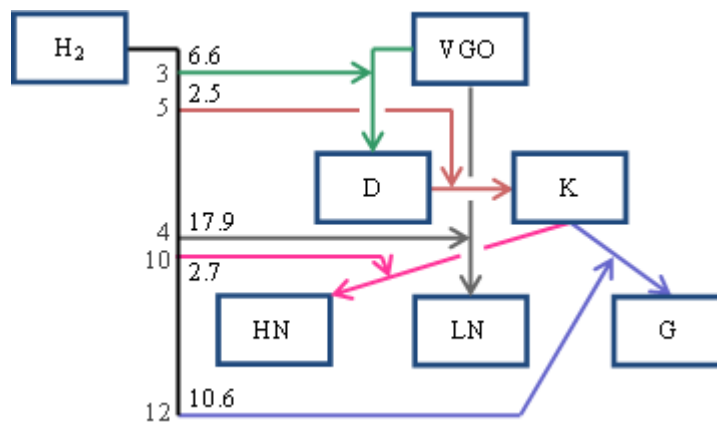


Figure 3.5. VGO-N1-R5 reaction network of VGO hydrocracking, consisting of six lumps, H<sub>2</sub> and five reactions.

Given this reaction network and stoichiometric coefficients, the component sources in Eq. (3.17) can be calculated as follows:

$$\underline{R}_c = \underline{\nu} \cdot \underline{r} \tag{3.19}$$

where  $\underline{\underline{v}}$  is the stoichiometric matrix of the reaction network (denoted in Table S5 in the Appendix) and  $\underline{r}$  is the reaction rate vector. For each of the five reactions (denoted by  $j$  in Eq. (3.20)), the standard rate equations are used, though they still remain lumped, hence the higher order:

$$r_j = k_j \cdot \prod_{i \in \{\text{reactants}\}} c_i^{-\underline{\underline{v}}\{i,j\}} \quad (3.20)$$

where  $k_j$  can be calculated following Eq. (3.2). Given the nature of lumped reactions, the formulation of the reactor heat balance is unconventional to a certain degree. The governing equation of the reactor temperature (Eq. (3.21)) is based on the assumption that 42 MJ of heat is released per kmol of hydrogen consumed ( $\Delta_r H \approx -4.2 \cdot 10^4 \text{ kJ kmol}_{\text{H}_2}^{-1}$ ) [230].

$$\frac{dT}{dl} = \frac{\Delta_r H}{\sum_{i=1}^7 (c_i \cdot M_i) \cdot \bar{c}_p} \cdot \frac{dc_{\text{H}_2}}{dl} \quad (3.21)$$

where the average heat capacity,  $\bar{c}_p$  can be calculated using Eq. (3.22). Individual heat capacities are listed in Table S4 in the Appendix.

$$\bar{c}_p = \sum_{i=1}^7 (w_i \cdot c_{p,i}) \quad (3.22)$$

The reactor may contain more than one catalyst layer; in that case, additional hydrogen is introduced into the reactor after each layer but the last one. That changes both the component concentrations and the reactor temperature. We can recalculate the former using Eq. (3.18); here, H<sub>2</sub> makeup is accounted for in the new  $\dot{V}_{in}$  value of the next layer. The following mixing equation obtains the new inlet temperature of the  $k^{\text{th}}$  layer:

$$T_{in}^k = \frac{\dot{m}_{out}^{k-1} \cdot \bar{c}_{p,out}^{k-1} \cdot T_{out}^{k-1} + \dot{m}_{\text{H}_2}^k \cdot c_{p,\text{H}_2} \cdot T_{\text{H}_2}}{(\dot{m}_{out}^{k-1} + \dot{m}_{\text{H}_2}^k) \cdot \bar{c}_{p,in}^k} \quad (3.23)$$

Eq. (3.23) is also used to determine the reactor inlet temperature (i.e., where  $k = 1$ ). In that case, the first term of the denominator stands for the properties of the VGO inlet (mass flow rate, specific heat capacity and temperature, respectively), while the second term depicts the initial H<sub>2</sub> introduced to the reactor.

The steady-state model of the plug flow reactor for was implemented and solved in MATLAB R2019a using the single-step, second-order solver based on a modified Rosenbrock formula called ode23s [226] called for each catalyst layer consecutively.

### 3.4 Model of a steady-state single tube reactor for HCl oxidation

Simulation of a single-tube reactor for HCl oxidation using CeO<sub>2</sub>–CuO/Y catalyst was reported earlier by Chen et al. [221]. Eq. (3.24) depicts the material balance as the HCl conversion itself as a function of the reactor length:

$$\frac{dx_{HCl}}{dz} = a \frac{A\rho_B r_{HCl}}{F_{HCl,0}} \quad (3.24)$$

where  $A$  is the cross-section of the tube,  $\rho_B$  is the density of the catalyst bed and  $F_{HCl,0}$  is the molar inflow rate of the HCl. The constant  $a$  models catalyst dilution so that the activity of the catalyst bed is proportional to the amount of catalyst diluted. From the conversion, the partial pressures of the components can be expressed as:

$$p_{HCl} = \frac{p \cdot x_{HCl,0} \cdot (1 - x_{HCl})}{1 + \delta \cdot x_{HCl,0} \cdot x_{HCl}} \quad (3.25)$$

$$p_{O_2} = \frac{p \cdot x_{O_2,0} + \delta \cdot p \cdot x_{HCl,0} \cdot x_{HCl}}{1 + \delta \cdot x_{HCl,0} \cdot x_{HCl}} \quad (3.26)$$

$$p_{Cl_2} = \frac{0.5 \cdot p \cdot x_{HCl,0} \cdot x_{HCl}}{1 + \delta \cdot x_{HCl,0} \cdot x_{HCl}} \quad (3.27)$$

$$p_{Cl_2} = p_{H_2O} \quad (3.28)$$

where  $\delta = (1 + 1 - 2 - 0.5)/2 = -0.25$  is the change of the total molecular number in the reaction (Eq. (2.2)). The reaction kinetics are reported by Tang et al. [220]:

$$r_{HCl} = \eta \frac{k_0 \exp\left(-\frac{E_a}{RT}\right) \left(p_{HCl}^2 p_{O_2}^{0.5} - \frac{p_{Cl_2} p_{H_2O}}{\sqrt{K/p}}\right)}{\left(1 + K_{HCl,0} \exp\left(\frac{Q_{HCl}}{RT}\right) p_{HCl} + K_{O_2,0} \exp\left(\frac{Q_{O_2}}{RT}\right) p_{O_2}^{0.5} + K_{Cl_2,0} \exp\left(\frac{Q_{Cl_2}}{RT}\right) p_{Cl_2}\right)^3} \quad (3.29)$$

where  $\eta$  is the effectiveness factor of the shaped catalyst. The reaction equilibrium constant,  $K$ , was determined following the method of Arnold and Kobe [109]:

$$\log K = \frac{5881.7}{T} - 0.93035 \cdot \log T + 1.37014 \cdot 10^{-4} T - 1.7584 \cdot 10^{-8} T^2 - 4.1744 \quad (3.30)$$

The temperature balance of the reactor accounts for the reaction heat as a source and the heat transfer induced by cooling:

$$\frac{dT}{dz} = \frac{\rho_B(-\Delta_r H)r_{HCl} - 4\kappa(T - T_0)D_i/(D_i^2 - D_t^2)}{c_p(G/M)} \quad (3.31)$$

where  $\kappa$  is the total heat transfer coefficient,  $T_0$  is the temperature of the heat transfer salt (HTS) used for cooling,  $c_p$  and  $M$  are the average heat capacity and the average molecular weight of the mixed gas, respectively, while  $G$  is the overall mass flow rate of the gas in the reactor.  $D_i$  is the internal diameter of the reactor, and  $D_t$  is the external diameter of a thermowell placed inside the tube.

The pressure drop of the non-empty reactor tube was modeled using the following equation:

$$\frac{dp}{dz} = f \frac{\rho_g v^2 (1 - \varepsilon)}{d_p \varepsilon^3} \quad (3.32)$$

where  $f$  is the friction coefficient,  $\rho_g$  is the density of the gaseous reaction mixture,  $v$  is the linear flow velocity,  $\varepsilon$  is the catalyst bed void fraction, and  $d_p$  is the pellet size of the shaped catalyst. All parameter values necessary to solve the balance equations are listed in Table S6 in the Appendix. The steady-state reactor model was implemented and solved in MATLAB R2011b using the variable-step, variable-order (VSVO) solver based on the numerical differentiation formulas called ode15s [226].

### 3.5 A few-step kinetic model for ethane pyrolysis (ETP)

In Chapter 8, I apply multiple global nonlinear optimization programs to identify the kinetic parameters of the VGO hydrocracking model from Section 3.2 and an ethane pyrolysis (ETP) model introduced here. This kinetic model involves real chemical reactions between regular components, describing the gas-phase autocatalytic pyrolysis of ethane, studied extensively by Nurislamova et al. [223] and Snytnikov et al. [222]. Table 3.3 lists the constituent reactions and the actual values of the corresponding kinetic parameters. There are multiple reasons behind the choice to investigate this reaction network more closely:

- The size of the reaction network is (15 reactions between 12 components, half of which are radicals) is comparable to the size of the previous examples.

- The reference values of the kinetic parameters are known – not just as identified parameters from elsewhere in the literature but supposedly with actual physical meaning as these reactions cover single microkinetic events (e.g. collision).

Table 3.3. List of reactions and kinetic parameters for the ethane pyrolysis model

Reaction	Pre-exponential factor [s <sup>-1</sup> or m <sup>3</sup> mol <sup>-1</sup> s <sup>-1</sup> ]	Activation energy [J mol <sup>-1</sup> ]
1 C <sub>2</sub> H <sub>6</sub> → CH <sub>3</sub> • + CH <sub>3</sub> •	10 <sup>16</sup>	3.6·10 <sup>5</sup>
2 CH <sub>3</sub> • + C <sub>2</sub> H <sub>6</sub> → CH <sub>4</sub> + C <sub>2</sub> H <sub>5</sub> •	10 <sup>7</sup>	5·10 <sup>4</sup>
3 C <sub>2</sub> H <sub>5</sub> • → C <sub>2</sub> H <sub>4</sub> + H•	3.16·10 <sup>13</sup>	1.7·10 <sup>5</sup>
4 H• + C <sub>2</sub> H <sub>6</sub> → H <sub>2</sub> + C <sub>2</sub> H <sub>5</sub> •	10 <sup>8</sup>	4·10 <sup>4</sup>
5 H• + C <sub>2</sub> H <sub>4</sub> → C <sub>2</sub> H <sub>5</sub> •	2.51·10 <sup>7</sup>	8.4·10 <sup>3</sup>
6 CH <sub>3</sub> • + C <sub>2</sub> H <sub>4</sub> → C <sub>3</sub> H <sub>7</sub> •	7.94·10 <sup>7</sup>	3.3·10 <sup>4</sup>
7 C <sub>3</sub> H <sub>7</sub> • → CH <sub>3</sub> • + C <sub>2</sub> H <sub>4</sub>	7.94·10 <sup>13</sup>	1.37·10 <sup>5</sup>
8 C <sub>2</sub> H <sub>5</sub> • + C <sub>2</sub> H <sub>5</sub> • → C <sub>2</sub> H <sub>4</sub> + C <sub>2</sub> H <sub>6</sub>	10 <sup>7</sup>	8.4·10 <sup>3</sup>
9 C <sub>3</sub> H <sub>7</sub> • + C <sub>2</sub> H <sub>4</sub> → C <sub>2</sub> H <sub>5</sub> • + C <sub>3</sub> H <sub>6</sub>	2.51·10 <sup>4</sup>	2.76·10 <sup>4</sup>
10 CH <sub>3</sub> • + C <sub>2</sub> H <sub>4</sub> → CH <sub>4</sub> + C <sub>2</sub> H <sub>3</sub> •	3.98·10 <sup>5</sup>	3.5·10 <sup>4</sup>
11 CH <sub>3</sub> • + C <sub>2</sub> H <sub>3</sub> • → CH <sub>4</sub> + C <sub>2</sub> H <sub>2</sub>	8.91·10 <sup>6</sup>	3.2·10 <sup>3</sup>
12 C <sub>2</sub> H <sub>3</sub> • + H• → C <sub>2</sub> H <sub>2</sub> + H <sub>2</sub>	10 <sup>7</sup>	-
13 C <sub>2</sub> H <sub>4</sub> → •C <sub>2</sub> H <sub>4</sub> •	6.31·10 <sup>15</sup>	2.53·10 <sup>5</sup>
14 •C <sub>2</sub> H <sub>4</sub> • + C <sub>2</sub> H <sub>6</sub> → CH <sub>3</sub> • + C <sub>3</sub> H <sub>7</sub> •	5.01·10 <sup>11</sup>	2.16·10 <sup>5</sup>
15 •C <sub>2</sub> H <sub>4</sub> • → C <sub>2</sub> H <sub>4</sub>	2.40·10 <sup>5</sup>	-

This means that, theoretically, if we generate a data set using these kinetic parameters and apply no further measurement noise, then use a global nonlinear optimization algorithm to identify the kinetic parameters of these 15 reactions from the generated data set, the program will ideally find the original values of the kinetic parameters associated with zero squared error.

Actually, the problem turned out to be a bit more sophisticated (see Section 8.4 for remarks.), but for the time being, I would like to introduce the reactor model



used to generate the data set. Assuming a steady-state operation and constant catalytic activity, the component mass balance equations of the system can be formalized as follows:

$$\frac{d\underline{c}}{dl} = \frac{1}{v} \cdot \underline{R}_c \quad (3.33)$$

where  $l$  is the length of the reactor,  $\underline{c}$  is the component concentration column vector (Eq. (3.34)),  $v$  is the linear flow velocity, and  $\underline{R}_c$  is the component source vector (Eq. (3.19)). The main reactor dimensions are given in Table 3.4.

Table 3.4. Ethane pyrolysis reactor main dimensions [223].

Size parameter	Value
$V_r$	$6.03 \cdot 10^{-6} \text{ m}^3$
$d_r$	0.016 m
$A_r$	$2.01 \cdot 10^{-4} \text{ m}^2$
$L_r$	0.030 m

$$\underline{c} = \begin{bmatrix} c_{H\cdot} \\ c_{H_2} \\ c_{CH_3\cdot} \\ c_{CH_4} \\ c_{C_2H_2} \\ c_{C_2H_3\cdot} \\ c_{C_2H_4} \\ c_{C_2H_4\cdot} \\ c_{C_2H_5\cdot} \\ c_{C_2H_6} \\ c_{C_3H_6} \\ c_{C_3H_7\cdot} \end{bmatrix} \quad (3.34)$$

The boundary condition of Eq. (3.33) can be calculated as follows:

$$\underline{c}_{l=0} = \frac{1}{\underline{M}} \circ \underline{w}_{in} \quad (3.35)$$

$$\underline{c}_{l=0} = \frac{1}{\sum_{i=1}^{12} \frac{w_{i,in}}{\rho_i}}$$

where  $\underline{M}$  is the molecular weight vector,  $\underline{w}_{in}$  is the inlet weight fraction vector, and  $\rho$  is the component density, calculated using Eq. (3.10). The inlet composition was chosen to be 20% (m/m)  $CH_4$ , 10% (m/m)  $C_2H_4$  and 70% (m/m)  $C_2H_6$  [222].

Individual component molecular weights and coefficients for calculating component densities are listed in Table S7 in the Appendix. The temperature of

the reactor ( $T$ ) varied from 950 to 1020 K at 10 K intervals. This range is in agreement with the experimental conditions used in [223] to estimate the rate parameters in Table 3.3, thus ensuring the validity of the kinetic model.

The linear flow velocity can be calculated from the initial GHSV value (0.05, 0.1, 0.2, 0.4, 0.7, 1, 1.6, or 2 s<sup>-1</sup>) and the change in composition along the length of the reactor:

$$v = GHSV \cdot \frac{V_r}{A_r} \cdot \frac{\bar{c}}{\bar{c}_{in}} \quad (3.36)$$

$$\bar{c} = \sum_{i=1}^{12} (X_i \cdot c_i) \quad (3.37)$$

The reactor model was implemented and solved in MATLAB 2017a; using the built-in a variable-step, variable-order (VSVO) multistep solver called ode15s [226,227].

## 4 Kinetic identification of plastic waste pyrolysis on zeolite-based catalysts

In the following Chapters I would like to present the results that will back up my theses. All but one topic will include kinetic parameter identification. Nevertheless, the identification procedure is only a tool and the focus of each Chapter will be something more novel. Chapter 4 builds on the experimental results and the pyrolysis reaction network introduced in Section 3.1. I propose a two-step iterative parameter identification method in Section 4.1 with that the values of the kinetic parameters can be straightforwardly determined without any a priori information of their range. Next, I show that the proposed lumped kinetic and reactor model is reasonably accurate and captures the key characteristics of the experimental system. The most important objective of this Chapter is to emphasize that the identified kinetic parameters of a lumped reaction network can be used to compare the various catalysts, and not only in the context of the experimental data. Section 4.4 answers how can we use the identified kinetic parameters to compare the performance of the catalysts in a scaled-up environment and how to choose a likely candidate to carry on to the actual scale-up process.

### 4.1 Identification strategy

As covered in Section 3.1.1, low-temperature pyrolysis of real plastic waste was carried out in a two-stage laboratory-scale reactor system using several different catalysts (Table 3.1). The first aim of this chapter is to identify the kinetic parameters of the reaction network shown in Figure 3.2 for all different catalysts. The main objective function is to minimize the squared error between experimental data and model results by varying the parameters of Eq. (4.1). The squared error between measurement (*exp*) and calculation (*cal*) is summarized for three temperature levels (*T*), five pseudocomponents (*c*) and all sampling points (*pt*) (one for the sums of P, P-, C and G; four to six for L+ and L-):

$$f^1(\underline{x}^n) = \sum_T \sum_{\text{comp}} \sum_{\text{pt}} (w_{\text{exp}} - w_{\text{cal}})^2 \quad (4.1)$$

Input variables of Eq. (4.1) are the kinetic parameters of the ten reactions defined in Section 3.1 (Figure 3.2). However, there are some difficulties arising during the determination of the search space for the minimization of the defined objective function. There is no information available about slow and fast reactions and though the activation energy values might be approximated from previous studies, they have relatively large deviations. Therefore, I propose an algorithm consisting of two identification and one approximation step (Figure 4.1).

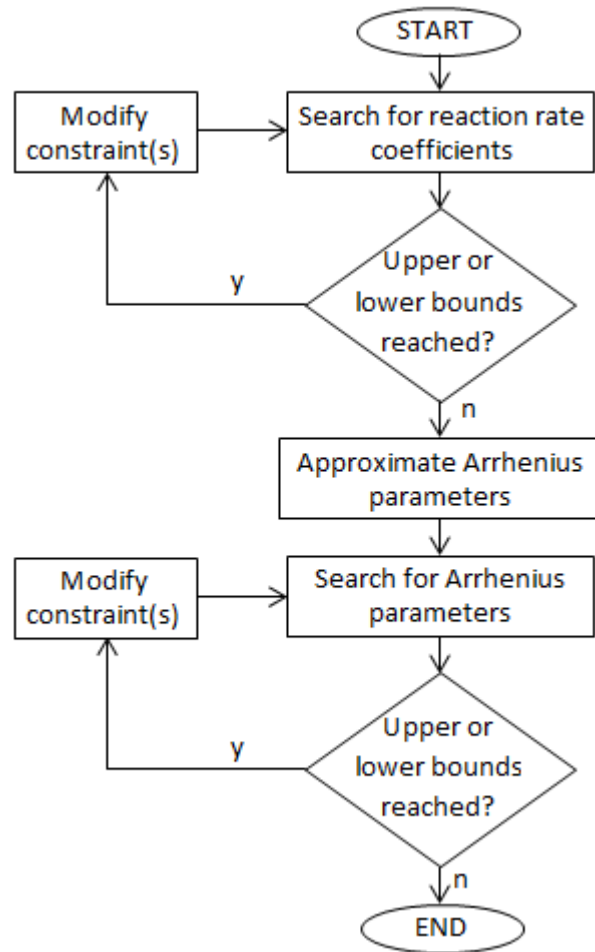


Figure 4.1. Kinetic parameter identification strategy.

In the first step, individual reaction rate coefficients (Eq. (3.1)) are determined at each temperature level, a total of 35 parameters (the different temperature level of the second reactor was also taken into consideration, but here only the last five reactions actually take place there).

$$\underline{x}^{n,1} = \left[ (\underline{k}_{425}^n)^T (\underline{k}_{455}^n)^T (\underline{k}_{485}^n)^T (\underline{k}_{380}^n)^T \right]^T \quad (4.2)$$

The superscript  $n$  in the decision variables indicates that the actual values were normalized between 0 and 1 for better convergence:

$$\underline{x}^{\text{act}} = \underline{x}^n \circ (\underline{\text{UB}} - \underline{\text{LB}}) + \underline{\text{LB}} \quad (4.3)$$

Between the variables, linear inequality constraints are formulated pairwise, 25 in total, such as

$$k_i(T_{\text{lower}}) \leq k_i(T_{\text{higher}}) \quad (4.4)$$

In this way, the input variables can be more independently varied because a given  $k_i(T)$  value only has an effect on the mass concentrations at the given temperature level. If a parameter value from the solution of the optimization problem reached the value of the corresponding upper or lower bound, the optimization run was repeated using a set of modified constraints ( $\pm 20\%$ ) but with the solution of the previous iteration as an initial guess. With this extension, rate coefficients with different magnitudes can be identified without any a priori information of the reaction rates.

In the second step, Arrhenius-parameters were approximated based on the results of the first step based on the linearized Arrhenius equation and the least-squares method. Lastly, the approximated values were used as an initial guess for searching for the final optimal values of Eq. (4.5). The decision variable vector  $\underline{x}^n$  of Eq. (4.1) can be expressed in the second step by Eq. (4.5):

$$\underline{x}^{\text{n},2} = \left[ (\underline{k}_0^n)^T (\underline{E}_a^n)^T \right]^T \quad (4.5)$$

The sequence in which the kinetic parameter identification should be carried out for the different experimental runs listed in Table 3.1 is not particularly straightforward. For example, if the kinetic parameters for thermal pyrolysis need to be identified, the corresponding experimental run (nr. 8 in Table 3.1) cannot be used alone because run nr. 7 is very similar (thermal pyrolysis in the 1<sup>st</sup> reactor but catalyst is present in the 2<sup>nd</sup>). On the other hand, the difference between the results of these two runs is related to the presence of catalyst in the 2<sup>nd</sup> reactor.

Therefore, kinetic parameters for different catalysts were identified in three phases (Table 4.1):

- Phase 1. Identify the rate coefficients for reactions on the structured Ni/Mo- $\text{Al}_2\text{O}_3$  catalyst ( $k^{NiMo}$ ). In this case, the second step of the identification procedure cannot be carried out because of the constant temperature in the 2<sup>nd</sup> reactor. During this phase, experimental runs (7, 8); (1, 2) and (3; 5) had been coupled so the contribution of the second reactor could be observed from the difference in measurement data. This also means that the dimensionality of the optimization problem is increased to 40 (because we deal with two catalysts at the same time). This is also the reason that the six experimental runs were not identified together. Final  $k^{NiMo}$  values were obtained by averaging the results of the three pairs of experimental runs. The exact values of Arrhenius parameters for the other reactions were not identified in this step.
- Phase 2. In the knowledge of  $k^{NiMo}$ , kinetic parameters for thermal pyrolysis can be identified from experimental runs 7 and 8, while Arrhenius parameters for reactions on CuZSM-5 (run 4) and FeZSM-5 catalysts (run 6) can also be parallelly determined.
- Phase 3. Arrhenius parameters for reactions on HZSM-5 (runs 1 and 2) and NiZSM-5 catalysts (runs 3 and 5) can be determined in parallel knowing  $k^{NiMo}$ ,  $k_0^{thermal}$  and  $E_a^{thermal}$  values.

Table 4.1. Suggested kinetic parameter identification sequence.

Phase	Experimental runs used for identification (Table 3.1)	Resulting kinetic parameters	Number of decision variables (Figure 4.1)
1. a	7, 8		
1. b	1, 2	$k^{\text{NiMo}}$	Step 1: 40
1. c	3, 5		
2. a	7, 8	$k_0^{\text{thermal}}$ $E_a^{\text{thermal}}$	Step 1: 35 Step 2: 20
2. b	4	$k_0^{\text{CuZSM-5}}$ $E_a^{\text{CuZSM-5}}$	
2. c	6	$k_0^{\text{FeZSM-5}}$ $E_a^{\text{FeZSM-5}}$	Step 1: 30 Step 2: 20
3. a	1, 2	$k_0^{\text{HZSM-5}}$ $E_a^{\text{HZSM-5}}$	
3. b	3, 5	$k_0^{\text{NiZSM-5}}$ $E_a^{\text{NiZSM-5}}$	

As noted in the introduction of Section 2.4, this coupling method can reduce the uncertainty of the identified kinetic parameters (because multiple experimental runs were used to estimate them). This would further reduce the effect of the noise of the experimental data on the identified model parameters. And this would open up the way to compare the catalysts themselves on the base of the identified parameters and to choose a reliable catalyst for processing such wastes. It can be stated that with the proper selection of pseudocomponents, the lumping approach is appropriate for catalyst evaluation and comparison, leading to a better understanding of the previous experimental results and the overall pyrolysis process. Hence, the results might also be used during process design or scale-up. I provide a detailed case study in Section 4.4.

Due to the complexity of the identification task, the use of a global nonlinear optimization algorithm is necessary. There are multiple alternatives available that have been successfully applied in the case of kinetic parameter identification such as genetic algorithms [81,231], simulated annealing [232] or direct search [233].

In this case, the NOMAD (Nonlinear Optimization by Mesh Adaptive Direct Search) software package was chosen that can be considered as an optimal tradeoff between speed and accuracy as it requires a relatively smaller number of function evaluations compared to other global optimization algorithms. NOMAD is intended for time-consuming black-box simulations with a relatively small number of variables [234,235]. It also has a MATLAB interface available that can be called directly from the OPTI Toolbox [236].

## 4.2 Reliability of the identified kinetic parameters

Identified values of kinetic parameters for all cases are available in detail in the appendix (Table S8). To address the reliability of the identified parameters, a local sensitivity study was performed by means of  $\pm 25\%$  perturbation of the pre-exponential factors and  $\pm 5\%$  perturbations of activation energies, on one parameter at a time [237]. In each step, the objective function (Eq. (4.1)) was evaluated; the obtained curves are shown in Figure 4.2.

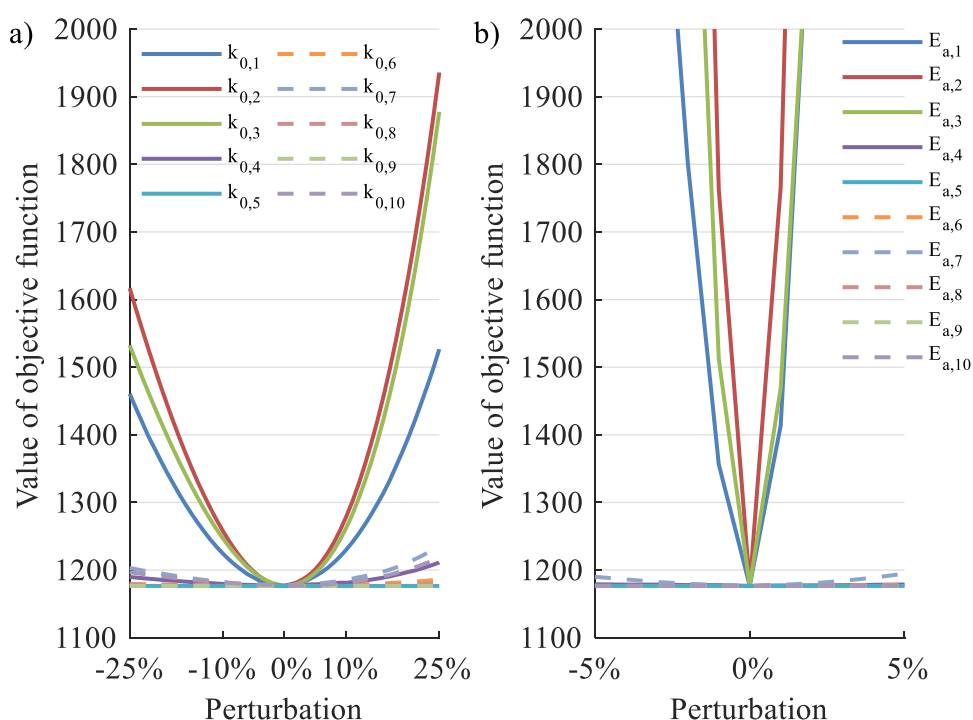


Figure 4.2. Local sensitivity analysis of calculated parameters for thermal pyrolysis. (a) pre-exponential factors; (b) activation energies.



Based on the results of the sensitivity analysis, it can be assumed that the suggested identification strategy and the NOMAD programming method give the optimal values of parameters since all curves have their minimum value at 0% and any modification of the given parameter leads to a higher objective function value. The model is the most sensitive to the changes in the values of kinetic parameters for the first three reactions ( $P \rightarrow P^-$ ,  $P \rightarrow L^+$ ,  $P \rightarrow L^-$ ), firstly because the concentrations of the involved components are higher (as the volume of the steady phase used as reference is smaller than the gas phase volume), secondly because the products  $P^-$ ,  $L^+$  and  $L^-$  are also important reactants for other reactions determining the final product composition.

The root of mean squared errors (RMSE) between pseudocomponent mass percentages from experimental data and simulation results for each temperature level and the complete data set were calculated and are listed in Table 4.2. Higher model errors were obtained in case of thermal pyrolysis with structured Ni/Mo- $Al_2O_3$  catalyst in the 2<sup>nd</sup> reactor, while model performance is the best for thermo-catalytic pyrolysis on FeZSM-5–Ni/Mo- $Al_2O_3$  catalysts. The results indicate that the suggested model and identification strategy can reproduce the experimental results. RMSE values for the four thermo-catalytic cases are roughly the same with the exception of NiZSM-5–Ni/Mo- $Al_2O_3$  catalyst (run nr. 5). This outlier indicates a higher error in the experimental data, perhaps even systematic that is not easy to be discovered. Based on these results, the case of NiZSM-5–Ni/Mo- $Al_2O_3$  catalyst is definitely worth to be revisited. From another viewpoint, this result also shows how useful and important the kinetic modeling of such processes can be. For thermal pyrolysis, the larger model errors might be connected with the longer run times of these experimental runs, resulting in the possible accumulation of both observational and model errors.

Table 4.2. Root-mean-square error (RMSE) between experimental and calculated data.

Catalyst in 1 <sup>st</sup> reactor	Catalyst in 2 <sup>nd</sup> reactor	425 °C	455 °C	485 °C	Temperature aggregated
-	-	3.6%	3.6%	2.2 %	3.2%
-	Ni/Mo	3.8%	4.7%	5.0 %	4.3%
HZSM-5	-	2.6%	1.2%	1.3 %	1.8%
HZSM-5	Ni/Mo	1.7%	1.3%	1.2 %	1.3%
NiZSM-5	-	1.6%	2.6%	3.1 %	2.4%
NiZSM-5	Ni/Mo	3.0%	3.9%	2.6 %	3.1%
CuZSM-5	Ni/Mo	1.3%	2.3%	1.6 %	1.7%
FeZSM-5	Ni/Mo	1.1%	1.2%	1.6 %	1.2%

### 4.3 Performance of the identified parameters

Experimental and calculated mass fractions as a function of time for pyrolysis on FeZSM-5/Ni/Mo catalyst and on NiZSM-5/-, NiZSM-5/Ni/Mo catalysts at 455 °C are shown in Figure 4.3 and Figure 4.4, respectively. The former represents a result with a fairly good agreement between experimental and simulated data, while in the case of the latter the root mean squared error is significantly higher.

The main reason for the higher errors that the solution represented in Figure 4.4 is a compromise from identifying the kinetic parameters from experimental runs 3 and 5 simultaneously and the residual errors between experimental data and model results are contradictory in the two cases. Due to the low residence time and concentrations of the pseudocomponents in the 2<sup>nd</sup> reactor, the model results cannot give back the relatively large difference between the two measurements. Whether this is an observational or a model error needs further investigation.

The difference between the experimental and model results might be also caused by the relatively simple flow model that has two assumptions: both reactors are ideally mixed, and all components are present only in one phase (P, P-, and C: solid / melted phase, L+ L-, G: gas phase). The former assumption is plausible given the shape of the reactor, the low volume, and low residence times of the components; the component mass transfer between the two phases, on the

other hand, is probably not instantaneous under the given experimental conditions. The inclusion of proper mass transfer in the reactor model might further increase its accuracy. Nevertheless, the gas yield increasing effect of the Ni/Mo catalyst can be clearly seen in Figure 4.4, meaning that the suggested model can sufficiently describe this phenomenon.

For all three examples listed, component concentrations reach a constant value approaching the end of the run indicating the end of the batch pyrolysis run that gives room for the optimization of the duration of run time.

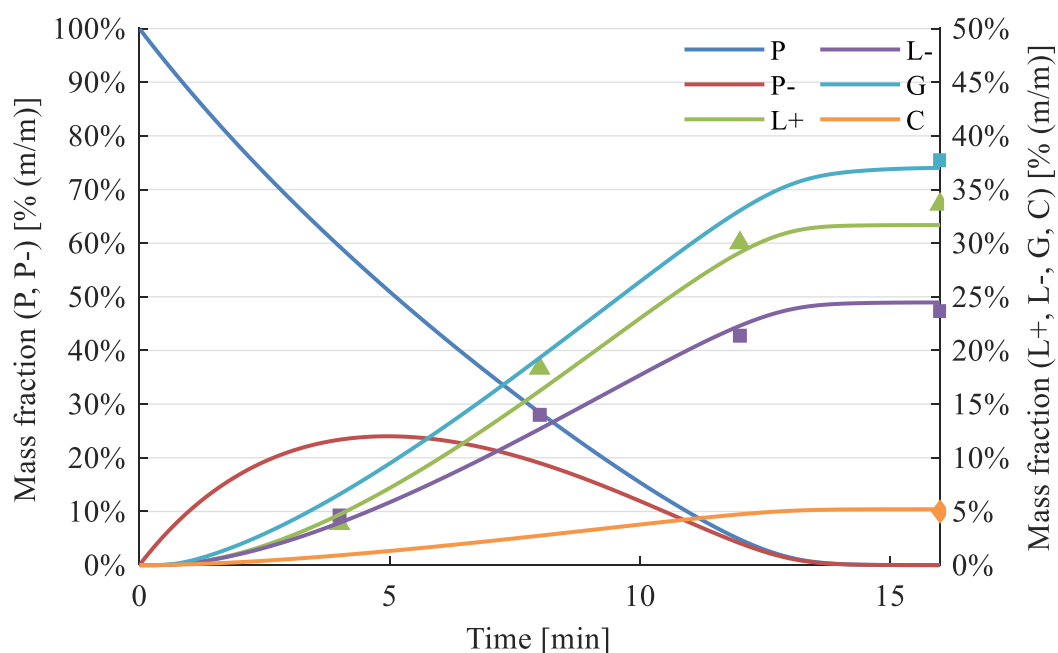


Figure 4.3. Pseudocomponent mass fractions from run nr. 6 at 455 °C – experimental (markers) and simulation (lines).

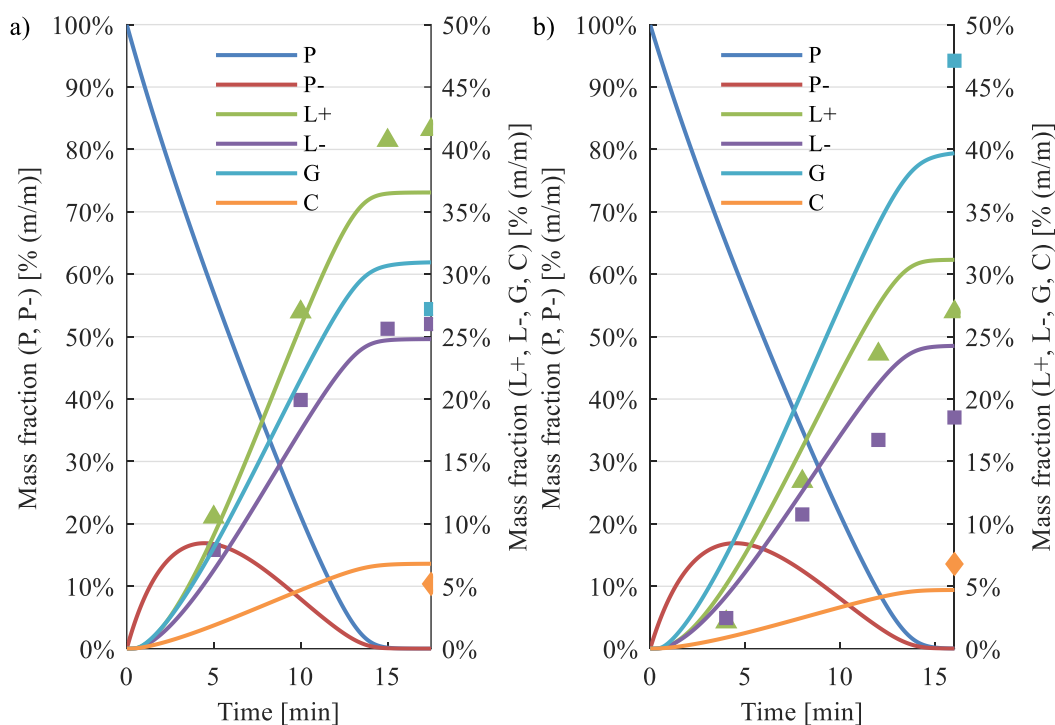


Figure 4.4. Pseudocomponent mass fractions from run nr. 3 (a) and 5 (b) at 455 °C – experimental (markers) and simulation (lines).

The results of the thermal pyrolysis at 425 °C are shown in Figure 4.5. Compared to the thermo-catalytic results shown previously, it can be seen that the thermal process is considerably slower, especially at lower temperatures, and the amount of gaseous products formed is lower, which corresponds to the preliminary assumptions and other literature results surveyed in Chapter 2. Part of the higher residual error comes from the fact that the concentrations of P and P- do not reach zero during the simulation run.

The overall amount of solid products is significantly higher without the introduction of catalysts, while the amount of liquid products remains mostly the same. Under catalytic conditions, however, the ratio of L- and L+ is higher (more components with lower molecular weight are produced) that is a consequence of the fact that ZSM-5 catalysts have high efficiency in the formation of lighter hydrocarbons, as previously indicated [224]. At 425 °C, the calculated liquid fractions appear to be systematically higher than the actual measured values. However, as mentioned earlier, Arrhenius-type kinetic parameters were identified usable at all temperature levels and using multiple datasets (seen in Table 4.1).

This can result in higher errors in some cases; on the other hand, it should be not necessarily considered a model error.

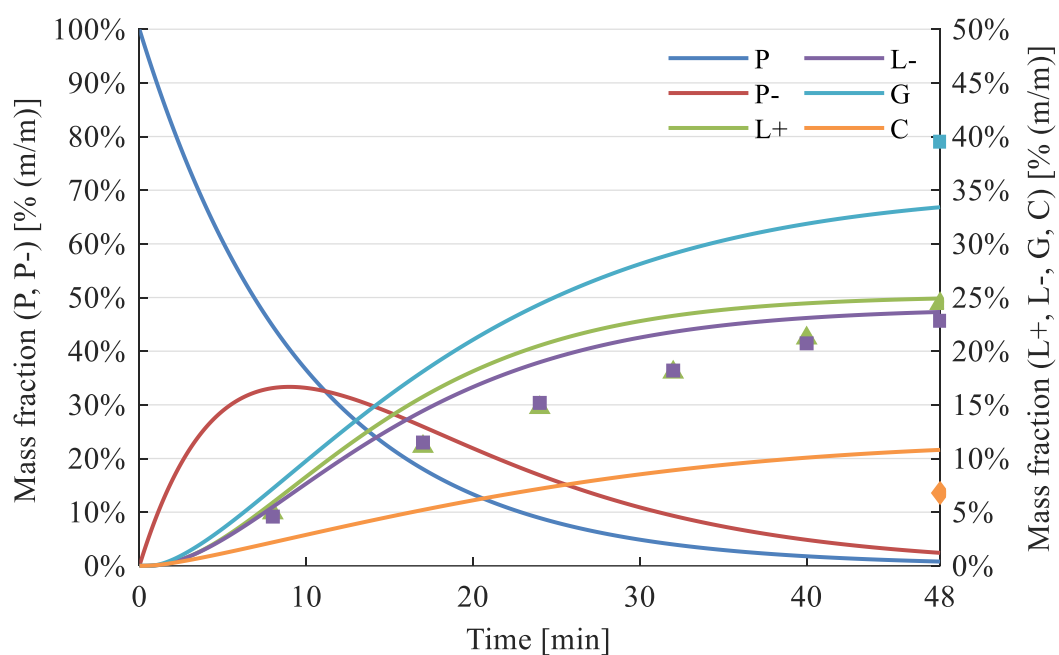


Figure 4.5. Pseudocomponent mass fractions from run nr. 8 at 425 °C – experimental (markers) and simulation (lines).

#### 4.4 Comparing the various zeolite-based catalysts

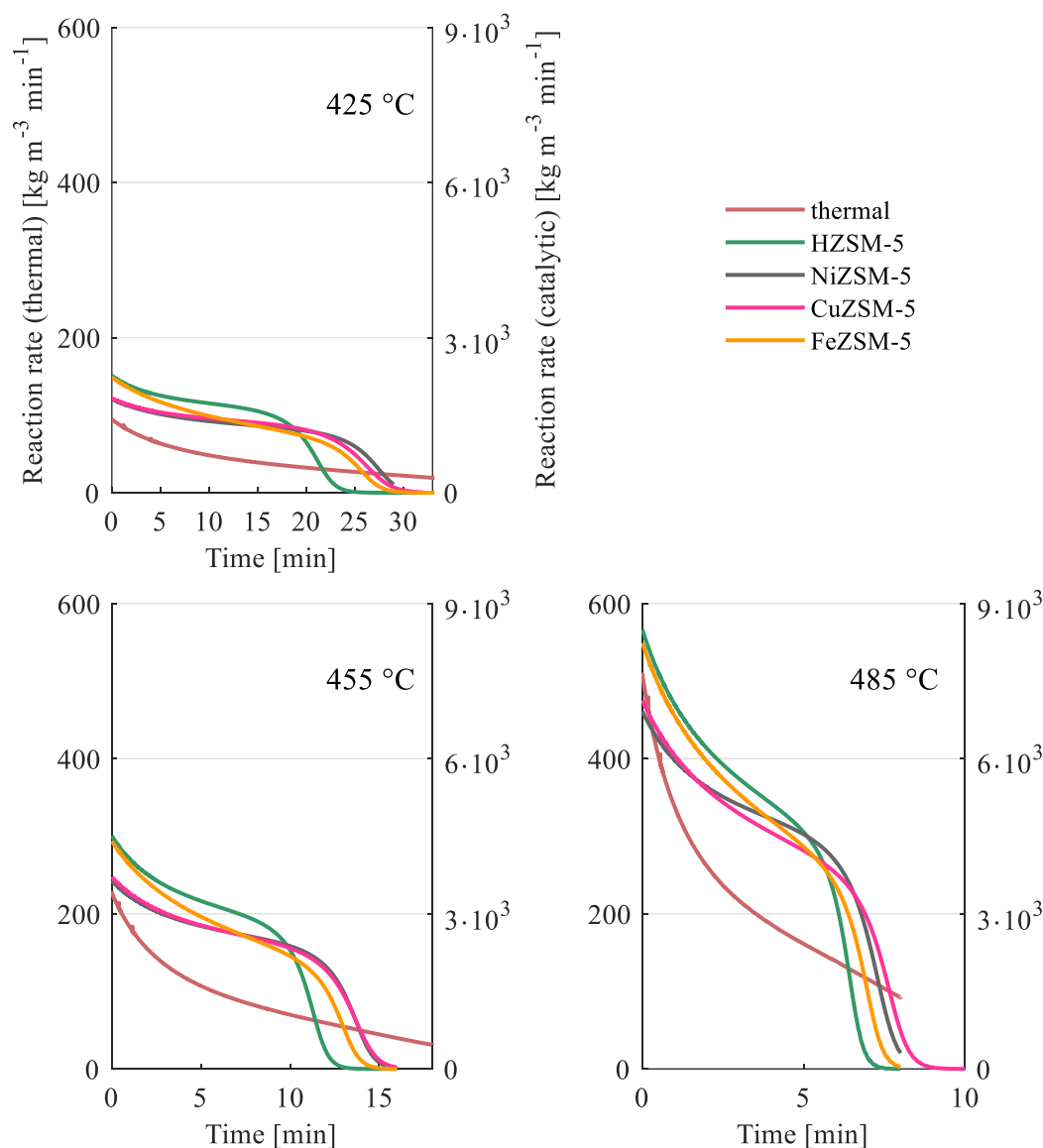


Figure 4.6. Rate of the  $P \rightarrow P^-$  reaction in case of thermal pyrolysis and in the presence of various catalysts at different temperatures

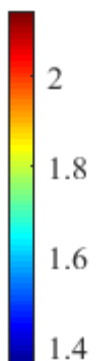
Now that we have a reliable kinetic model to investigate the pyrolysis process, we can use it to grade the various catalysts that have been applied to carry out the experiments (again, these were listed back in Table 3.1). We will be able to obtain some insight into their activity, for example, if we compare the reaction rate of the first reaction ( $P \rightarrow P^-$ ) on different catalysts. These reaction rates are shown in Figure 4.6 as a function of time. Note that the shapes of these functions are a bit

unconventional for a first-order reaction in the case of the thermo-catalytic processes; the reason behind this is the presence of the volume ratio of the catalyst and the reference phase in Eq. (3.4) that reaches high values as the conversion gets higher. It can also be seen that the reaction rates using the HZSM-5 or the FeZSM-5 catalysts are higher; therefore, the pyrolysis process overall is faster in these cases, making the application of these more favorable.

Another aspect that needs to be taken into consideration is that the main liquid product of the process is the L- as the lighter hydrocarbons are more likely to be used as fuel. Consequently, the ratio of the  $P- \rightarrow L+$  and the  $P- \rightarrow L-$  reactions can also be used to compare the catalysts investigated. This ratio is constant in the kinetic model given the nature of first-order reactions and the same reactant. The results for this comparison are listed in Table 4.3, using a further layer of coloring to distinct between the ratios more easily. Here the aim is to find the catalysts associated with lower values (i.e., where the rate of the  $P- \rightarrow L-$  is higher). Such is the CuZSM-5 catalyst. This would mean that while its overall activity (that can be derived from Figure 4.6) is lower, the product composition that can be achieved by using it is more preferable. The final choice of catalyst would depend on the specific application purpose of the pyrolysis process and the liquid product. Nevertheless, the model-based comparison of the catalysts can be a powerful tool in aiding that decision.

Table 4.3. Ratio of the rates of  $P- \rightarrow L+$  and  $P- \rightarrow L-$  reactions in case of thermal pyrolysis and in the presence of various catalysts at different temperatures

Catalyst	Temperature		
	425 °C	455 °C	485 °C
none (thermal)	1.353	1.721	2.146
HZSM	1.680	1.591	1.513
NiZSM	1.521	1.607	1.690
CuZSM	1.353	1.365	1.595
FeZSM	1.682	1.622	1.570



There is one more thing. One can argue that the observations we have made by far on the catalysts using the developed lumped kinetic model and the calculated reaction rates can also be derived from the experimental data directly (although not so straightforwardly). This is a fair point of argument, but the identified kinetic parameters have much more use. For example, we can use to pave the way of the reactor scale-up process. Its major aspects are as follows:

- Reactor layout. A possible layout of a reactor for processing shredded plastic waste is of a tubular design equipped with a screw to establish the flow of the partly solid components in the reactor.
- Flow model. The most elementary method to model such equipment is to approximate it with a plug flow reactor model similar to the one discussed in Section 3.2. This is a major difference compared to the previous simulations that involved two ideally mixed reactors.
- Size of the equipment, which is denoted in Table 4.4. The L/D value of the system was fixed at 10 to facilitate the evolution of the plug flow pattern.
- Catalyst : polymer ratio remained the same as was during the experiments on laboratory-scale (1:20) to ensure the validity of the kinetic model.

The velocity of the melted phase remained the same in the reactor (this would correspond to the rotational speed of the screw), while the velocity of the gaseous phase was calculated following Eq. (3.13). The catalyst was considered to be a separate component in the solid/melted phase.

Table 4.4. Sizing of a pilot-scale pyrolysis reactor

Parameter	Value
$L_r:d_r$ ratio [-]	10
$V_r$ [m <sup>3</sup> ]	0.05
$d_r$ [m]	0.185
$A_r$ [m <sup>2</sup> ]	0.027
$L_r$ [m]	1.85



Given the reactor model established, we can calculate the stationary product composition after the reactor. We can also carry out the optimization of the reactor inlet LHSV value. For all possible catalysts, the maximum possible LHSV value was calculated so that the amount of L<sub>-</sub> is maximal in the product:

$$\max(w_{L-}(LHSV, T)) \quad (4.6)$$

The results are shown in Table 4.5. This gives us a considerably more comprehensive insight on the problem of choosing the right catalyst as I have taken both the effect of the LHSV value and the temperature level into consideration and not only the rate of L<sub>-</sub> formation but the total amount formed from the feedstock is observed. And this is in fact the highest for the FeZSM-5 catalyst; because, although the percentage of the light liquid pseudocomponent is lower in the product, the superior LHSV value easily compensates and surpasses this; i.e. the productivity of the FeZSM-5 catalyst is the highest. This is caused by the fact that here we can carry out the process at a higher temperature level without the risk of gasification of the feedstock. This is an effect that has not been taken into consideration when I have compared the overall reaction rates.

Table 4.5. Maximizing the feedstock conversion ( $X_P$ ) and the amount of L<sub>-</sub> ( $w_{L-}$ ) in a tube reactor

Catalyst	LHSV [h <sup>-1</sup> ]	T [°C]	X <sub>P</sub>	w <sub>L-</sub>
HZSM-5	2.84	425	99.99%	42.14%
NiZSM-5	3.50	442	99.96%	38.93%
CuZSM-5	4.80	458	99.99%	32.67%
FeZSM-5	9.77	485	99.95%	40.24%

In conclusion, these results indicate that, on one hand, the type of catalyst has a significant effect on the pyrolysis process. On the other hand, by identifying the kinetic parameters of a lumped reaction system using the experimental data obtained by the application of different catalysts and comparing the identified values more systematically greatly facilitate the selection of the appropriate catalyst. The method discussed here also involves reactor scale-up calculations, i.e., we can choose the appropriate catalyst while having regard to the next phase of the design process.

## 4.5 Chapter summary

In this Chapter, I identified the kinetic parameters of the P-N0-R10 reaction network introduced in Section 3.1 in the case of several zeolite-based catalysts present, using a novel two-step identification process (Figure 4.1) whose application does not require any prior knowledge about the possible values of the kinetic parameters. The results indicate that the suggested model and identification strategy can reproduce the experimental results with the desired accuracy. In other words, the P-N0-R10 reaction network gives a good representation of the actual pyrolysis process; therefore, it can be used for pyrolysis modeling and supporting of scale-up and/or optimization tasks. I introduced a possible scenario for the scale-up process in Section 4.4 and showed that while the application of the CuZSM-5 catalyst results in a higher amount of lighter components in the liquid product, the productivity of the FeZSM-5 catalyst is higher because the lesser amount of gaseous products at high temperature levels.

Although I did not emphasize in this Chapter, some reaction rates in the identified reaction network are significantly lower than others (as indicated by the activation energies listed in Table S8) that gives space to the reduction of the kinetic model, an idea further investigated in Chapter 6. More importantly, it might be possible to increase the number of pseudocomponents present in the model without increasing the number of reactions, thereby describing the experimental data in greater detail. The details are discussed in Chapter 7.

## 5 Identification and observability of lumped kinetic models

The VGO-N0-R15 lumped reaction network shown in Figure 3.4 consists of no less than 15 reactions between six pseudocomponents. It includes every possible pathway on that a heavier compound can decompose into a lighter one, i.e., it is a form of safe-play for the kinetic modeling of hydrocracking. Moreover, the reaction network might be a little dense compared to the relative scarcity of the measurement data. Therefore, in this Chapter, I propose a systematic way to reduce the reaction network while preserving its ability to model the hydrocracking process with the required accuracy. Specifically, I did the following:

- I developed three different strategies to reduce the size of the reaction network and identify its kinetic parameters at the same time. I present these strategies in Section 5.1.
- In Section 5.2 I show that the reduction of the kinetic model is indeed necessary as several alternative networks exist that describe the experimental result at the same error level. In other words, the solution is uncertain.
- I introduce the observability criterion coming from the field on control theory in Section 5.3 that I will use to construct a reduced reaction network whose all states (i.e., rate coefficients) are observable; therefore, identifiable. I show that this extent of kinetic network reduction is achievable using one of the developed identification strategies.

### 5.1 Identification strategies

The main objective is to minimize the difference between the measured and calculated compositions, which is defined as

$$f^2(\underline{x}^n) = \sum_T \sum_{comp} \sum_{LHSV} \left( \frac{c_m - c_c}{c_m^{max}} \right)^2 \quad (5.1)$$

where  $c_m$  and  $c_c$  are the measured and calculated mass concentration values, respectively, while  $y_m^{max}$  represents the maximum measured mass concentration

value for a specific component (*comp*), including all temperature (*T*) and *LHSV* values. Measured mass concentration values originate from the previously mentioned work of Sadighi et al. [218], also given in Table S9 in the Appendix. In the absence of any information about the accuracy of the measured data, I did not address the effect of measurement error on the model solution thoroughly. Instead, I focused on the solution of the model and the optimization problem. Interestingly, the quality of the experimental data can be broadly assessed, as shown later in this Chapter. To solve the optimization problem, the NOMAD software package was used (refer to Section 4.1).

The objective function variables are the reaction kinetic parameters; however, one must address the fact that not all reactions are necessarily present in the system. Considering the full and all possible reduced networks, there are 32 777 possible variants that cannot be evaluated on a reasonable time horizon. The solution presents itself as to assign existence variables to each reaction and solve the obtained MINLP problem; however, since the objective function for a lumped kinetic reaction network is highly nonlinear and no a priori information is available for the reactions present, finding the best solution as the global minimum is at least time-consuming and involves various trial-and-error searches, regarding the algorithm parameters, such as the initial function value. In order to overcome that obstacle, I evaluated three different approaches.

The brief concept of the first, sensitivity-based selection strategy (shown in Figure 5.1) is described as follows:

1. For each reaction, the objective function value was calculated in a sensitivity study by varying the kinetic parameters of that reaction only from 1% to 200% of the middle of the related search intervals.
2. The reaction associated with the minimum objective function value was specified as part of the reaction network.
3. The kinetic parameters of the reaction network were identified by minimizing the function value from Eq. (5.1). That means the dimension of the search space was increased by 2 in each step (from 2 to 30 in total). The results from the previous run were used as initial values for the algorithm in the next iteration.

4. The specified reaction was marked so that it does not participate in further sensitivity studies.
5. The second, third, ..., 15<sup>th</sup> reaction was identified by repeating steps 1-4.

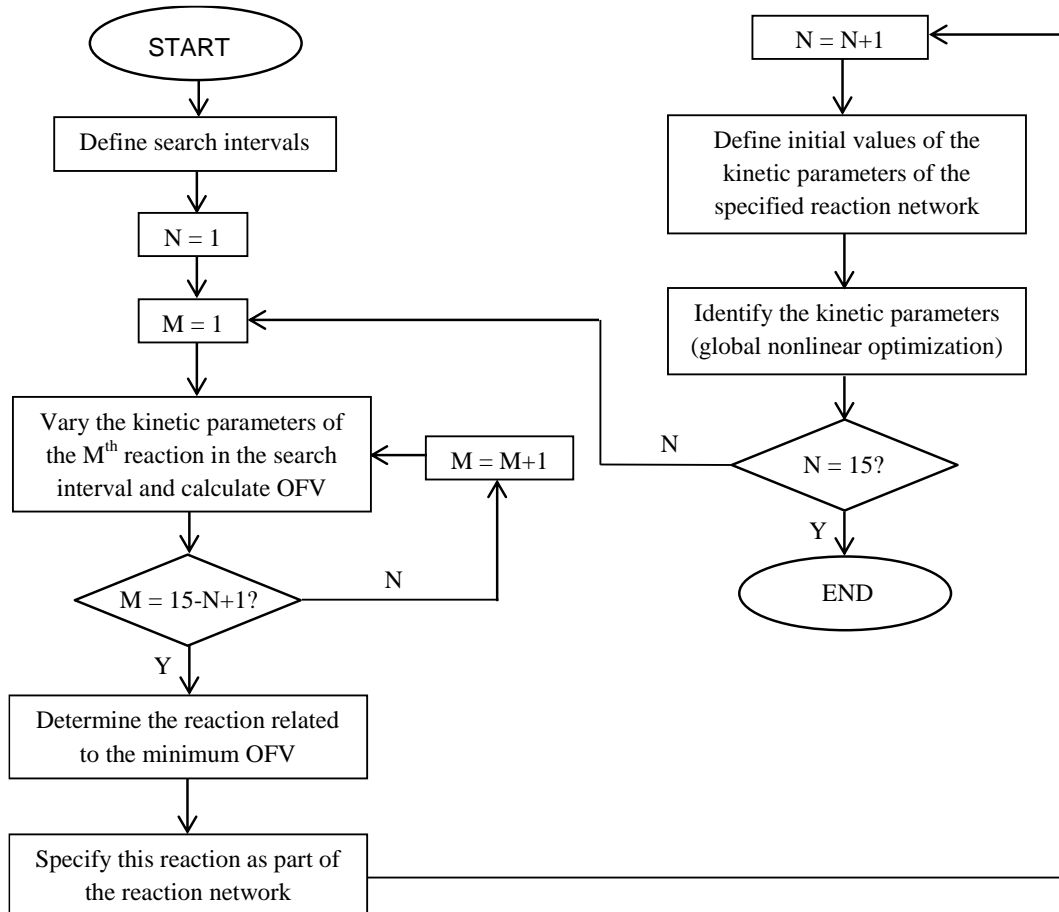


Figure 5.1. First reaction network identification strategy

The second strategy (top-down elimination) consists of the following steps (shown in Figure 5.2):

1. Identification of the kinetic parameters for the full reaction network.
2. Identification of the kinetic parameters for each subsystems consisting of one less reaction.
3. The elimination of that one reaction where the identified subsystem leads to the best results (i.e., minimum objective function value).
4. Further reactions were eliminated stepwise by repeating steps 2 and 3. The parameter values identified in the previous step were used as initial values in the next step.

This strategy is significantly more computation-intensive than the previous one as more than 100 nonlinear edge search problems must be solved in total. However, it has better convergence when applying the results of an  $n$ -reaction subsystem as the initial values of the next in a given step.

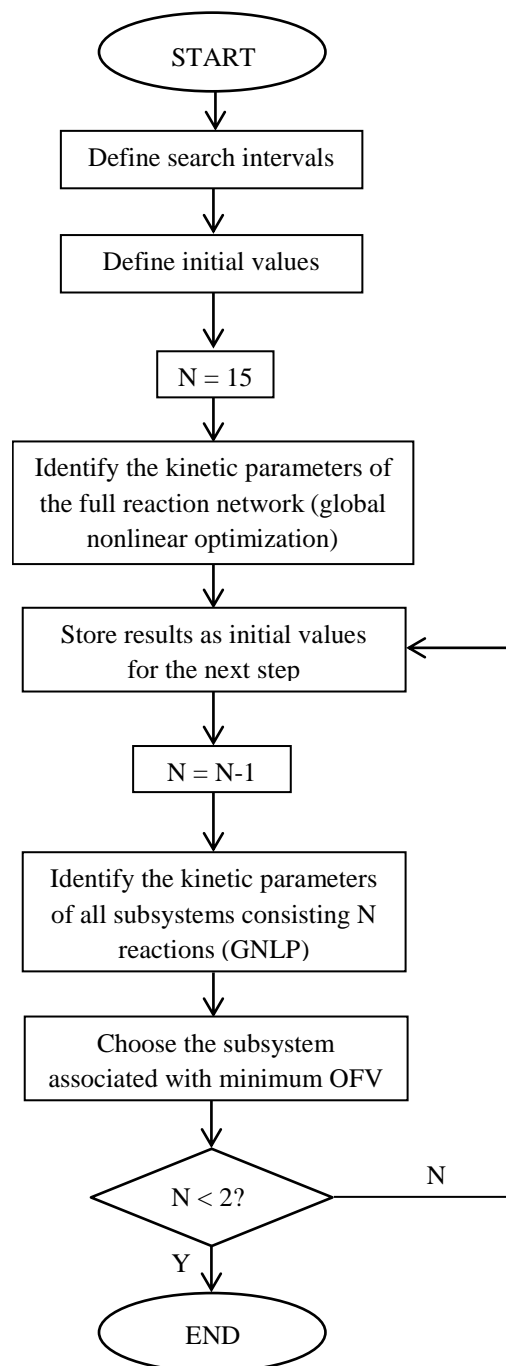


Figure 5.2. Second reaction network identification strategy

Finally, a third strategy (shown in Figure 5.3) was defined that covers the conventional MINLP approach with a stepwise extension of the search space:

1. For the first step, there are 15 binary existence variables and 30 kinetic parameters. The reaction subnetwork to be identified consists of one reaction (e.g., the sum of existence variables is 1). The program searches for the reaction where the value of the objective function is at minimum and identifies the parameters of that reaction while keeping the values of all other kinetic parameters at zero at the same time.
2. For each subsequent step, the number of existence variables is decreased by one as the program searches for an additional reaction to expand the reaction network to minimize the value of the objective function further. The kinetic parameters of that additional reaction, as well as those of the previously added reactions, are identified.

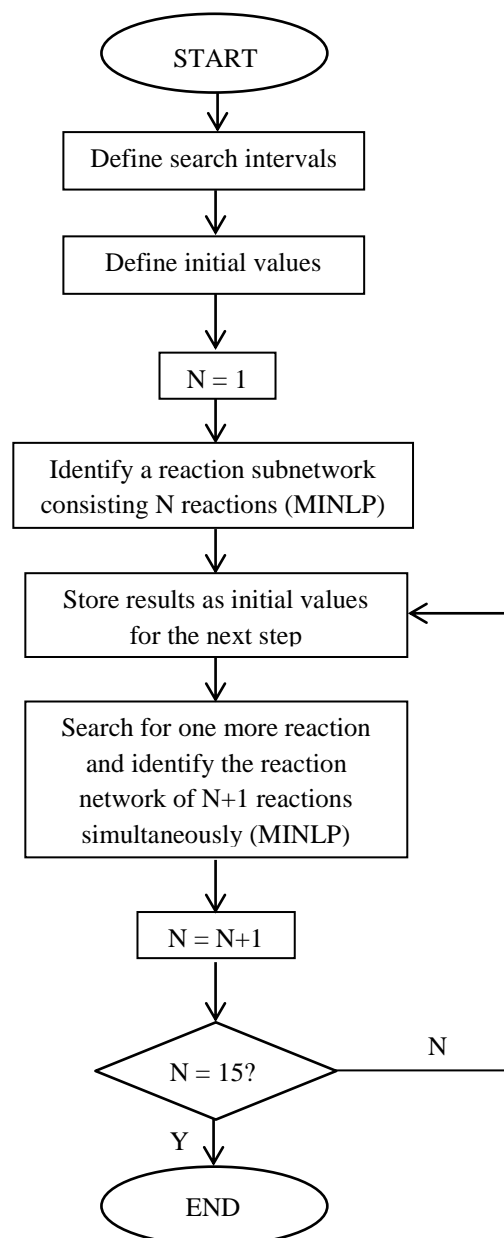


Figure 5.3. Third reaction network identification strategy

The vector of search variables,  $x$ , from Eq. (5.1) has a general form that is expressed in Eq. (5.2).

$$\underline{x}^n = \left[ \underline{exs}^T \quad \underline{k}_0^{nT} \quad \underline{E}_a^{nT} \right]^T \quad (5.2)$$

$\underline{x}^n$  is a column vector that consists of the existence variables and the normalized values (refer to Eq. (4.3)) of pre-exponential factors and activation energies searched for in a given step of a given strategy (hence, the length of  $\underline{exs}$  is zero for the first two strategies). All variables were normalized between 0 and 1 for faster and better convergence. The values of upper and lower bounds



(summarized in Table 5.1) were determined from a set of preliminary studies regarding the complete reaction network as no a priori data are available for the lumped reactions.

Table 5.1. Lower and upper bounds of kinetic parameters of the specified reactions used in every identification strategy

Reaction	$k_0$ [ $\text{m}^3 \text{h}^{-1} \text{m}_{\text{cat}}^{-3}$ ]		$E_a$ [ $\text{J mol}^{-1}$ ]	
	LB	UB	LB	UB
VGO $\rightarrow$ D	$3.6 \cdot 10^9$	$3.6 \cdot 10^{10}$		
VGO $\rightarrow$ K	$3.6 \cdot 10^{16}$	$3.6 \cdot 10^{17}$		
VGO $\rightarrow$ HN	360	3600		
VGO $\rightarrow$ LN	$3.6 \cdot 10^{13}$	$3.6 \cdot 10^{14}$		
VGO $\rightarrow$ G	360	3600		
D $\rightarrow$ K	$3.6 \cdot 10^{15}$	$3.6 \cdot 10^{16}$		
D $\rightarrow$ HN	36	360		
D $\rightarrow$ LN	3.6	36	0	$4 \cdot 10^5$
D $\rightarrow$ G	3.6	36		
K $\rightarrow$ HN	$3.6 \cdot 10^9$	$3.6 \cdot 10^{10}$		
K $\rightarrow$ LN	360	3600		
K $\rightarrow$ G	360	3600		
HN $\rightarrow$ LN	$3.6 \cdot 10^8$	$3.6 \cdot 10^9$		
HN $\rightarrow$ G	0.36	3.6		
LN $\rightarrow$ G	$3.6 \cdot 10^7$	$3.6 \cdot 10^8$		

## 5.2 Performance of the reaction network reduction algorithms

In the case of the initial reaction network identified as VGO-N0-R15 with 15 reactions, the identified kinetic parameters are shown in Figure 5.4. (Refer to Table S1 for all variations of the hydrocracking reaction network.) This is the so-called nominal case; the performance of every reduced reaction network should and will be compared to this. The numerical values of the kinetic parameters obtained using each identification strategy (three strategies and 15 steps – 45 reaction networks overall) can be found in the appendix (in from Table S10 to Table S15), while this and the next section contain the analysis of the apparent trends.

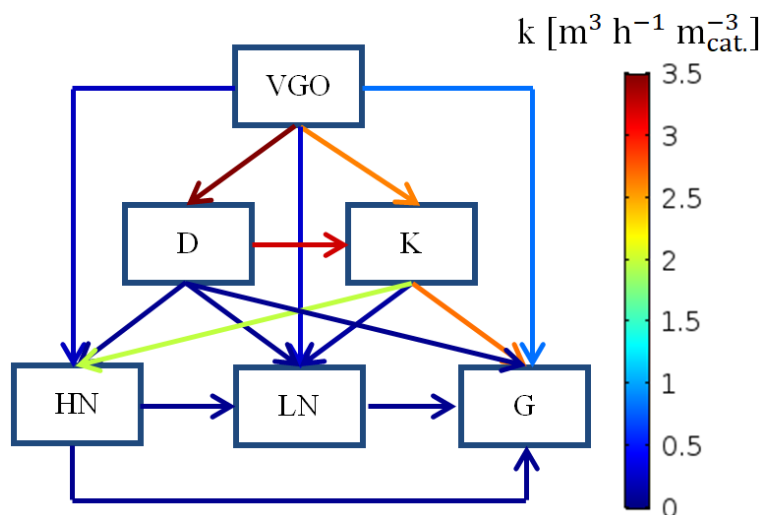


Figure 5.4. VGO-N0-R15 reaction network consisting of 6 component lumps and 15 lumped reactions

Firstly, I would like to show the accuracy of these reaction networks. The values of the objective function (Eq. (5.1)), which can be interpreted as the sum of normalized error between measured and calculated yields for all six lumps, are shown in Figure 5.5. The objective function values decrease exponentially, depending on the number of reactions considered in the model, depicted by a purple dashed line that is a result of the regression of an exponential decay function to the averages of the three objective function values against each set of reactions present. The values from each of the strategies decrease monotonously, which suggests that the results are mostly free from numerical errors. The results from the sensitivity-based elimination strategy are the closest to the average, likely because of its relatively simple structure. For the second case, small objective function values were obtained, even for a smaller number of reactions than in case of the other two strategies as the search space in this case included a higher number of reaction network subsystems, leading to more accurate results (at the cost of being more resource-intensive, however). The results from the MINLP-based stepwise extension are the least accurate; for example, there is a plateau between five and seven reactions where the objective function value remains the same, which leads to the conclusion that, while it seems to be a somewhat evident choice, this is the least suitable for model reduction in our case.

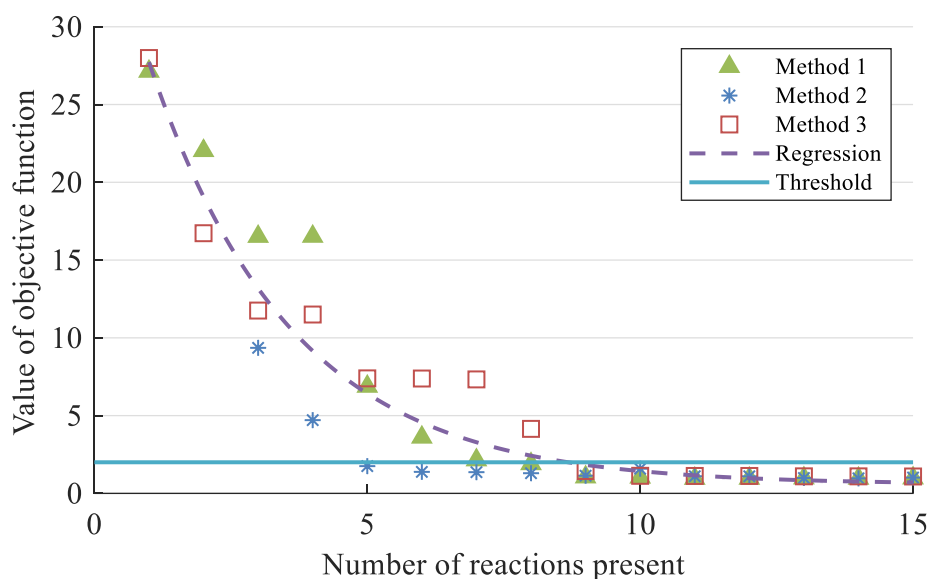


Figure 5.5. Objective function values for reaction subnetworks obtained by different model reduction methods

Although no sharp border can be drawn between accurate and inaccurate reaction networks, I have set up a threshold in Figure 5.5 above that the agreement of the identified system with the measured data rapidly lessens (up to the point where some of the lumps do not even appear). This was done after examining the different model results and obtained concentration profiles individually. The value of this limit is approximately 2.0 (marked with a solid blue line in Figure 5.5); two times higher than the lowest obtained objective function value. This is a soft threshold, i.e. an objective function value of 2.1 should not necessarily be discarded; moreover, this threshold value is an inherent part of the problem specified and cannot be considered as a general result. On the other hand, it can be used to indicate model accuracy.

Based on Figure 5.5, it can be assumed that minimum five reactions are necessary to describe the concentration changes of each defined lump in the system. This was obtained using Method 2. At nine reactions, all methods present a viable solution. More than nine reactions do not further reduce the error of the model significantly. The square of Pearson correlation coefficients between measured and calculated data for each lump and the overall data series are listed in Table 5.2. The results are compared to the original work by Sadighi et al. [219], and show a considerable improvement, even for a five-reaction subsystem,

probably due to the use of more-complex optimization algorithms. With the correlation factors for individual components taken into consideration, the results for the nine reaction subsystem obtained from the third strategy can be assumed to be the best, predicting the yields of all lumps except Diesel (D) adequately. The latter may as well indicate some underlying errors in the measured data, because, as can be seen in Table S9, the measurement values for the Diesel component have no clear trend as a function of LHSV. The reactor model introduced in Section 3.2 is not able to reproduce such behavior, and it is arguable whether that would be necessary, or there are just some underlying errors in the mass concentration values. Nevertheless, the obtained correlation values still present an improvement compared to the original model.

Table 5.2. Pearson correlations between measured and calculated data

	<b>Original work</b>	<b>5 reactions</b>		<b>9 reactions</b>	
		<b>Method 2</b>	<b>Method 1</b>	<b>Method 2</b>	<b>Method 3</b>
VGO	0.852	0.906	0.912	0.912	0.909
Diesel	0.018	0.409	0.346	0.318	0.401
Kerosene	0.731	0.920	0.921	0.913	0.916
Heavy Naphtha	0.814	0.893	0.890	0.892	0.897
Light Naphtha	0.652	0.937	0.945	0.947	0.827
Gas	0.816	0.753	0.796	0.789	0.841
Overall	0.589	0.928	0.932	0.931	0.931

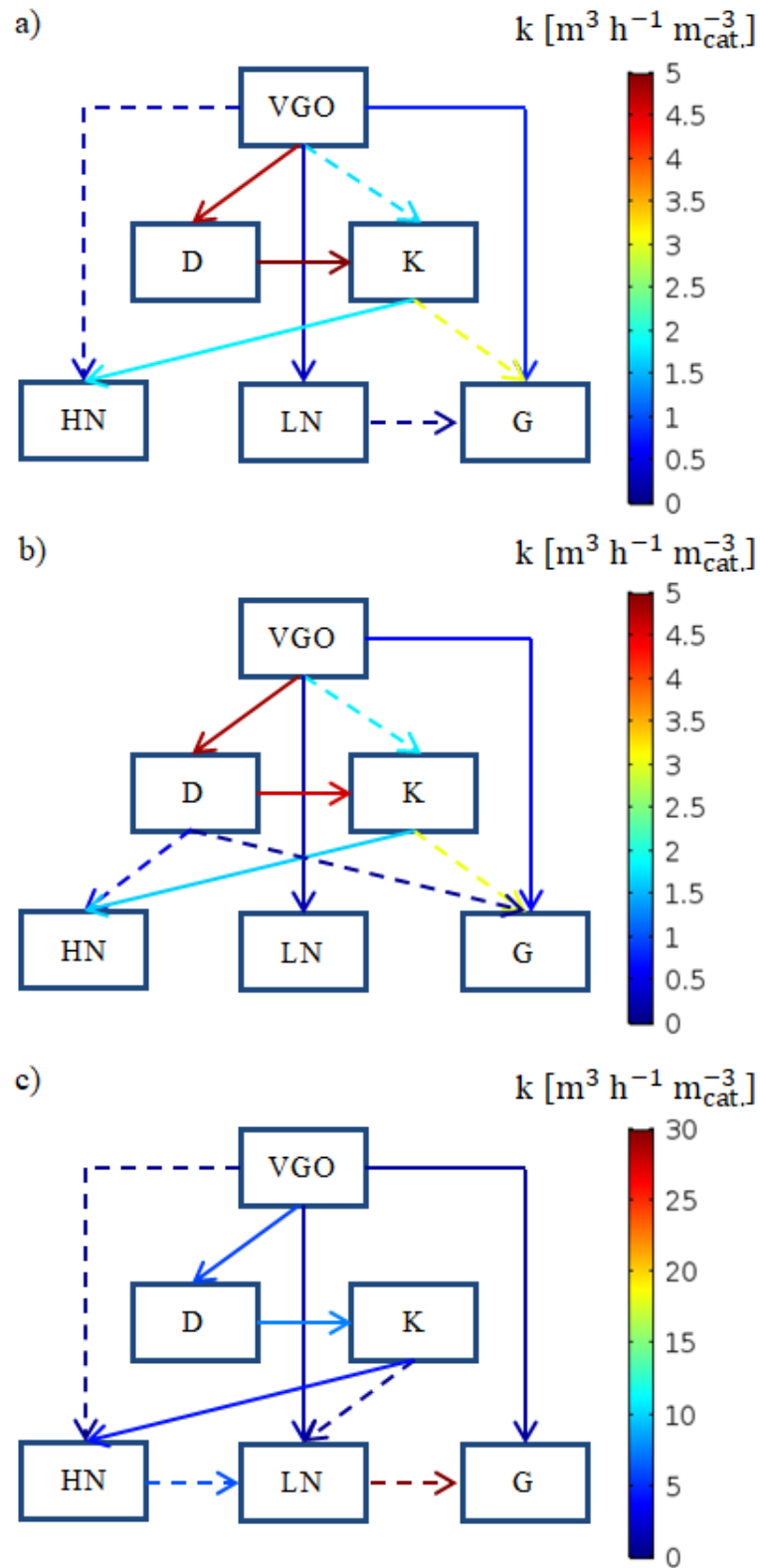


Figure 5.6. VGO-N0-R9 reaction networks consisting of 6 lumps and 9 reactions, obtained by (a) Method 1, (b) Method 2, and (c) Method 3. Reactions that are not present in all three networks are marked with dashed lines

Consequently, the nine-reaction subsystems identified with each strategy (VGO-N0-R9) have been investigated more thoroughly. (Refer to Table S1 for all variations of the hydrocracking reaction network.) The reduced reaction networks for all strategies are shown in Figure 5.6. (Again, refer to Table S10 to Table S15 in the Appendix for the numerical values.) It can be seen that there are only five of the nine reactions (VGO→D, VGO→LN, VGO→G, D→K, and K→HN, highlighted with red directed lines) are present in all three subsystems; in other words, these reaction networks differ significantly from each other, even though the resulting pseudocomponent yields are actually the same. Some of the differences can be explained with underlying consecutive reactions, i.e., a VGO→K lumped reaction can be substituted with a VGO→D→K consecutive pathway by choosing the values of the rate coefficients appropriately, whereas, in the case of other reactions (i.e., LN→G), these substitutions cannot be carried out.

### 5.3 Observability of the reaction networks

The existence of different reaction networks leading to almost the same results might explain the numerical uncertainties encountered while solving the optimization problems; however, more importantly, this raises some doubt about whether there exists a proper solution in the case of subnetworks consisting of nine (or more) reactions such that the objective function value has a global minimum.

In order to address this problem systematically and quantitatively, I investigated the observability of the extended state-space model. The reactor component balance equations expressed in Eq. (3.11) are similar to a state-space model in structure that has a general form as described in Eq. (5.3) and (5.4). Given that a plug-flow reactor model can be rewritten as a cascade of continuous stirred-tank reactors, the concentration changes along the axial coordinate of the reactor are mathematically equivalent to time derivatives. Therefore, in the case described here, residence time was defined as the ratio of reactor length and actual space velocity, eliminating the necessity of model conversion.

$$\frac{dx}{dt} = \underline{A} \cdot \underline{x} + \underline{B} \cdot \underline{u} \quad (5.3)$$

$$\underline{y} = \underline{C} \cdot \underline{x} \quad (5.4)$$

In the state-space model:

- $\underline{A}$  is the system matrix ( $\underline{A} = \eta \cdot \varepsilon' \cdot \underline{L}$ ),
- $\underline{x}$  is the state vector ( $\underline{x} = \underline{c}$ ),
- $\underline{y}$  is the output vector ( $\underline{y} = \underline{c}$ ; the concentrations of all lumps are measured),
- $\underline{C}$  is the output matrix ( $\underline{C} = \underline{I}$ ), and
- the term  $\underline{B} \cdot \underline{u}$  is negligible (there are no inputs).

This state-space model was extended to include the reaction rate coefficients as states as well. In other words, the state vector includes six states, accounting for the six components, and one additional state for each reaction present (Eq. (5.5)). For example, the state-space representations of the nine-reaction networks from Figure 5.6 have 15 states, while the original reaction network (Figure 5.4) has 21.

The output vector  $\underline{y}$  includes only the component concentrations in all cases because the rate coefficients are not measured. The output matrix was expanded with zero vectors to accommodate the increased number of states.

$$\underline{x}^e = [\underline{c}^T \quad \underline{k}^T]^T \quad (5.5)$$

One of the main consequences of the extension of the state-space model that it becomes nonlinear, because  $\underline{L}$  contains state variables in this interpretation. Hence, it should be linearized in order to study the observability and identifiability of the system. This step was carried out using complex step differentiation, which has been described elsewhere [238] that is well-known for its accuracy, even for small step sizes.

If the concentrations of six lumps are measured and 21 states are observable, all 15 reaction rate coefficients can be determined from the 6 states measured. However, if less than 21 states are observable, not all of the rate coefficients can be identified adequately. That has the practical consequence that two or more sets of parameter values in the model lead to the same output values. In other words, more kinetic parameters were identified in the given system than theoretically possible; therefore, that solution cannot be considered to be valid.

The number of observable states was determined by calculating the rank of the observability matrix (Eq. (5.6)), where  $A$  is the system matrix,  $C$  is the output matrix, and  $n$  is the number of states in the system:

$$\mathcal{O} = \begin{bmatrix} C \\ CA \\ CA^2 \\ \vdots \\ CA^{n-1} \end{bmatrix} \quad (5.6)$$

The state-space model was linearized around the reactor outlet; the results for the component VGO at 380 °C for each LHSV values are shown in Figure 5.7. For the sake of better understanding, both the original and the linearized state-space model were solved around the reactor outlet; naturally, the values for  $\ell > 1$  bear no physical meaning. The figure indicates good agreement between the results from solving the actual and the linearized state-space models; therefore, the system matrix of the latter can be used for the calculation of the observability matrix.

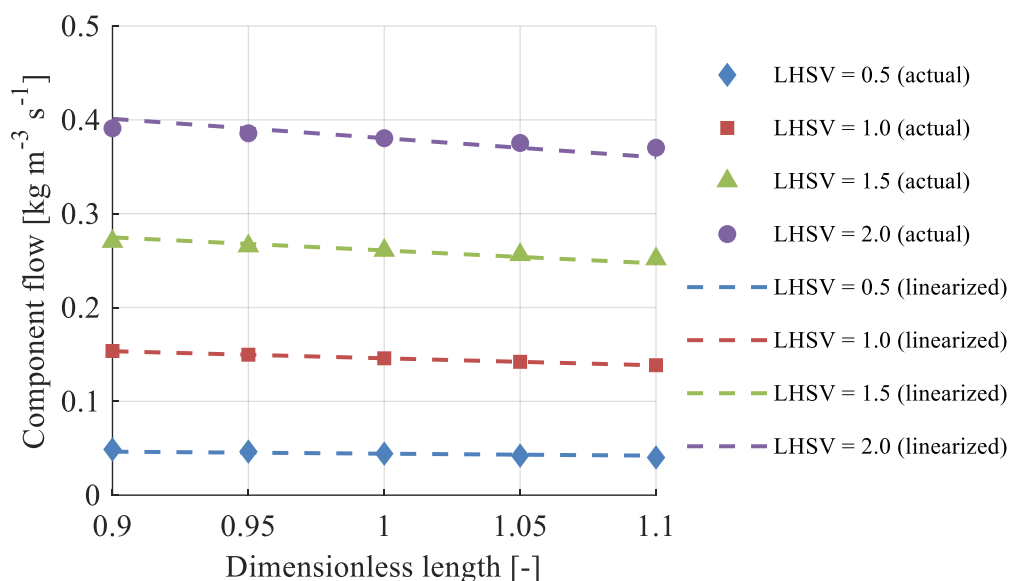


Figure 5.7. Results of the state-space model linearization at the outlet of the reactor for VGO at 380 °C

In Figure 5.8, the number of observable states is depicted as a function of states for the three strategies and for all identified reaction subnetworks. The discrete values are connected with solid lines for better readability. The ideal number of observable states would equal the number of actual states in the model (marked



with the blue line). It can be seen that neither of the investigated methods produces a kinetic model that has more than 11 observable states. As there are six measured components present, the maximum number of the observable reactions is only five. It can also be seen that Method 2 did produce a reduced reaction network that has 11 states (i.e., five reactions) and 11 observable states, whereas the application of Methods 1 and 3 only resulted in 10 observable states out of 11. The reason behind the unsatisfactory performance of the latter two methods is that in these cases the remaining 10 reactions were eliminated in such a way that the remaining five are not independent of each other. Such elimination could occur because the strategies do not consider any criteria for observability. The lesser number of observable states might as well explain the high difference between the objective function values that resulted from different strategies shown in Figure 5.5.

In the case of the second top-down elimination strategy (Method 2), the number of observable states for the reaction subsystems containing one and two reactions (i.e., seven and eight states) is very low; this is because only one lump has other-than-zero concentration at the reactor outlet, which counts as an actual measurement when calculating the rank of the observability matrix.

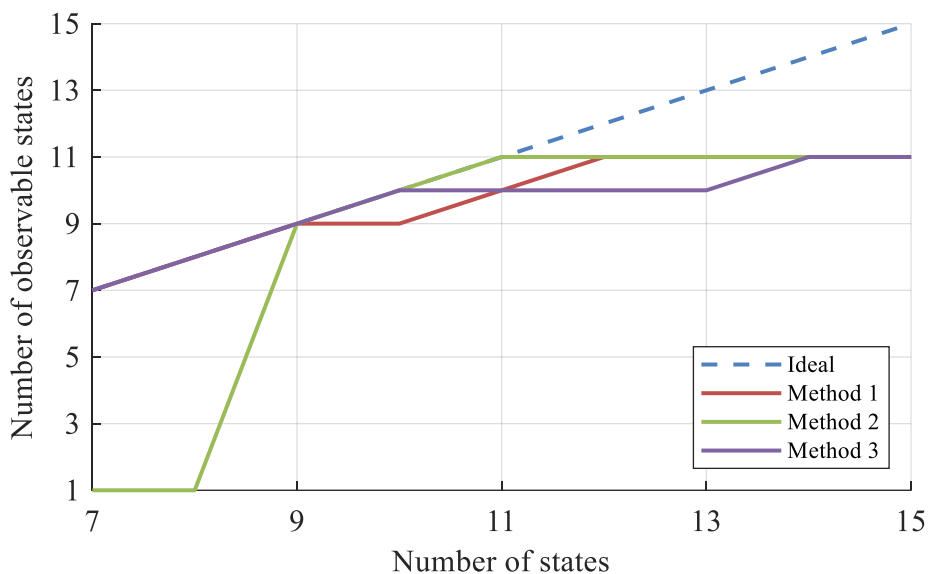


Figure 5.8. Observability of reaction networks consisting of 1-9 reactions, obtained using different methods

The final solution from the model reduction and identification, identified as VGO-N0-R5, is depicted in Figure 5.9. (Refer to Table S1 for all variations of the hydrocracking reaction network.) The model presented here somewhat disagrees with the well-known behavior of the hydrocracking reaction; in other words, the reactions do not follow a consecutive pattern (for example, Light Naphtha is produced from VGO instead of Heavy Naphtha). The main reason behind that observation is that the observability criterion strongly limits the number of reactions present in the final model; one pseudo-component can only be produced via one reaction pathway. In other words, there is only one possible 5-reaction subsystem where the consecutive reaction pathway occurs.

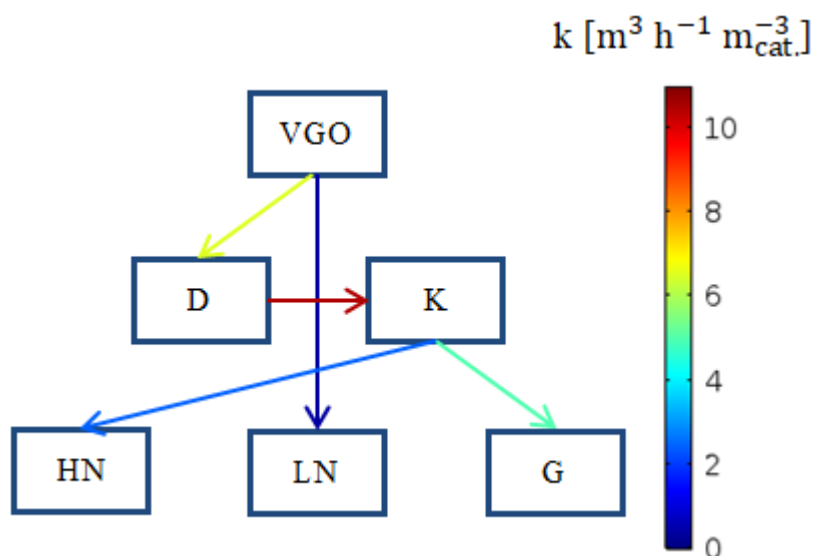


Figure 5.9. VGO-N0-R5 reaction network consisting of 5 reactions, obtained by Method 2

In order to gain more confidence in the goodness of the result in Figure 5.9, I also identified the kinetic parameters of the consecutive reaction network. The minimum objective function value associated with the consecutive pathway is 9.2, which is more than five times higher. Hence, there are two solutions. On the one hand, we could include more reactions, so the consecutive pathway is present and also the value of the objective function is acceptable. Alternatively, we might exclude some reactions from the consecutive pathway and in turn include the same number of nonconsecutive reactions, so the resulting model gives a good description of the concentration changes of the pseudo-components while the system remains also observable.

While the former approach describes the behavior of hydrocracking better, the latter ensures the certainty regarding the values of the identified kinetic parameters, which is more favorable in terms of process development and intensification. With the subsystem containing five reactions identified in the second strategy observable, the identified kinetic data represent an exact and unique solution that is the global minimum for 5 reactions, given that the performance of the optimization algorithm was good enough to find it.

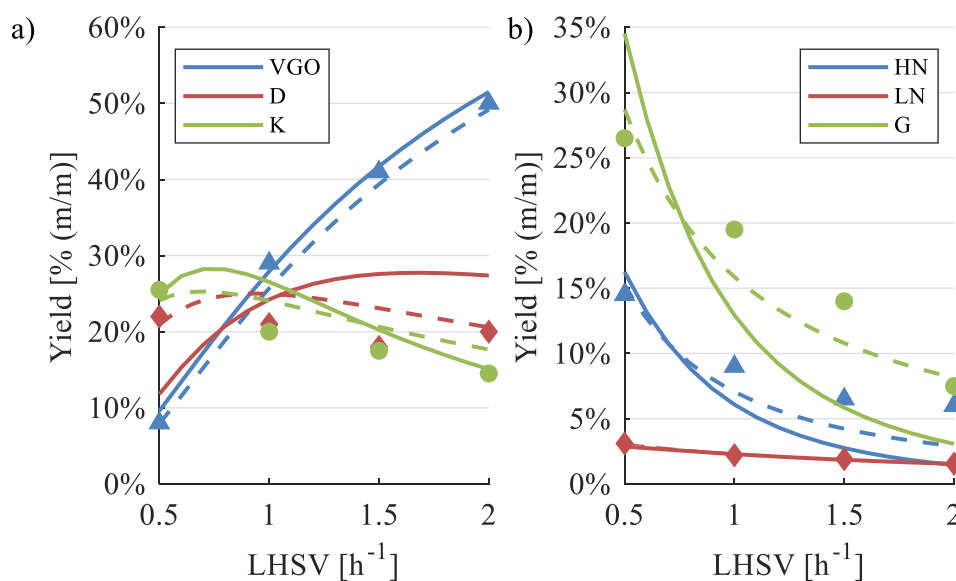


Figure 5.10. Pseudocomponent concentrations at the reactor outlet for different LHSV values at 410 °C. Data points represent measured data, dashed lines indicate the 15-reaction system results, and solid lines represent the 5-reaction system results.

The measured and calculated product compositions as a function of LHSV at 410 °C for 15 and 5 reactions present are shown in Figure 5.10. The shapes of the curves are mostly the same for the 5-reaction model and the original model consisting of 15 reactions. In some cases, the resulting curve from the former fits worse to the measured data (e.g., Gas); whereas, in other cases, the curve fitting is better (VGO). In some cases, somewhat poor correlation between measured and calculated data can be observed for both models (e.g., Diesel). However, the results of the sensitivity analysis on the kinetic parameters imply that this issue is related, at least in part, to measured data and could be overcome by the

application of different lumping strategies. This may well be part of a further investigation.

## 5.4 Chapter summary

An important issue regarding model reduction is that how many reactions can be identified from the data available. We can construct a reaction network that includes an arbitrary number of reactions. The VGO-N0-R15 reaction network investigated in this Chapter is a meaningful example because it includes every possible pathway on that a heavier compound can decompose into a lighter one. Firstly, I showed that this many reactions are a bit overkill in the sense of model error as at the worst case nine reactions are sufficient to describe the concentration changes in the experimental data. Secondly, I showed that the resulting VGO-N0-R9 reaction network can still be overdetermined because it is not clear which nine reactions to include from the original 15 in the reduced model. To address this problem, I introduced the concept of observability in reaction systems for lumped components. I evaluated the state-space model representation of the system to determine whether a given reaction system is observable, i.e., all kinetic parameters are theoretically identifiable. The investigation led to the construction of the VGO-N0-R5 reaction network. I investigate the uncertainties associated with the VGO-N0-R15 and R5 models in greater detail in Chapter 8.

Chapter 5 introduced the first method promised in Section 2.4 (Reducing the uncertainties in lumped reaction networks). The identification strategies proposed here, although very thorough, were very time-consuming and somewhat specific to the VGO hydrocracking problem. So in the next Chapter, I continue with a faster and more universal approach, namely, Global Sensitivity Analysis.

## 6 Reduction of lumped reaction networks using global sensitivity analysis

In the previous Chapter, I have introduced the concept of reducing reaction networks, developed three different novel methods to achieve it and used the observability criterion to ensure parameter identifiability. Chapter 6 takes a slightly different approach and has a dual purpose. Firstly, it discusses the applicability of Global Sensitivity Analysis (GSA) in the reduction of lumped reaction networks. I compare the five different GSA methods reviewed in Section 2.4.2 based on their performance, using the previously introduced case studies of real plastic waste pyrolysis (Section 3.1) and vacuum gas oil hydrocracking (Section 3.2).

Secondly, I present another method in this Chapter that can be used to assess the uncertainty of the reaction network. I calculate the confidence bounds of the kinetic parameters of both the full and the reduced models and use these to quantify parameter uncertainty. The aim of this Chapter is to illustrate how GSA can be used to construct lumped reaction networks with fewer parameters to be estimated with narrower confidence intervals; i.e., to show that the uncertainty of lumped kinetic models can be significantly diminished.

### 6.1 Choosing the right number of samples

For my calculations, I used the RS-HDMR implementation in MATLAB called GUI-HDMR by Ziehn and Tomlin [239]. All other methods were accessed in MATLAB by using the SAFE (Sensitivity Analysis for Everybody) Toolbox [240]. Both programs were constructed so to make these methods readily available and applicable with no requirement of detailed knowledge of any of the GSA algorithms mentioned before.

The key steps of the kinetic model reduction process can be summarized as follows:

- assign sensitivity indices for all reactions using different GSA methods;
- rank the reactions based on their sensitivity indices and eliminate as many reactions as possible while retaining a fair model fit;

- evaluate the performance of the proposed kinetic model reduction method;
- assess the uncertainty of the identified model parameters with their respective confidence intervals: narrower intervals indicate higher confidence in the reduced kinetic model.

To compute the sensitivity indices, the parameter space has to be sampled and the value of the objective function has to be calculated for each sample. In this Chapter, I have retained the use of the previously introduced objective functions (Eq. (4.1) and Eq. (5.1) for thermo-catalytic pyrolysis and VGO hydrocracking, respectively). I used uniform sample distributions, namely a one-at-a-time sampling strategy as described in [241] for EET, the search curve defined by Saltelli et al. [175] for FAST, and latin hypercube sampling for RS-HDMR, PAWN and VBSA. All methods result in a uniform sampling of the parameter space that is a reasonable approach because the model parameters are independent of each other, i.e., any combinations of the kinetic parameters can be used to evaluate the performance of the kinetic model (the experimental data and the corresponding minimum value of the objective function ultimately determine which combinations are actually applicable but this does not affect the sensitivity analysis itself).

Apart from the sampling method, the size of the sample also needs to be determined. For each method, I examined the convergence of sensitivity indices as a function of the sample size. An example of the results of this study is given in Figure 6.1 for RS-HDMR. Kinetic parameters with significantly low sensitivity indices were omitted. If the sample size is small, the sample does not interpret the objective function properly; this results in a high variance of the sensitivity indices. I defined a minimum sample size in case of all methods where the sensitivity indices had reached a quasi-constant value. The chosen sample sizes can be seen in Table 6.1. It should be noted that in the case of the FAST method there is a minimum sample size defined by Cukier et al. [174], and the convergence analysis showed that for larger number of samples the calculated sensitivity indices do not change at all; hence, in this case the minimum sample size was used.

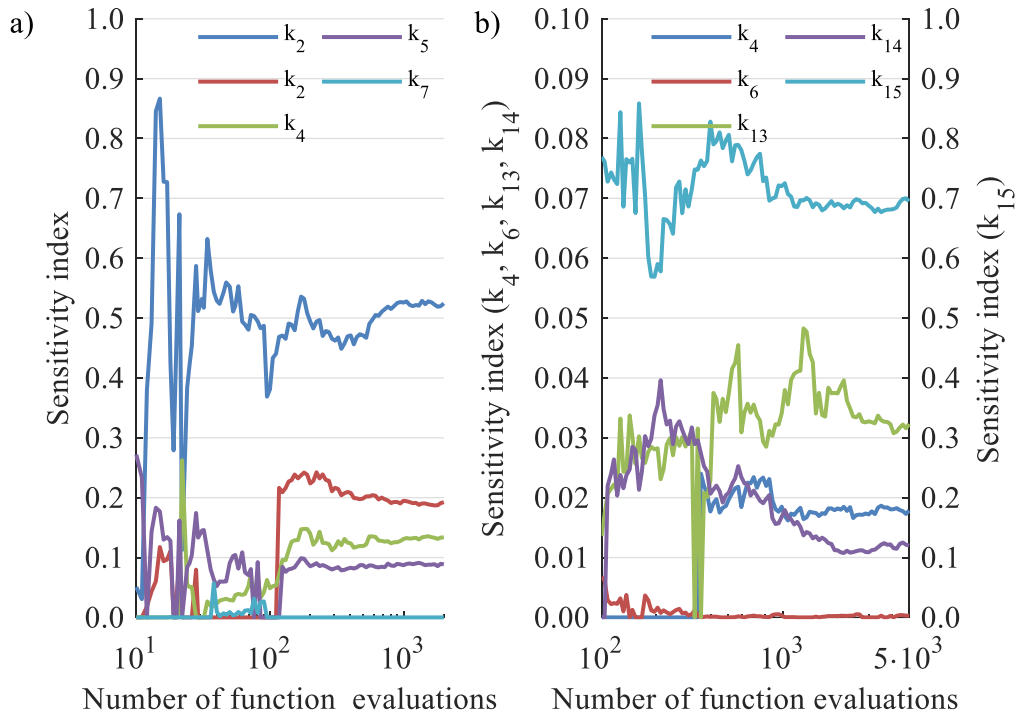


Figure 6.1. Convergence of RS-HDMR sensitivity indices in case of a) thermo-catalytic pyrolysis, b) VGO hydrocracking

Table 6.1. Sample sizes chosen for different GSA methods and case studies.

	Thermo-catalytic pyrolysis	VGO hydrocracking
EET	2 000	6 400
FAST	1 289	4 105
PAWN	13 700	45 300
RS-HDMR	1 000	3 000
VBSA	1 870	6 460

Using the determined sample sizes, I calculated the sensitivity indices, carried out the reduction of each lumped kinetic network and compared the results of the original and the reduced networks. Results for thermo-catalytic pyrolysis and VGO hydrocracking are discussed in Section 6.2 and Section 6.3, respectively. In Section 6.5, I discuss some further advantages of reaction network reduction and using global sensitivity analysis to that end.

## 6.2 Case study 1: thermo-catalytic pyrolysis

The computed sensitivity indices for different GSA methods are shown in Table 6.2. The presence of the reaction occurring in the first step ( $P \rightarrow P^-$ ) in the kinetic model is mandatory; therefore, the sensitivity of the model to it was not investigated. To achieve this, the associated kinetic parameters have to be fixed. Here I used the identified values from Chapter 4; alternatively, the sensitivity analysis could be implemented in two steps, where the first step involves all reactions, and the reaction rate coefficient of the first reaction can be approximated based on the behavior of the objective function.

In the case of the EET, FAST, and RS-HDMR methods, the obtained sensitivity indices would show that the only reactions  $r_2$ - $r_5$  influence the objective function significantly. For the other two methods, the obtained GSA indices of these reactions are still higher than of  $r_6$ - $r_{10}$ , but the magnitudes are similar. In Chapter 4, I performed a local sensitivity analysis (Figure 4.2), reaching the conclusion that the kinetic model is the most sensitive to the first three reactions. Given that the presence of the first five reactions in the kinetic model is theoretically enough to describe the concentration changes of all components, the most straightforward action is to eliminate  $r_6$ - $r_{10}$  from the original P-N0-R10 reaction network, obtaining the P-N0-R5 reduced kinetic model (Refer to Table S1 for all variations of the pyrolysis reaction network.). In P-N0-R5, all products are formed from the polymer feedstock, and no interactions between light components are present. This can be reasoned with the atmospheric pressure of the reactor and the low residence time of these lumps, resulting in a low collision frequency of the underlying compounds in the gas phase.<sup>1</sup>

---

<sup>1</sup> The low residence times of the  $L^+$  and  $L^-$  lumps also implicate one another type of model reduction that I investigate in Chapter 7.



Table 6.2. Different GSA indices for thermo-catalytic pyrolysis.

Reaction	Reactant	Product	EET	FAST	PAWN	RS-HDMR	VBSA
r <sub>2</sub>	P-	L+	3 165	0.516	0.685	0.527	0.474
r <sub>3</sub>	P-	L-	1 820	0.181	0.368	0.190	0.298
r <sub>4</sub>	P-	G	1 593	0.122	0.273	0.129	0.277
r <sub>5</sub>	P-	C	1 420	0.087	0.310	0.088	0.193
r <sub>6</sub>	L+	L-	1.515	2.90·10 <sup>-4</sup>	0.078	1.63·10 <sup>-5</sup>	0.110
r <sub>7</sub>	L+	G	0.679	6.37·10 <sup>-5</sup>	0.102	1.56·10 <sup>-5</sup>	0.109
r <sub>8</sub>	L+	C	2.926	4.46·10 <sup>-5</sup>	0.098	0	0.109
r <sub>9</sub>	L-	G	0.687	8.18·10 <sup>-5</sup>	0.077	0	0.109
r <sub>10</sub>	L-	C	1.746	7.09·10 <sup>-5</sup>	0.095	0	0.109

Figure 6.2a shows the reaction rate coefficients at 455 °C for the P-N0-R10 network (I determined these values using the methods described in Chapter 4). Coloring of arrows represents the values of rate coefficients in s<sup>-1</sup>. Note that while although the reaction rate coefficients of r<sub>6</sub> and r<sub>7</sub> have high values, the contribution of these reactions to the process is low. The reason behind this is the low concentration of L+ in the reactor. This effect can also be detected by comparing the reaction rates instead of the rate coefficients; nevertheless it would not be straightforward because, unlike the sensitivity indices, they are dependent on time.

Figure 6.2.b shows the identified P-N0-R5 reduced reaction network. The identification process of the reduced reaction network was carried out independently, i.e., I did not use the information available from the identification of the full reaction network. Numerical values are listed in Table S16 in the appendix. It can be seen that the rate coefficients of the remaining reactions compensate for the eliminated reactions as they have slightly larger values. On the other hand, the value of k<sub>1</sub> is slightly lower that might as well counter this effect.

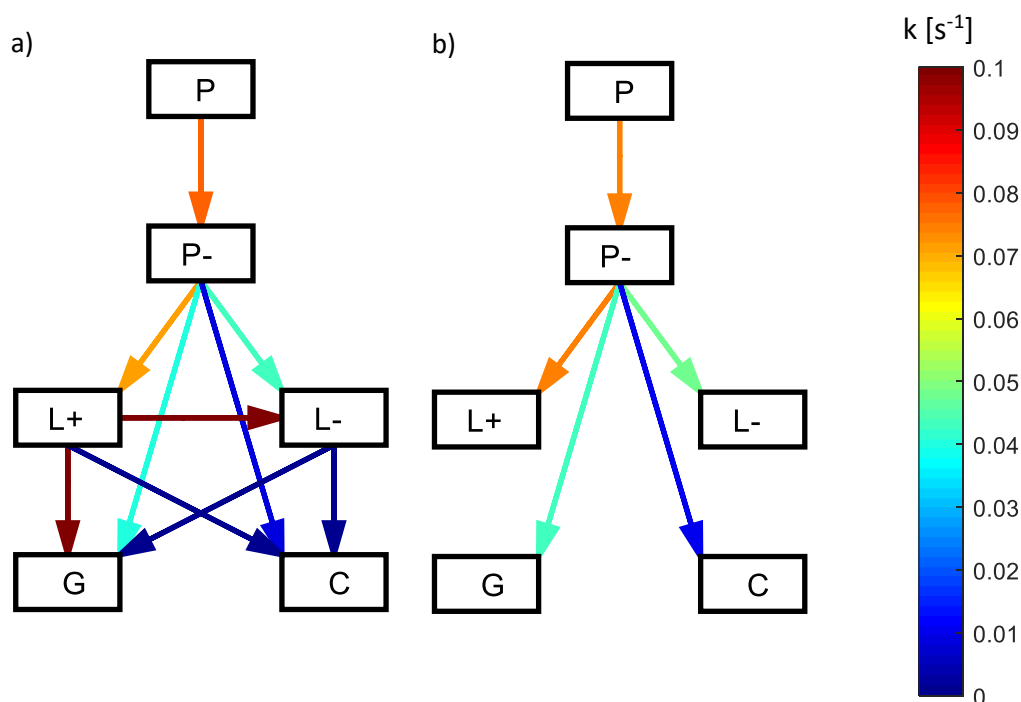


Figure 6.2. Identified reaction networks for thermo-catalytic pyrolysis at 455 °C  
 a) P-N0-R10, b) P-N0-R5 (GSA results)

Table 6.3. Root-mean-square error (RMSE) between experimental and calculated weight percentages of the component lumps.

	<b>P-N0-R10</b>	<b>P-N0-R5</b>
P	0.06‰	0.03‰
P-	0.06‰	0.05‰
L+	1.79%	1.52%
L-	1.01%	1.07%
G	0.88%	0.83%
C	0.14%	0.33%
Overall	1.23%	1.12%

To address the performance of the P-N0-R5 reaction network, I calculated the root-mean-square-error (RMSE) values for all pseudocomponents (between the experimental and calculated mass fractions so RMSE values are also specified as percentages); results are shown in Table 6.3. It can be seen that there is no considerable difference between the ability of the P-N0-R10 and P-N0-R5 reaction networks in predicting the product composition. In some cases, the error

value is even lower in the case of the reduced kinetic network; this might be due to the better performance of the optimization algorithm used for the identification in case of a lower number of decision variables.

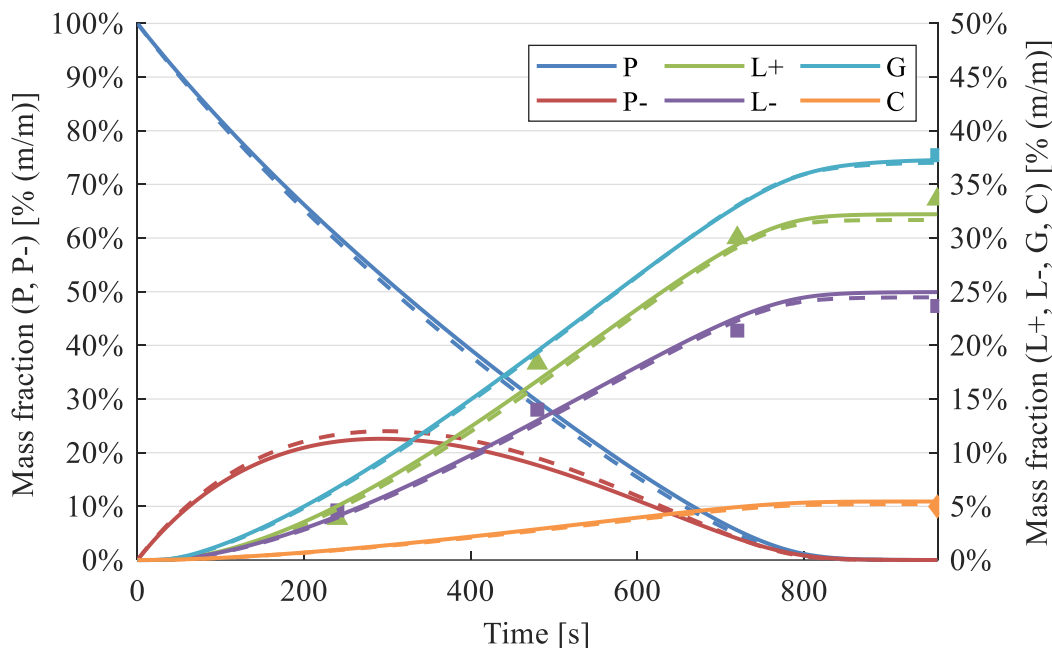


Figure 6.3. Pseudocomponent mass fractions in case of the reduced network for thermo-catalytic pyrolysis at 455 °C – experimental (markers); P-N0-R10 (dashed lines) and P-N0-R5 (solid lines)

Comparison of the simulated data with the complete and reduced reaction networks against measured data is shown in Figure 6.3 that also confirms the good prediction ability of the reduced network, thus the legitimacy of the global sensitivity analysis for carrying out this model reduction step. I would like to emphasize that the application of GSA requires no prior knowledge about the kinetic parameters; the full reaction network is only present in this section for the sake of comparison. This means we can use an arbitrarily large set of possible reactions, screen this super-network using GSA, and take only the number of reactions into consideration that can be identified in reality, either from the aspect of structural identifiability or regarding the performance of the chosen (global) nonlinear optimization algorithm.

### 6.3 Case study 2: VGO hydrocracking

The second case study involves the VGO hydrocracking model from Section 3.2 and is slightly more complex as there are 15 reactions present; all need to be taken into consideration in the sensitivity analysis. The resulting sensitivity indices are included in Table 6.4. I have shown in Chapter 5 that a reliable kinetic model can be constructed using five reactions, obtaining the VGO-N0-R5 reaction network. The first five reactions with the highest sensitivity indices are marked in Table 6.4; these are all the same except in the case of the PAWN method. However, these five reactions cannot be used to create a suitable reduced reaction network since only the LN and G pseudocomponents would appear in these as products.

Table 6.4. Different GSA indices for VGO hydrocracking.

Reaction	Reactant	Product	EET	FAST	PAWN	RS-HDMR	VBSA
r <sub>1</sub>	VGO	D	30.1	$3.1 \cdot 10^{-5}$	0.082	$6.51 \cdot 10^{-4}$	0.036
r <sub>2</sub>	VGO	K	32.6	$7.8 \cdot 10^{-6}$	0.085	$3.26 \cdot 10^{-4}$	0.029
r <sub>3</sub>	VGO	HN	35.9	$8.8 \cdot 10^{-6}$	0.077	$4.72 \cdot 10^{-5}$	0.037
r <sub>4</sub>	VGO	LN	<u>115</u>	<u>0.021</u>	<u>0.162</u>	<u>0.021</u>	<u>0.045</u>
r <sub>5</sub>	VGO	G	<u>122</u>	<u>0.024</u>	<u>0.153</u>	<u>0.026</u>	<u>0.101</u>
r <sub>6</sub>	D	K	9.64	$1.0 \cdot 10^{-5}$	0.092	$7.48 \cdot 10^{-4}$	0.028
r <sub>7</sub>	D	HN	11.6	$2.9 \cdot 10^{-5}$	0.067	$3.30 \cdot 10^{-4}$	0.030
r <sub>8</sub>	D	LN	36.4	$2.2 \cdot 10^{-3}$	0.113	$2.37 \cdot 10^{-3}$	0.031
r <sub>9</sub>	D	G	28.9	$1.4 \cdot 10^{-3}$	0.080	$1.75 \cdot 10^{-3}$	0.016
r <sub>10</sub>	K	HN	17.5	$6.1 \cdot 10^{-5}$	0.087	$3.68 \cdot 10^{-4}$	0.026
r <sub>11</sub>	K	LN	68.7	$8.0 \cdot 10^{-3}$	<u>0.175</u>	$7.84 \cdot 10^{-3}$	0.030
r <sub>12</sub>	K	G	49.8	$3.1 \cdot 10^{-3}$	0.100	0	0.035
r <sub>13</sub>	HN	LN	<u>139</u>	<u>0.027</u>	<u>0.315</u>	<u>0.028</u>	<u>0.093</u>
r <sub>14</sub>	HN	G	<u>86.1</u>	<u>0.011</u>	0.142	$9.08 \cdot 10^{-3}$	<u>0.037</u>
r <sub>15</sub>	LN	G	<u>528</u>	<u>0.515</u>	<u>0.680</u>	<u>0.703</u>	<u>0.548</u>

The baseline of the reduced reaction network should be constructed in such a way that all products are formed, and they are produced on the route to that the model shows the highest sensitivity. To formulate such a network, I applied

Dijkstra's shortest path algorithm [242]. Here the shortest path to a product is considered as the path consisting of the reactions with the highest sensitivity indices. Using this method, the resulting five-reaction base network contains reactions  $r_1$ ,  $r_6$ ,  $r_{10}$ ,  $r_{13}$  and  $r_{15}$  in case of using any GSA method; that is to say, the solely consecutive pathway in the reaction network can be isolated. This is a reasonable result as reaction  $r_{13}$  and  $r_{15}$  are the two associated with the highest sensitivity indices. Nevertheless, it should not be considered as trivial. For the first case study, the same algorithm leads to the fully parallel reaction network already discussed, and it can be speculated that for more complex systems with second-order reactions, the results may vary even more.

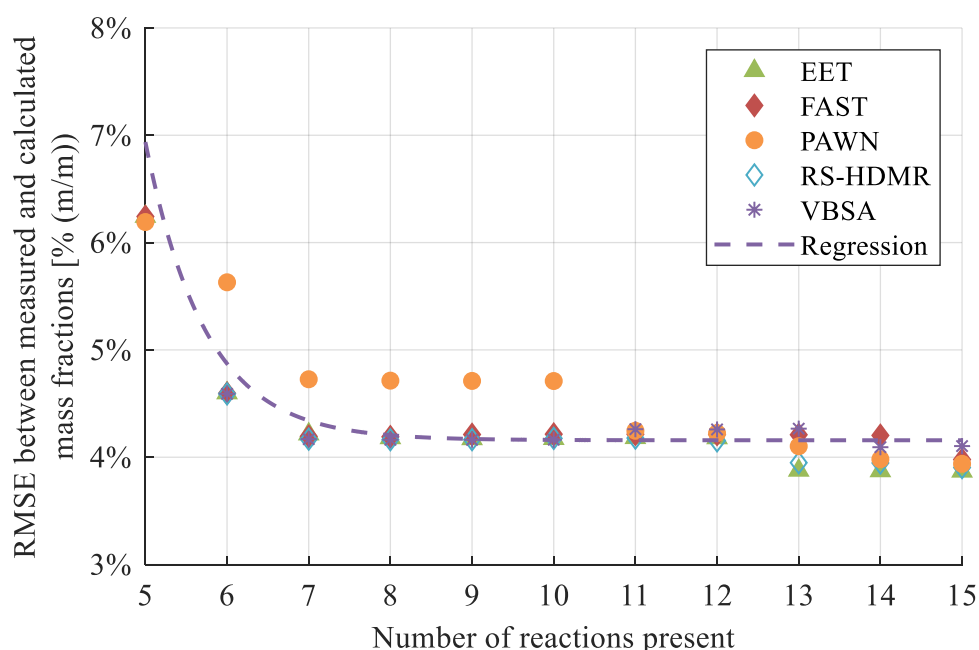


Figure 6.4. Root-mean-square-error for reaction subnetworks obtained using the sensitivity order obtained using different GSA methods

The remaining open question is that whether the solely consecutive pathway is sufficient to describe the mass concentration changes in the experimental data (Table S9). In order to answer that question, I performed a full-scale identification, meaning that after the identification of the reduced network associated with the most sensitive pathway, further reactions had been added, the one with the highest sensitivity index from the remaining set in each step for all GSA methods, and the reaction network was identified to evaluate its ability to

reproduce measured data. Results are shown in Figure 6.4, where each result is represented by the average RMSE value between experimental and calculated mass fractions.

It can be seen that the outcome for the investigated GSA methods are quite similar, with the exception of PAWN, in case of that the result is not as satisfactory as it is in case of other approaches. It also appears that eight or even nine reactions could be eliminated from the reaction network without substantially increasing model error. We can gain more insight if we look at the pseudocomponent RMSE values separately (Table 6.5). For seven reactions, the results do not differ from the results obtained using 15 reactions considerably. For six reactions, on the other hand, a major leap in the model error in case of G can be observed. Meanwhile, the absolute error in the case of LN might be a low value, but it represents a high relative error which is unfavorable because of the overall low concentration of this component (see Figure 6.6.b). On this basis, I have chosen the reduced network consisting of seven reactions, leading to the reduced reaction network VGO-N0-R7, shown in Figure 6.5b. (Refer to Table S1 for all variations of the pyrolysis reaction network.). Nevertheless, using even six reactions could be suitable under certain circumstances.

Table 6.5. Root-mean-square error (RMSE) between experimental and calculated mass fractions.

	<b>15 reactions</b>	<b>7 reactions</b>	<b>6 reactions</b>	<b>5 reactions</b>
VGO	6.7%	6.9%	6.8%	9.2%
D	5.2%	5.4%	5.5%	5.8%
K	2.4%	3.2%	3.1%	3.6%
HN	1.6%	2.3%	2.2%	2.7%
LN	0.3%	0.4%	0.8%	0.7%
G	3.9%	3.7%	5.8%	9.7%
Overall	4.0%	4.2%	4.6%	6.2%

Comparison of the full (VGO-N0-R15 from Figure 3.4) and the obtained reduced reaction network consisting of seven reactions (VGO-N0-R7) can be seen in Figure 6.5. Numerical values are listed in Table S17 in the appendix. As in the case of thermo-catalytic pyrolysis, the rate coefficients of the remaining reactions

have slightly higher values. The solely consecutive pathway, previously established as the maximally reduced reaction network using Dijkstra's shortest path algorithm, is associated with the highest rate coefficients. This also implies the eligibility of the GSA-based model reduction method; on the other hand, two additional reactions need to be implemented to reach the required model precision.

The average 4.0% and 4.2% error values for the complete and reduced reaction networks discussed above represent a moderate agreement between experimental data and simulation, as can be seen in Figure 6.6; therefore, the reduced network is capable of modeling the VGO hydrocracking process. It should be noted that the ability of the model to explain the changes in mass concentration in the case of the Diesel lump is somewhat unsatisfactory. On the other hand, the same can be observed for the full reaction network which indicates that this behavior of the reduced reaction network is inherent to the original model and can be overcome only by a different lumping strategy. These results also suggest that global sensitivity analysis can be effectively used to identify and subsequently eliminate reactions from an arbitrarily defined initial set.

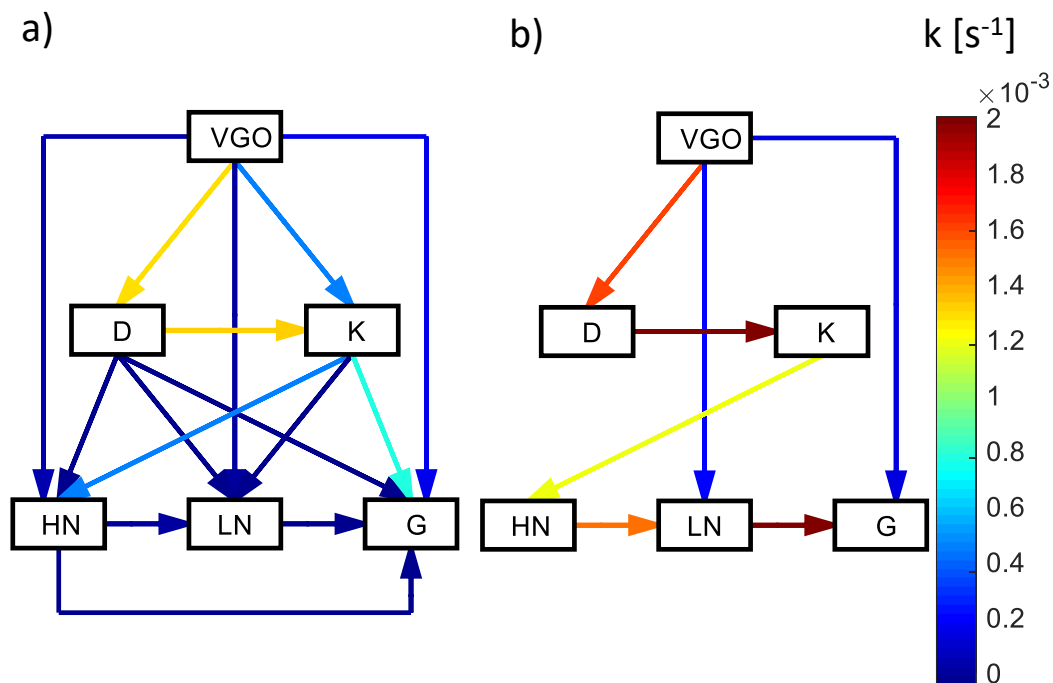


Figure 6.5. Identified reaction networks for VGO hydrocracking at 410 °C

a) VGO-N0-R15, b) VGO-N0-R7 (GSA results)

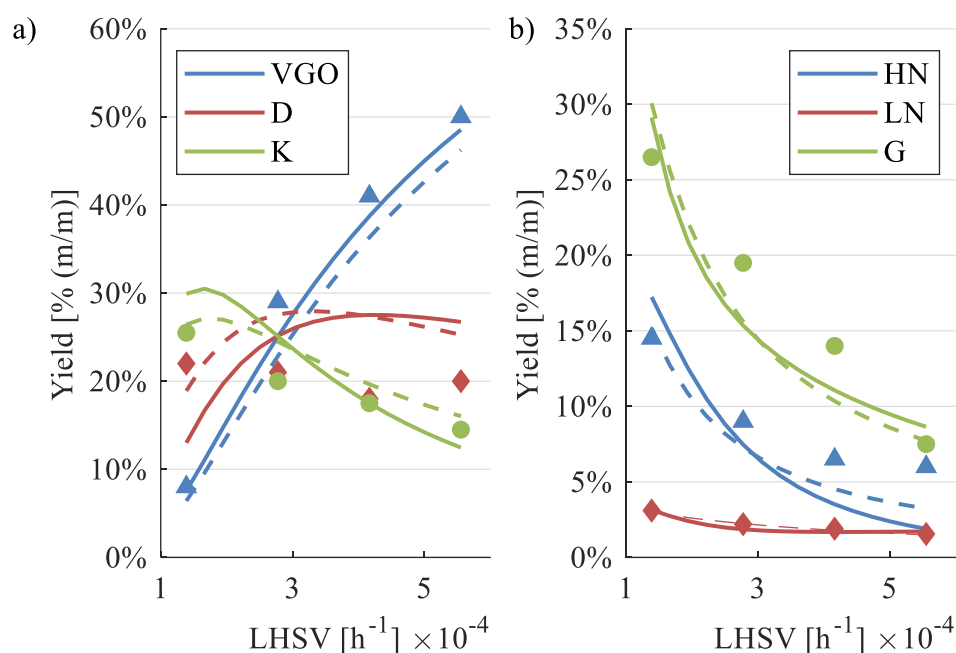


Figure 6.6. Pseudocomponent mass fractions in case of the reduced network for VGO hydrocracking at 410 °C – experimental (markers); complete (dashed lines) and reduced (solid lines) model

#### 6.4 Comparison of GSA methods

Good practice in GSA application involves applying multiple methods on one problem [240]. Following Liu and Homma [243], I evaluated the GSA methods investigated, assessing some key features:

- EET is only semi-quantitative that might not be favorable. On the other hand, only the sensitivity order of the reactions is taken into account here, in this case this is not considered as a disadvantage.
- FAST is easy to implement, requires no parametrization, even the recommended minimum sample size is available. It also has a low time requirement (i.e., it is a fast method – see Section 6.5).
- RS-HDMR comes with bundled variance reduction methods, making the computed sensitivity indices more stable (more independent on the actual sampling given the sample size). On the other hand, in some cases, the calculated sensitivity indices are actually zero, a property that is not exactly legitimate.



- PAWN requires a large number of samples. Both the unconditional and conditional CDFs are calculated, and that can be advantageous; on the other hand, this was not the case for the investigated examples.
- For VBSA, I have found that the numerical stability of the sensitivity indices in the case studies reported here is quite low, meaning the results on a given sample size showed high variance and were in some cases unrealistic (i.e., negative indices were calculated). This effect did not diminish with increasing the sample size.

On this basis, while also emphasizing that none of the methods can be ruled out based on two examples, I would prefer using EET, FAST and PAWN – three different methods with different theoretical backgrounds, giving reliable and stable results.

## 6.5 Effectiveness and performance

So far it has been ascertained that lumped reaction networks can be over-parametrized, a fact that gives space for reducing the number of reactions present in the model. Eventually, one important question arises, namely, what do we gain with the model reduction? Kinetic models constructed using discrete lumping, in general, are already simple. The main advantage of kinetic model reduction is the higher confidence in the identified parameters. I applied bootstrapping on the lumped kinetic models to estimate the confidence intervals of the identified kinetic parameters. The procedure involves the following steps:

1. Identify the parameters of the kinetic model (full or reduced network) using the experimental data available.
2. Generate a set of experimental conditions using a normal distribution with the experimental data as expected values and a  $\pm 5\%$  variation normally distributed ( $2\sigma$  confidence). I have chosen the reactor temperature (T) and the amount of raw material used in a batch ( $m_0$ ) in case of thermo-catalytic pyrolysis, and T and reactor feed liquid hourly space velocity (LHSV) in case of VGO hydrocracking.

3. Using the identified kinetic parameters in Step 1, generate a set of simulated experimental data using these experimental conditions, adding no further measurement error.
4. Identify a kinetic parameter set for every generated data set.
5. Because of Step 3, the value of the objective function can reach zero, and the location of this global minimum is known from Step 1. I have also established a threshold for the objective function and deemed the identification step successful if the value of the objective function was below this value ( $f^1(\underline{x}^n) \leq 10$  (Eq. (4.1)) for thermo-catalytic pyrolysis and  $f^2(\underline{x}^n) \leq 0.05$  (Eq. (5.1)) for VGO hydrocracking).
6. After reaching 100 successful identification steps, the algorithm was terminated.

With this algorithm the confidence in the identified model parameters can be assessed separately since there is no measurement error (because of Step 3) and the error of the optimization algorithm was also eliminated (in Step 5). If the confidence of a model parameter is high, the identified values will be close to each other (low standard deviation) and vice versa. The 100 identified values for each kinetic parameter were used to fit a probability distribution function. I tried out different solutions; here I use a Weibull-distribution fitted to each parameter and give 95% confidence intervals relative to the expected values to characterize parameter uncertainty. Lakshmanan and White used Weibull-distribution to model the distribution of activation energy [244]. Sánchez et al. applied several distributions to approximate distillation curves of the products of VGO hydrocracking, reaching the conclusion that only distributions of at least three parameters could be fitted appropriately, highlighting the Weibull and  $\gamma$  distributions among them [245]. It should be noted that based on my review of the literature, there is no direct antecedent of the method presented in this Section; nevertheless, the application of the Weibull distribution definitely looks promising.

Table 6.6. Confidence intervals for the identified parameters for VGO hydrocracking.

	VGO-N0-R15		VGO-N0-R7	
	Expected	95% confidence	Expected	95% confidence
k <sub>0,1</sub>	8.73·10 <sup>6</sup>	35%	9.14·10 <sup>6</sup>	25%
k <sub>0,2</sub>	6.95·10 <sup>13</sup>	42%		
k <sub>0,3</sub>	8.12·10 <sup>-1</sup>	51%		
k <sub>0,4</sub>	7.66·10 <sup>10</sup>	66%	8.98·10 <sup>10</sup>	34%
k <sub>0,5</sub>	6.42·10 <sup>-1</sup>	84%	6.57·10 <sup>-1</sup>	72%
k <sub>0,6</sub>	8.85·10 <sup>12</sup>	33%	6.01·10 <sup>12</sup>	110%
k <sub>0,7</sub>	6.11·10 <sup>-2</sup>	88%		
k <sub>0,8</sub>	6.79·10 <sup>-3</sup>	80%		
k <sub>0,9</sub>	6.54·10 <sup>-3</sup>	81%		
k <sub>0,10</sub>	6.69·10 <sup>6</sup>	67%	7.88·10 <sup>6</sup>	63%
k <sub>0,11</sub>	6.37·10 <sup>-1</sup>	88%		
k <sub>0,12</sub>	5.85·10 <sup>-1</sup>	104%		
k <sub>0,13</sub>	7.68·10 <sup>5</sup>	64%	9.33·10 <sup>5</sup>	21%
k <sub>0,14</sub>	6.09·10 <sup>-4</sup>	88%		
k <sub>0,15</sub>	6.38·10 <sup>4</sup>	81%	8.31·10 <sup>4</sup>	72%
E <sub>a,1</sub>	1.28·10 <sup>5</sup>	2%	1.27·10 <sup>5</sup>	1%
E <sub>a,2</sub>	2.23·10 <sup>5</sup>	2%		
E <sub>a,3</sub>	5.43·10 <sup>4</sup>	17%		
E <sub>a,4</sub>	1.98·10 <sup>5</sup>	3%	1.91·10 <sup>5</sup>	1%
E <sub>a,5</sub>	4.53·10 <sup>4</sup>	14%	4.57·10 <sup>4</sup>	11%
E <sub>a,6</sub>	2.07·10 <sup>5</sup>	1%	2.01·10 <sup>5</sup>	4%
E <sub>a,7</sub>	1.06·10 <sup>5</sup>	181%		
E <sub>a,8</sub>	1.60·10 <sup>5</sup>	159%		
E <sub>a,9</sub>	1.42·10 <sup>5</sup>	179%		
E <sub>a,10</sub>	1.32·10 <sup>5</sup>	4%	1.28·10 <sup>5</sup>	3%
E <sub>a,11</sub>	1.05·10 <sup>5</sup>	156%		
E <sub>a,12</sub>	3.67·10 <sup>4</sup>	23%		
E <sub>a,13</sub>	1.57·10 <sup>5</sup>	76%	1.15·10 <sup>5</sup>	1%
E <sub>a,14</sub>	1.36·10 <sup>5</sup>	223%		
E <sub>a,15</sub>	2.09·10 <sup>5</sup>	89%	9.14·10 <sup>4</sup>	6%

The corresponding probability distribution functions of these 100 successful identification steps are shown in from Figure S1 to Figure S22 in the Appendix.

For the sake of the length of this section, only the parameters of the more complex VGO hydrocracking model are considered here. The expected values of the identified kinetic parameters and the respective confidence intervals are denoted in Table 6.6. The 95% confidence intervals are given relative to the expected values. Except for  $k_{0,6}$ , the parameter confidence is retained, or, in many cases, become narrower for the reduced reaction network. Since the latter already has fewer parameters, this indicates higher confidence in the model itself. In order to demonstrate that, I have generated a set of 10,000 parameters using the fitted probability distributions and calculated the value of the objective function at each point. Results are plotted in histograms (Figure 6.7).

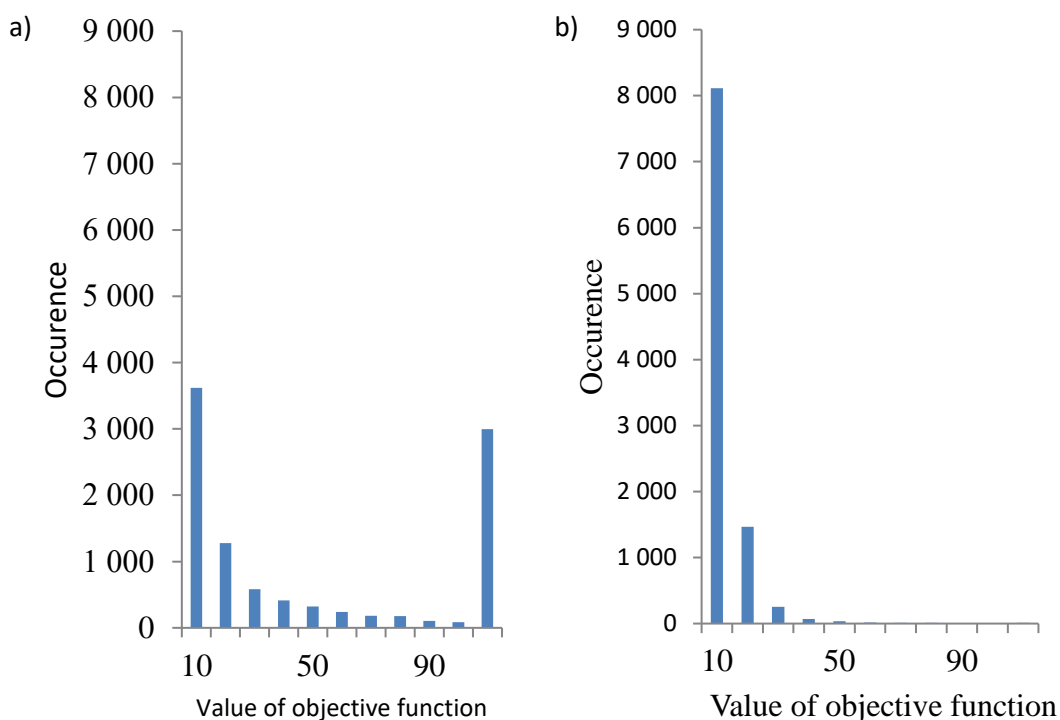


Figure 6.7. Occurrence of objective function values calculated using the PDFs of the kinetic parameters for VGO hydrocracking a) complete network, b) reduced network

For seven reactions, the objective function mostly returned the minimum value, in contrast to the results of the full reaction network. The reason behind this might be the correlation of the kinetic parameters (via the contributions of the related reactions to the same pseudocomponent mass concentrations); hence the probability distributions might not be the most accurate, yet the tendencies are

clear in comparison to the reduced model. In any case, the identification of 30 kinetic parameters with high correlations could be problematic, and this can be clearly avoided if we eliminate as many correlated variables as possible.

## 6.6 Chapter summary

Global Sensitivity Analysis is an easy to use and powerful method to distinct between the more and the less important model parameters. In this Chapter, I have applied this technique to reduce the number of reactions present in the two lumped reaction networks introduced in Chapter 3. It is essential to note that the reduction of these networks would be not useful just because the model fit remains more or less the same. The usefulness of this development would be at least questionable in the light of the vast computing capacities available nowadays.

Instead, based on the results discussed in this paper we can conclude that the reduction of these reaction networks greatly contributes to lessening the uncertainty in kinetic parameters, leading to more unbiased parameter estimation. The lower uncertainty of the underlying kinetic model is critical to achieve proper reactor design or operation and the proposed methods can contribute significantly to realize this objective. I showed that global sensitivity analysis is an effective tool in carrying out the model reduction step as it requires minimal information about the kinetic parameters; hence, it can be implemented before the actual parameter identification step. This is a major advantage compared to the methods described in Chapter 5 although I did not reach a reduced reaction network with all its states observable here.

Accordingly, if we define a number of pseudocomponents, we can screen an arbitrary large set of reactions and only identify the relevant reaction pathways, thus automating the building up of the network. This will be a key step in automating the lumping process itself, i.e. determining which lumps have decisive roles in describing the behavior of the chemical system investigated.



## **7 Structure of lumped reaction networks with correlating parameters**

The previous two Chapters dealt with the reduction of lumped reaction networks and the related advantages. The results indicate that the application of sparse reaction networks (i.e., where the ratio of reactions to components is relatively low) is desired. On the other hand, the absolute number of reactions was manageable even before the reduction of the kinetic model. This leads to the idea to increase the number of pseudocomponents present. In the case of the P-N0-R10 reaction network, this can be achieved with relative ease as the liquid product composition is available in a higher level of detail than just the introduced heavy and light liquid (L+ and L-) lumps.

Furthermore; in a chemical reaction network, whether it is a lumped or detailed one, the kinetic parameters might correlate to some extent simply through the amount of products to be formed. If the formation of two or more products has a strong correlation, we might even combine the corresponding reactions to reduce the size of the reaction network. This modeling step instinctively occurs when we have thousands of reactions, but it is usually not carried out in case of a lumped model because of its elementary nature.

In this Chapter I utilize both approaches. I show that the correlations between the amounts of liquid products can be utilized to increase both the number of correlated and uncorrelated lumps considered by applying some not so complicated structural modifications to the original model. This way, we can optimize the structure of the lumped reaction network so that we can capture the characteristics of the measurement rather efficiently without using an overcomplicated lumped reaction model full of uncertain parameters.

### **7.1 Revisiting the pyrolysis reactor network (P-N0-R10)**

In the P-N0-R10 lumped reaction network constructed for studying the pyrolysis of real plastic waste (Figure 3.2), the mass concentrations of the liquid lumps can be reasonably independent of each other. This makes the network really flexible and generally applicable. On the other hand, if there is a correlation between the mass concentrations, the kinetic parameters of the reactions also

become highly correlated. Thus it becomes unnecessary to identify them separately, and the correlation might also affect the performance of the nonlinear optimization algorithm used for the identification.

Taking a closer look at the ratio of these two liquid lumps at different temperature levels and different times (Figure 7.1a), we can reinforce our assumption on the matter of correlation. In Figure 7.1a, the black asterisks represent the measured values while the surface was estimated using biharmonic spline interpolation in MATLAB [246] to illustrate the effect in proper. It can be seen that the time dependence of the  $L^+/L^-$  ratio is much lower than its temperature dependence. In fact, the time dependence is minimal at 455 °C (7.5% change), moderate at 425 °C (32% change), and only at 485 °C is considerably high (77% change). This effect comes from the phenomena that the liquid composition remains roughly the same during the pyrolysis process at a given temperature, as can be seen in Figure 7.1b-d. Here the tendency is the same as the individual distribution curves of the samples collected at different times roughly overlap. The change in composition is more substantial at 485 °C than at the other two temperature levels; nevertheless, it still negligible.



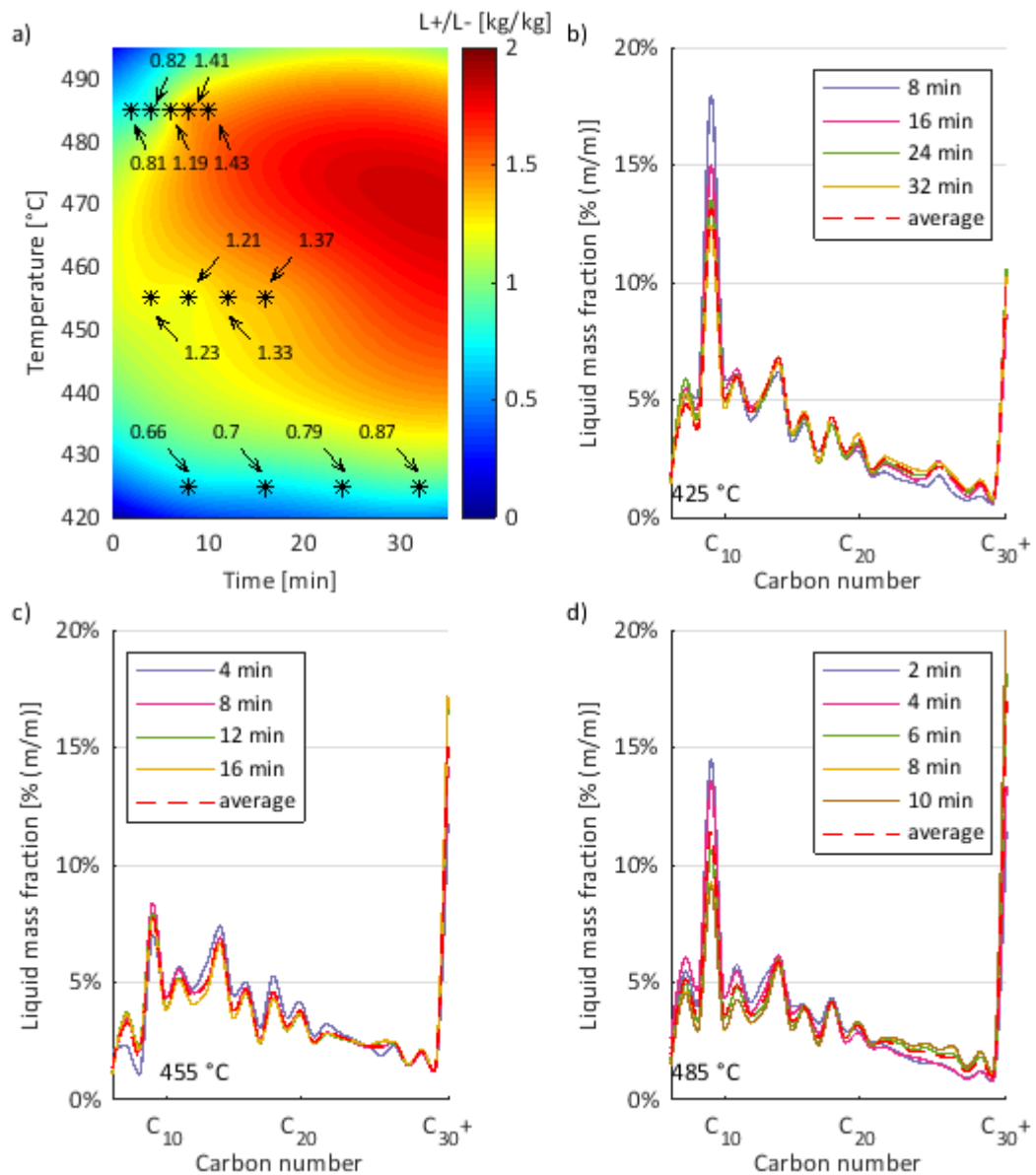


Figure 7.1. a) mass ratio of the L+ and L- lumps as a function of reaction time and temperature level b – d) mass distribution of the liquid product at different temperature levels

There are two main reasons behind the approximately constant liquid composition. On the one hand, the change in the composition of the polymer feedstock over time apparently does not affect the formation and release of the lighter products during the process. Although the polymer itself decomposes and shorter chains are formed, these intermediates are still non-volatile and remain part of the P- lump. On the other hand, the residence time of the liquid and gaseous components produced is meager due to the high nitrogen flow rate

(approx. 2 minutes); therefore, their influence in the reaction network is limited. The rate of the secondary reactions (with liquid lumps as reactants), thus their contribution to the final product composition is much lower, even negligible in some cases.

Hence, the key idea of this Chapter is to merge the two liquid lumps and reconstruct the reaction network in such a way that only the mass change of the total liquid product would be calculated explicitly. However, what do we gain by reforming the reaction network? Surely, we can halve the number of reactions, thus the number of parameters to be identified; on the other hand, dealing with the original P-N0-R10 network in Chapter 4 did not involve an insurmountable identification problem in itself. Moreover, with this method, we would only take an average composition of the liquid product into consideration; therefore, the model would become less accurate, especially at a higher temperature level. In other words, this structural simplification does not make much sense in itself. However, three different and exciting aspects arise. In the subsequent sections, I will show that these benefits far outweigh the disadvantage that the liquid composition is not entirely independent of time.

- Firstly, we are no longer restricted to calculate the amount of  $L_+$  and  $L_-$  from the total liquid amount; we can derive an arbitrary set of liquid products.
- Secondly, we can further modify the reaction network and include more, non-correlating components in our model. Specifically, I separated the liquid product into three lumps, paraffins, olefins, and isomers, based on the GC results.
- Thirdly, we show that the observed property of the quasi-constant mass distribution of the liquid product can be effectively used to reduce the necessary experimental work needed to follow the progress of the pyrolysis reaction. For example, we would only have to measure the total amount of liquid produced without further sampling.

The kinetic parameter identification problem formally remains the same as it was introduced in Section 4.1. The main difference here is in the reaction network

because in this Chapter I introduce multiple modified versions of the original P-N0-R10 network and calculate the concentrations accordingly.

## 7.2 First alternative reaction network (P-N1-R5)

The first case study involves calculating the concentrations of the original two liquid lumps,  $L_+$  and  $L_-$ , from the total amount of liquid product. Hence, the reconstruction of the P-N0-R10 reaction network involves merging these two components and eliminating the corresponding reactions. The modified structure of the P-N1-R5 network is shown in Figure 7.2, consisting of five reactions between five pseudocomponents. Note that the reaction corresponding to the coke formation from the liquid products was removed after some a priori reasoning on the nature of the experiments, i.e., the low residence time of the volatile products causes them to form insignificant amounts of coke directly. The removal was also supported by the fact that only trace amounts of solid products were found in the second stage of the batch reactor system.

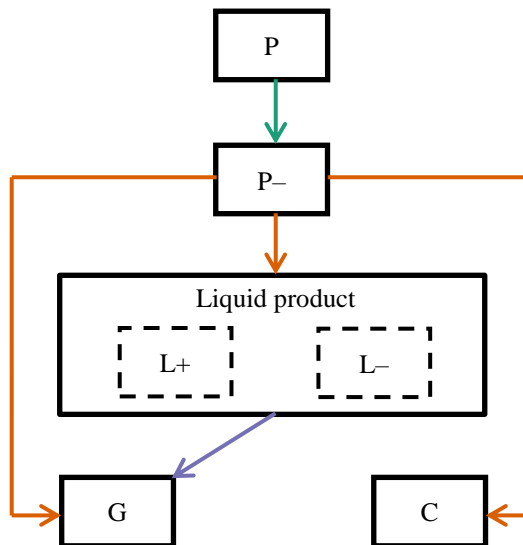


Figure 7.2. P-N1-R5 reaction network (N1) with the correlation between the  $L_+$  and  $L_-$  lumps taken into consideration

There are two possible scenarios available to estimate the amounts of  $L_+$  and  $L_-$  from the total liquid product. The first one is to use one average liquid composition regardless of the temperature ( $\bar{x}$ ) and the second is to apply one for each temperature level ( $\bar{x}_T$ ). This way, the significance of the temperature dependence of the liquid product composition can be quantitatively assessed. The

fractions of the L+ and L- lumps in the total amount of the liquid for the two scenarios are listed in Table 7.1.

Table 7.1. Estimated fractions of the L+ and L- lumps in the liquid product in the N1 network

Scenario	L+	L-
1. average for all temperatures ( $\bar{x}$ )	50.6%	49.4%
425 °C average ( $x_{425\text{ °C}}$ )	42.8%	57.2%
2. 455 °C average ( $x_{455\text{ °C}}$ )	56.2%	43.8%
485 °C average ( $x_{485\text{ °C}}$ )	52.3%	47.7%

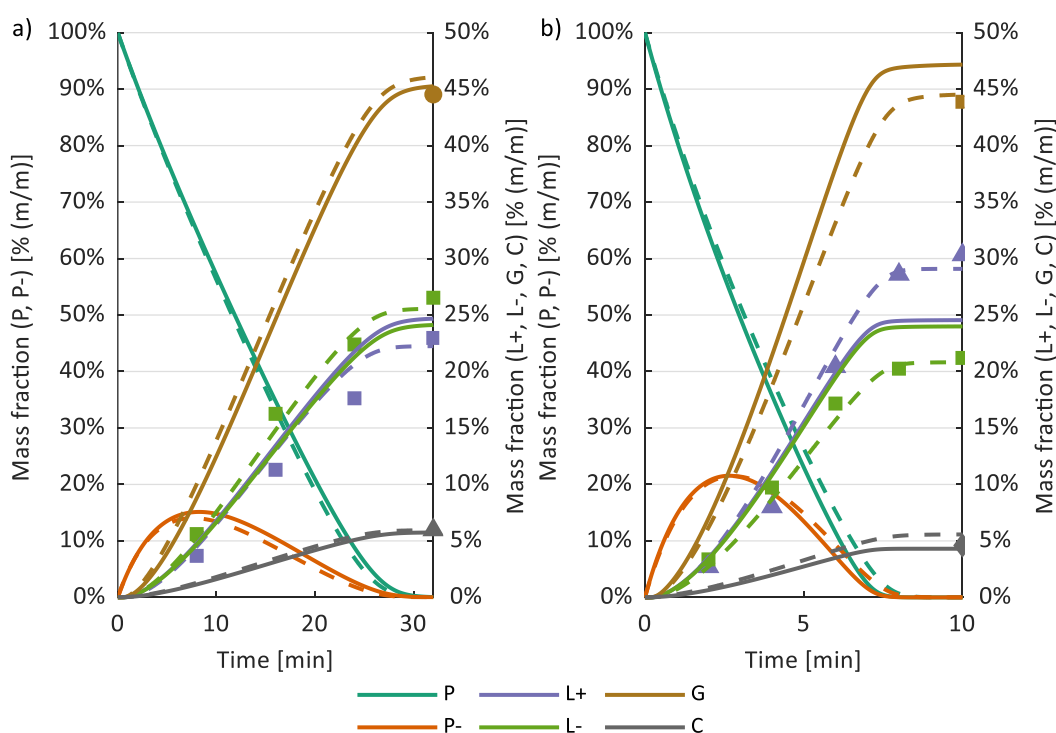


Figure 7.3. Pseudocomponent mass fractions at a) 425 °C b) 485 °C using one average liquid composition for all temperature levels (first scenario). Markers: experimental, dashed lines: P-N0-R10 reaction network results, solid lines: P-N1-R5 reaction network results

Let me compare these two scenarios. Experimental and calculated mass fractions as a function of time on CuZSM-5 / Ni/Mo-Al<sub>2</sub>O<sub>3</sub> catalyst can be seen in Figure 7.3 for the first, and in Figure 7.4 for the second scenario, both at 425 °C and 485 °C. It is apparent that the former involves one bit too much simplification

as the average 1:1 ratio of the two liquid lumps does not overlap with the actual proportions at different temperatures. Retrospectively, that might have been predicted from Figure 7.1a, but it also tests the modeling idea and shows that the model with correlating liquid lumps actually shows the same tendencies as those were apparent in the experimental results.

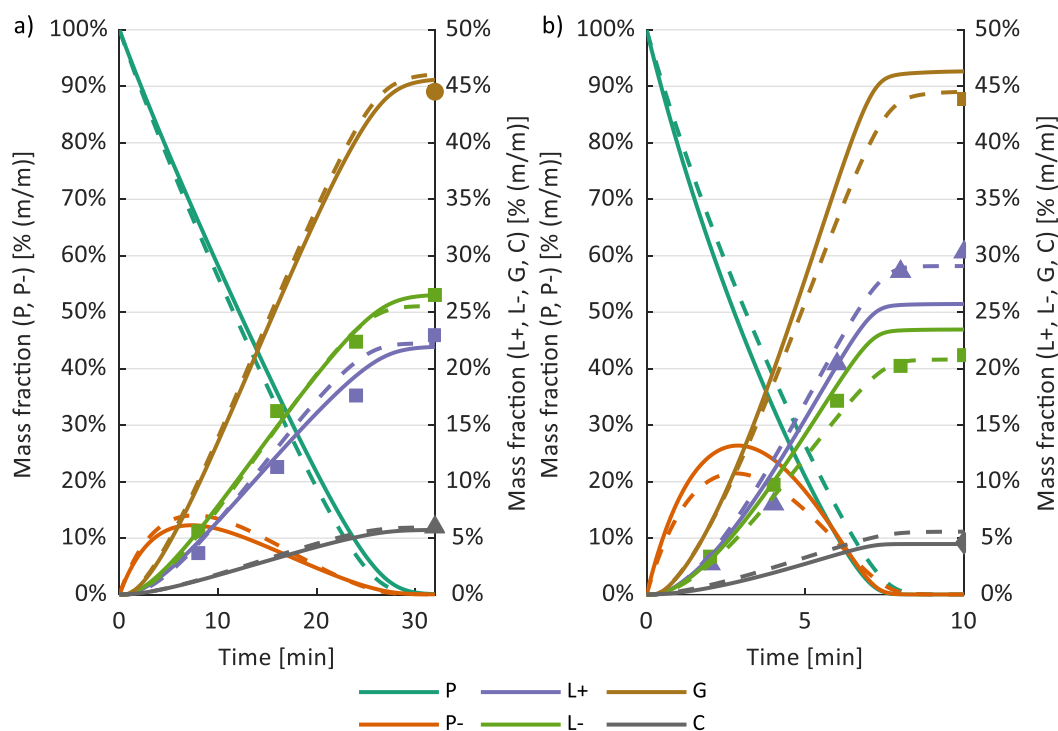


Figure 7.4. Pseudocomponent mass fractions at a) 425 °C b) 485 °C using one average liquid composition at each temperature level (second scenario). Markers: experimental, dashed lines: P-N0-R10 reaction network results, solid lines: P-N1-R5 reaction network results

In Figure 7.4, the agreement between measurement and simulation improves significantly compared to Figure 7.3, confirming the assumption that the temperature dependence of the liquid product composition is not negligible. The results are less convincing at 485 °C than at 425 °C, but this also follows our previous observation from Figure 7.1 that the time dependence of the L+:L- ratio is much higher at 485 °C. As I have stated in Section 7.1, the main model assumption is that it should work in cases when the residence time of the volatile components is negligible. This assumption has a stronger foundation at 425 °C, where the pyrolysis time is 32 minutes than at 485 °C, where it takes only

10 minutes. In other words, the reaction rates become comparable to the residence time of the volatile products at high temperatures; therefore, the interaction between them becomes more apparent. Nevertheless, this only causes a higher error towards the end of the pyrolysis process, on the last 20% of the time horizon.

As the interaction between the L<sup>+</sup> and L<sup>-</sup> lumps is limited due to low residence times, this would mean that – in terms of the P-N0-R10 reaction network – the P<sup>-</sup> → L<sup>+</sup> reaction is faster than the P<sup>-</sup> → L<sup>-</sup> reaction at a higher temperature. In other words, the activation energy of the former reaction would be higher. Accordingly, this is in line with my previous results [247].

To compare the two scenarios quantitatively, I also calculated the root of mean squared error (RMSE) values (listed in Table 7.2) between pseudocomponent mass percentages from experimental data and simulation results and compared them with the performance of the P-N0-R10 reaction network. The values indicate that the second scenario (i.e., one average liquid composition for each temperature level is used to express the amounts of L<sup>+</sup> and L<sup>-</sup>) is comparable to the performance of the original reaction network. In fact, its performance is only worse at 485 °C. One can also observe this in Figure 7.4, most prominently in case of L<sup>+</sup>, but it is also detectable for the G and C lumps upon closer inspection.

Nevertheless, the differences are well within the margin of error of the nonlinear optimization program used to estimate the kinetic parameters of the lumped reaction networks. In conclusion, these results indicate that the approximately constant mass distribution property of the liquid product can be effectively implemented into our model, thus significantly reducing the number of kinetic parameters to be identified. Though the composition of the liquid (fuel) product is not entirely time-independent in reality, this approximation does not significantly impact the accuracy of the model.

Table 7.2. Root-mean-square error (RMSE) between experimental and calculated data

	Original (N0)	Modified (N1)	
		First scenario	Second scenario
425 °C	1.27%	1.92%	0.92%
455 °C	2.23%	2.64%	1.75%
485 °C	1.53%	2.56%	2.06%
Temperature aggregated	1.72%	2.40%	1.67%

The identified kinetic parameters of the P-N1-R5 reaction network are listed in Table 7.3. The results from the two scenarios do not differ considerably; the main difference is in the estimated fractions of L+ and L-. The reaction between the L and G lumps has the highest activation energy, meaning that the interaction between the volatiles is limited (albeit observable) and only has a significant effect at higher temperatures. While the P-N1-R5 reaction network does not capture this, such weaker interactions might cause the observed higher variation in product composition over time at higher temperatures seen in Figure 7.1.

 Table 7.3. Identified kinetic parameters for plastic waste pyrolysis on CuZSM-5 / Ni/Mo-Al<sub>2</sub>O<sub>3</sub> catalysts for reaction network (N1)

Reaction		First scenario		Second scenario	
Reactant	Product	k <sub>0</sub> [s <sup>-1</sup> ]	E <sub>a</sub> [J mol <sup>-1</sup> ]	k <sub>0</sub> [s <sup>-1</sup> ]	E <sub>a</sub> [J mol <sup>-1</sup> ]
P	P-	2.73·10 <sup>6</sup>	1.05·10 <sup>5</sup>	1.61·10 <sup>7</sup>	1.15·10 <sup>5</sup>
P-	C	2.65·10 <sup>1</sup>	4.59·10 <sup>4</sup>	1.70·10 <sup>-1</sup>	1.53·10 <sup>4</sup>
P-	L	1.31·10 <sup>4</sup>	6.95·10 <sup>4</sup>	4.95·10 <sup>1</sup>	3.58·10 <sup>4</sup>
P-	G	7.54·10 <sup>3</sup>	6.68·10 <sup>4</sup>	2.68·10 <sup>1</sup>	3.26·10 <sup>4</sup>
L	G	1.14·10 <sup>22</sup>	3.08·10 <sup>5</sup>	9.78·10 <sup>21</sup>	3.11·10 <sup>5</sup>

### 7.3 Second alternative reaction network (P-N2-R9)

So far, I have successfully reduced the number of components (from six to five) and reactions (from ten to five) in the P-N1-R5 network. This result in itself is not that significant since the size of the original P-N0-R10 network was already manageable. On the other hand, it is possible to reallocate these parameters, i.e., after reducing the network in one direction, we can extend it in another to gain

more information about the pyrolysis process. During the pyrolysis experiments, concentrations of liquid product components with carbon numbers ranging from six to 30 were determined separately for paraffins (p), olefins (o), and isomeric components (i) (see Section 3.1.1). Therefore, I separated the liquid product in the kinetic model into these three lumps.

It still applies that given the average compositions of these three species (Figure 7.5a), we can express an arbitrary number of sub-components for each (in this case, heavy and light ends are present similar to in the case of the P-N1-R5 network). The resulting reaction network, called P-N2-R9, is denoted in Figure 7.5b, consisting of seven independent components and nine reactions between them, the latter is still one lesser than the reactions present in P-N0-R10. Furthermore, without the correlation taken into consideration, this reaction network would be much more complex. I have chosen the nine reactions present in the network from a larger set of possible pathways using Global Sensitivity Analysis, a powerful concept introduced in Section 2.4.2. For the sake of the length of the dissertation, the details are not presented here, but the procedure is very similar to the one discussed in Chapter 6.

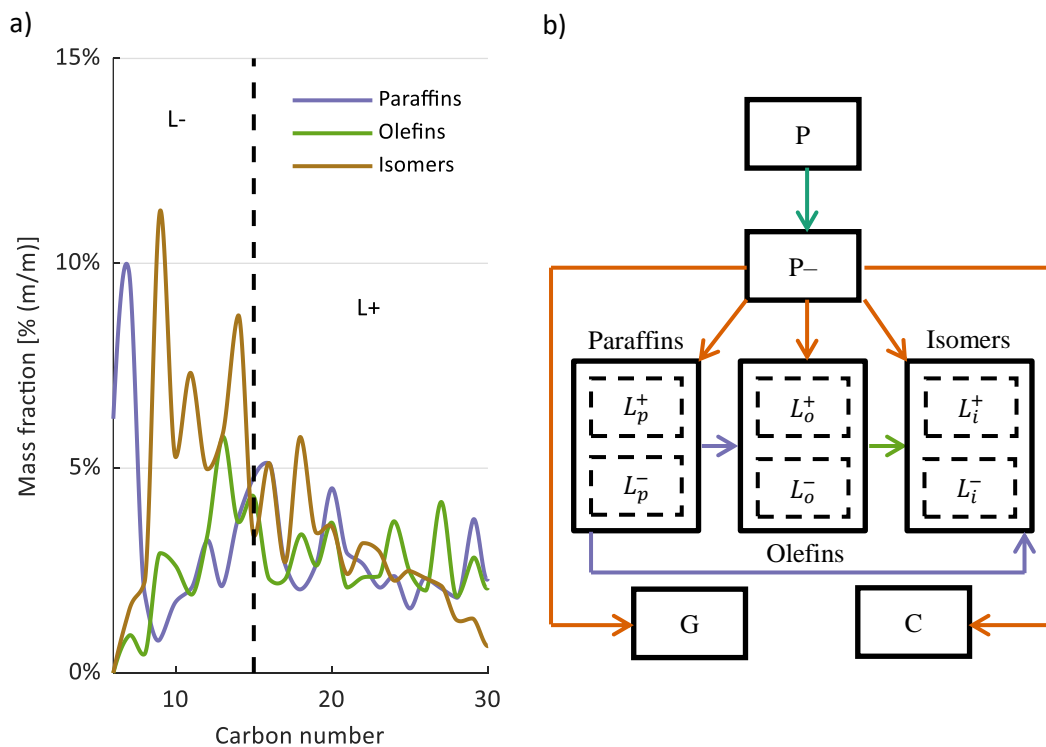


Figure 7.5. a) time-average liquid composition at 455 °C b) newly constructed reaction network (P-N2-R9) with six pairs of correlated liquid lumps.



As a drawback, we need information regarding the average composition of these three species at all three temperature levels, but this still does not require any interim measurement, only a detailed analysis at the end of each run that is already available. The P-N2-R9 reaction network considerably differs from P-N1-R5; therefore, its parameters should be identified separately, repeatedly solving Eq. (4.1). As the same plastic waste pyrolysis process is investigated here, the resulting kinetic parameters are necessarily linked to the parameters of the P-N1-R5 (and of P-N0-R10, by the way) network; however, for the sake of the length of this chapter, the discussion of these relations in detail here is omitted. Instead, I would like to emphasize that by using a reaction network of the same complexity, we can gain a much more detailed model regarding the nature of the primary liquid product (fuel).

I expressed the mass concentrations of the two lumps from each liquid product type as well as the fractions of P, P -, G, and C in Figure 7.6. Again, the agreement between experimental data and simulation is more than acceptable. The isomer content of the liquid product (and the proportion of the lighter isomers within it) is high, making the application of this CuZSM-5 / Ni/Mo-Al<sub>2</sub>O<sub>3</sub> catalyst system promising in terms of converting plastic wastes into liquid fuels via low-temperature pyrolysis. Nevertheless, the calculations detailed here can be carried out on any data set, regardless of the catalyst; this method might even help to compare them more effectively.

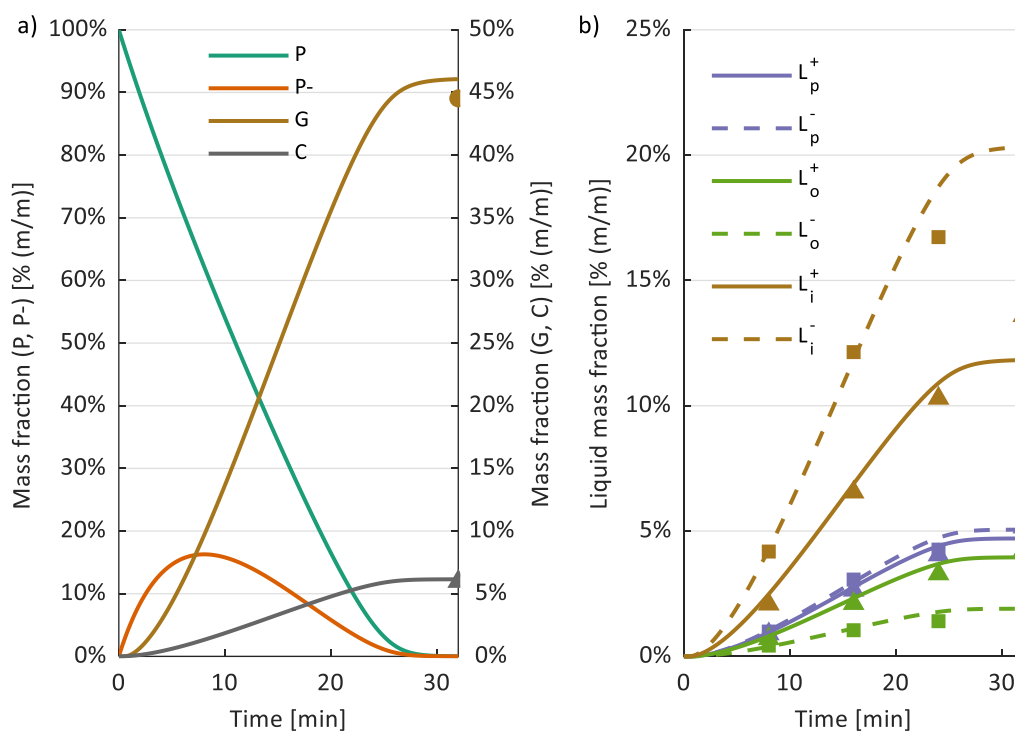


Figure 7.6. Pseudocomponent mass fractions at 425 °C for reaction network P-N2-R9 using one average liquid composition at each temperature level (3) and each liquid product type (3)

Table 7.4. Identified kinetic parameters for plastic waste pyrolysis on CuZSM-5 / Ni/Mo-Al<sub>2</sub>O<sub>3</sub> catalysts for reaction network P-N2-R9

Reaction		Kinetic parameters	
Reactant	Product	$k_0$ [s <sup>-1</sup> ]	$E_a$ [J mol <sup>-1</sup> ]
P	P-	$8.14 \cdot 10^5$	$9.72 \cdot 10^4$
P-	C	$2.13 \cdot 10^1$	$4.44 \cdot 10^4$
P-	L <sub>p</sub>	$2.70 \cdot 10^4$	$8.25 \cdot 10^4$
P-	L <sub>o</sub>	$7.82 \cdot 10^4$	$9.17 \cdot 10^4$
P-	L <sub>i</sub>	$8.23 \cdot 10^2$	$5.63 \cdot 10^4$
P-	G	$4.90 \cdot 10^3$	$6.43 \cdot 10^4$
L <sub>p</sub>	L <sub>o</sub>	$1.48 \cdot 10^5$	$6.85 \cdot 10^4$
L <sub>o</sub>	L <sub>i</sub>	$6.69 \cdot 10^2$	$2.55 \cdot 10^4$
L <sub>p</sub>	L <sub>i</sub>	$7.58 \cdot 10^4$	$5.68 \cdot 10^4$

The identified kinetic parameters for the P-N2-R9 reaction network are shown in Table 7.4. The values are in the same order of magnitude as were in the case of

P-N1-R5 (Table 7.3) because the underlying measurement has remained the same. The activation energies of the secondary reactions between the volatiles are lower, suggesting that these reactions have a more visible effect also at lower temperature levels, thus weakening the correlation between the three liquid groups, explaining why I have separated them in the kinetic model.

At this point, we have a reasonably simple lumped reaction network with only nine reactions to identify that can be considered optimal in such a way that it is capable of capturing all main characteristics of the measurement. And the best part that it is nothing more complex than the initial reaction network P-N0-R10 due to considering the correlations between product concentrations.

#### **7.4 Simplification of the experimental work**

Finally, there is one more way to make use of the nearly constant mass distribution of the liquid product. The original experimental work described in Section 3.1.1 involves the collection of liquid product samples at regular intervals, then analyzing them separately with gas chromatography, and then we still have to calculate the total product composition from the known sample compositions. This is rather tedious (especially when the sampling process is not automated) and time-consuming; so instead, it would be much easier if we collected the liquid product continuously and only analyze it after the plastic waste pyrolysis reaction was carried out. We can also couple this with the mass measurement of the liquid outlet. To validate this assumption, I remodeled the experimental data of plastic waste pyrolysis on FeZSM-5 / Ni/Mo catalyst system at 455 °C:

- I calculated the amount of total liquid product vs. time: {(0 min, 0 g), (4 min, 4.25 g), (8 min, 16.2 g), (12 min, 25.75 g), (16 min, 28.7 g)};
- interpolated between the data points using cubic convolution in MATLAB with 1 s frequency;
- added an approx. 3% time-invariant measurement noise to the interpolated data with normal distribution;
- calculated the mass distribution of the end product to be able to estimate liquid fractions from the amount of the total liquid product.

The kinetic parameters of the lumped reaction network P-N1-R5 were identified using this generated data set. The identified values are listed in Table 7.5. One noticeable aspect is that the rate of coke formation is nearly independent of the temperature. The reason behind this is more numerical than theoretical. In Figure 7.7.a, you can see that the calculated amounts of the gaseous and total liquid products are well within the related confidence bounds of the generated data set; only the amount of coke is higher than expected. This might further be improved if we modified the objective function because now the weight of 961 (16x60+1) measurement points associated with the liquid product in the objective function completely overwhelm the one data point associated with the coke byproduct; nevertheless, these results are still suitable.

Table 7.5. Identified kinetic parameters for plastic waste pyrolysis on FeZSM-5 / Ni/Mo-Al<sub>2</sub>O<sub>3</sub> catalysts for reaction network P-N1-R5

Reaction		Kinetic parameters	
Reactant	Product	k <sub>0</sub> [s <sup>-1</sup> ]	E <sub>a</sub> [J mol <sup>-1</sup> ]
P	P-	4.90·10 <sup>8</sup>	1.35·10 <sup>5</sup>
P-	C	1.79·10 <sup>-2</sup>	1.44·10 <sup>1</sup>
P-	L	1.31·10 <sup>2</sup>	4.21·10 <sup>4</sup>
P-	G	1.41·10 <sup>-1</sup>	3.28·10 <sup>3</sup>
L	G	4.14·10 <sup>8</sup>	2.56·10 <sup>5</sup>

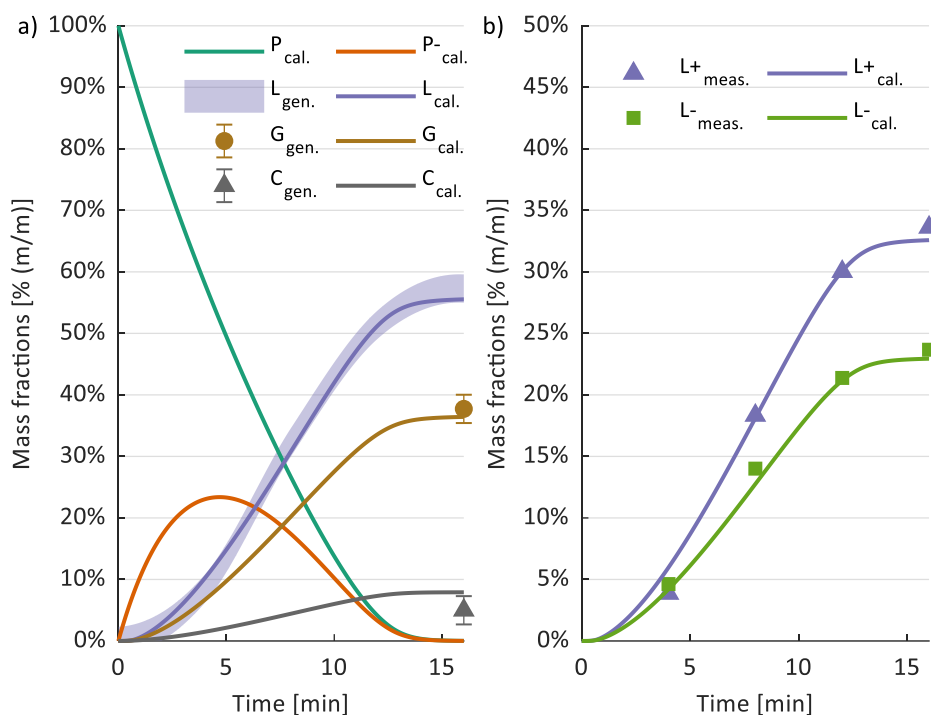


Figure 7.7. Pseudocomponent mass fractions at 455 °C for network P-N1-R5 for FeZSM-5 / Ni/Mo-Al<sub>2</sub>O<sub>3</sub> catalysts identified using generated measurement data

a) comparison with generated data b) comparison with original GC data

The amounts of L+ and L- derived from the total liquid product (L<sub>cal.</sub>) and the related values from the original experiment is shown in Figure 7.7.b. These are coinciding well with each other; therefore, it can be firmly suggested that the required experimental work to follow the plastic waste pyrolysis will be able to be cut down if the right conditions are met (this mainly corresponds to the low residence time of the volatile products).

## 7.5 Chapter summary

When carrying out the lumping process, it is crucial to band together all correlating components existing on the same time-scale while separating the non-correlating species at the same time. With this in mind, we can construct a lumped reaction network optimal in the sense that it captures as many characteristics of the related measurement as possible, yet its complexity remains in line with the somewhat elementary nature of the interim measurement often only available to follow a process.

In this Chapter, I made several modifications to the original P-N0-R10 reaction network introduced in Section 3.1. These modifications could be accomplished given the low residence time of the product components in the reactor, which results in their nearly constant composition. I have shown that this approach has multiple advantages. The first step was to merge the L<sup>+</sup> and L<sup>-</sup> lumps, which resulted in the P-N1-R5 reaction network. Comparing the mass concentration profiles obtained using this scheme and the previous one showed that the idea of correlated compositions is indeed viable, although the correlation becomes weaker as the temperature increases in the reactor system.

The second step was to increase the number of uncorrelated components in the reaction network (P-N2-R9). This way, the concentrations of paraffin, olefin, and isomeric components can be described separately, resulting in a better representation of the experimental data, without increasing the number of reactions present compared to the P-N0-R10 reaction network. It also became possible to reconsider the experimental methods required to follow the process to develop an actual interim measurement method suitable for scale-up as well. Hence, I believe the concepts unfolded in this work can prove to be useful when one would like to use such lumped reaction networks in reactor design and scale-up for fuel production, or wants to have a better understanding of the underlying chemical processes behind the measurement.

## 8 Kinetic identification problems and different optimization algorithms

At this point, we are already familiar with the concept of reducing the number of reactions in the reaction network. Chapter 5 introduced the concept of the observability of the kinetic parameters that theoretically would ensure their identifiability. In Chapter 6, I have calculated the confidence bounds of the kinetic parameters of the VGO-N0-R7 reaction network and compared them to the original VGO-N0-R15 network, and those results indicated a higher confidence in the model itself.

There are two aspects of kinetic parameter uncertainty that have not yet been addressed. Firstly, how much uncertainty is present in the original reaction network (i.e., VGO-N0-R15)? Clearly I have reduced it, but from what level, and might the original level be acceptable in itself? Secondly, to what extent the nonlinear optimization algorithm influences the solution? Following the idea from Section 2.4.4, I apply 23 different optimization algorithms on three different problems, the VGO-N0-R15 (Section 3.2), VGO-N0-R5 (Chapter 5), and the ETP model. The latter was introduced in Section 3.5 and has not yet been further investigated. In this Chapter, it serves as a reference to compare the optimization algorithms used for kinetic parameter identification because the exact solution is available (Table 3.3). This method leads to a third measure to quantify the uncertainty of the kinetic parameters and the model itself.

One of the main motives behind this Chapter is to reason about why I used a particular optimization algorithm (so far the NOMAD (Nonlinear Optimization by Mesh Adaptive Direct Search) software package [234,235]) to identify the kinetic parameters of lumped reaction networks. Therefore, most importantly, I have kept a practical approach in mind instead of dwelling into the theory of operations research.

### 8.1 Investigated kinetic models

The first two kinetic models investigated in this Chapter are from the field of discrete lumping. Specifically, they are two different versions of the kinetic model constructed to study vacuum gas oil hydrocracking. The model itself was

originally introduced in Section 3.2 and contained 15 reactions between 6 component lumps (VGO-N0-R15 in Figure 3.4). Secondly, in Chapter 5 I developed a method to eliminate reactions from the VGO-15 network to ensure its observability, ending up with a reduced kinetic model consisting of 5 reactions (VGO-N0-R5 in Figure 5.9).

Using a lumped kinetic model for benchmarking optimization algorithms is genuinely challenging because, unlike the standard problems, the location and value of the global minimum is unknown as the kinetic parameters have no reference values. Moreover, if we have two points whose difference in the objective function value is in the same range as the error of the measurement, it will become difficult to decide which one is correct. Even in the case of global optimization, one should set a target on what is considered an acceptable or successful result [248]. In this sense, if we have multiple different acceptable solutions; therefore, in a way we end up with multiple global minima, even if the function values are not precisely the same.

Thirdly, I investigate the few-step kinetic model for ethane pyrolysis (ETP) introduced in Section 3.5 that involves conventional chemical reactions between regular components. As stated there, I chose this problem because its kinetic parameters are known (Table 3.3). That makes the evaluation of the performance of the nonlinear optimization algorithms, at least at a first glance, quite easy, as all we would have to consider is whether we find these values during the identification or not.

## 8.2 The optimization target

Here I retain the use of the objective function from Chapter 5 because Eq. (5.1) performed well in the case of VGO hydrocracking. I have also applied it in case of the ETP model for the sake of simplicity and better comparison. Nevertheless, there are many options for an objective function to choose from and it certainly could affect the results. Unfortunately, comparing 23 algorithms and multiple objective functions at the same time would be impracticable within a reasonable time. A number of good quality studies have been carried out regarding the objective function. Siouris and Blakey compared nine different objective



functions, evaluating their performance under a genetic algorithm in case of a kinetic identification problem and concluded that there are two main types of objective functions regarding whether we treat all component concentrations as equally important or not [249]. The case discussed here is the latter because it would be disadvantageous if the algorithm “overlooked” some species because of their low concentrations. In my opinion, Eq. (5.1) is a valid and somewhat evident choice for this; on the other hand, there are some less apparent but seemingly also very suitable choices derived by the authors themselves.

For the formulation of the optimization problem, the lower and upper bounds of the kinetic parameters also have to be defined as most algorithms deal with constrained problems. These are listed in Table 8.1 to Table 8.3. In case of the ETP model, the constraints were defined following a preliminary sensitivity study starting out from the true values, whereas in case of the VGO-N0-R15 and VGO-N0-R5 models I mainly defined a wide radius based on the original values identified by Sadighi and Reza Zahedi [219], aiming to set the lower and upper bounds in a way that they will pose the smallest limitation as possible in practice. Hence, these constraints might differ from the ones listed in Table 5.1.

Table 8.1. Lower and upper bounds of kinetic parameters of the reactions in the VGO-N0-R15 model.

Reaction	Pre-exponential factor		Activation energy	
	[s <sup>-1</sup> ]		[J mol <sup>-1</sup> ]	
	LB	UB	LB	UB
VGO → D	10 <sup>1</sup>	10 <sup>4</sup>	10 <sup>4</sup>	4·10 <sup>5</sup>
VGO → K	10 <sup>11</sup>	10 <sup>14</sup>	10 <sup>4</sup>	4·10 <sup>5</sup>
VGO → HN	10 <sup>7</sup>	10 <sup>10</sup>	10 <sup>4</sup>	4·10 <sup>5</sup>
VGO → LN	10 <sup>14</sup>	10 <sup>17</sup>	10 <sup>4</sup>	4·10 <sup>5</sup>
VGO → G	10 <sup>4</sup>	10 <sup>7</sup>	10 <sup>4</sup>	4·10 <sup>5</sup>
D → K	10 <sup>4</sup>	10 <sup>7</sup>	10 <sup>4</sup>	4·10 <sup>5</sup>
D → HN	10 <sup>19</sup>	10 <sup>22</sup>	10 <sup>4</sup>	4·10 <sup>5</sup>
D → LN	10 <sup>3</sup>	10 <sup>6</sup>	10 <sup>4</sup>	4·10 <sup>5</sup>
D → G	10 <sup>-6</sup>	10 <sup>-3</sup>	10 <sup>4</sup>	4·10 <sup>5</sup>
K → HN	10 <sup>5</sup>	10 <sup>8</sup>	10 <sup>4</sup>	4·10 <sup>5</sup>
K → LN	10 <sup>-6</sup>	10 <sup>-3</sup>	10 <sup>4</sup>	4·10 <sup>5</sup>
K → G	10 <sup>-5</sup>	10 <sup>-2</sup>	10 <sup>4</sup>	4·10 <sup>5</sup>
HN → LN	10 <sup>-4</sup>	10 <sup>-1</sup>	10 <sup>4</sup>	4·10 <sup>5</sup>
HN → G	10 <sup>-5</sup>	10 <sup>-2</sup>	10 <sup>4</sup>	4·10 <sup>5</sup>
LN → G	10 <sup>-4</sup>	10 <sup>-1</sup>	10 <sup>4</sup>	4·10 <sup>5</sup>

Table 8.2. Lower and upper bounds of kinetic parameters of the reactions in the VGO-N0-R5 model

Reaction	Pre-exponential factor		Activation energy	
	[s <sup>-1</sup> ]		[J mol <sup>-1</sup> ]	
	LB	UB	LB	LB
VGO → D	10 <sup>6</sup>	10 <sup>9</sup>	10 <sup>4</sup>	4·10 <sup>5</sup>
VGO → LN	10 <sup>10</sup>	10 <sup>13</sup>	10 <sup>4</sup>	4·10 <sup>5</sup>
D → K	10 <sup>12</sup>	10 <sup>15</sup>	10 <sup>4</sup>	4·10 <sup>5</sup>
K → HN	10 <sup>6</sup>	10 <sup>9</sup>	10 <sup>4</sup>	4·10 <sup>5</sup>
K → G	10 <sup>-1</sup>	10 <sup>2</sup>	10 <sup>4</sup>	4·10 <sup>5</sup>

Table 8.3. Lower and upper bounds of kinetic parameters of the reactions in the ETP model

Reaction	Pre-exponential factor [s <sup>-1</sup> or m <sup>3</sup> mol <sup>-1</sup> s <sup>-1</sup> ]		Activation energy [J mol <sup>-1</sup> ]	
	LB	UB	LB	UB
C <sub>2</sub> H <sub>6</sub> → CH <sub>3</sub> • + CH <sub>3</sub> •	6·10 <sup>15</sup>	1.4·10 <sup>16</sup>	3.1·10 <sup>5</sup>	5·10 <sup>5</sup>
CH <sub>3</sub> • + C <sub>2</sub> H <sub>6</sub> → CH <sub>4</sub> + C <sub>2</sub> H <sub>5</sub> •	6·10 <sup>6</sup>	1.4·10 <sup>7</sup>	3·10 <sup>4</sup>	7·10 <sup>4</sup>
C <sub>2</sub> H <sub>5</sub> • → C <sub>2</sub> H <sub>4</sub> + H•	1.9·10 <sup>13</sup>	4.4·10 <sup>13</sup>	10 <sup>5</sup>	2.4·10 <sup>5</sup>
H• + C <sub>2</sub> H <sub>6</sub> → H <sub>2</sub> + C <sub>2</sub> H <sub>5</sub> •	6·10 <sup>7</sup>	1.4·10 <sup>8</sup>	2.4·10 <sup>4</sup>	5.6·10 <sup>4</sup>
H• + C <sub>2</sub> H <sub>4</sub> → C <sub>2</sub> H <sub>5</sub> •	1.5·10 <sup>7</sup>	3.5·10 <sup>7</sup>	5·10 <sup>3</sup>	1.2·10 <sup>4</sup>
CH <sub>3</sub> • + C <sub>2</sub> H <sub>4</sub> → C <sub>3</sub> H <sub>7</sub> •	4.7·10 <sup>7</sup>	1.1·10 <sup>8</sup>	2·10 <sup>4</sup>	4.6·10 <sup>4</sup>
C <sub>3</sub> H <sub>7</sub> • → CH <sub>3</sub> • + C <sub>2</sub> H <sub>4</sub>	4.7·10 <sup>13</sup>	1.1·10 <sup>14</sup>	8.2·10 <sup>4</sup>	1.67·10 <sup>5</sup>
C <sub>2</sub> H <sub>5</sub> • + C <sub>2</sub> H <sub>5</sub> • → C <sub>2</sub> H <sub>4</sub> + C <sub>2</sub> H <sub>6</sub>	6·10 <sup>6</sup>	1.4·10 <sup>7</sup>	5·10 <sup>3</sup>	1.2·10 <sup>4</sup>
C <sub>3</sub> H <sub>7</sub> • + C <sub>2</sub> H <sub>4</sub> → C <sub>2</sub> H <sub>5</sub> • + C <sub>3</sub> H <sub>6</sub>	1.5·10 <sup>4</sup>	3.5·10 <sup>4</sup>	1.6·10 <sup>4</sup>	3.8·10 <sup>4</sup>
CH <sub>3</sub> • + C <sub>2</sub> H <sub>4</sub> → CH <sub>4</sub> + C <sub>2</sub> H <sub>3</sub> •	2.4·10 <sup>5</sup>	5.6·10 <sup>5</sup>	2.1·10 <sup>4</sup>	4.9·10 <sup>4</sup>
CH <sub>3</sub> • + C <sub>2</sub> H <sub>3</sub> • → CH <sub>4</sub> + C <sub>2</sub> H <sub>2</sub>	5.4·10 <sup>6</sup>	1.25·10 <sup>7</sup>	1.9·10 <sup>3</sup>	4.5·10 <sup>3</sup>
C <sub>2</sub> H <sub>3</sub> • + H• → C <sub>2</sub> H <sub>2</sub> + H <sub>2</sub>	6·10 <sup>6</sup>	10 <sup>7</sup>	0	8·10 <sup>-1</sup>
C <sub>2</sub> H <sub>4</sub> → •C <sub>2</sub> H <sub>4</sub> •	3.8·10 <sup>15</sup>	8.8·10 <sup>15</sup>	2.2·10 <sup>5</sup>	3.5·10 <sup>5</sup>
•C <sub>2</sub> H <sub>4</sub> • + C <sub>2</sub> H <sub>6</sub> → CH <sub>3</sub> • + C <sub>3</sub> H <sub>7</sub> •	3·10 <sup>11</sup>	7·10 <sup>11</sup>	1.9·10 <sup>5</sup>	3·10 <sup>5</sup>
•C <sub>2</sub> H <sub>4</sub> • → C <sub>2</sub> H <sub>4</sub>	1.4·10 <sup>5</sup>	3.4·10 <sup>5</sup>	0	8·10 <sup>-1</sup>

It varies whether a specific algorithm can handle the different order of magnitude of the search variables. For the sake of simplicity, I used linearly normalized variables ( $\bar{x}_n$ ) between 0 and 1 (Eq. (4.3)) to assure that this does not affect the convergence of the algorithms.

The kinetic identification problems discussed in this section do not include more sophisticated linear and nonlinear constraints. Most of these algorithms cannot handle such problems; nevertheless, there would be some options available, even if not this many.

### 8.3 Identification methods

The algorithms discussed in this section have been chosen based on the following aspects:

- It is considered as a global optimization method or a metaheuristic one. If not, it was already applied in solving kinetic parameter identification problems in the literature. For example, the Active-Set Optimization or Levenberg-Marquardt algorithm is widely used in such works [82,250,251].
- For the sake of simplicity, we have only considered such algorithms that have a compatible interface with the implemented kinetic models. In general, the aim is to draw attention to the fact that there are several programs which we can choose from to solve the optimization problem, and it is beneficial to apply more than one in parallel.

The final list of the algorithms is shown in Table 8.4. There are at least two things that were not essential in compiling this list. Firstly, although I intended to make a comprehensive overview and to take all major types of algorithms into consideration, Table 8.4 is not a review of all possible choices. Secondly, I did not deal with the novelty of these algorithms in terms of operations research. I was aware of the explosion in the field of “novel” metaheuristic algorithms, i.e., in some cases, only the nomenclature of the proposed algorithm shows some novelty, and any natural phenomenon could be an inspiration [252]. The most obvious example of this is the Harmony Search algorithm picked to pieces by Weyland [253]. On the other hand, the main idea of this Chapter is not to make a comparative study (mainly because the results would absolutely depend on the case studies), but to point out how the application of multiple algorithms gives a much better understanding of a given complex problem. Furthermore, the aim is to consider two (or more) algorithms that have two (or more) different outcomes, even if the underlying math happens to be the same. (In this sense, the application of only one metaheuristic algorithm might also be satisfactory.)

Table 8.4. List of nonlinear optimization algorithms considered for comparison.

<b>Nr.</b>	<b>Name</b>	<b>Short name</b>	<b>Type</b>
1	Active-Set Optimization [254,255]	active-set	derivative-based
2	Biogeography-Based Optimization [256,257]	BBO	evolutionary
3	Bees Algorithm [258,259]	BeA	swarm-based
4	Cultural Algorithm [260,261]	CA	evolutionary
5	Evolution Strategy with Covariance Matrix Adaptation [262]	CMA-ES	evolutionary
6	Controlled Random Search with local mutation [263,264]	CRS2	evolutionary
7	SCH Evolutionary Algorithm [263,265]	ESCH	evolutionary
8	Enhanced Scatter Search [266,267]	eSS	scatter search
9	Firefly Algorithm [268,269]	FA	swarm-based
10	Genetic Algorithm [270]	GA	evolutionary
11	Harmony Search [271,272]	HS	evolutionary
12	Interior Point Algorithm [255,273]	interior-point	derivative-based
13	Improved Stochastic Ranking Evolution Strategy [263,274]	ISRES	evolutionary
14	Levenberg-Marquardt [275,276]	LM	derivative-based
15	Nonlinear Optimization with Mesh Adaptive Direct Search [234–236]	NOMAD	direct search
16	MATLAB Particle Swarm Optimization [277,278]	particleswarm	swarm-based
17	Pattern Search [279,280]	patternsearch	direct search
18	Constrained Particle Swarm Optimization [281]	psopt	swarm-based
19	Particle Swarm Pattern Search [282–284]	PSwarm	swarm-based
20	Shuffled Complex Evolution [285,286]	SCE-UA	evolutionary
21	Constrained Simplex Method [287]	simplex	direct search
22	Simulated Annealing [288,289]	simulanneal	direct search
23	Sequential Quadratic Programming [255,290]	sqp	derivative-based

For the sake of keeping the size of the comparison study at bay, most options of these algorithms were left on their default values. This way, the “raw” efficiency of the algorithms can be compared. One exception is the sample size of the initial values that was standardized as 40 for the VGO-N0-R15 and VGO-N0-R5 models, and 100 for the ethane pyrolysis model. In the case of the algorithms that work with one initial value vector, that resulted in a multi-start approach using each initial value as a starting point. In the case of population-based algorithms, the sample size corresponds to the size of the initial population. Due to the stochastic nature of these algorithms, parallel runs were conducted starting from the same population. The number of parallel runs was chosen to be three and ten for the VGO and ETP models, respectively. In all cases, the result associated with the minimum objective function value was accepted.

#### **8.4 Reaching the optimization target**

I compared the solutions of the applied optimization algorithms from a fixed-target viewpoint. A zero objective function value in Eq. (5.1) corresponds to a case where there is no residual error between the experimental and model results. It is not necessarily the goal to reach a zero value, especially if measurement noise is present, but this provides a joint reference, making the comparison of the results from different kinetic models possible. Figure 8.1 shows the objective function values reached in the case of the VGO model as a function of the computational time, while Figure 8.2 shows these values for the ETP model. For all kinetic models, there is a group of successful algorithms that can be separated from the others because they are associated with significantly lower objective function values (an approximate value of 2 in the case of the VGO models, and below 1 in the case of the ETP model). Each successful solution of the optimization problem can be interpreted as a slightly different realization of the same kinetic model, but with different parameters.

It can be seen in Figure 8.1 that noticeably more algorithms were successful in the case of the VGO-N0-R15 model and the associated objective function values are generally lower; on the other hand, the variance of the results is higher. This is a classic case of the bias-variance tradeoff between the two models with different

complexity. Hence, the total model error can be estimated. Assuming a normal distribution of the results from the successful runs, the errors are  $f(\underline{x}^n) = 0.84 \pm 0.32$  and  $f(\underline{x}^n) = 1.87 \pm 0.12$  for the full and the reduced reaction networks, respectively. This representation of the total model error combines the actual error (represented by the objective function value in the case of a particular algorithm) with the uncertainty of the model; the latter is represented by the several solutions that produce similar model errors. This observation justifies the assumption from Chapter 1 that the error of the model can be reasonably low even in the case where the values of the model parameters cannot be identified with high certainty.

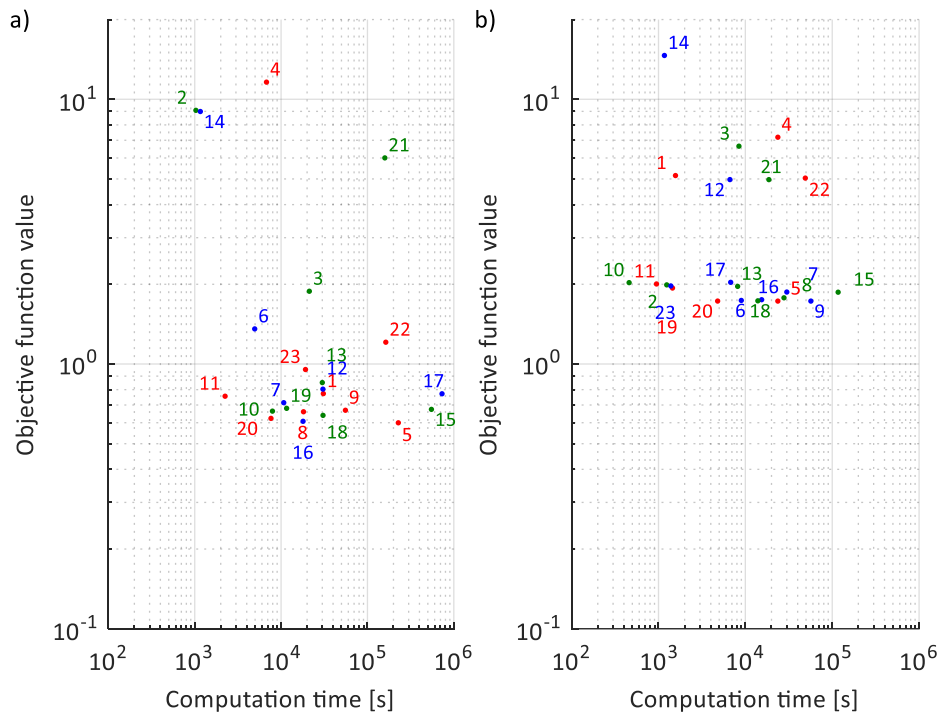


Figure 8.1. Performance of different algorithms for VGO hydrocracking a) VGO-N0-R15 b) VGO-N0-R5.

Figure 8.2, which shows the performance of the algorithms in the case of the ETP model, is analogous to Figure 8.1. Because here reaching  $f(\underline{x}^n) = 0$  is a realistic target due to lack of measurement noise, the performance of the successful algorithms is associated with significantly lower objective function values. The number of successful algorithms (six), however, is significantly smaller than in the previous cases, mainly because second-order reactions are also present in the system, increasing its complexity. This is also the reason behind the

higher computational time requirements, with the exception of the eSS (8) algorithm, indicating the advantages of combined global and local optimization approaches, as pointed out elsewhere [207]. The acceptable error level of the model is  $f(\underline{x}^n) = 0.07 \pm 0.11$ , in line with the expected target value.

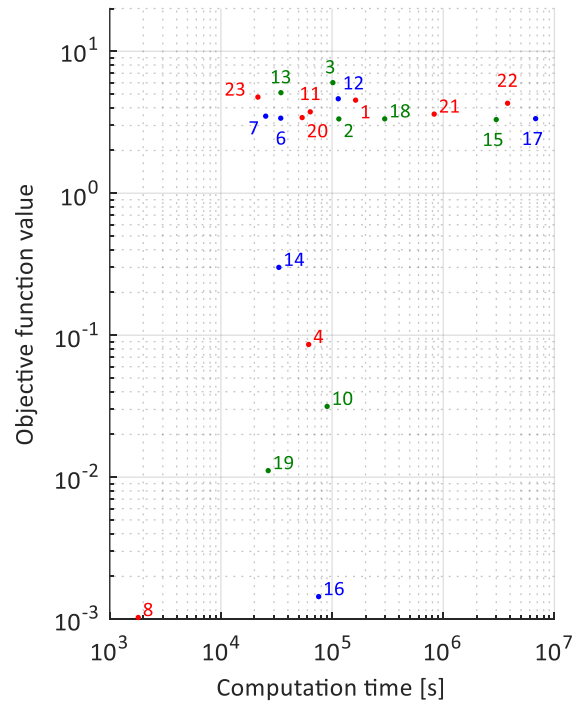


Figure 8.2. Performance of different algorithms for ethane pyrolysis.

As mentioned earlier, in the case of the VGO hydrocracking models, the location and the value of the global minimum are unknown. However, at this point, it can be suggested that the error level of the VGO-N0-R15 and VGO-N0-R5 models reported above quantifies the global minimum. Firstly, the size and nature of the optimization problems are very similar, i.e., they are kinetic identification problems with the same number of parameters to be identified for the ETP and VGO-N0-R15 model. Secondly, the complexity of the VGO-N0-R15 and VGO-N0-R5 models is lower. Given that the performance of the successful algorithms characterizes the global optimum in the case of the more complex ETP problem, it stands to reason to suggest that the estimated total error values of the VGO-N0-R15 and VGO-N0-R5 models also correspond to the global optimum. In conclusion, the application of different nonlinear optimization methods on the



same kinetic identification problem provides a convenient way to estimate the location of the global minimum and the total model error with high certainty.

### 8.5 The importance of model reduction

As mentioned in Section 8.4, the VGO-N0-R15 model has a lower error but also higher variance. Figure 8.1 only shows this in the case of the objective function values, but it is also worth examining how the identified kinetic parameter sets differ from each other. To that end, their correlation should be examined, because high correlation would indicate that the kinetic parameters obtained by the application of different GNLOPT algorithms are similar. The correlation coefficient of two kinetic parameters (denoted as  $A$  and  $B$ ) can be calculated using the following equation:

$$\rho(A, B) = \frac{1}{N-1} \sum_{i=1}^N \left( \frac{A_i - \mu_A}{\sigma_A} \right) \left( \frac{B_i - \mu_B}{\sigma_B} \right) \quad (8.1)$$

where  $\mu$  and  $\sigma$  are the mean and standard deviation of the parameters, and  $N$  is the number of observations (i.e., the number of kinetic parameter sets obtained in the successful runs). Graphical representations of the obtained correlation matrices in the case of the VGO-N0-R15 and VGO-N0-R5 models can be seen in Figure 8.3. Here, the tendency is the same as earlier, namely, the VGO-N0-R15 results show significantly higher variation; in fact, the correlation values are close to zero. This result is inconsistent with the very nature of the reaction network from Figure 3.4 as the reactions should correlate through the concentrations of the component lumps. At the very least, the pre-exponential factors and activation energy values corresponding to the same reaction should be strongly correlated. The lack of this indicates high uncertainty in the identified kinetic parameters.

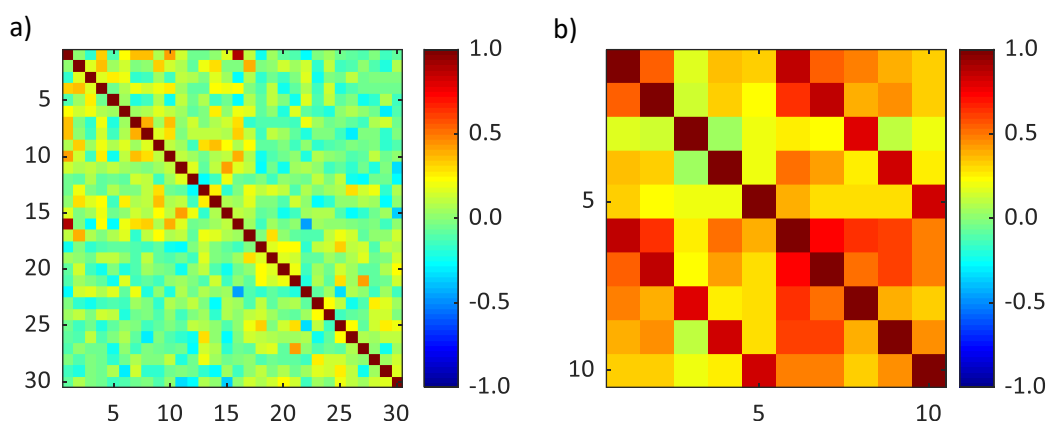


Figure 8.3: Correlation between the identified parameters in the case of the a) VGO-N0-R15 and b) VGO-N0-R5 model

On the other hand, the correlation matrix of the kinetic parameters of the VGO-N0-R5 model in Figure 8.3b has significantly higher values, in other words, the identified parameters have lesser uncertainty. This is an important result because lumped reaction networks are generally dense like the VGO-N0-R15 example. It is possible to identify the kinetic parameters of such networks so that the error of the model is reasonably low; nevertheless, the uncertainty of the identified parameters would stuck at a high level, hindering the application of these models to solve reactor scale-up and design problems. Instead, it is important to reduce the reaction network to keep the uncertainties in the model as low as possible even if the error of the model is acceptable as it is in the case of the results obtained using the VGO-N0-R15 model.

## 8.6 Differences between the identified kinetic parameters

So far only the overall performance of the identified kinetic parameters has been evaluated based on Eq. (5.1). For example, there were 16 successful optimization methods in the case of the VGO-N0-R5 model in Figure 8.1b, associated with approximately the same objective function values. In addition, it is worth to investigate the possible difference between the results more in-depth. An effective way to do that is to compute the difference between the concentration profiles obtained using the identified kinetic parameters. The standard deviation of the simulated pseudocomponent mass concentrations was calculated in case of

the VGO-N0-R5 model (using the ESCH, eSS, GA, HS, NOMAD, and PSwarm algorithms) by the following equation:

$$STD = \sqrt{\frac{1}{N-1} \sum_{i=1}^N \left( c_{i,cal} - \frac{1}{N} \sum_{j=1}^N c_{j,cal} \right)^2} \quad (8.2)$$

where  $N$  is the number of observations, i.e., the number of calculated mass concentrations from each global minimum at a given temperature and LHSV value. The resulting standard deviations are the highest in the case of the VGO and D lumps, as depicted in Figure 8.4. Therefore, even though the value of the objective function is nearly the same, the calculated mass concentrations can differ considerably under certain operating conditions.

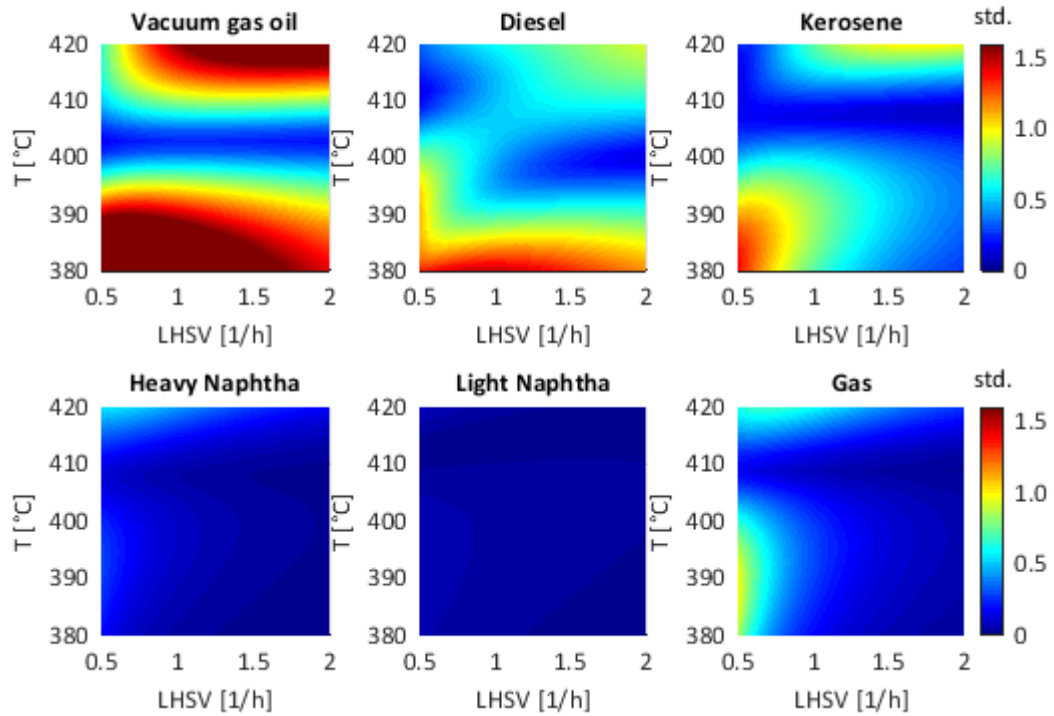


Figure 8.4. Standard deviation of mass concentrations calculated using kinetic parameters at different global minima

High standard deviation values highlight the possible experimental conditions where further measurements would be advantageous [47]. For example, the results of carrying out the hydrocracking experiment at 380 °C anew, and subsequently identifying of the kinetic parameters would enhance the

performance of the kinetic model. This is a further advantage of the application of multiple algorithms during the kinetic parameter identification.

## **8.7 Chapter summary**

Studies assessing the performance of nonlinear optimization algorithms in kinetic model identification are scarce in the literature, and the reason behind this is simple: there is no one “best” algorithm for all cases. Even in the case of the three identification problems discussed in this Chapter, some algorithms performed well in one case and not so well in the other. On the other hand, the application of multiple algorithms in connection with the same identification problem might as well provide further insight on its nature. The difference between the objective function values can characterize the variance of the model. Moreover, the difference between the solutions behind the objective function values (i.e., the kinetic parameter sets) can characterize the uncertainty of the model. This type of characterization provides an absolute measure, in contrast to the methods discussed in the previous Chapters.

## **9 Optimal temperature profile of a fixed-bed heterocatalytic reactor**

So far, I have dealt with reaction networks, kinetic identification problems and the uncertainties related to them. Nevertheless, a heterocatalytic process is much more than just the reactions. Hence, the last two Chapters of my dissertation aim to broaden the scope and focus on reactor design. This can be formulated as an optimization problem as well, but in order to do that, we need to express the optimal design as a single scalar value, i.e., we have to formulate the related objective function. As I have already mentioned in Section 8.2, this is not obvious even in the case of kinetic parameter identification, not to mention the reactor design.

The case study investigated in this Chapter is the process of HCl oxidation, introduced in Sections 2.1.3 and 2.3.1, which is a mildly exothermic reaction leading to equilibrium. Increasing the temperature of the reactor increases the reaction rate but lowers the equilibrium conversion. Moreover, we can have multiple catalyst layers with different activities, and we can split the cooling system of the reactor to have a multi-zoned temperature control; in other words, we have several different ways to design the reactor. Therefore, the main question to be answered in Chapter 9 is how can we define the optimal design of the reactor and how can we translate that definition into a single objective function.

- I show in Section 9.3 that the maximization of the conversion (the straightforward or naive approach) is a bit underwhelming as we can end up with different reactor designs without the tools to differentiate between them.
- In Section 9.4 I define three other optimization cases whose aim is to optimize the reactor temperature profile whilst maintaining a sufficient conversion level. The optimal temperature profile of the fixed-bed HCl oxidation reactor is the key to select optimal reactor design because it can directly affect the lifespan of the catalyst used in the system.

The method suggested here is expected to be applicable regardless of the catalyst present, given that the detailed kinetic model for HCl conversion over the particular catalyst is available.

### 9.1 The reactor design problem

In this chapter I investigate a fixed-bed reactor for HCl oxidation loaded with  $\text{CeO}_2/\text{CuO}$  catalyst. This is a reasonable coupling as the catalytic activity of  $\text{CeO}_2$  and  $\text{CuO}$  are in the same order [291] and the compound has been proven to be stable in long-term [53,220]. Chen et al. investigated such a process in a laboratory-scale reactor using a graded catalyst bed utilizing 11 stages (plus 2 inert sections as the top and the bottom of the reactor filled with alumina spheres 1.2 and 0.6 m long, respectively) [221]. The catalyst activity of the stages alternated between values 1 and 0.3, as can be seen in Figure 9.1 on the overall activity profile of the reactor. The refrigerant on the shell side is the molten mixture of  $\text{KNO}_3$ ,  $\text{NaNO}_2$  and  $\text{NaNO}_3$  53%:40%:7% (m/m) in two independent circuits, equally divided with respect to the length of the reactor; the temperature of the two stages set to 380 and 410 °C, respectively.

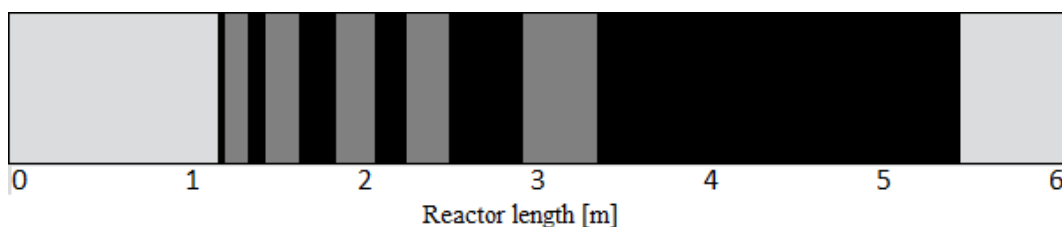


Figure 9.1. Original catalyst activity profile of the reactor. Light gray: zero activity (alumina spheres); dark gray: low activity (0.3); black: high activity (1)

With this design, they reached an HCl conversion value above 83% (n/n) in the reactor. It can be assumed that the catalyst activity profile was designed in such a relatively complicated way in order to facilitate temperature control, avoid local overheating, and allow the system to cool back to a manageable temperature.

In spite of these precautions, temperature gradients above  $250\text{ °C m}^{-1}$  can be observed in their work. Moreover, introducing the catalyst in 11+2 layers per tube into an industrial reactor with approximately 10 000 tubes would be extremely time-consuming, not to mention the high possibility of making an error while carrying out such a monotonous task. Therefore, the aim of my work was the

systematic optimization of the reactor design and conversion process, searching for a possible simplification of this design.

## 9.2 Optimization strategy

On the basis of preliminary studies, I formulated three different approaches of reactor design that are technically feasible.

- **Method A:** the reactor can be filled with catalyst layers with different activities, while the reactor remains undivided from the shell side with only one cooling circuit.
- **Method B:** the reactor can be filled with only one layer of catalyst (with a defined activity), while the reactor shell side will be divided into multiple zones with different temperature stages each.
- **Method C:** the previous two methods can be combined so that each shell zone is coupled with a catalyst layer in the reactor with a certain activity and with a length equal to the length of the shell zone.

The general number of catalyst layers (or cooling zones),  $N$ , varied from 1 to 6 in our investigations; this has been proved sufficient as can be seen later. The 6 m reactor length and the lengths of the two inert sections were considered as given values and therefore remained constant, leaving 4.2 m of effective reactor length in the optimization problems solved. For solving the optimization problem, the NOMAD software package was used (refer to Section 4.1).

## 9.3 Maximizing HCl conversion

In case 1, the objective function for optimization was to maximize HCl conversion by all three methods. The optimization problem is formalized as

$$\max(x_{HCl}(z = 4.2)) \quad (9.1)$$

One important process constraint was considered (i.e., the overall temperature maximum in the reactor (Eq. (9.2)). This coincides with previous studies investigating the performance of CuO–CeO<sub>2</sub> catalysts.

$$T_{max} \leq 437 \text{ }^\circ\text{C} \quad (9.2)$$

The degrees of freedom are the length and activity of each catalyst layer plus the temperature of the cooling zone (method A); the length and temperature of

each shell zone plus the overall activity of the catalyst layer (method B); and finally, the length of zones, plus the temperature of the cooling zone and catalyst activity in each layer (method C).

The achievable conversion values as functions the number of zones in case 1 are located along a saturation curve, as shown in Figure 9.2. (The saturation curve is drawn as a dashed line as these functions actually have discrete domains.) A plateau of 82.3% (n/n) emerges that means the reaction becomes controlled by the equilibrium conversion. Theoretically, lowering the reactor temperature would lead to higher conversion values; however, the resulting decrease in the reaction rate compensates for this effect. Therefore, it can be stated that the achieved conversion value is a practical maximum in this system.

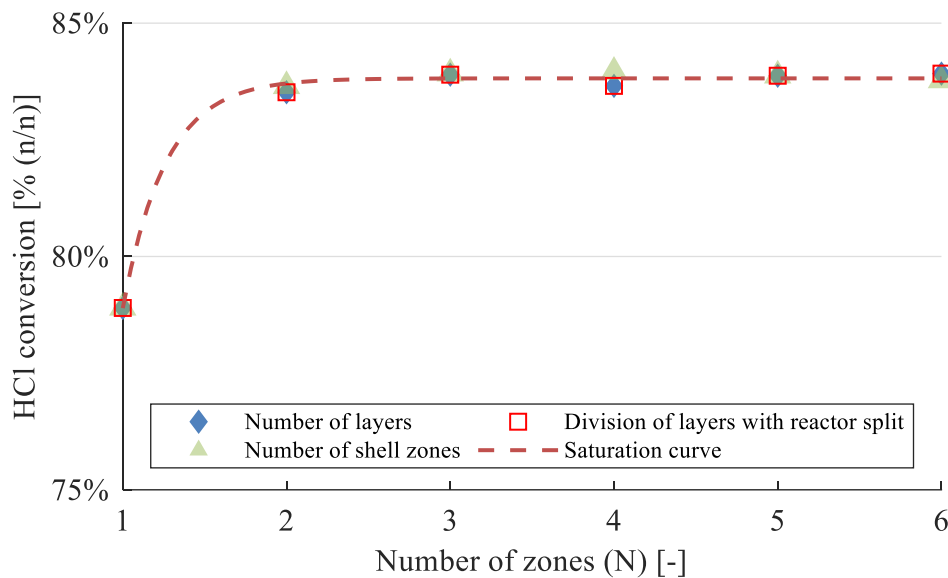


Figure 9.2. Maximum achievable HCl conversion in the reactor by dividing it to  $N \in [1, 6]$  zones

Given that three zones are satisfactory to reach the desired conversion value, I compared the reactor temperature profiles for the solutions given by methods A-C. Figure 9.3 shows the temperature profiles for a three-zone reactor. It can be clearly seen that there is a difference between the results of each method. Method A has two local maxima in reactor temperature. That is actually a result of the fact that the last two catalyst zones have equal activity values (a numeric value of 1). More notably, the overall temperature change is around 40 °C, as opposed to those in the other two methods that have a difference 2-fold larger, and the



temperature also increases more rapidly along the first 0.5 m of the reactor, which could indicate the possibility of the formation of hotspots.

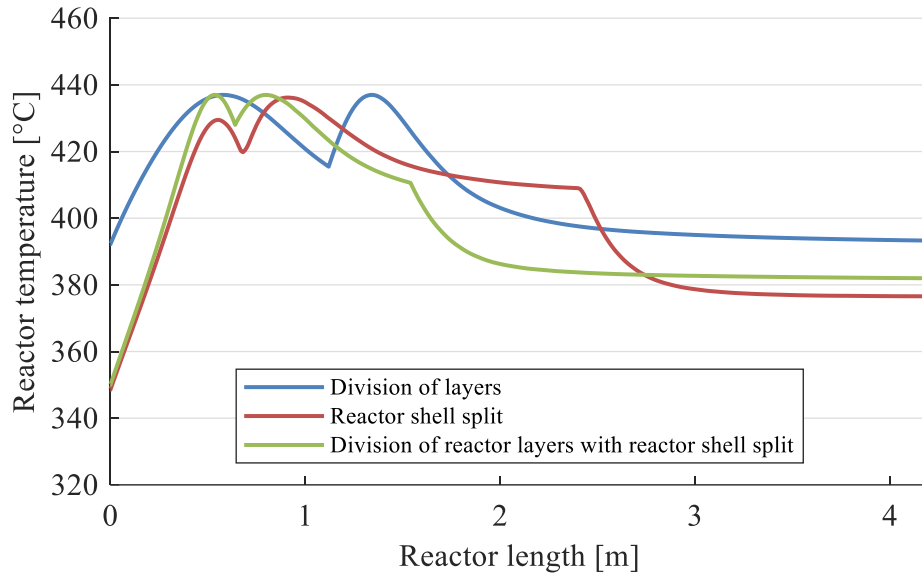


Figure 9.3. Temperature profiles of a three-zoned reactor optimized for maximum conversion

#### 9.4 Optimizing reactor temperature profile

The previously described recognition leads to the wish to reformulate the objective function in order to better address the temperature changes occurring in the reactor. Our aim was to smooth the reactor temperature profile; hence, I constructed three objective functions (summarized in Table 9.1) that can be capable of addressing this problem.

- **Case 2:** reactor temperature maximum minimization. If the maximum temperature is low, then high temperature rises cannot occur in the reactor.
- **Case 3:** standard temperature maxima in each zone in the reactor. If the difference between temperature maxima is low, then this would indicate the smoothness of the temperature profile. Standard deviation was calculated from

$$STD = \left( \frac{1}{N-1} \sum_{i=1}^n (T_i - \bar{T})^2 \right)^{\frac{1}{2}} \quad (9.3)$$

- **Case 4:** a more sophisticated version of case 3. Here the standard deviation of reactor temperature was taken as the objective function. Temperature values were obtained at 0.01 m intervals; the standard deviation of this set was calculated with Eq. (9.3). This case is an exception, as not only the effective reactor length but also the whole 6 m length was considered in the objective function.

The newly constructed objective functions do not involve an explicit temperature constraint such as Eq. (9.2) because the presence of an increasing number of nonlinear constraints affects the performance of the optimization algorithm negatively. Moreover, the results of the temperature profile optimization also satisfy Eq. (9.2) in most cases, as you will see later.

Table 9.1. Developed objective functions for the optimization of the reactor temperature profile.

	case 2	case 3	case 4
objective function	$Q = T_{max}$	$Q = STD(\{T_{i,max}\})$ $i: \text{zone nr.}$	$Q = STD(\{T_{z=z_n}\})$ $z_n = 0.01n$ $n = 0, 1, \dots 600$
nonlinear constraint		$0.82 \leq x_{HCl} \leq 1$	

The minimized values of the objective functions for each case, including the three methods for reactor zoning described earlier, are shown in Table 9.2. These values cannot be compared directly to each other for different cases as values of maximum temperature in case 2 are much higher than values of temperature deviations in cases 3 and 4; however, all these cases were formulated to smooth the temperature profile. Therefore, that will be analyzed both qualitatively and quantitatively hereinafter.

Table 9.2. Minimized values of objective functions for the optimization of the reactor temperature profile.

	<b>Zone nr.</b>	<b>case 2 [°C]</b>	<b>case 3 [°C]</b>	<b>case 4 [°C]</b>
Division of layers (Method A)	1	482.9	70.0	25.9
	2	450.1	25.7	11.7
	3	435.7	16.0	11.2
	4	447.9	15.4	11.3
	5	435.7	15.2	11.1
	6	423.9	12.9	11.8
Reactor shell split (Method B)	1	474.0	68.3	25.5
	2	410.8	28.8	17.4
	3	395.9	31.2	17.4
	4	393.6	34.9	17.4
	5	404.3	33.8	18.1
	6	414.6	35.1	19.5
Division of layers with reactor split (Method C)	1	476.5	69.1	26.0
	2	436.9	18.7	16.4
	3	405.3	17.6	9.5
	4	424.9	10.5	6.3
	5	402.8	11.8	10.9
	6	426.1	16.1	16.5

For quantitative analysis, the results were elevated based on how rapidly the temperature changes in the reactor as a rapid increase may lead to the local overheating in the reactor as stated earlier. The differential quotient of the temperature and the reactor length was calculated on a 0.01 m basis to obtain the approximation of the temperature gradient:

$$\text{grad } T \approx \frac{\Delta T}{\Delta x} \quad (9.4)$$

The maximum gradients, as well as the maximum temperatures for each case and method, are listed in Table 9.3.

It would appear that none of the three objective functions can be selected as the best one, as the minimum value for each method was obtained in different cases.

This could indicate that the causation between temperature deviation and the gradient is not as strong as was expected. There is a possibility of the existence of another objective function that is more suitable to address temperature changes in the reactor, leaving room for future improvements. The results from each case for a given method and number of zones sometimes differ considerably. Because of the motive for designing the cases is the same, I decided to treat the 18 results per a given method as one group and selected the minimum value of temperature gradient maximum regardless of the case.

In general, the number of zones and the maximum temperature gradients are inversely proportional. This was expected as with a higher number of zones the degrees of freedom of the system increase which in turn should lead to better temperature control. With the addition of another zone, the trivial solution is to duplicate one zone from the previous solution; therefore, the solution should be the same or better. Nevertheless, in some cases the gradients become higher with the addition of another zone. This comes presumably from the specific behavior of the NOMAD algorithm.

Table 9.3. Maximum values of temperatures and gradients in case of optimized temperature profiles in the reactor

	Number of layers	Case 2		Case 3		Case 4	
		grad(T) <sub>max</sub>	T <sub>max</sub>	grad(T) <sub>max</sub>	T <sub>max</sub>	grad(T) <sub>max</sub>	T <sub>max</sub>
Division of layers (Method A)	1	370.0	474.3	399.9	484.8	412.0	483.8
	2	177.7	450.3	149.6	429.9	174.9	432.7
	3	155.6	435.9	103.9	427.3	129.9	429.6
	<b>4</b>	173.3	448.0	<b>95.7</b>	<b>428.2</b>	124.9	429.2
	5	157.8	435.9	95.0	430.4	104.5	428.1
	6	133.5	424.1	99.5	426.5	106.5	430.0
Reactor shell split (Method B)	1	369.7	474.2	369.7	474.2	383.8	474.9
	2	172.6	398.9	142.3	397.9	155.8	417.1
	3	137.7	395.0	137.1	395.4	151.5	412.2
	<b>4</b>	<b>133.0</b>	<b>392.4</b>	146.6	395.1	159.1	421.3
	5	132.8	393.4	227.6	402.5	154.8	415.9
	6	132.3	393.0	200.4	413.0	154.5	414.8
Division of layers with reactor split (Method C)	1	370.3	474.4	393.6	479.3	392.7	478.8
	2	137.4	400.6	137.6	420.1	167.7	426.5
	<b>3</b>	<b>134.0</b>	<b>393.3</b>	142.4	429.9	121.5	419.3
	4	134.4	393.2	158.5	418.1	139.6	419.6
	5	133.1	396.1	155.1	415.8	131.2	427.6
	6	162.3	390.7	147.1	417.1	135.9	418.8

Apparently, the lowest gradient values are obtained as a result of case 2 and method A. For only one zone in the reactor (i.e., without a graded catalyst bed), the optimization algorithm is not effective since the only variable is the catalyst activity and there is a minimum value for HCl conversion is defined. Moreover, the maximum temperature exceeds the limitation. I compared the obtained temperature profiles from 2 to 6 zones (Figure 9.4.). For two layers of catalyst, the temperature maximum and the slope drop drastically. The addition of a third layer further decreases the value of the maximum temperature gradient. Upon further increasing the number of search variables, the slopes become slightly more gentle except for that with five layers where the temperature gradient maximum becomes higher again. The number of hot-spots is not equivalent to the number of layers. The reason is that the activities of two catalyst layers are permitted to be the same, for example, in the case of five layers the activities of the first and second layers are both around 0.15. As the maximum temperature gradients for 4, 5, and 6 layers are almost the same, it can be assumed that the minimum value can be reached with the introduction of four layers in the catalyst bed.

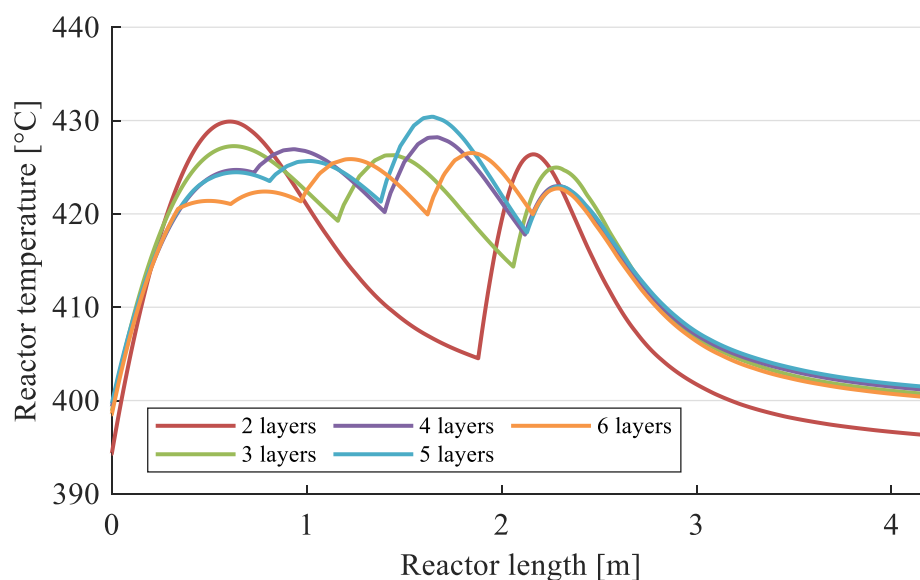


Figure 9.4. Reactor temperature profiles obtained by minimizing the standard deviation of the overall temperature profile of the reactor with zoning the catalyst bed

For method A, the lowest temperature gradient was provided using the objective function in case 3; for methods B and C, case 2 was the most successful.

The possible best solutions were emphasized in Table 9.3. The respective temperature profiles and temperature gradients are shown in Figure 9.5.

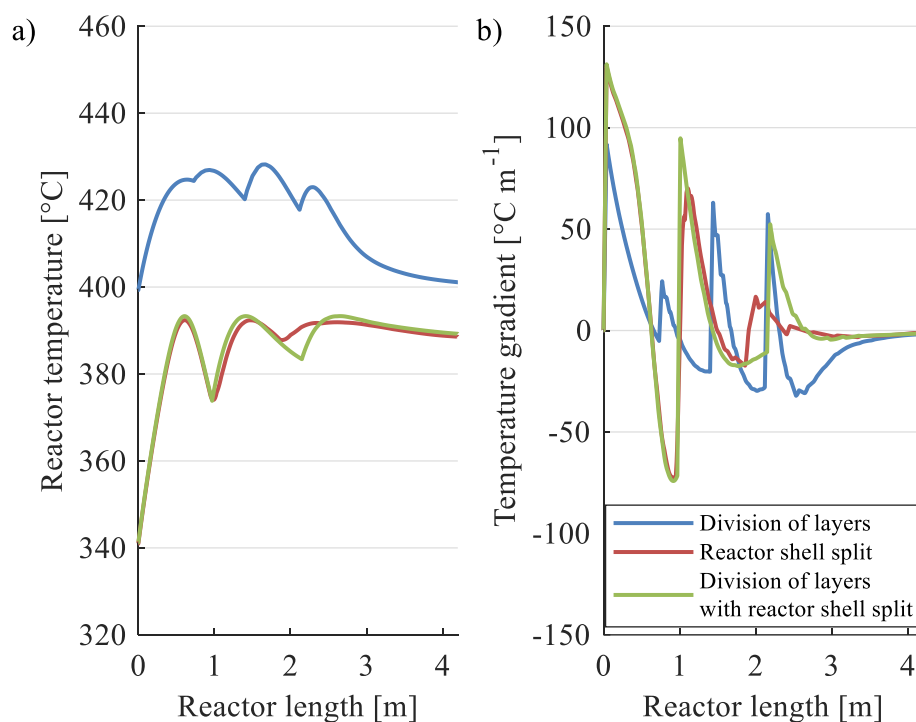


Figure 9.5. Temperature profiles (a) and gradients (b) of reactors resulting temperature profile optimization

In the case of methods B and C, the results show great similarities apart from that the temperature gradient toward the third maximum being lower for method B. For method A, gradients are significantly lower, whereas the temperature itself is higher. The reason behind the higher temperatures is that in this case, the reactor shell is not split into multiple zones, resulting in an overall higher temperature profile to achieve the desired conversion at the reactor outlet. On the other hand, the presence of four catalyst layers with different activities ensures that the reactor temperature will not shoot up due to the heat of reaction released.

As it was described previously, the CeO<sub>2</sub>-based catalysts are less sensitive to high temperatures. (In the catalyst stability tests carried out by Tang et al., it was stated that there is no obvious change in activity at 430 °C for 1200 h.) [62]. In other words, this advantage has a lesser priority. This implies that splitting the reactor shell is not necessary for temperature profile optimization in HCl conversion unless the catalyst activity decreases considerably during continuous

operation. This scenario should be further investigated; e.g., catalyst deactivation model(s) should be integrated into the simulator.

Table 9.4. Optimized reactor configuration of reactors resulting temperature profile optimization

		zone 1	zone 2	zone 3	zone 4
Division of layers (Case 3, Method A)	Catalyst activity [-]	0.15	0.20	0.42	1
	Catalyst bed length [m]	0.73	0.67	0.72	2.08
	Shell temperature [°C]	399			
Reactor shell split (Case 2, Method B)	Catalyst activity [-] <sup>2</sup>	1			
	Shell zone length [m]	1.03	0.84	0.82	1.51
	Shell zone temperature [°C]	341	374	384	387
Division of layers with reactor split (Case 2, Method C)	Catalyst activity [-]	1	0.99	1	- <sup>3</sup>
	Zone length [m]	0.97	1.18	2.05	- <sup>3</sup>
	Shell zone temperature [°C]	341	374	387	- <sup>3</sup>

The final values of optimization variables are summarized in Table 9.4. This shows the reason behind the similarity of the temperature profiles for methods B and C, as the catalyst activity does not actually change in method C, indicating that the effect of this variable has significantly less effect to the absolute value of the objective function than reactor shell temperature, as a result, the catalyst activity is only lower than 1 in case of method A, where the shell temperature has less impact. On this basis, controlling the reactor shell temperature for each zone seems to be more effective. Meanwhile, it can be altered without shutting down the reactor and changing the catalyst layers, and deactivation of the catalyst can be compensated for with the increase of the temperature for a given zone. In conclusion, while splitting the reactor shell is not necessary for temperature profile optimization in HCl conversion, it might be considered as it results in a more flexible system.

<sup>2</sup> Not a degree of freedom.

<sup>3</sup> Not present.



## 9.5 Chapter summary

In this Chapter, I investigated the heterocatalytic oxidation of HCl into Cl<sub>2</sub> (the Deacon process), carried out in a fixed-bed tubular reactor. I considered three different design methods: the application of graded catalyst beds, multiple cooling zones, and finally, the coupling of the previous two into a generalized reactor zone. The number of zones (N) varied from 1 to 6 in the investigations. The results obtained by using the initial objective function for HCl conversion maximization have shown that while reaching the equilibrium conversion is possible, this method does not properly address the temperature changes occurring in the reactor.

Hence, I constructed three new objective functions, evaluated their results using the axial temperature gradient of the reactor temperature as a main indicator. With this method, the temperature deviation along the reactor length can be reduced to a reasonably low level using four catalyst beds with different activities. While splitting of the reactor shell is not necessary, a more flexible system can be achieved with it as shell side temperature may be altered during the course of normal operation of the reactor in order to counter catalyst deactivation. This brings us to the weak point of the investigation presented in this Chapter, as it does not involve this phenomenon. Therefore, a final case study is coming in the next Chapter, which, among other uncertain parameters, also takes deactivation into account.



## 10 Uncertainties of lumped reaction networks in reactor design

The final problem investigated in my thesis connects the topic of lumped reaction networks and reactor design. Lumped reaction networks are extensively used to model complex processes such as hydrocracking. Despite this, studies on the further applicability of these networks during reactor scale-up and design are notably sparser. The application of a lumped reaction network to solve such problems requires dealing with a wide range of uncertainties, e.g., reaction kinetics, the heat of reaction, or pseudocomponent densities. In this Chapter, the design procedure of a trickle-bed hydrocracking reactor with multiple catalyst layers is carried out using a few-step lumped reaction network. The uncertain parameters are considered in a stochastic objective function using uniform probability distributions. Moreover, I extend this approach to catalyst deactivation as well, pointing out that this phenomenon can also be interpreted as a form of uncertainty, instead of estimating the activity using more complex and resource-intensive dynamic simulations. The results obtained by the application of the stochastic design method are compared to the performance of the conventional model-based design as well. An improved test of robustness is applied to evaluate the performance of the reactors under various uncertain conditions. The results indicate that the application of the suggested methods can simplify the structure of the hydrocracking reactor. For example, a fewer number of catalyst layers will be required while retaining the robustness of the reactor at the same time.

### 10.1 Conventional design method

The layout of the reactor to be designed, which is a general trickle-bed unit (see Section 2.3.2 and Section 3.3), is illustrated in Figure 10.1, including the notation of the design variables that should be determined. These can be divided into two groups: operating variables (1-3) with controllable values, and structural parameters (4) that are not dynamically scalable with the reactor load during normal operation. Since the reactor should be designed so that it can be operated at different load levels, the former were determined at four distinct LHSV values (0.5; 1; 1.5; and  $2 \text{ h}^{-1}$ ). The design variables are the following:

- The inlet temperature of the vacuum gas oil ( $T_{VGO}$ );

- The inlet temperature of the hydrogen ( $T_{H_2}$  in Eq. (3.23)). Here, the same value has been applied for every  $H_2$  inlet. It would be possible to set different values before each layer; however, the preliminary results had shown that it would not affect the solution significantly. (The difference is illustrated in Table S21 and Table S22 in the Appendix.)
- The proportion of  $H_2$  that is introduced before each catalyst layer, from which  $\dot{m}_{H_2}^k$  can be calculated that is in turn used in Eq. (3.18)) and Eq. (3.23). Since the sum of these should be 1, the number of degrees of freedom is one less than the number of operating variables.
- Lastly, the ratio of the length of each layer to the total length ( $L_1/L_r$ ,  $L_2/L_r \dots L_n/L_r$ ) should also be determined. Similarly, the number of degrees of freedom is one less than the number of catalyst layers since the value of  $L_r$  has been fixed.

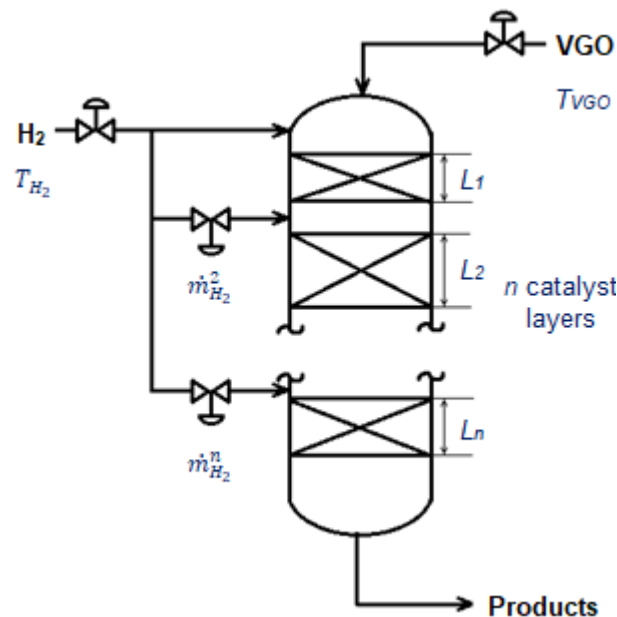


Figure 10.1. Schematics of the VGO hydrocracking reactor with the design variables.

The estimation of the design variables can be formulated as an optimization problem (Eq. (10.1)) to determine them as such to achieve optimal operation of the hydrocracking unit, defined as follows:

- the amount of residual VGO needs to be minimized;
- the amount of diesel produced needs to be maximized;

- the maximum temperature of the reactor should be lower than 410 °C to prevent catalyst deactivation and thermal runaway [292];
- for the same reasons, the maximum temperature elevation on one catalyst layer should be under 50 °C [293].

$$f(\underline{x}) = \sum_{LHSV} \begin{cases} 1.5 w_{VGO}\% - w_D\% & \text{if } T_{max} \leq 410 \\ & \& \Delta T_{max}^k \leq 50 \\ 2000 & \text{otherwise} \end{cases} \quad (10.1)$$

where  $\underline{x}$  is the vector of design variables to be determined,  $w$  is the weight percentage of a component lump in the product,  $T_{max}$  is the maximum temperature of the reactor, and  $\Delta T_{max}^k$  is the maximum of the elevations of the temperature calculated for each catalyst layer. We considered the minimization of the remaining VGO 1.5 times more important and took the amount of diesel with a negative sign into an account in order to maximize its production. If either of the two temperature constraints is not satisfied, the calculated result from the reactor model will be discarded, and the objective function will return a large value. This way, solutions with inadmissible temperature profiles will be ignored. Catalyst deactivation or cycle length does not appear in the objective function at this point, because catalyst time-on-stream is not included in the reactor model. A possible workaround solution is introduced in the next section.

Lower and upper bounds of model variables are listed in Table 10.1. Additionally, linear inequality constraints have been placed to ensure that the sum of hydrogen makeup and catalyst layer length ratios remain below 1 (0.95, to be more precise) so that by all means, we will get a valid final value if we subtract the sum of these from 1.

Table 10.1. Lower and upper bounds of search variables for constrained optimization.

Variable	Lower Bound	Upper Bound
$T_{VGO}$	380 °C	420 °C
$T_{H_2}$	50 °C	350 °C
$\dot{m}_{H_2}^k / \dot{m}_{H_2}$	0.05	0.85
$L_k / L_r$	0.05	0.85

Eq. (10.1) focuses on the output of the reactor and does not consider capital and operational expenditures. The reason behind this is that the size of the reactor is not on the industrial scale and this investigation is only one aspect of the scale-up process. Furthermore, the inclusion of cost estimations would introduce another layer of uncertainty that in turn would make the assessment of uncertainties associated with lumped reaction networks more difficult. Nevertheless, the effect of economic estimations needs further investigation.

## **10.2 Stochastic design method**

There are a number of additional model parameters whose values cannot be relied on with strong confidence. Most of these are inherent to the fact that a lumped reaction network is used, which involves a great deal of simplification.

- Catalyst deactivation. As the components contributing to deactivation are not addressed separately, a simple deactivation function (Eq. (2.3)) should be used, and, for the same reason, the value of  $\alpha$  is not known with full confidence.
- Reaction kinetics. In Chapters 5-8 I have developed several different methods to reduce the uncertainties associated with lumped reaction networks; however, as was shown particularly in Chapter 8, it is not possible to eliminate all of them. So the question here is how the existence of multiple possible kinetic parameter sets that provide more or less the same fit to the experimental data affects the design process.
- The heat of reaction. The rule of thumb used in Eq. (3.21) leaves room for some guesswork even if theoretical calculations support this value. Moreover, it could strongly affect the operation of the hydrocracking unit as the heat of reaction directly influences the reactor temperature.
- Component densities. The reactor model assumes a quasi-homogeneous phase, mainly because, in the case of lumped components, it is quite the headache to calculate gas-liquid equilibrium. On the other hand, the presence of the gas phase can be accounted for by varying the density of the components in a broader range.

Another effect that has not been considered during the conventional reactor design is catalyst time-on-stream ( $ToS$  in Eq. (2.3)). The standard method to calculate with  $ToS$  is to implement it in a dynamic simulator; on the other hand, such simulators are more complex and resource-intensive. Instead, we have formalized it as an uncertain parameter. A convenient way to think about this is by realizing that the time-on-stream is not directly observable; therefore, it can formally be handled as an uncertain value.

The stochastic design method includes an objective function in that, before solving the reactor model, uniformly sampled random variables are generated that affect the solution of the model between the limits listed in Table 10.2. The limits of the deactivation parameter were determined based on the work of Rashidzadeh et al. [151]. The catalyst activity coefficient,  $\varphi$ , was calculated using the generated  $\alpha$  and  $ToS$  values, and then it was used as an additional multiplying factor in Eq. (3.17). The heat of reaction and the component densities were multiplied by a random correction factor to account for their uncertainties. This way, the uncertain parameters may change in a wide range. The actual ranges are probably smaller; therefore, this assumption can be considered as a form of safety margin during the reactor design process.

I assessed the uncertainties of the reaction kinetics in a slightly different way. Firstly, I repeatedly identified the kinetic parameters against the measured values reported in the work of Sadighi et al. [218] mentioned above, using four different derivative-free optimization algorithms (Enhanced Scatter Search (eSS) [266,267], MATLAB Genetic Algorithm (ga) [270], MATLAB Particle Swarm Optimization (particleswarm) [277,278], Nonlinear Optimization with Mesh Adaptive Direct Search (NOMAD) [234,235]). I conducted ten runs using each program. The identified 40 sets of kinetic parameters are listed in Table S18 and in Table S19 in the Appendix. The key idea here that although the root of mean squared error (RMSE) values associated with the separate runs (also listed in Table S3) are reasonably small, the identified parameters themselves vary on a broader scale. Therefore, there may be such temperature and LHSV ranges where the results calculated with different kinetic parameter sets locally deviate from each other, resulting in a form of uncertainty. Because the kinetic parameters of

the five reactions are not independent of each other, one set was chosen randomly before solving the reactor model, denoted as a uniform random integer between 1 and 40.

Table 10.2. Lower and upper bounds of uncertain parameters of the reactor model.

Uncertain Parameter	Lower Limit	Upper Limit	Nominal value
$\alpha$ [ $\text{h}^{-1}$ ]	$5 \cdot 10^{-5}$	$1.5 \cdot 10^{-4}$	$9.172 \cdot 10^{-5}$
$ToS$ [h]	0	8000	0
ID of the reaction kinetic parameter set	1	40	27
$\Delta_r H$ perturbation	-20%	20%	0%
$\rho$ perturbation (separately for the six lumps)	-40%	10%	0%

To solve the reactor design optimization problem (both the conventional (deterministic) and stochastic cases), the MATLAB R2019a Genetic Algorithm [270] was used that is a nondeterministic, population-based, global nonlinear optimization (GNLOPT) method suitable for minimizing highly nonlinear functions such as our case study. We chose the population size as 50 times the number of decision variables in the case of the conventional method, while in the case of the stochastic method, the multiplying factor was chosen to be 100.

### 10.3 Conventional design results

One of the first decisions that have to be made in connection with the hydrocracking reactor design is the number of catalyst layers because the optimization problems formed above actually get separated on the axis of this decision. In other words, each choice of the number of layers has its own objective function with an increasing number of decision variables. In the case of a reactor with no layering, we get eight decision variables, while in the case of six layers, we get 33. For each number of layers considered, we carried out the optimization problem three times using different random seeds, denoting the results of the run associated with the minimum objective function value in Table 10.3. (The values of the design variables associated with each column can be seen in Table S20 to Table S26 in the Appendix.) Results exhibit diminishing returns,



i.e., while both the conversion and the amount of Diesel produced increases with the number of layers, the benefit from introducing another catalyst layer to the reactor becomes lesser for each new layer.

Table 10.3. Nominal operating conditions of the hydrocracking reactor designed using a conventional method in case of different numbers of catalyst layers and averaged over LHSV values.

Number of Layers	1	2	3	4	5	6
Objective Function Value	255.1	213.4	155.2	138.4	130.1	120.9
$\bar{w}_{VGO}$ [% (m/m)]	62.1%	56.9%	47.4%	46.0%	44.9%	43.4%
$\bar{w}_D$ [% (m/m)]	29.4%	32.0%	32.3%	34.4%	34.9%	34.9%
$\bar{T}_{max}$ [°C]	403.9	401.7	401.2	404.4	407.6	409.4
$\overline{\Delta T_{max}^k}$ [°C]	48.0	33.2	42.0	29.7	24.0	21.0

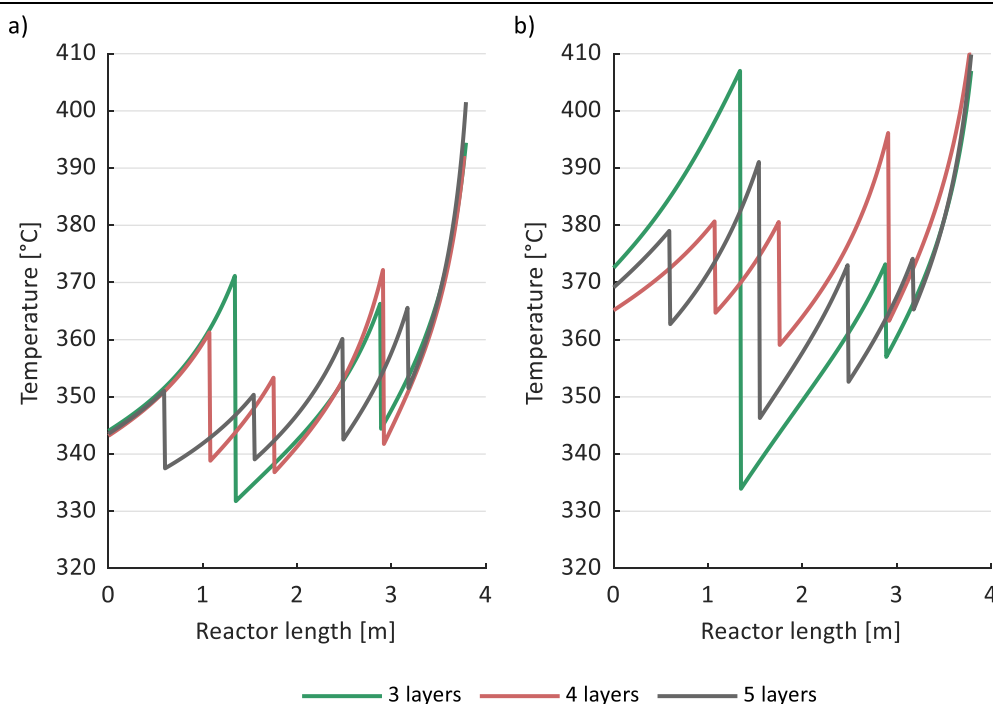


Figure 10.2. Temperature profiles of the hydrocracking reactor designed using a conventional method in case of different numbers of catalyst layers and different LHSV values – a)  $0.5 \text{ h}^{-1}$ , b)  $2 \text{ h}^{-1}$ .

Reactor temperature profiles are shown in Figure 10.2 in the case of LHSV values of  $0.5 \text{ h}^{-1}$  and  $2 \text{ h}^{-1}$ . For intermediate LHSV values, refer to Figure S23 in the Appendix. The difference between the reactors designed is much more

prominent at a higher load level. Furthermore, increasing the number of layers from four to five gives a smaller additional benefit than the inclusion of the fourth layer compared to the case of three, apart from the temperature profile getting smoother to some extent. On this basis, the optimal number of catalyst layers seems to be between three and five, consistent with the industrial practice for a single reactor. Taking into consideration the CAPEX as well, three layers could be a reliable answer. However, the conventional design method does not calculate with several additional uncertain parameters; hence the results might not be sufficiently accurate.

#### **10.4 Reactor sensitivity to uncertain parameters**

One way to differentiate between the solutions shown in Figure 10.2 is to assess their sensitivity to the various uncertain parameters introduced in Section 10.2. To achieve this, I calculated the corresponding sensitivity indices using the Fourier Amplitude Sensitivity Test (FAST) (see Section 2.4.2). The sensitivity indices are shown in Figure 10.3. It can be seen that only the four parameters denoted on the left side have a considerable effect on the objective function in the range specified in Table 10.2. In other words, the designed reactor already shows high robustness against the uncertainty in reaction kinetics and the majority of the pseudocomponent densities.

The behavior of the reactor will be less sensitive to catalyst deactivation if more catalyst layers are present (although there is a minor increase in the case of five layers), and the tendency is the same for the heat of reaction. These results meet with the expectations – more layers result in lower temperature gradients and steadier reaction rates, and both of these could contribute to a decline of sensitivity to the uncertain parameters in connection with the reactions. The only parameter sticking out of the queue is the sensitivity to the feedstock density ( $\rho_{VGO}$ ). This value affects the reactor performance on a high level, influencing both the flow velocity and mass concentrations, explaining the high sensitivity index that does not really become lower in case of more layers. It can be assumed that the effect of lower density, thus higher velocity and lower residence time

could only be countered by a higher reactor length (volume), but that is a fixed value in our investigation.

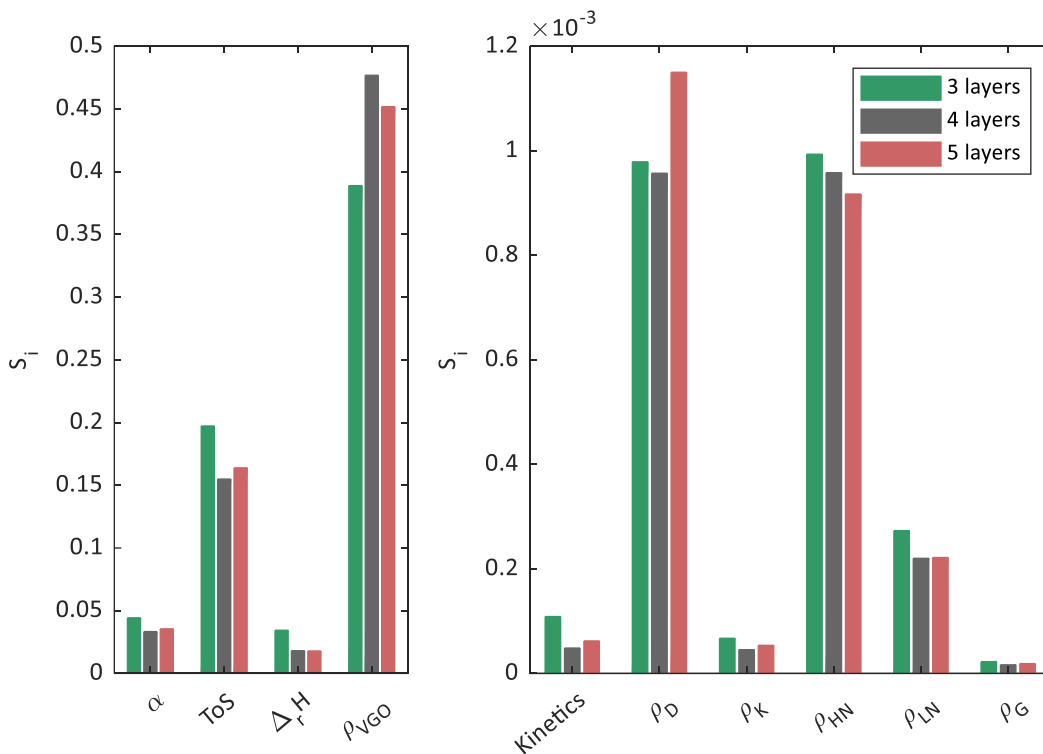


Figure 10.3. Sensitivity indices of the hydrocracking reactor designed using the conventional method to different uncertain parameters.

I have also performed a local sensitivity analysis to illustrate the effect of each uncertain parameter. We used a one-at-a-time approach, varying only one uncertain parameter per run and leaving all the others at their nominal value given in Table 10.2. Results are given in Figure 10.4 for the hydrocracking reactor with four catalyst layers. (Cases of three and five layers are shown in Figure S24 and Figure S25 in the Appendix due to the high degree of similarity.) It can be seen that the behavior of the reactor is most sensitive to the heat of reaction and to the VGO density. Under certain conditions, the objective function reaches zero that indicates a thermal runaway (the mass concentrations of VGO and D both reaches zero), or at least such part of the domain where the reactor model is not valid. It is important to mention that the chance of actual runaway is less than that Figure 10.4 indicates as several operating variables are present that could be used to control the reactor (e.g., the temperature of  $H_2$  could be lowered). Nevertheless, this should be taken into account to test reactor robustness.

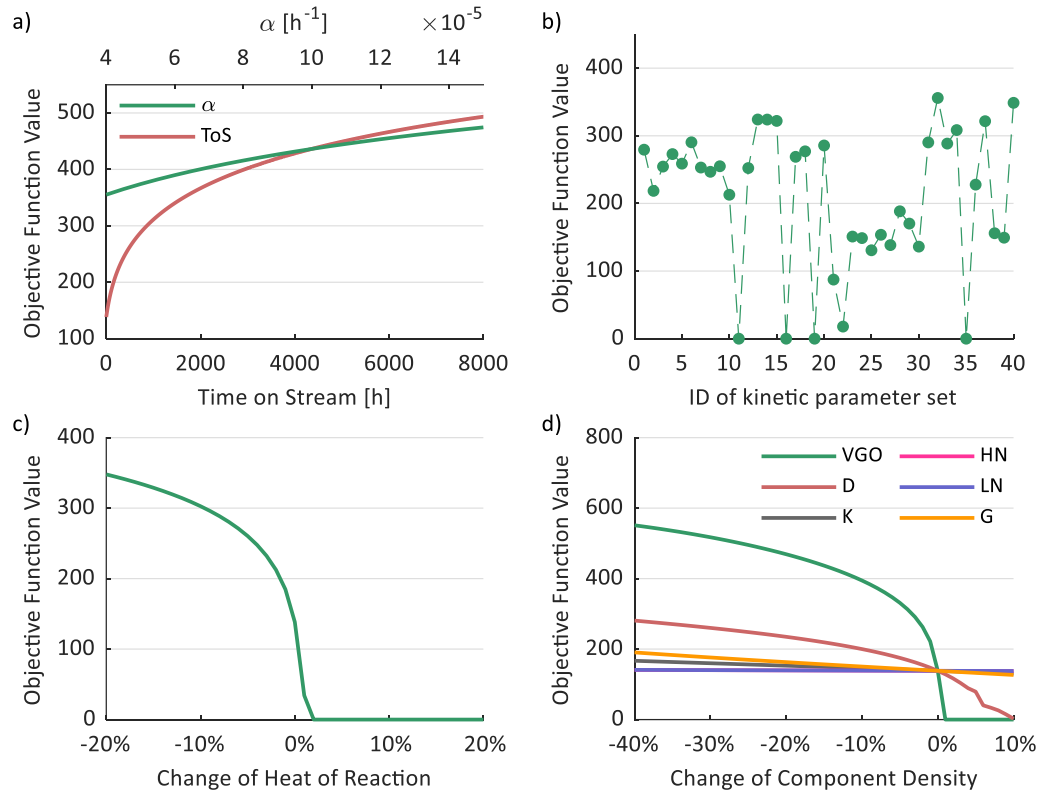


Figure 10.4. Local sensitivity analysis of the hydrocracking reactor with four catalyst layers to different uncertain parameters designed using the conventional method.

In conclusion, the uncertainty analysis showed that designing the hydrocracking reactor with at least four catalyst layers instead of three would increase its robustness. Moreover, I have identified four parameters to that all reactor designs investigated are highly sensitive. In the second half of the discussion, I evaluate the stochastic design approach and how it affects the robustness of the reactor.

## 10.5 Stochastic design results and comparison

In the case of stochastic design, for each number of layers considered, we carried out the optimization step 20 times using different random seeds and averaged the results. At this point, the cumulative average became nearly constant. The resulting design variables characterize the average performance of the reactor under various uncertain conditions. Design variables obtained by the conventional and the stochastic methods are compared in Figure 10.5. (Similar

outcomes of cases with three and five layers can be found in Figure S26 and Figure S27 in the Appendix.) The heights of the bars were normalized between the lower and upper bound of the search variables (Table 10.1) for the sake of better visibility. A significant difference in the results is that the contribution of the last catalyst layer appears to be smaller, given its shorter length and the lower amount of hydrogen introduced. The change can be related to, for example, that the catalyst deactivation phenomenon was taken into account during the stochastic design, which results in lower average reaction rates, hence the higher amount of hydrogen make-ups and longer catalyst layers.

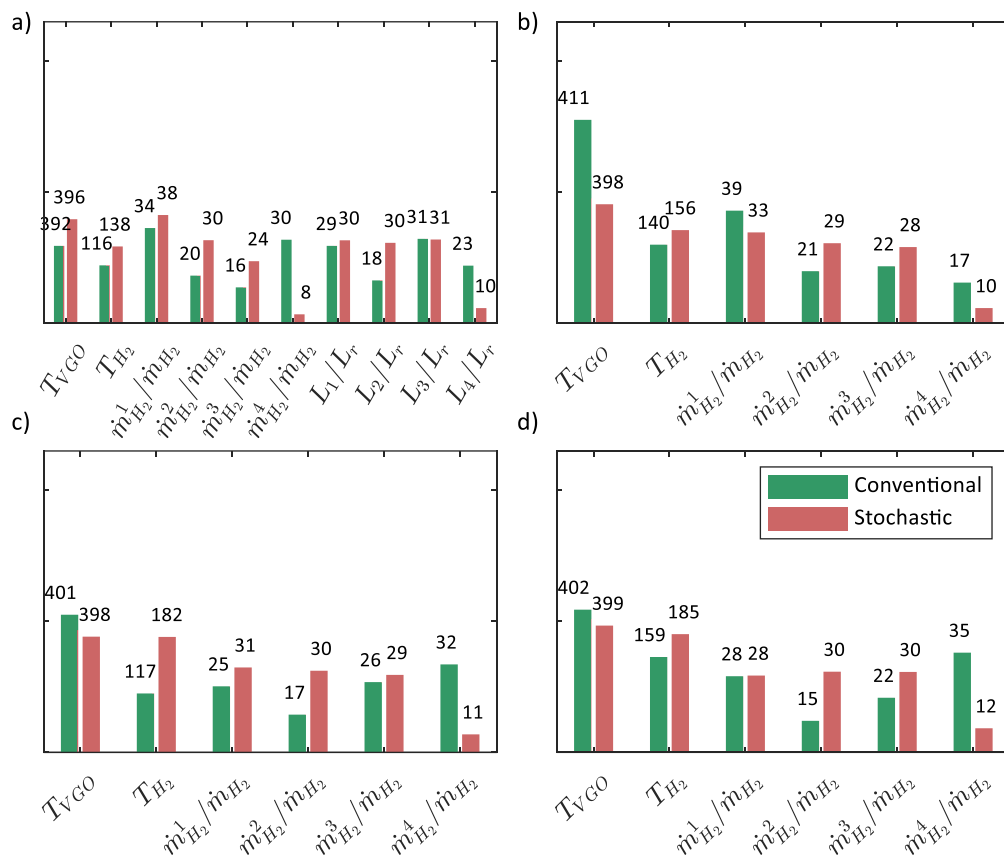


Figure 10.5. Nominal values of design variables of the hydrocracking reactor with four catalyst layers in case of different LHSV values – a)  $0.5 \text{ h}^{-1}$ , b)  $1 \text{ h}^{-1}$ , c)  $1.5 \text{ h}^{-1}$ , d)  $2 \text{ h}^{-1}$ .

### 10.6 Robustness of reactor design

It also needs to be investigated whether the stochastic design method represents an improvement. One method to measure this is to calculate the deviation of the

objective function caused by the variation of the uncertain parameters. Here, a lower deviation represents a more robust solution [134]. The objective function was evaluated at the sampling points denoted in Table 10.4 using a uniform sampling method. The number of sampling points for each uncertain parameter is proportional to its GSA index.

Table 10.4. Maps of the uncertain parameter space for the tests or robustness.

Uncertain Parameter	Lower Limit	Upper Limit	Sample size
$\alpha$	$4 \cdot 10^{-5}$	$1.5 \cdot 10^{-4}$	3 points
$ToS$	0	8000	7 points
$\Delta_r H$ perturbation	-20%	20%	3 points
$\rho_{VGO}$ perturbation	-40%	10%	8 points
Total			504

We should not overlook the fact that we have multiple design variables (e.g., inlet temperatures, makeup H<sub>2</sub> ratios) that can be modified during the course of normal operation. In order to take this effect into account, we can recalculate the values of the operating variables by solving the same GNLOPT problem and objective function. The previously identified layer length values remained the same, simulating an already constructed reactor rather than designing a new one for each uncertain parameter.

Further exploring this idea, the usage of the same constraints as in Table 10.1 would be disadvantageous because these cover a wide range, and during normal operation, such substantial changes in the values of process variables cannot be carried out (at least on a reasonable time horizon). Therefore, we defined a distance metric between two uncertain parameter sets as follows:

$$d_u = \sqrt{\sum_{j=1}^4 \left( (u_j^n - u_{j,nom}^n) \cdot Si_j \right)^2} \quad (10.2)$$

where  $u_j$  is the actual value of the  $j^{th}$  uncertain parameter in the small map,  $u_{j,nom}$  is the nominal value,  $Si_j$  is the corresponding global sensitivity index. The superscript  $n$  denotes that the values of the uncertain parameters have been normalized between 0 and 1 using their corresponding lower and upper bounds

from Table 10.1. Using the distance metrics, the corresponding constraints can be defined as:

$$LB_{act} = LB_{min} \cdot \frac{d_{u,act}}{d_{u,max}} \quad (10.3)$$

$$UB_{act} = UB_{max} \cdot \frac{d_{u,act}}{d_{u,max}} \quad (10.4)$$

In other words, we have narrowed the search intervals based on the extent to that an uncertain parameter combination differs from the nominal values listed in Table 10.2. Narrowing the search intervals might contribute to lesser capital expenditure and a shorter payback period as well because it essentially translates into narrower control regions of the inlet temperatures that in turn would result in the need for a less powerful auxiliary heat exchanger to maintain process control.

The minimum lower and the maximum upper deviations of the operating variables ( $LB_{min}$  and  $UB_{max}$ , respectively) were determined as follows:

- the constraints for the VGO inlet temperature would remain the same as in Table 10.1 considering the relatively narrow interval;
- in the case of the temperature of the H<sub>2</sub> inlet,  $LB_{min}$  is 25 °C lower, and  $UB_{max}$  is 25 °C higher than the value associated with the nominal case. The values of the operating parameters at the nominal uncertainty level are denoted in Table S27 in the Appendix.
- Finally, in the case of the H<sub>2</sub> makeup ratios, a ±10% constraint was applied in the same manner.

After formulating and solving the optimization problems, I calculated the probability densities of the objective function in each case. These are depicted in Figure 10.6.

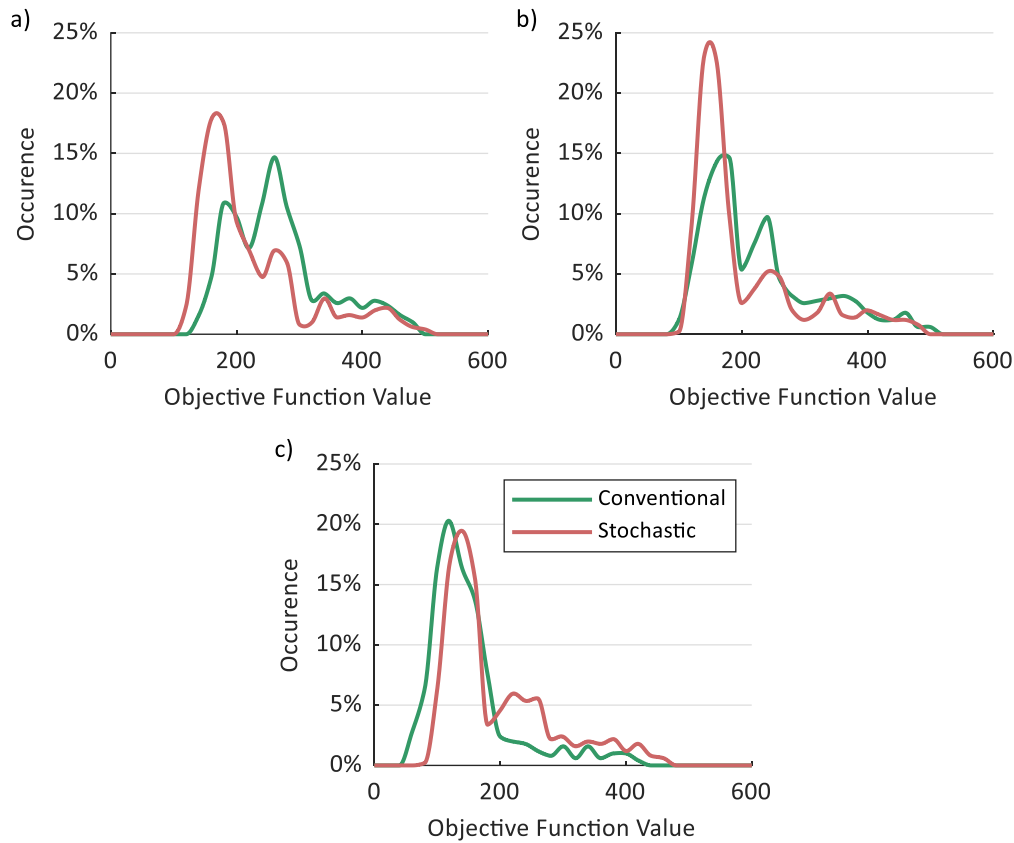


Figure 10.6. Probability density of the optimized objective function values in the space of uncertain parameters in case of the hydrocracking reactor with a) three b) four c) five catalyst layers.

The plots are notably different, as in the case of four layers a definite improvement is visible, while in the case of five layers, there is none – one could say the stochastic design method actually presents a setback. The reason behind this is that a hydrocracking reactor with more catalyst layers is fundamentally more robust because there are more control options that could negate the effects of uncertainties. Consequently, in the case of a reactor with a fewer number of catalyst layers, the investigation on the effects of uncertain parameters is beneficial, resulting in a reactor design where the operation is less sensitive to the fluctuations of the uncertain parameters. On the other hand, if more catalyst layers are present, the advantages of the stochastic design methods will dissipate. They are not inherently better than conventional methods. In my opinion, this is a significant result; nevertheless, based on our literature review, it is seldom emphasized.



## 10.7 Chapter summary

The so-called lumping approach is a powerful tool to model the kinetics of complex processes such as hydrocracking. On the other hand, such reactor models have several uncertain parameters that do not always get the proper attention. In order to deal with these uncertain parameters, I applied a stochastic design approach. Although stochastic methods are commonly used for plant modeling, they are seldom applied to design a single unit. On the other hand, I found that stochastic optimization is well suited to handle the uncertainties of lumped reaction networks. I also investigated whether the stochastic approach represents an improvement over the conventional method. I applied GSA to measure the robustness of the reactor design. An improved test of robustness was also developed, consisting of the sampling of the uncertain parameter space and then testing whether the operating variables can be used to control the designed reactor in order to maintain optimal operation (conversion, product composition, and reactor temperature profile).

In conclusion, it can be stated that the application of a stochastic design method can simplify the reactor design. In the specific case investigated, this would mean a fewer number of catalyst layers or a more effective heat exchanger explicitly designed for a narrower temperature interval to control reactor inlet temperature. All of these might contribute to lesser capital expenditure and a shorter payback period. Nevertheless, the application of a stochastic design method is not automatically advantageous; rather, its usefulness depends on how flexibly the designed reactor system can be operated. If more control options are available to negate the effects of uncertainties, the performance of the conventionally designed reactor will also be satisfactory. The limit to that a stochastic design approach holds advantages over the conventional method still needs to be investigated; nevertheless, the case study presented in this Chapter provides a good starting point to assess and counter the effect of uncertainties during the design of heterocatalytic processes.



## 11 Final remarks and farewell

This dissertation can be separated into two major parts. The first one is about the nature of lumped reaction networks. I used two of such case studies, involving the pyrolysis of real plastic waste and the hydrocracking of vacuum gas oil. Chapter 4 introduces the basic outline of how to identify the kinetic parameters given the nature of the available experimental data. I developed a lumped reaction network and a two-step identification strategy to determine the kinetic parameters under various catalytic conditions without any a priori information available on the activation energies. More importantly, this chapter introduces a model-based scale-up approach to evaluate the performance of the various zeolite-based catalysts used in the experimental work.

One of the key observations of my work was that lumped reaction networks usually tend to be overparametrized, i.e., the number of lumped reactions included in the kinetic model is too much compared to how detailed the related experimental data is. That in turn results in parametric uncertainty that should be dealt with before we can apply a lumped reaction network in reactor design. Therefore, I introduced multiple methods to quantify and reduce these uncertainties, presented in Chapters 5-8.

In Chapter 5, I developed a kinetic parameter identification strategy that produces a reduced lumped reaction network whose all states are observable. Starting from the VGO-N0-R15 reaction network, I carried out sequential identification and reaction network reduction steps to select those that significantly influence the product composition under the given experimental conditions. By examining the state-space model representation of the resulting reduced reaction networks, I successfully found the VGO-N0-R5 network with all parameters observable and therefore identifiable.

In Chapter 6, I proved that the reduction of the reaction network increases the confidence of the kinetic parameters. Applying global sensitivity analysis methods, I have confirmed that the elimination of the reactions whose kinetic parameters the model is not sensitive to, the confidence intervals characterizing the remaining model parameters is typically become narrower. I concluded that even if we identify the kinetic parameters of several reactions from a relatively

low-resolution experimental data, the high uncertainties of the identified values significantly influence the possible future application of the model in process design.

By examining the experimental data of the pyrolysis of real plastic waste, I recognized that under certain conditions the liquid product composition remains constant. I utilized the correlations between the amounts of liquid products in Chapter 7 to increase the number of pseudocomponents without increasing the number of reactions present in the lumped reaction network.

I took the characterization of kinetic parameter uncertainty one step further in Chapter 8 and quantified the uncertainty of the reaction networks not just relative to each other by estimating the variance of the objective function. To that end, I used 23 different nonlinear optimization algorithms per identification problem, using the VGO-N0-R15 and VGO-N0-R5 reaction networks, and a more regular few-step kinetic model for ethane pyrolysis that could be used as a reference on the performance of the algorithms as the exact values of the parameters to be identified were already available prior to the investigation (Table 3.3). In the case of the specific examples, I deemed the performance of the Enhanced Scatter Search, Genetic, and Particle Swarm Optimization algorithms as best.

I showed that the correlation between the identified kinetic parameter sets provides a measure to parameter uncertainty. If the correlations are low, the difference between the identified kinetic parameter sets will be high regardless the reasonably low model error. Generally this would be unfavorable because it means that the true values of the parameters cannot be determined. Finally, starting out from the underlying differences between the calculated product compositions, I was able to point out the direction where further experimental work should be carried out in order to increase the reliability of the kinetic model.

The second major part of my dissertation turns to the design of heterocatalytic processes. In Chapter 9 I conducted a case study where the process itself was not uncertain (instead, the kinetics HCl oxidation to  $\text{Cl}_2$  is well known), but the question of how to define the optimal heterocatalytic reactor design remained open. It would be unwise to assume that my answer to that question is the only correct one; nevertheless, it is adequate and has been recognized for its novelty.

Finally, in Chapter 10 I combined the topic of lumped reaction networks (with uncertain parameters) and heterocatalytic reactor design and carried out both the conventional and stochastic model-based design process of a trickle-bed hydrocracking reactor. Here I have come up with the conclusion that the advantage of the stochastic approach (i.e., design under uncertainty) will diminish if we the flexibility of the reactor increases (such as in the case of adding another catalyst layer and thus increasing the number of process variables we can use to control its operation).

Throughout my dissertation, I introduced several alternative reaction networks to describe the same process (summarized in Table S1), and this inevitably raises the question whether a “best” choice exists. In my opinion there is no such network. Nevertheless, Global Sensitivity Analysis was proved to be the most versatile tool. Aside from its use in Chapter 6, I have applied it during the construction of P-N2-R9 (Figure 7.5b); moreover, I was able to use the same method to assess reactor sensitivity to all possible sources of uncertainties, determining the key uncertain parameters needs to be addressed in order to achieve robust design. On this ground, the application of P-N0-R5, P-N2-R9, and VGO-N0-R7 reaction networks is more favorable as these could be determined with relative ease. On the other hand, I purposefully carried on the VGO-N0-R5 network in reactor design (thus constructing VGO-N1-R5 in Section 3.3) mainly because it did meet the observability criterion established in Section 5.3, which, in my opinion, indicates strong reliability. It would be very useful to compare the VGO-N0-R5 and VGO-N0-R7 reaction networks in terms of model variance (Chapter 8) and applicability during reactor design (Chapter 10); unfortunately, this is beyond the scope of this dissertation.

Research work associated with obtaining any kind of academic degree can never be completed but only halted. While I am certain that my dissertation is coherent as I tied the loose ends to the best of my knowledge, there are many points of interest that one can explore:

- The question of how many discrete lumps to include in the kinetic model is only briefly explored in Chapter 7 (that instead focused on the correlations between them) and how should we define them as the

introduction of  $L_+$  and  $L_-$  in the pyrolysis reaction network in Section 3.1.2 was somewhat arbitrary.

- Global sensitivity analysis, in theory, could be used to automate the lumping process itself, i.e., one might determine which lumps have decisive roles in describing the behavior of the chemical system investigated.
- I only mentioned in Section 8.2 that the formulation of the objective function can also have an effect on the uncertainty of the kinetic model, but I have actually not yet been able to investigate it.
- It would also be beneficial to study the dynamic behavior and controllability of the heterocatalytic reactors designed in Chapters 9 and 10, especially to investigate the effect of catalyst deactivation more in-depth.

That is to say, there is still much to do. But like most scientific texts, this one has already become long and dry, so this would be the end for now. I hope that the scientific community will find my contribution to the topics included in my dissertation useful. With that, it is time to say goodbye. Have fun with reducing uncertainties!

## Theses

From the bird's eye view, I investigated four distinct topics using four case studies in my dissertation. I summarized the related results in four theses. The relations between the theses and the various sections of my dissertation are denoted in Table 12.1. It goes without saying that the references in this table are not necessarily comprehensive; rather, their main purpose is to facilitate navigation throughout this work.

Table 12.1. Relations between major topics, reactor models and theses.

	<b>Pyrolysis of real plastic waste</b>	<b>Vacuum gas oil hydrocracking</b>	<b>HCl oxidation</b>	<b>Ethane pyrolysis</b>
Process model development <sup>4</sup>	Section 3.1 Section 4.3 <i>Thesis #3</i> <sup>5</sup>	Section 3.3  <i>Thesis #4</i>		
Reduction of reaction network	Section 6.2 Section 7.2 <i>Thesis #1</i> <i>Thesis #3</i>	Section 5.2 Section 6.3 <i>Thesis #1</i>		
Parameter identifiability		Section 5.3 Section 6.5 Section 8.4 Section 8.5 <i>Thesis #1</i> <i>Thesis #2</i>		Section 8.4     <i>Thesis #2</i>
Reactor design	Section 4.4 <i>Thesis #3</i>	Chapter 10 <i>Thesis #4</i>	Chapter 9 <i>Thesis #4</i>	

<sup>4</sup> Reactor models taken from the literature are not present in this list.

<sup>5</sup> i.e., thesis statement

**Thesis #1.** I developed new strategies that can be applied to reduce uncertainties associated with the kinetic parameters of lumped reaction networks.

- I reduced the number of reactions present in the reaction network to ensure the observability of all kinetic parameters, following the definition from the field of control theory. Such a reaction network is identifiable with high certainty.
- I applied Global Sensitivity Analysis to identify and eliminate such reactions whose influence on the final product composition is low. Although an arbitrary complex lumped reaction network can be constructed from a given experimental data set, the associated parameter uncertainty also increases with the complexity, placing a soft upper limit on the number of identifiable parameters.

Related publications: 1, 2, 8, 11

**Thesis #2.** I applied multiple global nonlinear optimization algorithms to identify the kinetic parameters of the same reaction network parallel and concluded that the different performance of the algorithms is related to the uncertainty of the model.

- I quantified the model variance and total model error in the case of lumped reaction kinetic models.
- I showed that the uncertainty of the kinetic model can be characterized with the correlation of the identified parameter sets.
- The underlying differences between the calculated mass concentration profiles point out the direction where further experimental work should be carried out to increase the reliability of the model.

Related publications: 3, 9



**Thesis #3.** After studying the thermo-catalytic pyrolysis of real plastic waste, I developed a model-based method for catalyst comparison.

- I developed a lumped reaction network and a two-step identification strategy to determine the kinetic parameters of the lumped reaction network without any a priori information available on the activation energies.
- I utilized the correlations between the amounts of liquid products to increase the number of pseudocomponents without the necessity of including additional reactions.
- I compared the performance of the catalysts using the model-based approach and a reactor model inspired by the possible scale-up method of the real plastic waste pyrolysis process.

Related publications: 4, 5, 10, 12, 13

**Thesis #4.** I developed new methods for the model-based design of fixed-bed heterocatalytic reactors, with special regard to parameter uncertainties and operation aspects.

- I investigated the conditions under that we can use lumped reaction networks in the design procedure. I mapped out the various uncertain parameters in a stochastic objective function during the model-based design and optimization of the reactor. Moreover, I extended this approach to catalyst deactivation as well; pointing out that this phenomenon can also be interpreted as a form of uncertainty.
- I constructed new objective functions to define the optimal operation of a fixed-bed heterocatalytic reactor for HCl oxidation. I have developed a method that can be used to optimize the reactor temperature profile as well as the yield, using the temperature gradient and standard deviation, achieving a smooth temperature profile that can extend the lifespan of the applied catalyst.

Related publications: 6, 7, 14, 15

**Publications related to theses****Articles in international journals**

1. Z. Till, T. Varga, L. Szabó, T. Chován, Identification and Observability of Lumped Kinetic Models for Vacuum Gas Oil Hydrocracking, *Energy Fuels* 31 (2017) 12654-12664.  
<https://doi.org/10.1021/acs.energyfuels.7b02040>. SCImago Journal Ranking: Q1, Impact factor: 3.024
2. Z. Till, T. Varga, J. Sója, N. Miskolczi, T. Chován, Reduction of lumped reaction networks based on global sensitivity analysis. *Chem. Eng. J. (Amsterdam, Neth.)* (2019), 121920.  
<https://doi.org/10.1016/j.cej.2019.121920>. SCImago Journal Ranking: Q1 (D1), Impact factor: 10.652
3. Z. Till, T. Chován, T. Varga. Improved understanding of reaction kinetic identification problems using different nonlinear optimization algorithms. *J. Taiwan Inst. Chem. Eng.* 111 (2020), 73-79.  
<https://doi.org/10.1016/j.jtice.2020.05.013>. SCImago Journal Ranking: Q1, Impact factor: 4.794 (2019)
4. Z. Till, T. Varga, J. Sója, N. Miskolczi, T. Chován, Kinetic identification of plastic waste pyrolysis on zeolite-based catalysts. *Energy Convers. Manage.* 173 (2018), 320-330.  
<https://doi.org/10.1016/j.enconman.2018.07.088>. SCImago Journal Ranking: Q1 (D1), Impact factor: 7.181
5. Z. Till, T. Varga, J. Sója, N. Miskolczi, T. Chován, Structural assessment of lumped reaction networks with correlating parameters. *Energy Convers. Manage.* 209 (2020), 112632.  
<https://doi.org/10.1016/j.enconman.2020.112632>. SCImago Journal Ranking: Q1 (D1), Impact factor: 8.208 (2019)

6. Z. Till, T. Varga, J. Réti, T. Chován, Optimization Strategies in a Fixed-Bed Reactor for HCl Oxidation. *Ind. Eng. Chem. Res.* 56 (2017), 5352-5359.  
<https://doi.org/10.1021/acs.iecr.7b00750>. SCImago Journal Ranking: Q1, Impact factor: 3.141
7. Z. Till, T. Chován, T. Varga, Uncertainties of lumped reaction networks in reactor design. *Ind. Eng. Chem. Res.* 59 (2020), 10531-10541.  
<https://doi.org/10.1021/acs.iecr.0c00549>. SCImago Journal Ranking: Q1, Impact factor: 3.573 (2019)

#### Articles in conference publications

8. Z. Till, T. Varga, T. Chován, Kinetic identification of reaction network consisting chemical lumps for vacuum gas oil hydrocracking. In *Műszaki Kémiai Napok 2017: Chemical Engineering Conference 2017*, Veszprém, Hungary, Apr. 25-27, 2017; J. Abonyi, M. Klein, A. Balogh, Eds.; University of Pannonia: Veszprém, Hungary (2017), 23-28.
9. Z. Till, T. Varga, T. Chován, Comparing nonlinear optimization algorithms in the identification of lumped reaction networks. In *Konferencia Kiadvány, Műszaki Kémiai Napok*, Veszprém, Hungary, Apr. 16-18, 2019; A. Balogh, M. Klein, Eds.; University of Pannonia: Veszprém, Hungary (2019), 89-94.
10. Z. Till, T. Varga, J. Sója, N. Miskolczi, T. Chován, Kinetic Identification of Plastic Waste Pyrolysis on Zeolite-based Catalysts. In *Műszaki Kémiai Napok*, Veszprém, Hungary, Apr. 24-26, 2018; A. Balogh, M. Klein, Eds.; University of Pannonia: Veszprém, Hungary (2018), 93-98.

**Conference abstracts**

11. Z. Till, T. Varga, T. Chován, Reduction of Lumped Reaction Networks Based on Global Sensitivity Analysis. In *XXIII International Conference on Chemical Reactors (CHEMREACTOR-23)*, Ghent, Belgium, Nov. 5-8, 2018; A. Noskov, G. Marin, A. Zagoruiko, K. Van Geem, Eds.; Boreskov Institute of Catalysis of the Siberian Branch of the Russian Academy of Sciences: Novosibirsk: Russia (2018), 37-38.
12. Z. Till, T. Varga, J. Sója, N. Miskolczi, T. Chován, Dealing with Structural Uncertainties in Lumped Reaction Networks. In *Book of Abstracts: 12<sup>th</sup> European Congress of Chemical Engineering. 5<sup>th</sup> European Congress of Applied Biotechnology*, Florence, Italy, Sep. 15-19, 2019; Italian Association of Chemical Engineering (AIDIC): Italy (2019), 1060-1061.
13. Z. Till, T. Varga, J. Sója, N. Miskolczi, T. Chován, Pseudokomponensekből álló reakcióhálózatok strukturális bizonytalanságának vizsgálata. In *Absztraktkötet. Tavaszi Szél Konferencia 2019. Nemzetközi Multidiszciplináris Konferencia*, Debrecen, Hungary, May 3-5, 2019; K. Németh, Ed.; Association of Hungarian PhD and DLA Students: Budapest, Hungary (2019), 320.
14. Z. Till, T. Chován, T. Varga, Kísérleti üzemi sósav oxidációs reaktor köpenytér kialakításának optimalizálása. In *XXII. Nemzetközi Vegyészkonferencia*, Timișoara, Romania, Nov. 3-6, 2016; K. Majdik, Ed.; Hungarian Technical Scientific Society of Transylvania (HTSST): Cluj-Napoca, Romania (2016).
15. Z. Till, T. Varga, T. Chován, Model-based optimization of HCl oxidation. In *Tavaszi Szél Konferencia 2017: Nemzetközi Multidiszciplináris Konferencia: Absztraktkötet*, Miskolc, Hungary, March 31 - Apr. 2., 2017; G. Keresztes, Zs. Kohus, K. Szabó P., D. Tokody, Eds.; Association of Hungarian PhD and DLA Students: Budapest, Hungary: Budapest, Hungary (2017), 340.

## Publications not related to theses

### Articles in international journals

16. O. P. Hamadi, T. Varga, Z. Till, Z. Eller, J. Hancsók, Model based investigation of catalyst fouling in case of special hydrocracking of sunflower oil and kerosene mixture, *Energy Fuels* 33 (3) (2019), 2575-2853.  
<https://doi.org/10.1021/acs.energyfuels.8b04085>. SCImago Journal Ranking: Q1, Impact factor: 3.421

### Articles in Hungarian journals

17. Z. Till, B. Molnár, A. Egedy, T. Varga, CFD Based Qualification of Mixing Efficiency of Stirred Vessels, *Period. Polytech., Chem. Eng.* 63 (1) (2019), 226-238.  
<https://doi.org/10.3311/PPch.12245>. SCImago Journal Ranking: Q2, Impact factor: 1.257

### Articles in conference publications

18. Z. Till, T. Varga, J. Sója, N. Miskolczi, T. Chován, Kinetic Modeling of Plastic Waste Pyrolysis in a Laboratory Scale Two-stage Reactor. In *Computer-Aided Chemical Engineering (43)*, Graz, Austria, Jun. 10-13. 2018; A. Friedl, J. J. Klemeš, S. Radl, P. S. Varbanov, T. Wallek, Eds.; 28<sup>th</sup> European Symposium on Computer Aided Process Engineering Part A.; Elsevier: Amsterdam, Netherlands (2018), 349-354.

### Conference abstracts

19. O. P. Hamadi, T. Varga, Z. Till, Z. Eller, J. Hancsók, Kinetic model development of special hydrocracking of sunflower oil and petroleum mixture. In *Book of Abstracts: 12<sup>th</sup> European Congress of Chemical Engineering. 5<sup>th</sup> European Congress of Applied Biotechnology*, Florence, Italy, Sep. 15-19, 2019; Italian Association of Chemical Engineering (AIDIC): Italy (2019), 1070-1071.

20. Z. Till, A. Egedy, T. Varga, T. Chován, Többkeverős berendezések vizsgálata numerikus áramlástan szimuláció alkalmazásával. In *Műszaki Kémiai Napok 2016: Konferencia Kiadvány*, Veszprém, Hungary, Apr. 26-28, 2016; F. Vonderviszt, M. Bokrossy-Csiba, Zs. Törösváry-Kovács, Eds.; Research Institute of Biomolecular and Chemical Engineering, Faculty of Information Technology, University of Pannonia: Veszprém, Hungary (2019), 130.

## References

- [1] B.W. Bequette, *Process dynamics: modeling, analysis, and simulation*, Prentice Hall PTR, Upper Saddle River, N.J, 1998.
- [2] C.J.H. Jacobsen, Novel class of ammonia synthesis catalysts, *Chem. Commun.* (2000) 1057–1058. <https://doi.org/10.1039/b002930k>.
- [3] S. Su, P. Zaza, A. Renken, Catalytic dehydrogenation of methanol to water-free formaldehyde, *Chem. Eng. Technol.* 17 (1994) 34–40. <https://doi.org/10.1002/ceat.270170106>.
- [4] P.R. Robinson, G.E. Dolbear, Hydrotreating and Hydrocracking: Fundamentals, in: C.S. Hsu, P.R. Robinson (Eds.), *Pract. Adv. Pet. Process.*, Springer New York, New York, NY, 2006: pp. 177–218. [https://doi.org/10.1007/978-0-387-25789-1\\_7](https://doi.org/10.1007/978-0-387-25789-1_7).
- [5] R. Wade, J. Vislocky, T. Maesen, D. Torchia, Hydrocracking catalyst and processing developments, *Pet. Technol. Q.* 14 (2009) 81–86.
- [6] V.A. Sadykov, L.A. Isupova, I.A. Zolotarskii, L.N. Bobrova, A.S. Noskov, V.N. Parmon, E.A. Brushtein, T.V. Telyatnikova, V.I. Chernyshev, V.V. Lunin, Oxide catalysts for ammonia oxidation in nitric acid production: properties and perspectives, *Appl. Catal. Gen.* 204 (2000) 59–87. [https://doi.org/10.1016/S0926-860X\(00\)00506-8](https://doi.org/10.1016/S0926-860X(00)00506-8).
- [7] K.J. Ivin, J.J. Rooney, C.D. Stewart, M.L.H. Green, R. Mahtab, Mechanism for the stereospecific polymerization of olefins by Ziegler–Natta catalysts, *J Chem Soc Chem Commun.* (1978) 604–606. <https://doi.org/10.1039/C39780000604>.
- [8] C. Potter, S. Baron, Kinetics of the catalytic formation of phosgene, *Chem. Eng. Prog.* 47 (1951) 473–480.
- [9] R. Miandad, M.A. Barakat, A.S. Aburiazaiza, M. Rehan, A.S. Nizami, Catalytic pyrolysis of plastic waste: A review, *Process Saf. Environ. Prot.* 102 (2016) 822–838. <https://doi.org/10.1016/j.psep.2016.06.022>.
- [10] X. Hu, M. Gholizadeh, Biomass pyrolysis: A review of the process development and challenges from initial researches up to the commercialisation stage, *J. Energy Chem.* 39 (2019) 109–143. <https://doi.org/10.1016/j.jechem.2019.01.024>.

- [11] P. Wauthoz, M. Ruwet, T. Machej, P. Grange, Influence of the preparation method on the V<sub>2</sub>O<sub>5</sub>/TiO<sub>2</sub>/SiO<sub>2</sub> catalysts in selective catalytic reduction of nitric oxide with ammonia, *Appl. Catal.* 69 (1991) 149–167. [https://doi.org/10.1016/S0166-9834\(00\)83298-4](https://doi.org/10.1016/S0166-9834(00)83298-4).
- [12] W.W. Duecker, J.R. West, eds., *The manufacture of sulfuric acid*, Reinhold Pub. Corp., 1959.
- [13] J. Xu, G.F. Froment, Methane steam reforming, methanation and water-gas shift: I. Intrinsic kinetics, *AIChE J.* 35 (1989) 88–96. <https://doi.org/10.1002/aic.690350109>.
- [14] Directive 2008/98/EC of the European Parliament and of the Council of 19 November 2008 on waste and repealing certain Directives (Text with EEA relevance), 2008. <http://data.europa.eu/eli/dir/2008/98/oj/eng> (accessed February 7, 2018).
- [15] N. Singh, D. Hui, R. Singh, I.P.S. Ahuja, L. Feo, F. Fraternali, Recycling of plastic solid waste: A state of art review and future applications, *Compos. Part B Eng.* 115 (2017) 409–422. <https://doi.org/10.1016/j.compositesb.2016.09.013>.
- [16] R.E. Guedes, A.S. Luna, A.R. Torres, Operating parameters for bio-oil production in biomass pyrolysis: A review, *J. Anal. Appl. Pyrolysis.* 129 (2018) 134–149. <https://doi.org/10.1016/j.jaap.2017.11.019>.
- [17] Y. Ding, C. Wang, M. Chaos, R. Chen, S. Lu, Estimation of beech pyrolysis kinetic parameters by Shuffled Complex Evolution, *Bioresour. Technol.* 200 (2016) 658–665. <https://doi.org/10.1016/j.biortech.2015.10.082>.
- [18] B. Kunwar, S.R. Chandrasekaran, B.R. Moser, J. Deluhery, P. Kim, N. Rajagopalan, B.K. Sharma, Catalytic Thermal Cracking of Postconsumer Waste Plastics to Fuels. 2. Pilot-Scale Thermochemical Conversion, *Energy Fuels.* 31 (2017) 2705–2715. <https://doi.org/10.1021/acs.energyfuels.6b02996>.
- [19] P.A. Owusu, N. Banadda, A. Zziwa, J. Seay, N. Kiggundu, Reverse engineering of plastic waste into useful fuel products, *J. Anal. Appl. Pyrolysis.* (2018). <https://doi.org/10.1016/j.jaap.2017.12.020>.



- [20] A. Ayanoğlu, R. Yumrutaş, Production of gasoline and diesel like fuels from waste tire oil by using catalytic pyrolysis, *Energy*. 103 (2016) 456–468. <https://doi.org/10.1016/j.energy.2016.02.155>.
- [21] S.T. Kumaravel, A. Murugesan, A. Kumaravel, Tyre pyrolysis oil as an alternative fuel for diesel engines – A review, *Renew. Sustain. Energy Rev.* 60 (2016) 1678–1685. <https://doi.org/10.1016/j.rser.2016.03.035>.
- [22] X. Zhang, H. Lei, S. Chen, J. Wu, Catalytic co-pyrolysis of lignocellulosic biomass with polymers: a critical review, *Green Chem.* 18 (2016) 4145–4169. <https://doi.org/10.1039/C6GC00911E>.
- [23] K. Kositkanawuth, A. Bhatt, M. Sattler, B. Dennis, Renewable Energy from Waste: Investigation of Co-pyrolysis between Sargassum Macroalgae and Polystyrene, *Energy Fuels*. 31 (2017) 5088–5096. <https://doi.org/10.1021/acs.energyfuels.6b03397>.
- [24] T. Wang, Q. Zhang, M. Ding, C. Wang, Y. Li, Q. Zhang, L. Ma, Bio-gasoline Production by Coupling of Biomass Catalytic Pyrolysis and Oligomerization Process, *Energy Procedia*. 105 (2017) 858–863. <https://doi.org/10.1016/j.egypro.2017.03.401>.
- [25] C. Fehér, E. Kriván, Z. Eller, J. Hancsók, R. Skoda-Földes, The Use of Ionic Liquids in the Oligomerization of Alkenes, (2014). <https://doi.org/10.5772/57478>.
- [26] E. Kriván, J. Hancsók, Oligomerization of Light FCC Naphtha with Ion Exchange Resin Catalyst, *Top. Catal.* 58 (2015) 939–947. <https://doi.org/10.1007/s11244-015-0462-1>.
- [27] A. Krutof, K. Hawboldt, Blends of pyrolysis oil, petroleum, and other bio-based fuels: A review, *Renew. Sustain. Energy Rev.* 59 (2016) 406–419. <https://doi.org/10.1016/j.rser.2015.12.304>.
- [28] M. Syamsiro, H. Saptoadi, T. Norsujianto, P. Noviasri, S. Cheng, Z. Alimuddin, K. Yoshikawa, Fuel Oil Production from Municipal Plastic Wastes in Sequential Pyrolysis and Catalytic Reforming Reactors, *Energy Procedia*. 47 (2014) 180–188. <https://doi.org/10.1016/j.egypro.2014.01.212>.

- [29] S. Bezergianni, A. Dimitriadis, G.-C. Faussone, D. Karonis, Alternative Diesel from Waste Plastics, *Energies*. 10 (2017) 1750. <https://doi.org/10.3390/en10111750>.
- [30] S.M. Al-Salem, A. Antelava, A. Constantinou, G. Manos, A. Dutta, A review on thermal and catalytic pyrolysis of plastic solid waste (PSW), *J. Environ. Manage.* 197 (2017) 177–198. <https://doi.org/10.1016/j.jenvman.2017.03.084>.
- [31] R. Miandad, M. Rehan, A.-S. Nizami, M.A. El-Fetouh Barakat, I.M. Ismail, The Energy and Value-Added Products from Pyrolysis of Waste Plastics, in: O.P. Karthikeyan, K. Heimann, S.S. Muthu (Eds.), *Recycl. Solid Waste Biofuels Bio-Chem.*, Springer Singapore, Singapore, 2016: pp. 333–355. [https://doi.org/10.1007/978-981-10-0150-5\\_12](https://doi.org/10.1007/978-981-10-0150-5_12).
- [32] J. Shah, M.R. Jan, F. Mabood, F. Jabeen, Catalytic pyrolysis of LDPE leads to valuable resource recovery and reduction of waste problems, *Energy Convers. Manag.* 51 (2010) 2791–2801. <https://doi.org/10.1016/j.enconman.2010.06.016>.
- [33] L.S. Diaz-Silvarrey, K. Zhang, A.N. Phan, Monomer recovery through advanced pyrolysis of waste high density polyethylene (HDPE), *Green Chem.* 20 (2018) 1813–1823. <https://doi.org/10.1039/C7GC03662K>.
- [34] A. Marcilla, M.I. Beltrán, R. Navarro, Thermal and catalytic pyrolysis of polyethylene over HZSM5 and HUSY zeolites in a batch reactor under dynamic conditions, *Appl. Catal. B Environ.* 86 (2009) 78–86. <https://doi.org/10.1016/j.apcatb.2008.07.026>.
- [35] F. Ateş, N. Miskolczi, N. Borsodi, Comparison of real waste (MSW and MPW) pyrolysis in batch reactor over different catalysts. Part I: Product yields, gas and pyrolysis oil properties, *Bioresour. Technol.* 133 (2013) 443–454. <https://doi.org/10.1016/j.biortech.2013.01.112>.
- [36] H. Palza, C. Aravena, M. Colet, Role of the Catalyst in the Pyrolysis of Polyolefin Mixtures and Used Tires, *Energy Fuels*. 31 (2017) 3111–3120. <https://doi.org/10.1021/acs.energyfuels.6b02660>.

- [37] R. Sahu, B.J. Song, J.S. Im, Y.-P. Jeon, C.W. Lee, A review of recent advances in catalytic hydrocracking of heavy residues, *J. Ind. Eng. Chem.* 27 (2015) 12–24. <https://doi.org/10.1016/j.jiec.2015.01.011>.
- [38] Sagi D., Hollo A., Varga G., Hancsok J., Fuel purpose hydrotreating of free fatty acid by-products and heavy straight run gas oil, *Chem. Eng. Trans.* 52 (2016) 883–888. <https://doi.org/10.3303/CET1652148>.
- [39] B.S. Rana, R. Kumar, R. Tiwari, R. Kumar, R.K. Joshi, M.O. Garg, A.K. Sinha, Transportation fuels from co-processing of waste vegetable oil and gas oil mixtures, *Biomass Bioenergy.* 56 (2013) 43–52. <https://doi.org/10.1016/j.biombioe.2013.04.029>.
- [40] Directive 2009/28/EC of the European Parliament and of the Council of 23 April 2009 on the promotion of the use of energy from renewable sources and amending and subsequently repealing Directives 2001/77/EC and 2003/30/EC (Text with EEA relevance), 2009. <https://eur-lex.europa.eu/eli/dir/2009/28/oj>.
- [41] T.F. O'Brien, T.V. Bommaraju, F. Hine, History of the chloralkali industry, in: *Handb. Chlor-Alkali Technol. Vol Fundam.*, Springer, New York, 2005.
- [42] H. Selin, Global Environmental Law and Treaty-Making on Hazardous Substances: The Minamata Convention and Mercury Abatement, *Glob. Environ. Polit.* 14 (2014) 1–19. [https://doi.org/10.1162/GLEP\\_a\\_00208](https://doi.org/10.1162/GLEP_a_00208).
- [43] C. Six, F. Richter, Isocyanates, Organic, in: *Ullmanns Encycl. Ind. Chem.*, Wiley-VCH Verlag GmbH & Co. KGaA, 2000. [https://doi.org/10.1002/14356007.a14\\_611](https://doi.org/10.1002/14356007.a14_611).
- [44] H. Deacon, Manufacture of Chlorine, U.S. Patent 85730 A, 1868.
- [45] H.Y. Pan, R.G. Minet, S.W. Benson, T.T. Tsotsis, Process for Converting Hydrogen Chloride to Chlorine, *Ind. Eng. Chem. Res.* 33 (1994) 2996–3003. <https://doi.org/10.1021/ie00036a014>.
- [46] F. Wattimena, W. Sachtler, Catalyst research for the shell chlorine process, *Stud. Surf. Sci. Catal.* 7 (1981) 816–827.

- [47] A.P. Amrute, C. Mondelli, J. Pérez-Ramírez, Kinetic aspects and deactivation behaviour of chromia-based catalysts in hydrogen chloride oxidation, *Catal. Sci. Technol.* 2 (2012) 2057. <https://doi.org/10.1039/c2cy20185b>.
- [48] K. Iwanaga, K. Seki, T. Hibi, K. Issoh, T. Suzuta, M. Nakada, Y. Mori, T. Abe, The Development of Improved Hydrogen Chloride Oxidation Process, RD Rep. Sumitomo Kagaku. (2004).
- [49] H. Ando, Y. Uchida, K. Seki, C. Knapp, N. Omoto, M. Kinoshita, Trends and Views in the Development of Technologies for Chlorine Production from Hydrogen Chloride, RD Report for Sumitomo Kagaku. (2010). [http://www.sumitomo-chem.co.jp/english/rd/report/theses/docs/01\\_chlorine\\_production\\_e.pdf](http://www.sumitomo-chem.co.jp/english/rd/report/theses/docs/01_chlorine_production_e.pdf).
- [50] K. Seki, Development of RuO<sub>2</sub>/Rutile-TiO<sub>2</sub> Catalyst for Industrial HCl Oxidation Process, *Catal. Surv. Asia.* 14 (2010) 168–175. <https://doi.org/10.1007/s10563-010-9091-7>.
- [51] A. Wolf, L. Mleczko, S. Schubert, Verfahren zur herstellung von chlor durch gasphasenoxidation von chlorwasserstoff in gegenwart eines ceroxid-katalysators, WO2010133313 A1, 2010. <http://www.google.ch/patents/WO2010133313A1> (accessed December 3, 2017).
- [52] J. Pérez-Ramírez, C. Mondelli, T. Schmidt, O.F.-K. Schlüter, A. Wolf, L. Mleczko, T. Dreier, Sustainable chlorine recycling via catalysed HCl oxidation: from fundamentals to implementation, *Energy Environ. Sci.* 4 (2011) 4786. <https://doi.org/10.1039/c1ee02190g>.
- [53] Z. Fei, H. Liu, Y. Dai, W. Ji, X. Chen, J. Tang, M. Cui, X. Qiao, Efficient catalytic oxidation of HCl to recycle Cl<sub>2</sub> over the CuO–CeO<sub>2</sub> composite oxide supported on Y type zeolite, *Chem. Eng. J.* 257 (2014) 273–280. <https://doi.org/10.1016/j.cej.2014.07.033>.
- [54] M. Hammes, M. Valtchev, M.B. Roth, K. Stöwe, W.F. Maier, A search for alternative Deacon catalysts, *Appl. Catal. B Environ.* 132–133 (2013) 389–400. <https://doi.org/10.1016/j.apcatb.2012.11.034>.

- [55] H. Over, R. Schomäcker, What Makes a Good Catalyst for the Deacon Process?, *ACS Catal.* 3 (2013) 1034–1046. <https://doi.org/10.1021/cs300735e>.
- [56] A. Martínez-Arias, A.B. Hungría, G. Munuera, D. Gamarra, Preferential oxidation of CO in rich H<sub>2</sub> over CuO/CeO<sub>2</sub>: Details of selectivity and deactivation under the reactant stream, *Appl. Catal. B Environ.* 65 (2006) 207–216. <https://doi.org/10.1016/j.apcatb.2006.02.003>.
- [57] Shin WS, Jung CR, Han J, Nam SW, Lim TH, Hong SA, Lee HI, Development of Au/CeO<sub>2</sub> Catalysts for Preferential Oxidation of CO in PEMFC, *J. Ind. Eng. Chem.* 10 (2004) 302–308.
- [58] A. Trovarelli, Catalytic Properties of Ceria and CeO<sub>2</sub>-Containing Materials, *Catal. Rev.* 38 (1996) 439–520. <https://doi.org/10.1080/01614949608006464>.
- [59] A. Gómez-Cortés, Y. Márquez, J. Arenas-Alatorre, G. Díaz, Selective CO oxidation in excess of H<sub>2</sub> over high-surface area CuO/CeO<sub>2</sub> catalysts, *Catal. Today.* 133–135 (2008) 743–749. <https://doi.org/10.1016/j.cattod.2007.12.083>.
- [60] M. Moser, C. Mondelli, T. Schmidt, F. Girgsdies, M.E. Schuster, R. Farra, L. Szentmiklósi, D. Teschner, J. Pérez-Ramírez, Supported CeO<sub>2</sub> catalysts in technical form for sustainable chlorine production, *Appl. Catal. B Environ.* 132–133 (2013) 123–131. <https://doi.org/10.1016/j.apcatb.2012.11.024>.
- [61] M. Moser, G. Vilé, S. Colussi, F. Krumeich, D. Teschner, L. Szentmiklósi, A. Trovarelli, J. Pérez-Ramírez, Structure and reactivity of ceria–zirconia catalysts for bromine and chlorine production via the oxidation of hydrogen halides, *J. Catal.* 331 (2015) 128–137. <https://doi.org/10.1016/j.jcat.2015.08.024>.
- [62] A.P. Amrute, C. Mondelli, M. Moser, G. Novell-Leruth, N. López, D. Rosenthal, R. Farra, M.E. Schuster, D. Teschner, T. Schmidt, J. Pérez-Ramírez, Performance, structure, and mechanism of CeO<sub>2</sub> in HCl oxidation to Cl<sub>2</sub>, *J. Catal.* 286 (2012) 287–297. <https://doi.org/10.1016/j.jcat.2011.11.016>.

- [63] A.P. Amrute, G.O. Larrazábal, C. Mondelli, J. Pérez-Ramírez,  $\text{CuCrO}_2$  Delafossite: A Stable Copper Catalyst for Chlorine Production, *Angew. Chem.* 125 (2013) 9954–9957. <https://doi.org/10.1002/ange.201304254>.
- [64] K. Feng, C. Li, Y. Guo, W. Zhan, B. Ma, B. Chen, M. Yuan, G. Lu, Effect of KCl on the performance of Cu-K-La/ $\gamma$ - $\text{Al}_2\text{O}_3$  catalyst for HCl oxidation, *Chin. J. Catal.* 35 (2014) 1359–1363. [https://doi.org/10.1016/S1872-2067\(14\)60166-2](https://doi.org/10.1016/S1872-2067(14)60166-2).
- [65] L.P. de Oliveira, D. Hudebine, D. Guillaume, J.J. Verstraete, A Review of Kinetic Modeling Methodologies for Complex Processes, *Oil Gas Sci. Technol. – Rev. D’IFP Energ. Nouv.* 71 (2016) 45. <https://doi.org/10.2516/ogst/2016011>.
- [66] J. Wei, J.C.W. Kuo, Lumping Analysis in Monomolecular Reaction Systems. Analysis of the Exactly Lumpable System, *Ind. Eng. Chem. Fundam.* 8 (1969) 114–123. <https://doi.org/10.1021/i160029a019>.
- [67] J.C.W. Kuo, J. Wei, Lumping Analysis in Monomolecular Reaction Systems. Analysis of Approximately Lumpable System, *Ind. Eng. Chem. Fundam.* 8 (1969) 124–133. <https://doi.org/10.1021/i160029a020>.
- [68] A. Aboulkas, K. El harfi, A. El Bouadili, Thermal degradation behaviors of polyethylene and polypropylene. Part I: Pyrolysis kinetics and mechanisms, *Energy Convers. Manag.* 51 (2010) 1363–1369. <https://doi.org/10.1016/j.enconman.2009.12.017>.
- [69] R. Chen, X. Xu, S. Lu, Y. Zhang, S. Lo, Pyrolysis study of waste phenolic fibre-reinforced plastic by thermogravimetry/Fourier transform infrared/mass spectrometry analysis, *Energy Convers. Manag.* 165 (2018) 555–566. <https://doi.org/10.1016/j.enconman.2018.03.092>.
- [70] S.R. Chandrasekaran, B. Kunwar, B.R. Moser, N. Rajagopalan, B.K. Sharma, Catalytic Thermal Cracking of Postconsumer Waste Plastics to Fuels. 1. Kinetics and Optimization, *Energy Fuels.* 29 (2015) 6068–6077. <https://doi.org/10.1021/acs.energyfuels.5b01083>.

- [71] P. Straka, O. Bičáková, M. Šupová, Thermal conversion of polyolefins/polystyrene ternary mixtures: Kinetics and pyrolysis on a laboratory and commercial scales, *J. Anal. Appl. Pyrolysis*. 128 (2017) 196–207. <https://doi.org/10.1016/j.jaap.2017.10.010>.
- [72] J. Cai, W. Wu, R. Liu, An overview of distributed activation energy model and its application in the pyrolysis of lignocellulosic biomass, *Renew. Sustain. Energy Rev.* 36 (2014) 236–246. <https://doi.org/10.1016/j.rser.2014.04.052>.
- [73] F. Codignole Luz, S. Cordiner, A. Manni, V. Mulone, V. Rocco, Biomass fast pyrolysis in screw reactors: Prediction of spent coffee grounds bio-oil production through a monodimensional model, *Energy Convers. Manag.* 168 (2018) 98–106. <https://doi.org/10.1016/j.enconman.2018.04.104>.
- [74] T. Huang, B. Liu, Z. Wang, X. Guo, Kinetic model for hydrocracking of Iranian heavy crude with dispersed catalysts in slurry-phase, *Pet. Sci. Technol.* 35 (2017) 1846–1851. <https://doi.org/10.1080/10916466.2017.1367801>.
- [75] J. Li, T. Li, H. Ma, Q. Sun, C. Li, W. Ying, D. Fang, Kinetics of coupling cracking of butene and pentene on modified HZSM-5 catalyst, *Chem. Eng. J.* 346 (2018) 397–405. <https://doi.org/10.1016/j.cej.2018.04.061>.
- [76] W. Song, W. Zhong, M. Yang, W. Du, F. Qian, A new lumped kinetic model of an industrial hydrocracking process, *Chem. Eng. Trans.* (2017) 673–678. <https://doi.org/10.3303/CET1761110>.
- [77] H. Harode, M. Ramteke, Axial dispersion modeling of industrial hydrocracking unit and its multiobjective optimization, *Chem. Eng. Res. Des.* 121 (2017) 57–68. <https://doi.org/10.1016/j.cherd.2017.02.033>.
- [78] S. Sánchez, M.A. Rodríguez, J. Ancheyta, Kinetic Model for Moderate Hydrocracking of Heavy Oils, *Ind. Eng. Chem. Res.* 44 (2005) 9409–9413. <https://doi.org/10.1021/ie050202+>.
- [79] S. Sánchez, J. Ancheyta, Effect of Pressure on the Kinetics of Moderate Hydrocracking of Maya Crude Oil, *Energy Fuels*. 21 (2007) 653–661. <https://doi.org/10.1021/ef060525y>.

- [80] J. Ancheyta, S. Sánchez, M.A. Rodríguez, Kinetic modeling of hydrocracking of heavy oil fractions: A review, *Catal. Today*. 109 (2005) 76–92. <https://doi.org/10.1016/j.cattod.2005.08.015>.
- [81] H. Jiang, S. Huang, Eight-Lump Reaction Kinetic Model for the Maximizing Isoparaffin Process for Cleaning Gasoline and Enhancing Propylene Yield, *Energy Fuels*. 30 (2016) 10770–10776. <https://doi.org/10.1021/acs.energyfuels.6b02208>.
- [82] H. Wang, F. Dai, Y. Yang, Z. Li, C. Li, S. Zhang, Catalyst Grading Optimization and Kinetic Simulation of the Shale Oil Hydrotreating Process, *Energy Fuels*. 31 (2017) 4353–4360. <https://doi.org/10.1021/acs.energyfuels.6b02720>.
- [83] Z.-M. Cheng, Z.-B. Huang, T. Yang, J.-K. Liu, H.-L. Ge, L.-J. Jiang, X.-C. Fang, Modeling on scale-up of an ebullated-bed reactor for the hydroprocessing of vacuum residuum, *Catal. Today*. 220–222 (2014) 228–236. <https://doi.org/10.1016/j.cattod.2013.08.021>.
- [84] C.J. Calderón, J. Ancheyta, Modeling of Slurry-Phase Reactors for Hydrocracking of Heavy Oils, *Energy Fuels*. 30 (2016) 2525–2543. <https://doi.org/10.1021/acs.energyfuels.5b02807>.
- [85] A.A. Forghani, M. Jafarian, P. Pendleton, D.M. Lewis, Mathematical modelling of a hydrocracking reactor for triglyceride conversion to biofuel: model establishment and validation: Analysis of a hydrocracking reactor for triglyceride conversion, *Int. J. Energy Res.* 38 (2014) 1624–1634. <https://doi.org/10.1002/er.3244>.
- [86] E.B. Ledesma, A.A. Mullery, J.V. Vu, J.N. Hoang, Lumped Kinetics for Biomass Tar Cracking Using 4-Propylguaiacol as a Model Compound, *Ind. Eng. Chem. Res.* 54 (2015) 5613–5623. <https://doi.org/10.1021/acs.iecr.5b01022>.
- [87] Y.K. Ong, S. Bhatia, The current status and perspectives of biofuel production via catalytic cracking of edible and non-edible oils, *Energy*. 35 (2010) 111–119. <https://doi.org/10.1016/j.energy.2009.09.001>.



- [88] Y. Han, F. Stankovikj, M. Garcia-Perez, Co-hydrotreatment of tire pyrolysis oil and vegetable oil for the production of transportation fuels, *Fuel Process. Technol.* 159 (2017) 328–339. <https://doi.org/10.1016/j.fuproc.2017.01.048>.
- [89] B. Periyasamy, Reaction pathway analysis in thermal cracking of waste cooking oil to hydrocarbons based on monomolecular lumped kinetics, *Fuel*. 158 (2015) 479–487. <https://doi.org/10.1016/j.fuel.2015.05.066>.
- [90] B. Csukás, M. Varga, N. Miskolczi, S. Balogh, A. Angyal, L. Bartha, Simplified dynamic simulation model of plastic waste pyrolysis in laboratory and pilot scale tubular reactor, *Fuel Process. Technol.* 106 (2013) 186–200. <https://doi.org/10.1016/j.fuproc.2012.07.024>.
- [91] G. Elordi, G. Lopez, M. Olazar, R. Aguado, J. Bilbao, Product distribution modelling in the thermal pyrolysis of high density polyethylene, *J. Hazard. Mater.* 144 (2007) 708–714. <https://doi.org/10.1016/j.jhazmat.2007.01.101>.
- [92] M. Artetxe, G. Lopez, M. Amutio, J. Bilbao, M. Olazar, Kinetic modelling of the cracking of HDPE pyrolysis volatiles on a HZSM-5 zeolite based catalyst, *Chem. Eng. Sci.* 116 (2014) 635–644. <https://doi.org/10.1016/j.ces.2014.05.044>.
- [93] S.M. Al-Salem, P. Lettieri, Kinetic study of high density polyethylene (HDPE) pyrolysis, *Chem. Eng. Res. Des.* 88 (2010) 1599–1606. <https://doi.org/10.1016/j.cherd.2010.03.012>.
- [94] P. Costa, F. Pinto, A.M. Ramos, I. Gulyurtlu, I. Cabrita, M.S. Bernardo, Study of the Pyrolysis Kinetics of a Mixture of Polyethylene, Polypropylene, and Polystyrene, *Energy Fuels*. 24 (2010) 6239–6247. <https://doi.org/10.1021/ef101010n>.
- [95] F. Ding, L. Xiong, C. Luo, H. Zhang, X. Chen, Kinetic study of low-temperature conversion of plastic mixtures to value added products, *J. Anal. Appl. Pyrolysis.* 94 (2012) 83–90. <https://doi.org/10.1016/j.jaap.2011.11.013>.

- [96] R.W.J. Westerhout, J. Waanders, J.A.M. Kuipers, W.P.M. van Swaaij, Recycling of Polyethene and Polypropene in a Novel Bench-Scale Rotating Cone Reactor by High-Temperature Pyrolysis, *Ind. Eng. Chem. Res.* 37 (1998) 2293–2300. <https://doi.org/10.1021/ie970704q>.
- [97] L.S. Diaz Silvarrey, A.N. Phan, Kinetic study of municipal plastic waste, *Int. J. Hydrog. Energy.* 41 (2016) 16352–16364. <https://doi.org/10.1016/j.ijhydene.2016.05.202>.
- [98] K. Dussan, S. Dooley, R. Monaghan, Integrating compositional features in model compounds for a kinetic mechanism of hemicellulose pyrolysis, *Chem. Eng. J.* 328 (2017) 943–961. <https://doi.org/10.1016/j.cej.2017.07.089>.
- [99] A.G. Gayubo, B. Valle, B. Aramburu, C. Montero, J. Bilbao, Kinetic model considering catalyst deactivation for the steam reforming of bio-oil over Ni/La<sub>2</sub>O<sub>3</sub>- $\alpha$ -Al<sub>2</sub>O<sub>3</sub>, *Chem. Eng. J.* 332 (2018) 192–204. <https://doi.org/10.1016/j.cej.2017.09.063>.
- [100] C.S. Laxminarasimhan, R.P. Verma, P.A. Ramachandran, Continuous lumping model for simulation of hydrocracking, *AIChE J.* 42 (1996) 2645–2653. <https://doi.org/10.1002/aic.690420925>.
- [101] H. Sildir, Y. Arkun, B. Cakal, D. Gokce, E. Kuzu, A dynamic non-isothermal model for a hydrocracking reactor: Model development by the method of continuous lumping and application to an industrial unit, *J. Process Control.* 22 (2012) 1956–1965. <https://doi.org/10.1016/j.jprocont.2012.08.016>.
- [102] G. Mazloom, F. Farhadi, F. Khorasheh, Kinetic modeling of pyrolysis of scrap tires, *J. Anal. Appl. Pyrolysis.* 84 (2009) 157–164. <https://doi.org/10.1016/j.jaap.2009.01.006>.
- [103] W. Marquardt, Model-Based Experimental Analysis of Kinetic Phenomena in Multi-Phase Reactive Systems, *Chem. Eng. Res. Des.* 83 (2005) 561–573. <https://doi.org/10.1205/cherd.05086>.

- [104] N. Bhatt, S. Visvanathan, Incremental Kinetic Identification based on Experimental data From Steady-state Plug Flow Reactors, in: K.V. Gernaey, J.K. Huusom, R. Gani (Eds.), *Comput. Aided Chem. Eng.*, Elsevier, 2015: pp. 593–598. <https://doi.org/10.1016/B978-0-444-63578-5.50094-3>.
- [105] G. Madras, G.Y. Chung, J.M. Smith, B.J. McCoy, Molecular Weight Effect on the Dynamics of Polystyrene Degradation, *Ind. Eng. Chem. Res.* 36 (1997) 2019–2024. <https://doi.org/10.1021/ie9607513>.
- [106] S. Lin, W. Yu, X. Wang, C. Zhou, Study on the Thermal Degradation Kinetics of Biodegradable Poly(propylene carbonate) during Melt Processing by Population Balance Model and Rheology, *Ind. Eng. Chem. Res.* 53 (2014) 18411–18419. <https://doi.org/10.1021/ie404049v>.
- [107] S.M. Walas, *Chemical process equipment: selection and design*, Butterworths, Boston, 1988.
- [108] G.F. Froment, J. De Wilde, K.B. Bischoff, *Chemical reactor analysis and design*, 3rd ed, Wiley, Hoboken, N.J, 2011.
- [109] C.W. Arnold, K.A. Kobe, Thermodynamics of the Deacon Process, *Chem. Eng. Prog.* 48 (1952) 293–296.
- [110] W.L. Luyben, Catalyst dilution to improve dynamic controllability of cooled tubular reactors, *Comput. Chem. Eng.* 37 (2012) 184–190. <https://doi.org/10.1016/j.compchemeng.2011.07.017>.
- [111] P. Sadhukhan, E.E. Petersen, Oxidation of naphthalene in packed-bed reactor with catalyst activity profile: A design scheme for improved reactor stability and higher product yield, *AIChE J.* 22 (1976) 808–810. <https://doi.org/10.1002/aic.690220428>.
- [112] K. Deller, H. Krause, L. Schmidhammer, W. Dafinger, Cylindrically formed catalyst for the oxychlorination of ethylene, US5166120A, 1992. <https://patents.google.com/patent/US5166120A/en> (accessed April 2, 2019).

- [113] Y. Nie, P.M. Witt, A. Agarwal, L.T. Biegler, Optimal Active Catalyst and Inert Distribution in Catalytic Packed Bed Reactors: ortho-Xylene Oxidation, *Ind. Eng. Chem. Res.* 52 (2013) 15311–15320. <https://doi.org/10.1021/ie4005699>.
- [114] M. Moser, L. Rodríguez-García, J. Pérez-Ramírez, Catalyst Distribution Strategies in Fixed-Bed Reactors for Bromine Production, *Ind. Eng. Chem. Res.* 53 (2014) 9067–9075. <https://doi.org/10.1021/ie4036675>.
- [115] M. Shahrokhi, G.R. Baghmisheh, Modeling, simulation and control of a methanol synthesis fixed-bed reactor, *Chem. Eng. Sci.* 60 (2005) 4275–4286. <https://doi.org/10.1016/j.ces.2004.12.051>.
- [116] J.L. Cheong, Y. Shao, S.J.R. Tan, X. Li, Y. Zhang, S.S. Lee, Highly Active and Selective Zr/MCF Catalyst for Production of 1,3-Butadiene from Ethanol in a Dual Fixed Bed Reactor System, *ACS Sustain. Chem. Eng.* 4 (2016) 4887–4894. <https://doi.org/10.1021/acssuschemeng.6b01193>.
- [117] R. Vakili, R. Eslamloueyan, Design and Optimization of a Fixed Bed Reactor for Direct Dimethyl Ether Production from Syngas Using Differential Evolution Algorithm, *Int. J. Chem. React. Eng.* 11 (2013) 147–158. <https://doi.org/10.1515/ijcre-2012-0026>.
- [118] A. Montebelli, C.G. Visconti, G. Groppi, E. Tronconi, S. Kohler, Optimization of compact multitubular fixed-bed reactors for the methanol synthesis loaded with highly conductive structured catalysts, *Chem. Eng. J.* 255 (2014) 257–265. <https://doi.org/10.1016/j.cej.2014.06.050>.
- [119] J. Adler, J.W. Enig, The critical conditions in thermal explosion theory with reactant consumption, *Combust. Flame.* 8 (1964) 97–103. [https://doi.org/10.1016/0010-2180\(64\)90035-5](https://doi.org/10.1016/0010-2180(64)90035-5).
- [120] E. Bauman, A. Varma, J. Lorusso, M. Dente, M. Morbidelli, Parametric sensitivity in tubular reactors with co-current external cooling, *Chem. Eng. Sci.* 45 (1990) 1301–1307. [https://doi.org/10.1016/0009-2509\(90\)87122-9](https://doi.org/10.1016/0009-2509(90)87122-9).
- [121] K.F. Jensen, W.H. Ray, The bifurcation behavior of tubular reactors, *Chem. Eng. Sci.* 37 (1982) 199–222. [https://doi.org/10.1016/0009-2509\(82\)80155-3](https://doi.org/10.1016/0009-2509(82)80155-3).

- [122] S. Bashir, T. Chovan, B.J. Masri, A. Mukherjee, A. Pant, S. Sen, P. Vijayaraghavan, J.M. Berty, Thermal runaway limit of tubular reactors, defined at the inflection point of the temperature profile, *Ind. Eng. Chem. Res.* 31 (1992) 2164–2171. <https://doi.org/10.1021/ie00009a014>.
- [123] A. Kummer, T. Varga, Feeding trajectory optimization in fed-batch reactor with highly exothermic reactions, *Comput. Chem. Eng.* 98 (2017) 1–11. <https://doi.org/10.1016/j.compchemeng.2016.12.008>.
- [124] J.A. Moulijn, A.E. van Diepen, F. Kapteijn, Catalyst deactivation: is it predictable?: What to do?, *Appl. Catal. Gen.* 212 (2001) 3–16. [https://doi.org/10.1016/S0926-860X\(00\)00842-5](https://doi.org/10.1016/S0926-860X(00)00842-5).
- [125] H. Sildir, Y. Arkun, B. Cakal, D. Gokce, E. Kuzu, Plant-wide hierarchical optimization and control of an industrial hydrocracking process, *J. Process Control.* 23 (2013) 1229–1240. <https://doi.org/10.1016/j.jprocont.2013.07.007>.
- [126] H.A. Farag, N.S. Yousef, R. Farouq, Modeling and simulation of a hydrocracking unit, *J. Eng. Sci. Technol.* 11 (2016) 881–898.
- [127] N. Bhutani, A.K. Ray, G.P. Rangaiah, Modeling, Simulation, and Multi-objective Optimization of an Industrial Hydrocracking Unit, *Ind. Eng. Chem. Res.* 45 (2006) 1354–1372. <https://doi.org/10.1021/ie050423f>.
- [128] H. Zhou, J. Lu, Z. Cao, J. Shi, M. Pan, W. Li, Q. Jiang, Modeling and optimization of an industrial hydrocracking unit to improve the yield of diesel or kerosene, *Fuel.* 90 (2011) 3521–3530. <https://doi.org/10.1016/j.fuel.2011.02.043>.
- [129] B. Celse, V. Costa, F. Wahl, J.J. Verstraete, Dealing with uncertainties: Sensitivity analysis of vacuum gas oil hydrotreatment, *Chem. Eng. J.* 278 (2015) 469–478. <https://doi.org/10.1016/j.cej.2014.11.098>.
- [130] P.L.T. Duong, L.Q. Minh, T.N. Pham, J. Goncalves, E. Kwok, M. Lee, Uncertainty quantification and global sensitivity analysis of complex chemical processes with a large number of input parameters using compressive polynomial chaos, *Chem. Eng. Res. Des.* 115 (2016) 204–213. <https://doi.org/10.1016/j.cherd.2016.09.035>.

- [131] L.Q. Minh, P.L.T. Duong, M. Lee, Global Sensitivity Analysis and Uncertainty Quantification of Crude Distillation Unit Using Surrogate Model Based on Gaussian Process Regression, *Ind. Eng. Chem. Res.* 57 (2018) 5035–5044. <https://doi.org/10.1021/acs.iecr.7b05173>.
- [132] E. Vlad, C.S. Bildea, G. Bozga, Robust Optimal Design of an Glycerol Etherification Process, *Chem. Eng. Technol.* 36 (2013) 251–258. <https://doi.org/10.1002/ceat.201200274>.
- [133] M.A. Qyyum, P.L.T. Duong, L.Q. Minh, S. Lee, M. Lee, Dual mixed refrigerant LNG process: Uncertainty quantification and dimensional reduction sensitivity analysis, *Appl. Energy.* 250 (2019) 1446–1456. <https://doi.org/10.1016/j.apenergy.2019.05.004>.
- [134] C.Y. Wen, T.M. Chang, Optimal Design of Systems Involving Parameter Uncertainty, *Ind. Eng. Chem. Process Des. Dev.* 7 (1968) 49–53. <https://doi.org/10.1021/i260025a010>.
- [135] J. Steimel, S. Engell, Optimization-based support for process design under uncertainty: A case study, *AIChE J.* 62 (2016) 3404–3419. <https://doi.org/10.1002/aic.15400>.
- [136] E.N. Pistikopoulos, Uncertainty in process design and operations, *Comput. Chem. Eng.* 19 (1995) 553–563. [https://doi.org/10.1016/0098-1354\(95\)87094-6](https://doi.org/10.1016/0098-1354(95)87094-6).
- [137] B.H. Gebreslassie, Y. Yao, F. You, Design under uncertainty of hydrocarbon biorefinery supply chains: Multiobjective stochastic programming models, decomposition algorithm, and a Comparison between CVaR and downside risk, *AIChE J.* 58 (2012) 2155–2179. <https://doi.org/10.1002/aic.13844>.
- [138] J. Liu, Y. Zhou, M. Zhu, C. Deng, J.-Y. Lee, Optimization of Refinery Hydrogen Network with Parametric Uncertainties, in: *Comput. Aided Chem. Eng.*, Elsevier, 2019: pp. 77–82. <https://doi.org/10.1016/B978-0-12-818597-1.50013-8>.

- [139] J. Gong, D.J. Garcia, F. You, Unraveling Optimal Biomass Processing Routes from Bioconversion Product and Process Networks under Uncertainty: An Adaptive Robust Optimization Approach, *ACS Sustain. Chem. Eng.* 4 (2016) 3160–3173. <https://doi.org/10.1021/acssuschemeng.6b00188>.
- [140] K. Tong, J. Gong, D. Yue, F. You, Stochastic Programming Approach to Optimal Design and Operations of Integrated Hydrocarbon Biofuel and Petroleum Supply Chains, *ACS Sustain. Chem. Eng.* 2 (2014) 49–61. <https://doi.org/10.1021/sc400267t>.
- [141] F. Xie, Y. Huang, A multistage stochastic programming model for a multi-period strategic expansion of biofuel supply chain under evolving uncertainties, *Transp. Res. Part E Logist. Transp. Rev.* 111 (2018) 130–148. <https://doi.org/10.1016/j.tre.2018.01.015>.
- [142] C.J. Calderón, J. Ancheyta, Modeling, simulation, and parametric sensitivity analysis of a commercial slurry-phase reactor for heavy oil hydrocracking, *Fuel* 244 (2019) 258–268. <https://doi.org/10.1016/j.fuel.2019.01.138>.
- [143] A. Alvarez-Majmutov, J. Chen, Stochastic Modeling and Simulation Approach for Industrial Fixed-Bed Hydrocrackers, *Ind. Eng. Chem. Res.* 56 (2017) 6926–6938. <https://doi.org/10.1021/acs.iecr.7b01743>.
- [144] A.R.G. Mukkula, S. Engell, Application of Iterative Real-time Optimization in an Intensified Continuous Plant at Pilot Plant Scale, in: *Book Abstr. 12th Eur. Congr. Chem. Eng. 5th Eur. Congr. Appl. Biotechnol.*, The Italian Association of Chemical Engineering, Florence, Italy, 2019: pp. 824–826.
- [145] E. Manek, J. Haydary, Hydrocracking of vacuum residue with solid and dispersed phase catalyst: Modeling of sediment formation and hydrodesulfurization, *Fuel Process. Technol.* 159 (2017) 320–327. <https://doi.org/10.1016/j.fuproc.2017.02.003>.
- [146] A. Galadima, O. Muraza, Hydrocracking catalysts based on hierarchical zeolites: A recent progress, *J. Ind. Eng. Chem.* 61 (2018) 265–280. <https://doi.org/10.1016/j.jiec.2017.12.024>.

- [147] E. Furimsky, F.E. Massoth, Deactivation of hydroprocessing catalysts, *Catal. Today*. 52 (1999) 381–495. [https://doi.org/10.1016/S0920-5861\(99\)00096-6](https://doi.org/10.1016/S0920-5861(99)00096-6).
- [148] D. Gökçe, Model predictive controller design of hydrocracker reactors, *Turk. J. Electr. Eng. Comput. Sci.* 19 (2011) 817–825. <https://doi.org/10.3906/elk-1007-584>.
- [149] E. Rodríguez, G. Félix, J. Ancheyta, F. Trejo, Modeling of hydrotreating catalyst deactivation for heavy oil hydrocarbons, *Fuel*. 225 (2018) 118–133. <https://doi.org/10.1016/j.fuel.2018.02.085>.
- [150] A.H. Al-Rashidy, T.A. Al-Attas, S.A. Ali, S.A. Al-Bogami, S.A. Razzak, M.M. Hossain, Hydrocracking of LVGO Using Dispersed Catalysts Derived from Soluble Precursors: Performance Evaluation and Kinetics, *Ind. Eng. Chem. Res.* 58 (2019) 14709–14718. <https://doi.org/10.1021/acs.iecr.9b02658>.
- [151] M. Rashidzadeh, A. Ahmad, S. Sadighi, Studying of Catalyst Deactivation in a Commercial Hydrocracking Process (ISOMAX), *J. Pet. Sci. Technol.* 1 (2011). <https://doi.org/10.22078/jpst.2010.26>.
- [152] P.J. Becker, B. Celse, D. Guillaume, V. Costa, L. Bertier, E. Guillon, G. Pirngruber, A continuous lumping model for hydrocracking on a zeolite catalysts: model development and parameter identification, *Fuel*. 164 (2016) 73–82. <https://doi.org/10.1016/j.fuel.2015.09.057>.
- [153] A. Elkilani, M. Fahim, Six-Lump Hydrocracking Model for Maximizing Aviation Turbine Kerosene, *Pet. Sci. Technol.* 33 (2015) 237–244. <https://doi.org/10.1080/10916466.2011.608399>.
- [154] A. Afshar Ebrahimi, H. Mousavi, H. Bayesteh, J. Towfighi, Nine-lumped kinetic model for VGO catalytic cracking; using catalyst deactivation, *Fuel*. 231 (2018) 118–125. <https://doi.org/10.1016/j.fuel.2018.04.126>.
- [155] I. Elizalde, J. Ancheyta, Dynamic modeling and simulation of a naphtha catalytic reforming reactor, *Appl. Math. Model.* 39 (2015) 764–775. <https://doi.org/10.1016/j.apm.2014.07.013>.



- [156] I. Elizalde, F.S. Mederos, V.Y. Mena-Cervantes, R. Hernández-Altamirano, J.A.D. Muñoz, Dynamic modeling of adiabatic reactor for hydrocracking of VGO by using of the continuous lumping approach, *Fuel Process. Technol.* 152 (2016) 200–206. <https://doi.org/10.1016/j.fuproc.2016.07.005>.
- [157] B. Umana, N. Zhang, R. Smith, Development of Vacuum Residue Hydrodesulphurization–Hydrocracking Models and Their Integration with Refinery Hydrogen Networks, *Ind. Eng. Chem. Res.* 55 (2016) 2391–2406. <https://doi.org/10.1021/acs.iecr.5b04161>.
- [158] F. Auger, M. Hilairt, J.M. Guerrero, E. Monmasson, T. Orłowska-Kowalska, S. Katsura, Industrial Applications of the Kalman Filter: A Review, *IEEE Trans. Ind. Electron.* 60 (2013) 5458–5471. <https://doi.org/10.1109/TIE.2012.2236994>.
- [159] R. Kalman, Mathematical Description of Linear Dynamical Systems, *J. Soc. Ind. Appl. Math. Ser. Control.* 1 (1963) 152–192. <https://doi.org/10.1137/0301010>.
- [160] Y.-Y. Liu, J.-J. Slotine, A.-L. Barabási, Observability of complex systems, *Proc. Natl. Acad. Sci.* 110 (2013) 2460–2465. <https://doi.org/10.1073/pnas.1215508110>.
- [161] P.D. Wentzell, M.I. Karayannis, S.R. Crouch, Simultaneous kinetic determinations with the kalman filter, *Anal. Chim. Acta.* 224 (1989) 263–274. [https://doi.org/10.1016/S0003-2670\(00\)86564-2](https://doi.org/10.1016/S0003-2670(00)86564-2).
- [162] Min. Gui, S.C. Rutan, Determination of Initial Concentration of an Analyte by Kinetic Detection of the Intermediate Product in Consecutive First-Order Reactions Using an Extended Kalman Filter, *Anal. Chem.* 66 (1994) 1513–1519. <https://doi.org/10.1021/ac00081a025>.
- [163] D. Dochain, State observers for tubular reactors with unknown kinetics, *J. Process Control.* 10 (2000) 259–268. [https://doi.org/10.1016/S0959-1524\(99\)00020-7](https://doi.org/10.1016/S0959-1524(99)00020-7).

- [164] W. Chen, X. Lu, C. Yao, G. Zhu, Z. Xu, An efficient approach based on bi-sensitivity analysis and genetic algorithm for calibration of activated sludge models, *Chem. Eng. J.* 259 (2015) 845–853. <https://doi.org/10.1016/j.cej.2014.07.131>.
- [165] F. Karst, M. Maestri, H. Freund, K. Sundmacher, Reduction of microkinetic reaction models for reactor optimization exemplified for hydrogen production from methane, *Chem. Eng. J.* 281 (2015) 981–994. <https://doi.org/10.1016/j.cej.2015.06.119>.
- [166] A. Saltelli, M. Ratto, T. Andres, F. Campolongo, J. Cariboni, D. Gatelli, M. Saisana, S. Tarantola, *Global Sensitivity Analysis. The Primer*, John Wiley & Sons, Ltd, Chichester, UK, 2007. <https://doi.org/10.1002/9780470725184>.
- [167] B. Iooss, P. Lemaître, A Review on Global Sensitivity Analysis Methods, in: G. Dellino, C. Meloni (Eds.), *Uncertain. Manag. Simul.-Optim. Complex Syst.*, Springer US, Boston, MA, 2015: pp. 101–122. [https://doi.org/10.1007/978-1-4899-7547-8\\_5](https://doi.org/10.1007/978-1-4899-7547-8_5).
- [168] A.S. Tomlin, E. Agbro, V. Nevrlý, J. Dlabka, M. Vašínek, Evaluation of Combustion Mechanisms Using Global Uncertainty and Sensitivity Analyses: A Case Study for Low-Temperature Dimethyl Ether Oxidation: COMBUSTION MECHANISMS USING GLOBAL UNCERTAINTY AND SENSITIVITY ANALYSES, *Int. J. Chem. Kinet.* 46 (2014) 662–682. <https://doi.org/10.1002/kin.20877>.
- [169] É. Valkó, T. Varga, A.S. Tomlin, T. Turányi, Investigation of the effect of correlated uncertain rate parameters on a model of hydrogen combustion using a generalized HDMR method, *Proc. Combust. Inst.* 36 (2017) 681–689. <https://doi.org/10.1016/j.proci.2016.07.061>.
- [170] M.D. Morris, Factorial Sampling Plans for Preliminary Computational Experiments, *Technometrics.* 33 (1991) 161–174. <https://doi.org/10.1080/00401706.1991.10484804>.

- [171] M. Matsuka, R.D. Braddock, T. Hanaoka, K. Shimura, T. Miyazawa, S. Hirata, Effect of Process-Condition-Dependent Chain Growth Probability and Methane Formation on Modeling of the Fischer–Tropsch Process, *Energy Fuels*. 30 (2016) 7971–7981. <https://doi.org/10.1021/acs.energyfuels.6b01010>.
- [172] D. Inman, L.J. Vimmerstedt, B. Bush, D. Stright, S. Peterson, Application of Variance-Based Sensitivity Analysis to a Large System Dynamics Model, *ArXiv180310722 Stat.* (2018). <http://arxiv.org/abs/1803.10722> (accessed November 22, 2018).
- [173] G. Li, H. Rabitz, General formulation of HDMR component functions with independent and correlated variables, *J. Math. Chem.* 50 (2012) 99–130. <https://doi.org/10.1007/s10910-011-9898-0>.
- [174] R.I. Cukier, C.M. Fortuin, K.E. Shuler, A.G. Petschek, J.H. Schaibly, Study of the sensitivity of coupled reaction systems to uncertainties in rate coefficients. I Theory, *J. Chem. Phys.* 59 (1973) 3873–3878. <https://doi.org/10.1063/1.1680571>.
- [175] A. Saltelli, S. Tarantola, K.P.-S. Chan, A Quantitative Model-Independent Method for Global Sensitivity Analysis of Model Output, *Technometrics*. 41 (1999) 39–56. <https://doi.org/10.1080/00401706.1999.10485594>.
- [176] I.M. Sobol, Sensitivity estimates for nonlinear mathematical models, *Math. Model. Comput. Exp.* 1 (1993) 407–414.
- [177] A. Saltelli, P. Annoni, I. Azzini, F. Campolongo, M. Ratto, S. Tarantola, Variance based sensitivity analysis of model output. Design and estimator for the total sensitivity index, *Comput. Phys. Commun.* 181 (2010) 259–270. <https://doi.org/10.1016/j.cpc.2009.09.018>.
- [178] G. Li, S.-W. Wang, H. Rabitz, S. Wang, P. Jaffé, Global uncertainty assessments by high dimensional model representations (HDMR), *Chem. Eng. Sci.* 57 (2002) 4445–4460. [https://doi.org/10.1016/S0009-2509\(02\)00417-7](https://doi.org/10.1016/S0009-2509(02)00417-7).

- [179] B. Batiot, T. Rogaume, A. Collin, F. Richard, J. Luche, Sensitivity and uncertainty analysis of Arrhenius parameters in order to describe the kinetic of solid thermal degradation during fire phenomena, *Fire Saf. J.* 82 (2016) 76–90. <https://doi.org/10.1016/j.firesaf.2016.03.007>.
- [180] L. Xu, Y. Jiang, R. Qiu, Parametric study and global sensitivity analysis for co-pyrolysis of rape straw and waste tire via variance-based decomposition, *Bioresour. Technol.* 247 (2018) 545–552. <https://doi.org/10.1016/j.biortech.2017.09.141>.
- [181] G. Li, C. Cai, Estimation parameters of hydrocracking model with NSGA-ii (Non-dominated Sorting Genetic Algorithm) by using discrete kinetic lumping model, *Fuel.* 200 (2017) 333–344. <https://doi.org/10.1016/j.fuel.2017.03.078>.
- [182] L. da R. Novaes, N.S. de Resende, V.M.M. Salim, A.R. Secchi, Modeling, simulation and kinetic parameter estimation for diesel hydrotreating, *Fuel.* 209 (2017) 184–193. <https://doi.org/10.1016/j.fuel.2017.07.092>.
- [183] F. Pianosi, T. Wagener, A simple and efficient method for global sensitivity analysis based on cumulative distribution functions, *Environ. Model. Softw.* 67 (2015) 1–11. <https://doi.org/10.1016/j.envsoft.2015.01.004>.
- [184] A. Saltelli, S. Tarantola, F. Campolongo, M. Ratto, *Sensitivity Analysis in Practice: A Guide to Assessing Scientific Models*, John Wiley & Sons, Ltd, Chichester, UK, 2004.
- [185] E.C. Martinez, LUMPING OF COMPONENTS AND REACTIONS IN COMPLEX REACTION NETWORKS†, *Chem. Eng. Commun.* 93 (1990) 1–24. <https://doi.org/10.1080/00986449008911434>.
- [186] V. Calemme, C. Gambaro, W.O. Parker, R. Carbone, R. Giardino, P. Scorletti, Middle distillates from hydrocracking of FT waxes: Composition, characteristics and emission properties, *Catal. Today.* 149 (2010) 40–46. <https://doi.org/10.1016/j.cattod.2009.03.018>.

- [187] G. Elordi, M. Olazar, G. Lopez, M. Artetxe, J. Bilbao, Product Yields and Compositions in the Continuous Pyrolysis of High-Density Polyethylene in a Conical Spouted Bed Reactor, *Ind. Eng. Chem. Res.* 50 (2011) 6650–6659. <https://doi.org/10.1021/ie200186m>.
- [188] M.R. Djokic, H. Muller, N.D. Ristic, A.R. Akhras, S.H. Symoens, G.B. Marin, K.M. Van Geem, Combined characterization using HT-GC × GC-FID and FT-ICR MS: A pyrolysis fuel oil case study, *Fuel Process. Technol.* 182 (2018) 15–25. <https://doi.org/10.1016/j.fuproc.2018.10.007>.
- [189] J.A. Onwudili, N. Insura, P.T. Williams, Composition of products from the pyrolysis of polyethylene and polystyrene in a closed batch reactor: Effects of temperature and residence time, *J. Anal. Appl. Pyrolysis.* 86 (2009) 293–303. <https://doi.org/10.1016/j.jaap.2009.07.008>.
- [190] L. Ying, J. Zhu, Y. Cheng, L. Wang, X. Li, Kinetic modeling of C2–C7 olefins interconversion over ZSM-5 catalyst, *J. Ind. Eng. Chem.* 33 (2016) 80–90. <https://doi.org/10.1016/j.jiec.2015.09.021>.
- [191] Y. Zheng, Q. Tang, T. Wang, J. Wang, Lumping Strategy in Kinetic Modeling of Vacuum Pyrolysis of Plant Oil Asphalt, *Energy Fuels.* 29 (2015) 1729–1734. <https://doi.org/10.1021/ef502530q>.
- [192] G. Özsin, A.E. Pütün, TGA/MS/FT-IR study for kinetic evaluation and evolved gas analysis of a biomass/PVC co-pyrolysis process, *Energy Convers. Manag.* 182 (2019) 143–153. <https://doi.org/10.1016/j.enconman.2018.12.060>.
- [193] F. Xu, B. Wang, D. Yang, J. Hao, Y. Qiao, Y. Tian, Thermal degradation of typical plastics under high heating rate conditions by TG-FTIR: Pyrolysis behaviors and kinetic analysis, *Energy Convers. Manag.* 171 (2018) 1106–1115. <https://doi.org/10.1016/j.enconman.2018.06.047>.
- [194] B. Wei, P. Zou, X. Zhang, X. Xu, C. Wood, Y. Li, Investigations of Structure–Property–Thermal Degradation Kinetics Alterations of Tahe Asphaltene Caused by Low Temperature Oxidation, *Energy Fuels.* 32 (2018) 1506–1514. <https://doi.org/10.1021/acs.energyfuels.7b03565>.

- [195] K. Hashimoto, I. Hasegawa, J. Hayashi, K. Mae, Correlations of kinetic parameters in biomass pyrolysis with solid residue yield and lignin content, *Fuel*. 90 (2011) 104–112. <https://doi.org/10.1016/j.fuel.2010.08.023>.
- [196] B. Browning, P. Afanasiev, I. Pitault, F. Couenne, M. Tayakout-Fayolle, Detailed kinetic modelling of vacuum gas oil hydrocracking using bifunctional catalyst: A distribution approach, *Chem. Eng. J.* 284 (2016) 270–284. <https://doi.org/10.1016/j.cej.2015.08.126>.
- [197] A. Németh, M. Blazsó, P. Baranyai, T. Vidóczy, Thermal degradation of polyethylene modeled on tetracontane, *J. Anal. Appl. Pyrolysis*. 81 (2008) 237–242. <https://doi.org/10.1016/j.jaap.2007.11.012>.
- [198] M. Arabiourrutia, G. Lopez, R. Aguado, J. Bilbao, M. Olazar, Coupling gas flow pattern and kinetics for tyre pyrolysis modelling, *Chem. Eng. Sci.* 201 (2019) 362–372. <https://doi.org/10.1016/j.ces.2019.02.025>.
- [199] H. Puron, P. Arcelus-Arrillaga, K.K. Chin, J.L. Pinilla, B. Fidalgo, M. Millan, Kinetic analysis of vacuum residue hydrocracking in early reaction stages, *Fuel*. 117 (2014) 408–414. <https://doi.org/10.1016/j.fuel.2013.09.053>.
- [200] K.G. Santos, T.S. Lira, M. Gianesella, F.S. Lobato, V.V. Murata, M.A.S. Barrozo, BAGASSE PYROLYSIS: A COMPARATIVE STUDY OF KINETIC MODELS, *Chem. Eng. Commun.* 199 (2012) 109–121. <https://doi.org/10.1080/00986445.2011.575906>.
- [201] F. Trejo, J. Ancheyta, S. Sánchez, M.A. Rodríguez, Comparison of Different Power-law Kinetic Models for Hydrocracking of Asphaltenes, *Pet. Sci. Technol.* 25 (2007) 263–275. <https://doi.org/10.1080/10916460601054735>.
- [202] G. Félix, J. Ancheyta, Comparison of hydrocracking kinetic models based on SARA fractions obtained in slurry-phase reactor, *Fuel*. 241 (2019) 495–505. <https://doi.org/10.1016/j.fuel.2018.11.153>.

- [203] R. Gomez-Gonzalez, F.J. Cerino-Córdova, A.M. Garcia-León, E. Soto-Regalado, N.E. Davila-Guzman, J.J. Salazar-Rabago, Lead biosorption onto coffee grounds: Comparative analysis of several optimization techniques using equilibrium adsorption models and ANN, *J. Taiwan Inst. Chem. Eng.* 68 (2016) 201–210. <https://doi.org/10.1016/j.jtice.2016.08.038>.
- [204] K.-Y. Li, X. Huang, C. Fleischmann, G. Rein, J. Ji, Pyrolysis of Medium-Density Fiberboard: Optimized Search for Kinetics Scheme and Parameters via a Genetic Algorithm Driven by Kissinger’s Method, *Energy Fuels*. 28 (2014) 6130–6139. <https://doi.org/10.1021/ef501380c>.
- [205] H.E. Kissinger, Reaction Kinetics in Differential Thermal Analysis, *Anal. Chem.* 29 (1957) 1702–1706. <https://doi.org/10.1021/ac60131a045>.
- [206] H. Ghahraloud, M. Farsi, Modeling and optimization of methanol oxidation over metal oxide catalyst in an industrial fixed bed reactor, *J. Taiwan Inst. Chem. Eng.* 81 (2017) 95–103. <https://doi.org/10.1016/j.jtice.2017.10.003>.
- [207] V. Kumar, P. Balasubramanian, Kinetic parameter estimation in hydrocracking using hybrid particle swarm optimization, *Fuel*. 88 (2009) 2171–2180. <https://doi.org/10.1016/j.fuel.2009.05.004>.
- [208] L.M. Rios, N.V. Sahinidis, Derivative-free optimization: a review of algorithms and comparison of software implementations, *J. Glob. Optim.* 56 (2013) 1247–1293. <https://doi.org/10.1007/s10898-012-9951-y>.
- [209] P. Civicioglu, E. Besdok, A conceptual comparison of the Cuckoo-search, particle swarm optimization, differential evolution and artificial bee colony algorithms, *Artif. Intell. Rev.* 39 (2013) 315–346. <https://doi.org/10.1007/s10462-011-9276-0>.
- [210] N. Hansen, A. Auger, R. Ros, S. Finck, P. Pošík, Comparing results of 31 algorithms from the black-box optimization benchmarking BBOB-2009, in: *Proc. 12th Annu. Conf. Comp Genet. Evol. Comput. - GECCO 10*, ACM Press, Portland, Oregon, USA, 2010: p. 1689. <https://doi.org/10.1145/1830761.1830790>.

- [211] T. Zhang, C. Leyva, G.F. Froment, J. Martinis, Vacuum Gas Oil Hydrocracking on NiMo/USY Zeolite Catalysts. Experimental Study and Kinetic Modeling, *Ind. Eng. Chem. Res.* 54 (2015) 858–868. <https://doi.org/10.1021/ie503567b>.
- [212] S.M. Baker, K. Schallau, B.H. Junker, Comparison of different algorithms for simultaneous estimation of multiple parameters in kinetic metabolic models, *J. Integr. Bioinforma.* (2010). <https://doi.org/10.2390/biecoll-jib-2010-133>.
- [213] A.F. Villaverde, F. Froehlich, D. Weindl, J. Hasenauer, J.R. Banga, Benchmarking optimization methods for parameter estimation in large kinetic models, *BioRxiv.* (2018). <https://doi.org/10.1101/295006>.
- [214] H. Stitt, M. Marigo, S. Wilkinson, T. Dixon, How Good is Your Model?, *Johns. Matthey Technol. Rev.* 59 (2015) 74–89. <https://doi.org/10.1595/205651315X686804>.
- [215] A. Al-Matouq, T. Vincent, A convex optimization framework for the identification of homogeneous reaction systems, *Automatica.* 114 (2020) 108823. <https://doi.org/10.1016/j.automatica.2020.108823>.
- [216] D. Rodrigues, J. Billeter, D. Bonvin, Global Identification of Kinetic Parameters via the Extent-based Incremental Approach, in: *Comput. Aided Chem. Eng.*, Elsevier, 2017: pp. 2119–2124. <https://doi.org/10.1016/B978-0-444-63965-3.50355-X>.
- [217] M. Ayyıldız, K. Çetinkaya, Comparison of four different heuristic optimization algorithms for the inverse kinematics solution of a real 4-DOF serial robot manipulator, *Neural Comput. Appl.* 27 (2016) 825–836. <https://doi.org/10.1007/s00521-015-1898-8>.
- [218] S. Sadighi, A. Ahmad, A. Irandoukht, Modeling a Pilot Fixed-Bed Hydrocracking Reactor via a Kinetic Base and Neuro-Fuzzy Method, *J. Chem. Eng. Jpn.* 43 (2010) 174–185. <https://doi.org/10.1252/jcej.09we162>.
- [219] S. Sadighi, G. Reza Zahedi, Comparison of Kinetic-based and Artificial Neural Network Modeling Methods for a Pilot Scale Vacuum Gas Oil Hydrocracking Reactor, *Bull. Chem. React. Eng. Catal.* 8 (2013). <https://doi.org/10.9767/bcrec.8.2.4722.125-136>.



- [220] J. Tang, X. Chen, Z. Fei, J. Zhao, M. Cui, X. Qiao, HCl Oxidation To Recycle Cl<sub>2</sub> over a Cu/Ce Composite Oxide Catalyst. Part 1. Intrinsic Kinetic Study, *Ind. Eng. Chem. Res.* 52 (2013) 11897–11903. <https://doi.org/10.1021/ie400200g>.
- [221] X. Chen, Y. Dai, Z. Fei, J. Tang, M. Cui, X. Qiao, HCl Oxidation To Recycle Cl<sub>2</sub> over a Cu/Ce Composite Oxide Catalyst. Part 2. Single-Tube-Reactor Simulation, *Ind. Eng. Chem. Res.* 54 (2015) 9931–9937. <https://doi.org/10.1021/acs.iecr.5b02351>.
- [222] V.N. Snytnikov, T.I. Mischenko, V.I. Snytnikov, I.G. Chernykh, A reactor for the study of homogeneous processes using laser radiation energy, *Chem. Eng. J.* 150 (2009) 231–236. <https://doi.org/10.1016/j.cej.2009.02.028>.
- [223] L.F. Nurislamova, O.P. Stoyanovskaya, O.A. Stadnichenko, I.M. Gubaidullin, V.N. Snytnikov, A.V. Novichkova, Few-Step Kinetic Model of Gaseous Autocatalytic Ethane Pyrolysis and Its Evaluation by Means of Uncertainty and Sensitivity Analysis, *Chem. Prod. Process Model.* 9 (2014). <https://doi.org/10.1515/cppm-2014-0008>.
- [224] N. Miskolczi, J. Sója, E. Tulok, Thermo-catalytic two-step pyrolysis of real waste plastics from end of life vehicle, *J. Anal. Appl. Pyrolysis.* 128 (2017) 1–12. <https://doi.org/10.1016/j.jaap.2017.11.008>.
- [225] N. Miskolczi, T. Juzsakova, J. Sója, Preparation and application of metal loaded ZSM-5 and  $\gamma$ -zeolite catalysts for thermo-catalytic pyrolysis of real end of life vehicle plastics waste, *J. Energy Inst.* (2017). <https://doi.org/10.1016/j.joei.2017.10.017>.
- [226] L. Shampine, M. Reichelt, The MATLAB ODE Suite, *SIAM J. Sci. Comput.* 18 (1997) 1–22. <https://doi.org/10.1137/S1064827594276424>.
- [227] L. Shampine, M. Reichelt, J. Kierzenka, Solving Index-1 DAEs in MATLAB and Simulink, *SIAM Rev.* 41 (1999) 538–552. <https://doi.org/10.1137/S003614459933425X>.
- [228] G. Szederkényi, Computing sparse and dense realizations of reaction kinetic systems, *J. Math. Chem.* 47 (2010) 551–568. <https://doi.org/10.1007/s10910-009-9525-5>.

- [229] S. Sadighi, A. Ahmad, M. Rashidzadeh, 4-Lump kinetic model for vacuum gas oil hydrocracker involving hydrogen consumption, *Korean J. Chem. Eng.* 27 (2010) 1099–1108. <https://doi.org/10.1007/s11814-010-0172-0>.
- [230] S. Mohanty, D.N. Saraf, D. Kunzru, Modeling of a hydrocracking reactor, *Fuel Process. Technol.* 29 (1991) 1–17. [https://doi.org/10.1016/0378-3820\(91\)90013-3](https://doi.org/10.1016/0378-3820(91)90013-3).
- [231] R. Chen, X. Xu, Y. Zhang, S. Lo, S. Lu, Kinetic study on pyrolysis of waste phenolic fibre-reinforced plastic, *Appl. Therm. Eng.* 136 (2018) 484–491. <https://doi.org/10.1016/j.applthermaleng.2018.03.045>.
- [232] T. Billa, S.R. Horton, M. Sahasrabudhe, C. Saravanan, Z. Hou, P. Agarwal, J. Lucio-Vega, M.T. Klein, Enhancing the value of detailed kinetic models through the development of interrogative software applications, *Comput. Chem. Eng.* 106 (2017) 512–528. <https://doi.org/10.1016/j.compchemeng.2017.07.009>.
- [233] R.E. Hayes, F.H. Bertrand, C. Audet, S.T. Kolaczowski, Catalytic Combustion Kinetics: Using a Direct Search Algorithm to Evaluate Kinetic Parameters from Light-Off Curves, *Can. J. Chem. Eng.* 81 (2008) 1192–1199. <https://doi.org/10.1002/cjce.5450810608>.
- [234] S. Le Digabel, Algorithm 909: NOMAD: Nonlinear optimization with the MADS algorithm, *ACM Trans. Math. Softw. TOMS.* 37 (2011) 44.
- [235] C. Audet, S. Le Digabel, C. Tribes, NOMAD user guide, *Les cahiers du GERAD*, 2009. [https://www.gerad.ca/nomad/Downloads/user\\_guide.pdf](https://www.gerad.ca/nomad/Downloads/user_guide.pdf).
- [236] J. Currie, D. Wilson, OPTI: Lowering the Barrier Between Open Source Optimizers and the Industrial MATLAB User, (2012). <http://focapo.cheme.cmu.edu/2012/proceedings/data/papers/024.pdf>.
- [237] L.A. Alcázar, J. Ancheyta, Sensitivity analysis based methodology to estimate the best set of parameters for heterogeneous kinetic models, *Chem. Eng. J.* 128 (2007) 85–93. <https://doi.org/10.1016/j.cej.2006.10.012>.
- [238] J.R.R.A. Martins, P. Sturdza, J.J. Alonso, The Complex-step Derivative Approximation, *ACM Trans Math Softw.* 29 (2003) 245–262. <https://doi.org/10.1145/838250.838251>.

- [239] T. Ziehn, A.S. Tomlin, GUI-HDMR – A software tool for global sensitivity analysis of complex models, *Environ. Model. Softw.* 24 (2009) 775–785. <https://doi.org/10.1016/j.envsoft.2008.12.002>.
- [240] F. Pianosi, F. Sarrazin, T. Wagener, A Matlab toolbox for Global Sensitivity Analysis, *Environ. Model. Softw.* 70 (2015) 80–85. <https://doi.org/10.1016/j.envsoft.2015.04.009>.
- [241] F. Campolongo, A. Saltelli, J. Cariboni, From screening to quantitative sensitivity analysis. A unified approach, *Comput. Phys. Commun.* 182 (2011) 978–988. <https://doi.org/10.1016/j.cpc.2010.12.039>.
- [242] E.W. Dijkstra, A note on two problems in connexion with graphs, *Numer. Math.* 1 (1959) 269–271. <https://doi.org/10.1007/BF01386390>.
- [243] Q. Liu, T. Homma, A new computational method of a moment-independent uncertainty importance measure, *Reliab. Eng. Syst. Saf.* 94 (2009) 1205–1211. <https://doi.org/10.1016/j.ress.2008.10.005>.
- [244] C.C. Lakshmanan, N. White, A New Distributed Activation Energy Model Using Weibull Distribution for the Representation of Complex Kinetics, *Energy Fuels*. 8 (1994) 1158–1167. <https://doi.org/10.1021/ef00048a001>.
- [245] S. Sánchez, J. Ancheyta, W.C. McCaffrey, Comparison of Probability Distribution Functions for Fitting Distillation Curves of Petroleum, *Energy Fuels*. 21 (2007) 2955–2963. <https://doi.org/10.1021/ef070003y>.
- [246] D.T. Sandwell, Biharmonic spline interpolation of GEOS-3 and SEASAT altimeter data, *Geophys. Res. Lett.* 14 (1987) 139–142. <https://doi.org/10.1029/GL014i002p00139>.
- [247] Z. Till, T. Varga, J. Sója, N. Miskolczi, T. Chován, Kinetic identification of plastic waste pyrolysis on zeolite-based catalysts, *Energy Convers. Manag.* 173 (2018) 320–330. <https://doi.org/10.1016/j.enconman.2018.07.088>.
- [248] E.M.T. Hendrix, B. Gazdag-Tóth, Introduction to nonlinear and global optimization, Springer, New York, NY, 2010.
- [249] S. Siouris, S. Blakey, Fitness functions for evolutionary optimization of rate parameters in chemically reacting systems, *Chem. Eng. Sci.* 196 (2019) 354–365. <https://doi.org/10.1016/j.ces.2018.11.009>.

- [250] M. Amutio, G. Lopez, J. Alvarez, R. Moreira, G. Duarte, J. Nunes, M. Olazar, J. Bilbao, Pyrolysis kinetics of forestry residues from the Portuguese Central Inland Region, *Chem. Eng. Res. Des.* 91 (2013) 2682–2690. <https://doi.org/10.1016/j.cherd.2013.05.031>.
- [251] Q.-K. Liu, D.-Q. Zhu, X.-C. Tan, P.-Q. Yuan, Z.-M. Cheng, W.-K. Yuan, J.-Y. Yang, Lumped reaction kinetic models for pyrolysis of heavy oil in the presence of supercritical water, *AIChE J.* 62 (2016) 207–216. <https://doi.org/10.1002/aic.14978>.
- [252] K. Sörensen, Metaheuristics-the metaphor exposed, *Int. Trans. Oper. Res.* 22 (2015) 3–18. <https://doi.org/10.1111/itor.12001>.
- [253] D. Weyland, A critical analysis of the harmony search algorithm—How not to solve sudoku, *Oper. Res. Perspect.* 2 (2015) 97–105. <https://doi.org/10.1016/j.orp.2015.04.001>.
- [254] M.J.D. Powell, Variable Metric Methods for Constrained Optimization, in: A. Bachem, B. Korte, M. Grötschel (Eds.), *Math. Program. State Art*, Springer Berlin Heidelberg, Berlin, Heidelberg, 1983: pp. 288–311. [https://doi.org/10.1007/978-3-642-68874-4\\_12](https://doi.org/10.1007/978-3-642-68874-4_12).
- [255] The Mathworks, Inc., Find minimum of constrained nonlinear multivariable function, *MATLAB Doc.* (2018). <https://www.mathworks.com/help/optim/ug/fmincon.html> (accessed January 29, 2019).
- [256] S.M.K. Heris, Biogeography-Based Optimization (BBO) in MATLAB, Yarpiz. (2015). <http://yarpiz.com/239/ypea113-biogeography-based-optimization> (accessed January 29, 2019).
- [257] D. Simon, Biogeography-Based Optimization, *IEEE Trans. Evol. Comput.* 12 (2008) 702–713. <https://doi.org/10.1109/TEVC.2008.919004>.
- [258] S.M.K. Heris, Bees Algorithm (BeA) in MATLAB, Yarpiz. (2015). <http://yarpiz.com/315/ypea115-bees-algorithm> (accessed January 29, 2019).
- [259] D.T. Pham, A. Ghanbarzadeh, E. Koc, S. Otri, S. Rahim, M. Zaidi, *The bees algorithm*, Manufacturing Engineering Centre, Cardiff University, United Kingdom, 2005.

- [260] S.M.K. Heris, Cultural Algorithm (CA) in MATLAB, Yarpiz. (2015). <http://yarpiz.com/425/ypea125-cultural-algorithm> (accessed January 29, 2019).
- [261] R.G. Reynolds, An introduction to cultural algorithms, in: Proc. Third Annu. Conf. Evol. Program., World Scientific Publishing Co. Pte. Ltd., River Edge, NJ, 1994: pp. 131–139.
- [262] N. Hansen, A. Ostermeier, Completely Derandomized Self-Adaptation in Evolution Strategies, *Evol. Comput.* 9 (2001) 159–195. <https://doi.org/10.1162/106365601750190398>.
- [263] S.G. Johnson, The NLOpt nonlinear-optimization package, (2007). <http://ab-initio.mit.edu/nlopt> (accessed January 29, 2019).
- [264] W.L. Price, Global optimization by controlled random search, *J. Optim. Theory Appl.* 40 (1983) 333–348. <https://doi.org/10.1007/BF00933504>.
- [265] C.H. da Silva Santos, M.S. Goncalves, H.E. Hernandez-Figueroa, Designing Novel Photonic Devices by Bio-Inspired Computing, *IEEE Photonics Technol. Lett.* 22 (2010) 1177–1179. <https://doi.org/10.1109/LPT.2010.2051222>.
- [266] J.A. Egea, R. Martí, J.R. Banga, An evolutionary method for complex-process optimization, *Comput. Oper. Res.* 37 (2010) 315–324. <https://doi.org/10.1016/j.cor.2009.05.003>.
- [267] J.A. Egea, D. Henriques, T. Cokelaer, A.F. Villaverde, A. MacNamara, D.-P. Danciu, J.R. Banga, J. Saez-Rodriguez, MEIGO: an open-source software suite based on metaheuristics for global optimization in systems biology and bioinformatics, *BMC Bioinformatics.* 15 (2014) 136. <https://doi.org/10.1186/1471-2105-15-136>.
- [268] S.M.K. Heris, Firefly Algorithm (FA) in MATLAB, Yarpiz. (2015). <http://yarpiz.com/259/ypea112-firefly-algorithm> (accessed January 29, 2019).
- [269] X.-S. Yang, Nature-inspired metaheuristic algorithms, 2. ed, Luniver Press, Frome, 2010.

- [270] The Mathworks, Inc., How the Genetic Algorithm Works, MATLAB Doc. (2019). <https://www.mathworks.com/help/gads/how-the-genetic-algorithm-works.html> (accessed January 29, 2020).
- [271] S.M.K. Heris, Harmony Search in MATLAB, Yarpiz. (2015). <http://yarpiz.com/92/yypea117-harmony-search> (accessed January 29, 2019).
- [272] Zong Woo Geem, Joong Hoon Kim, G.V. Loganathan, A New Heuristic Optimization Algorithm: Harmony Search, SIMULATION. 76 (2001) 60–68. <https://doi.org/10.1177/003754970107600201>.
- [273] R.H. Byrd, M.E. Hribar, J. Nocedal, An Interior Point Algorithm for Large-Scale Nonlinear Programming, SIAM J. Optim. 9 (1999) 877–900. <https://doi.org/10.1137/S1052623497325107>.
- [274] T.P. Runarsson, X. Yao, Search Biases in Constrained Evolutionary Optimization, IEEE Trans. Syst. Man Cybern. Part C Appl. Rev. 35 (2005) 233–243. <https://doi.org/10.1109/TSMCC.2004.841906>.
- [275] The Mathworks, Inc., Solve nonlinear least-squares (nonlinear data-fitting) problems, MATLAB Doc. (2018). <https://www.mathworks.com/help/optim/ug/lsqnonlin.html>.
- [276] J.J. Moré, The Levenberg-Marquardt algorithm: Implementation and theory, in: G.A. Watson (Ed.), Numer. Anal., Springer Berlin Heidelberg, Berlin, Heidelberg, 1978: pp. 105–116. <https://doi.org/10.1007/BFb0067700>.
- [277] J. Kennedy, R. Eberhart, Particle swarm optimization, in: Proc. ICNN95 - Int. Conf. Neural Netw., IEEE, Perth, WA, Australia, 1995: pp. 1942–1948. <https://doi.org/10.1109/ICNN.1995.488968>.
- [278] The Mathworks, Inc., Particle Swarm Optimization Algorithm, MATLAB Doc. (2019). <https://www.mathworks.com/help/gads/particle-swarm-optimization-algorithm.html> (accessed January 29, 2020).
- [279] C. Audet, J.E. Dennis, Analysis of Generalized Pattern Searches, SIAM J. Optim. 13 (2002) 889–903. <https://doi.org/10.1137/S1052623400378742>.

- [280] The Mathworks, Inc., Find minimum of function using pattern search, MATLAB Doc. (2018). <https://www.mathworks.com/help/gads/patternsearch.html> (accessed January 29, 2019).
- [281] B. Birge, PSOt - a particle swarm optimization toolbox for use with Matlab, in: Proc. 2003 IEEE Swarm Intell. Symp. SIS03 Cat No03EX706, IEEE, Indianapolis, Indiana, USA, 2003: pp. 182–186. <https://doi.org/10.1109/SIS.2003.1202265>.
- [282] A.I.F. Vaz, L.N. Vicente, A particle swarm pattern search method for bound constrained global optimization, *J. Glob. Optim.* 39 (2007) 197–219. <https://doi.org/10.1007/s10898-007-9133-5>.
- [283] A.I.F. Vaz, L.N. Vicente, PSwarm: a hybrid solver for linearly constrained global derivative-free optimization, *Optim. Methods Softw.* 24 (2009) 669–685. <https://doi.org/10.1080/10556780902909948>.
- [284] H.A. Le Thi, A.I.F. Vaz, L.N. Vicente, Optimizing radial basis functions by d.c. programming and its use in direct search for global derivative-free optimization, *TOP.* 20 (2012) 190–214. <https://doi.org/10.1007/s11750-011-0193-9>.
- [285] Q. Duan, S. Sorooshian, V. Gupta, Effective and efficient global optimization for conceptual rainfall-runoff models, *Water Resour. Res.* 28 (1992) 1015–1031. <https://doi.org/10.1029/91WR02985>.
- [286] S.M.K. Heris, Shuffled Complex Evolution in MATLAB, Yarpiz. (2015). <http://yarpiz.com/80/ypea110-shuffled-complex-evolution> (accessed January 29, 2019).
- [287] J. D’Errico, fminsearchbnd, fminsearchcon, MathWorks File Exch. (2012). <https://www.mathworks.com/matlabcentral/fileexchange/8277-fminsearchbnd-fminsearchcon> (accessed January 29, 2019).
- [288] V. Černý, Thermodynamical approach to the traveling salesman problem: An efficient simulation algorithm, *J. Optim. Theory Appl.* 45 (1985) 41–51. <https://doi.org/10.1007/BF00940812>.

- [289] The Mathworks, Inc., Find minimum of function using simulated annealing algorithm, MATLAB Doc. (2018). <https://www.mathworks.com/help/gads/simulannealbnd.html> (accessed January 29, 2019).
- [290] J. Nocedal, S. Wright, Numerical Optimization, Springer New York, 2006. <https://doi.org/10.1007/978-0-387-40065-5>.
- [291] A.P. Amrute, C. Mondelli, M.A.G. Hevia, J. Pérez-Ramírez, Mechanism–Performance Relationships of Metal Oxides in Catalyzed HCl Oxidation, ACS Catal. 1 (2011) 583–590. <https://doi.org/10.1021/cs200075j>.
- [292] G.W. Hampton, P. Robinson, Controlling hydrocracker temperature excursions, (2011). [https://www.researchgate.net/profile/Paul\\_Robinson12/publication/274717882\\_Controlling\\_Hydrocracker\\_Temperature\\_Excursions/links/5527e1a80cf2779ab78ae142/Controlling-Hydrocracker-Temperature-Excursions.pdf](https://www.researchgate.net/profile/Paul_Robinson12/publication/274717882_Controlling_Hydrocracker_Temperature_Excursions/links/5527e1a80cf2779ab78ae142/Controlling-Hydrocracker-Temperature-Excursions.pdf) (accessed December 16, 2019).
- [293] M. Bricker, V. Thakkar, J. Petri, Hydrocracking in Petroleum Processing, in: S.A. Treese, P.R. Pujadó, D.S.J. Jones (Eds.), Handb. Pet. Process., Springer International Publishing, Cham, 2015: pp. 317–359. [https://doi.org/10.1007/978-3-319-14529-7\\_3](https://doi.org/10.1007/978-3-319-14529-7_3).



## Appendix

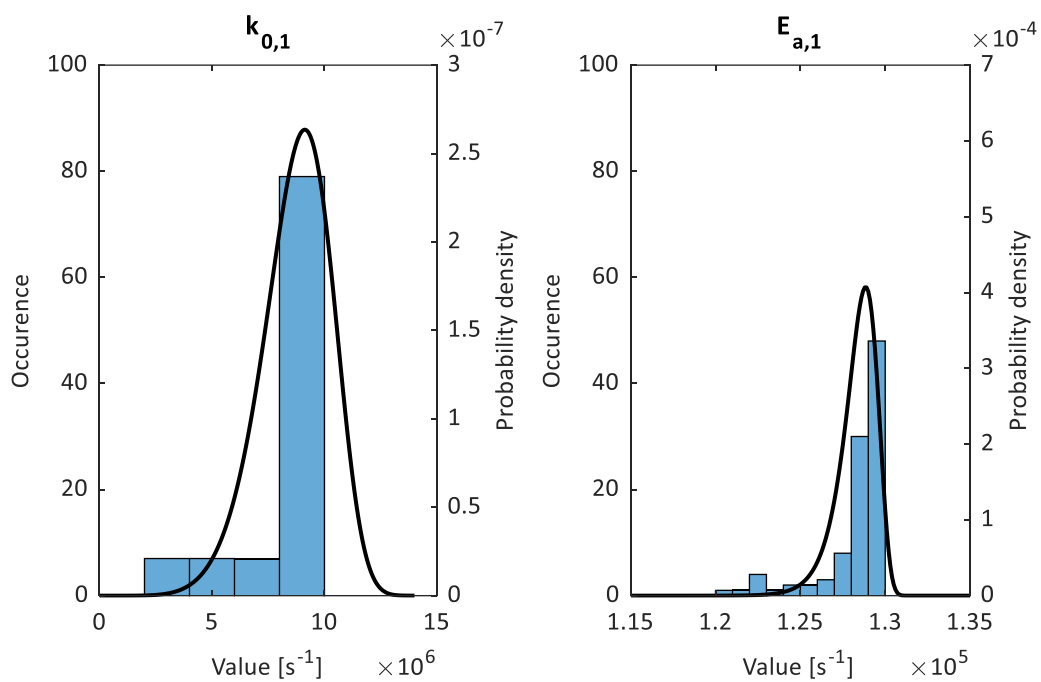


Figure S1. Identified kinetic parameters of the 1<sup>st</sup> reaction for every generated data set using bootstrapping and the fitted Weibull-distribution in case of the complete reaction network for VGO hydrocracking.

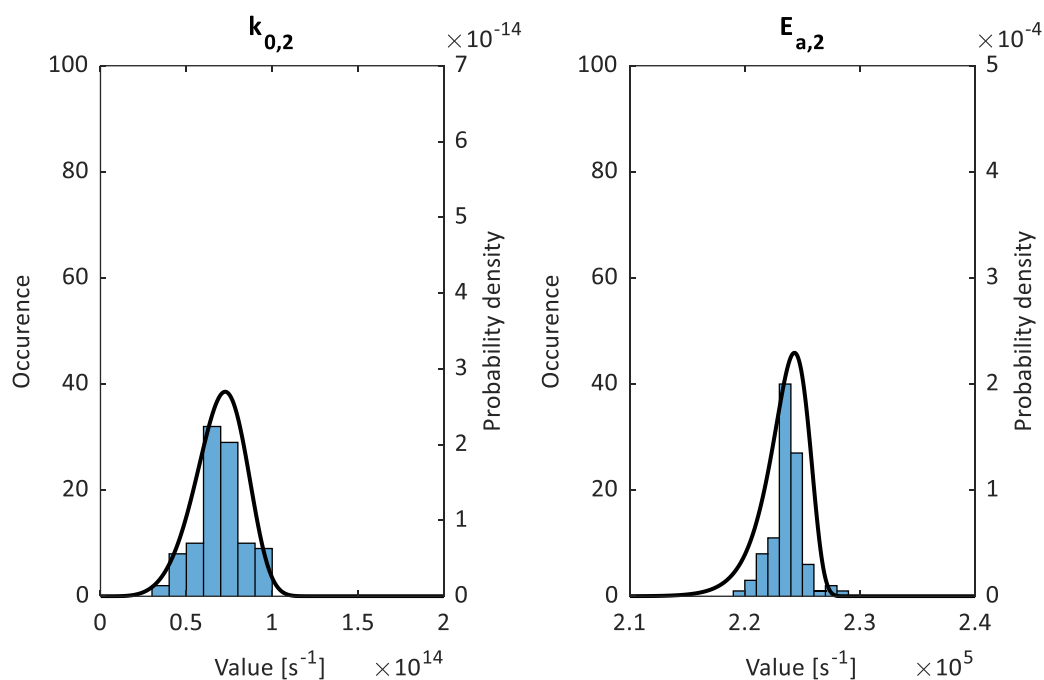


Figure S2. Identified kinetic parameters of the 2nd reaction for every generated data set using bootstrapping and the fitted Weibull-distribution in case of the complete reaction network for VGO hydrocracking.

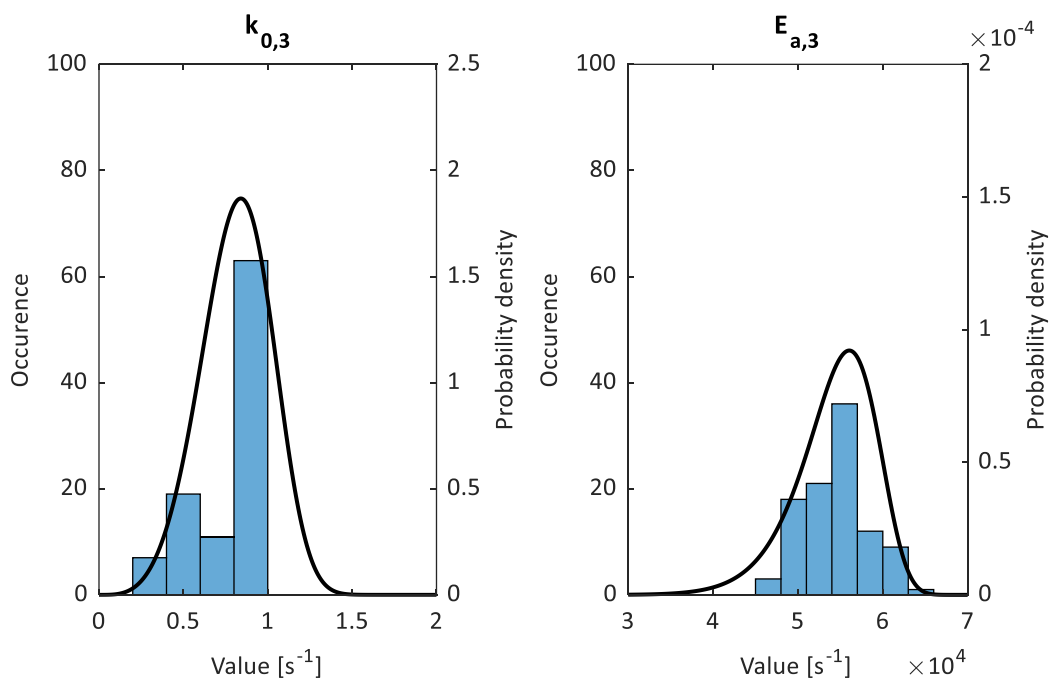


Figure S3. Identified kinetic parameters of the 3rd reaction for every generated data set using bootstrapping and the fitted Weibull-distribution in case of the complete reaction network for VGO hydrocracking.

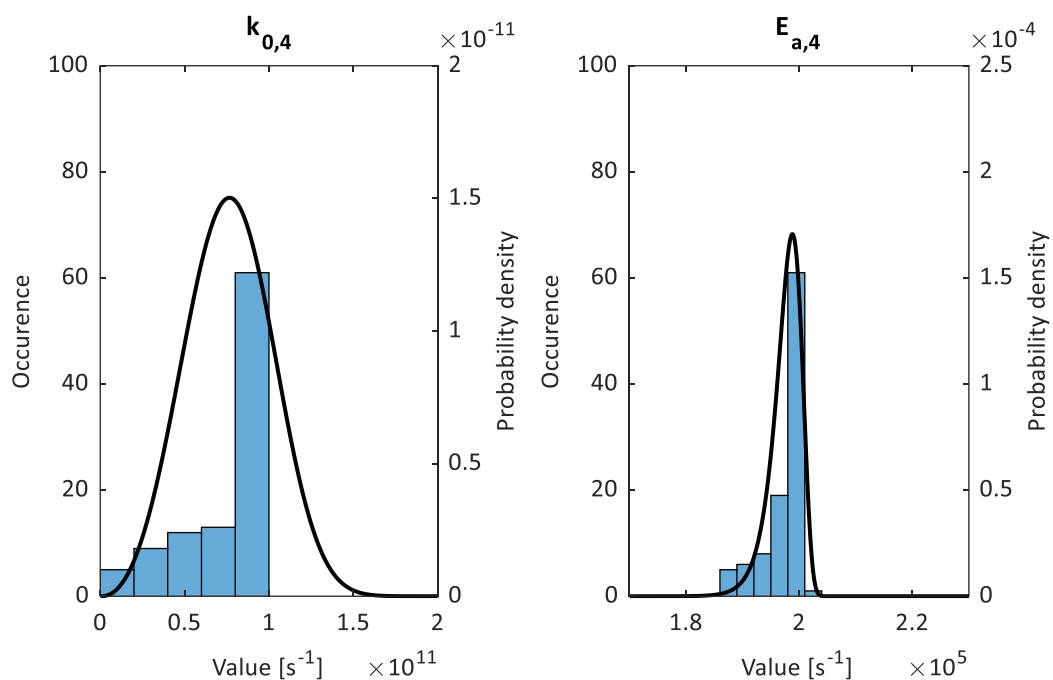


Figure S4. Identified kinetic parameters of the 4th reaction for every generated data set using bootstrapping and the fitted Weibull-distribution in case of the complete reaction network for VGO hydrocracking.

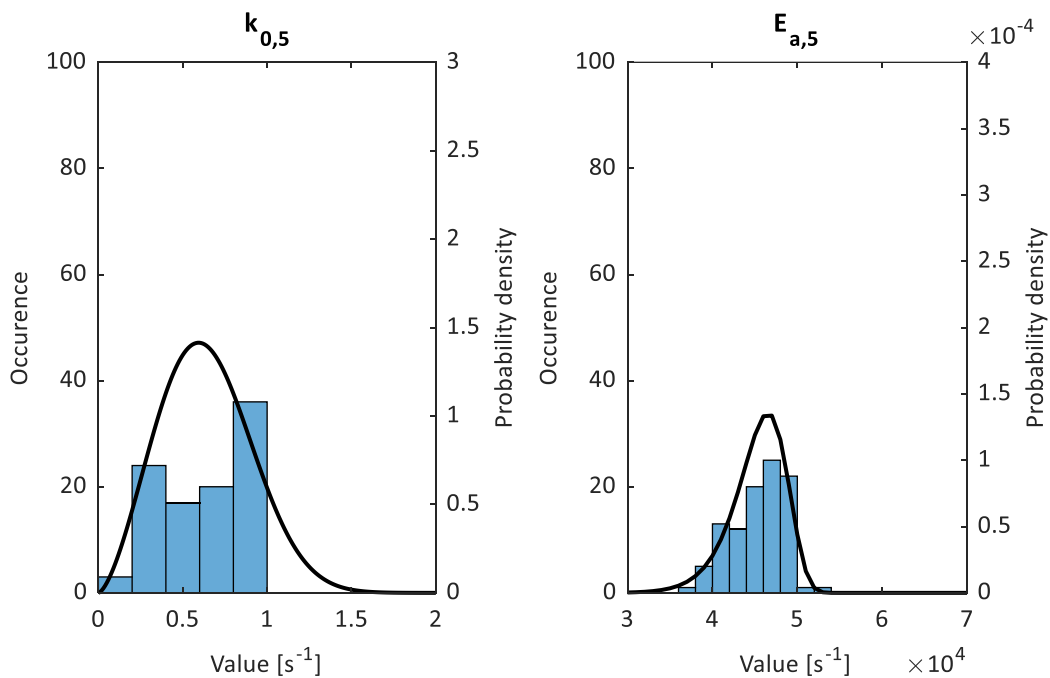


Figure S5. Identified kinetic parameters of the 5<sup>th</sup> reaction for every generated data set using bootstrapping and the fitted Weibull-distribution in case of the complete reaction network for VGO hydrocracking.

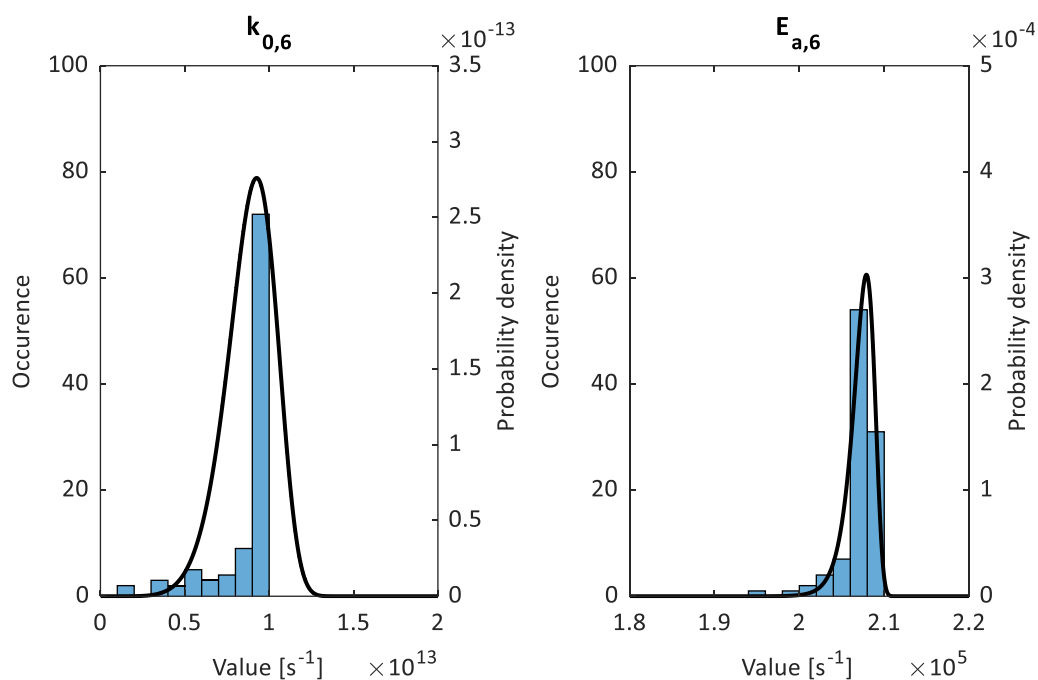


Figure S6. Identified kinetic parameters of the 6<sup>th</sup> reaction for every generated data set using bootstrapping and the fitted Weibull-distribution in case of the complete reaction network for VGO hydrocracking.

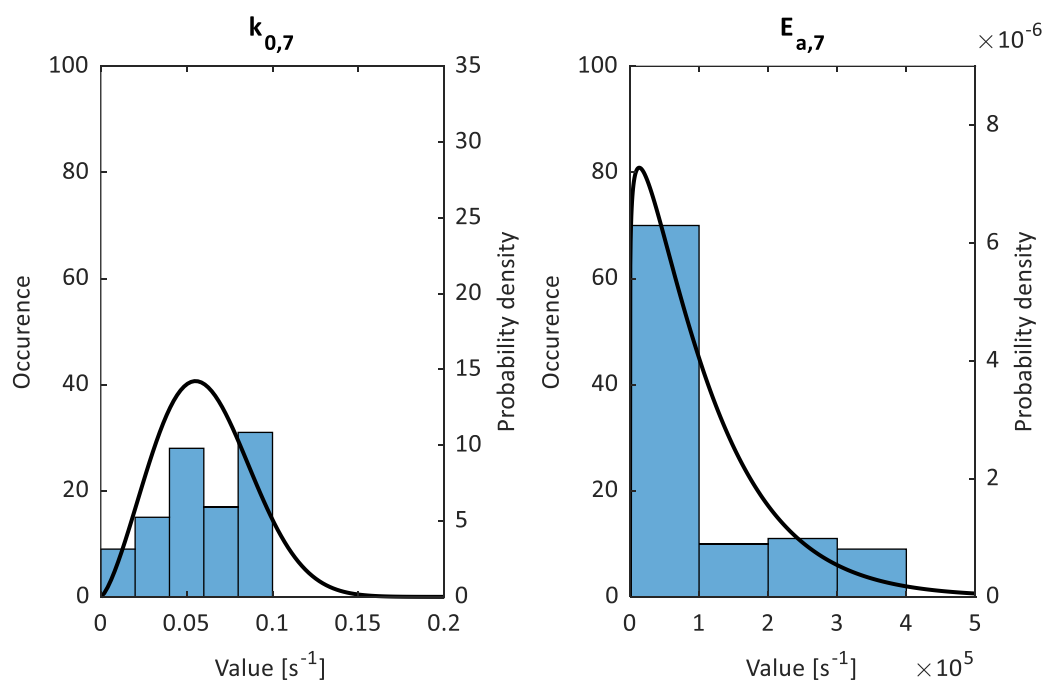


Figure S7. Identified kinetic parameters of the 7<sup>th</sup> reaction for every generated data set using bootstrapping and the fitted Weibull-distribution in case of the complete reaction network for VGO hydrocracking.

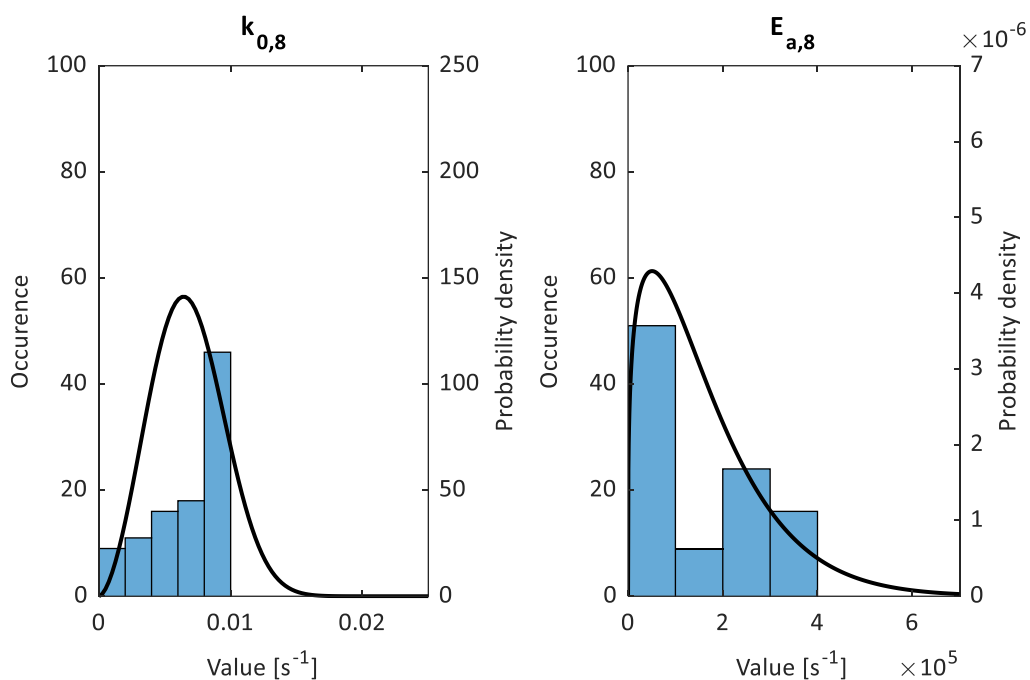


Figure S8. Identified kinetic parameters of the 8<sup>th</sup> reaction for every generated data set using bootstrapping and the fitted Weibull-distribution in case of the complete reaction network for VGO hydrocracking.

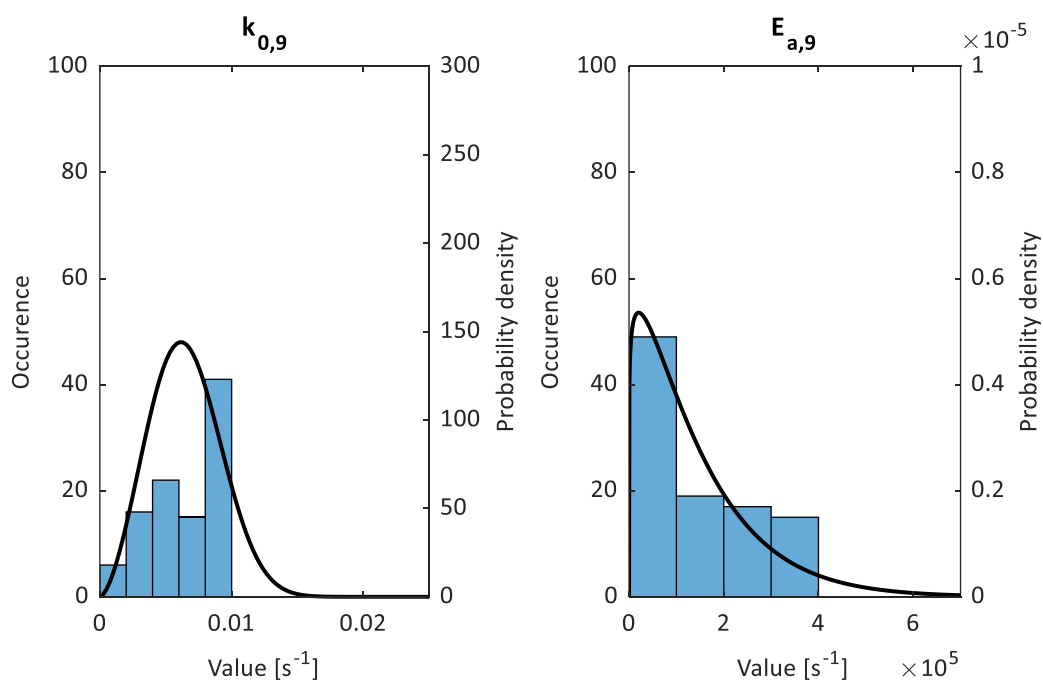


Figure S9. Identified kinetic parameters of the 9<sup>th</sup> reaction for every generated data set using bootstrapping and the fitted Weibull-distribution in case of the complete reaction network for VGO hydrocracking.

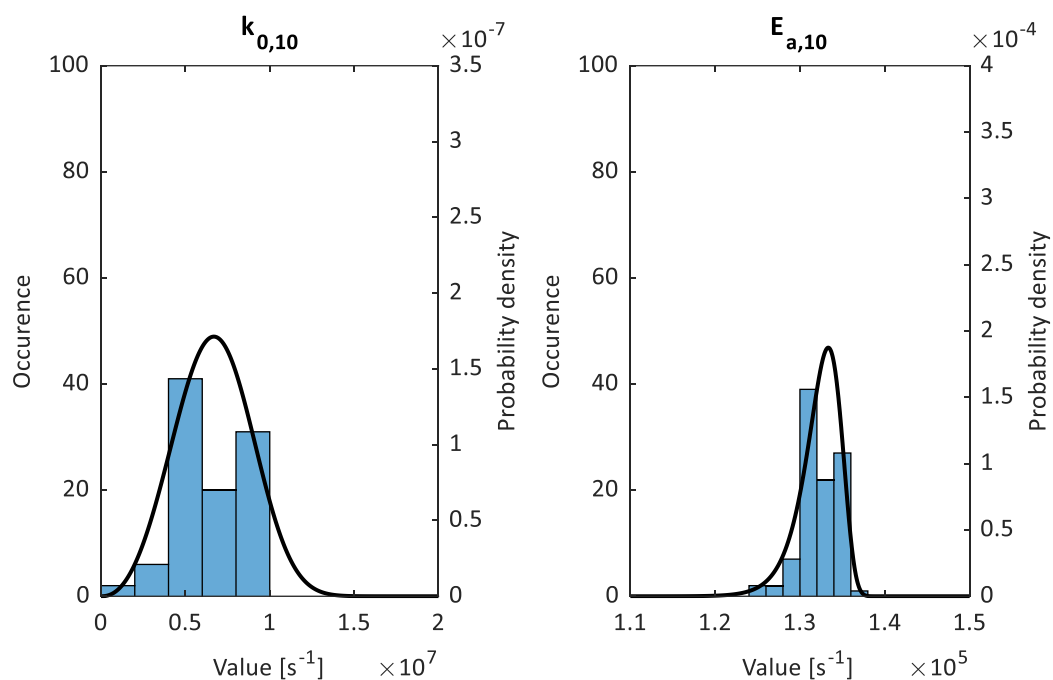


Figure S10. Identified kinetic parameters of the 10<sup>th</sup> reaction for every generated data set using bootstrapping and the fitted Weibull-distribution in case of the complete reaction network for VGO hydrocracking.

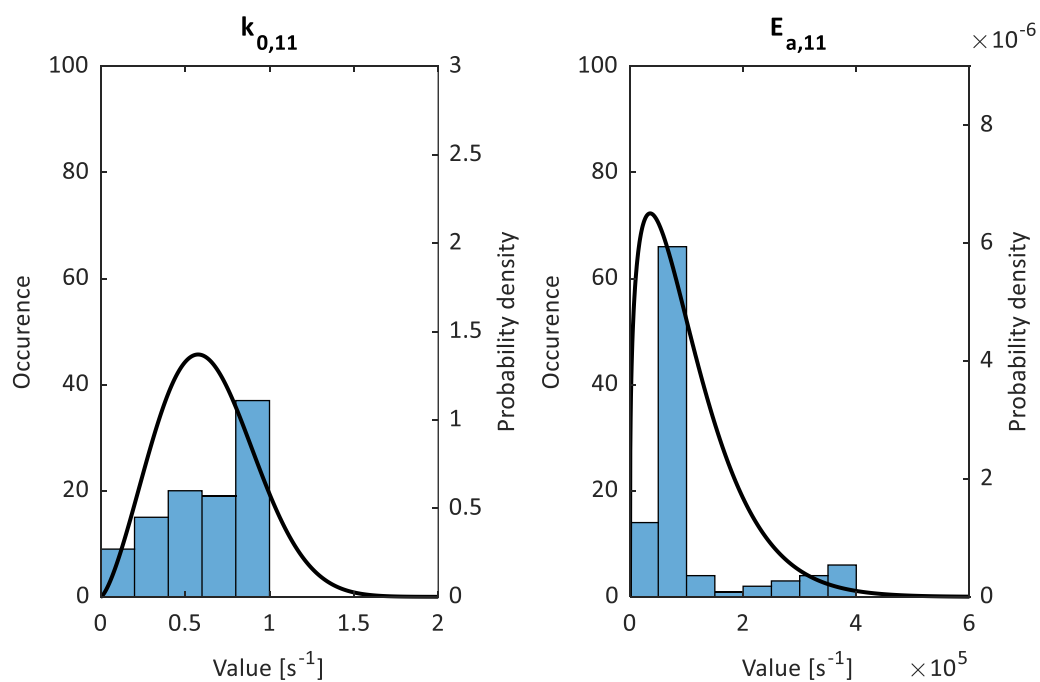


Figure S11. Identified kinetic parameters of the 11<sup>th</sup> reaction for every generated data set using bootstrapping and the fitted Weibull-distribution in case of the complete reaction network for VGO hydrocracking.

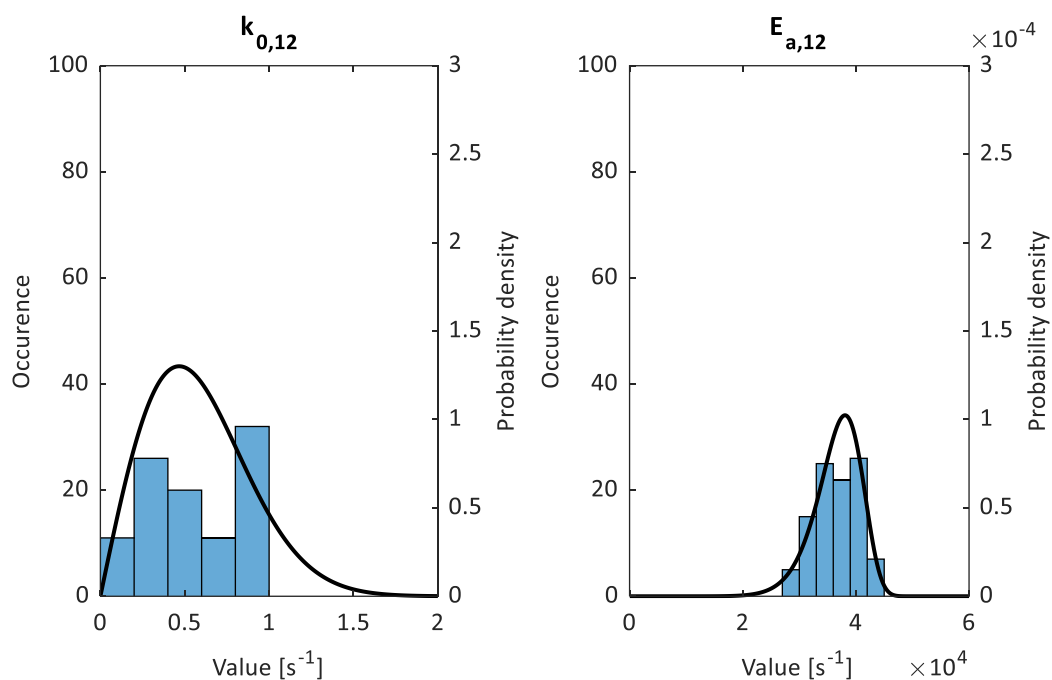


Figure S12. Identified kinetic parameters of the 12<sup>th</sup> reaction for every generated data set using bootstrapping and the fitted Weibull-distribution in case of the complete reaction network for VGO hydrocracking.

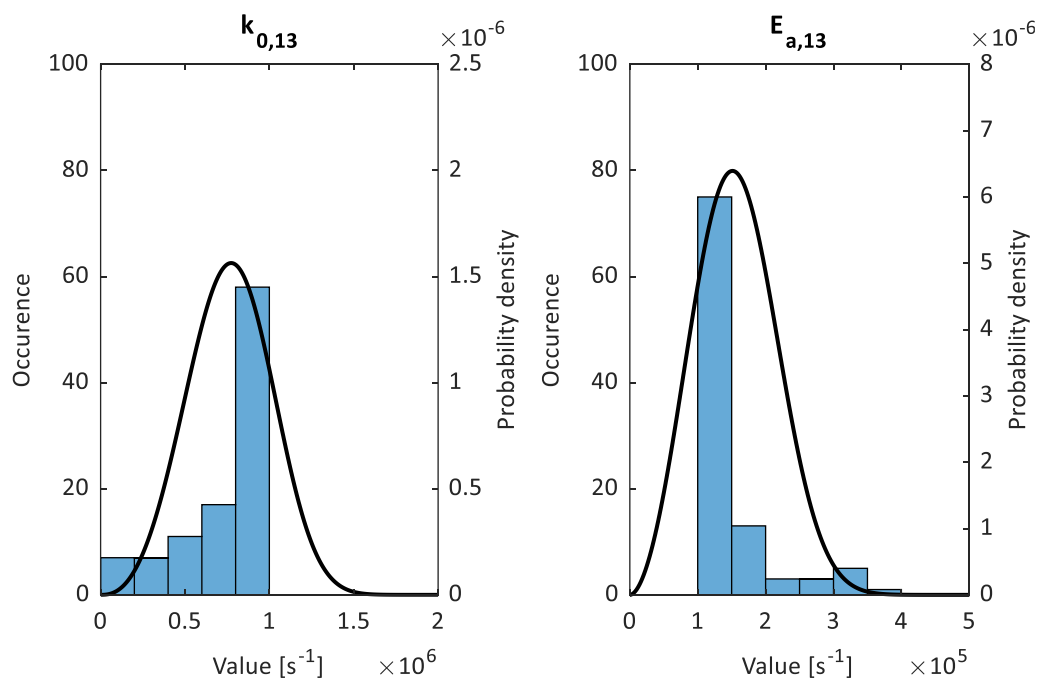


Figure S13. Identified kinetic parameters of the 13<sup>th</sup> reaction for every generated data set using bootstrapping and the fitted Weibull-distribution in case of the complete reaction network for VGO hydrocracking.

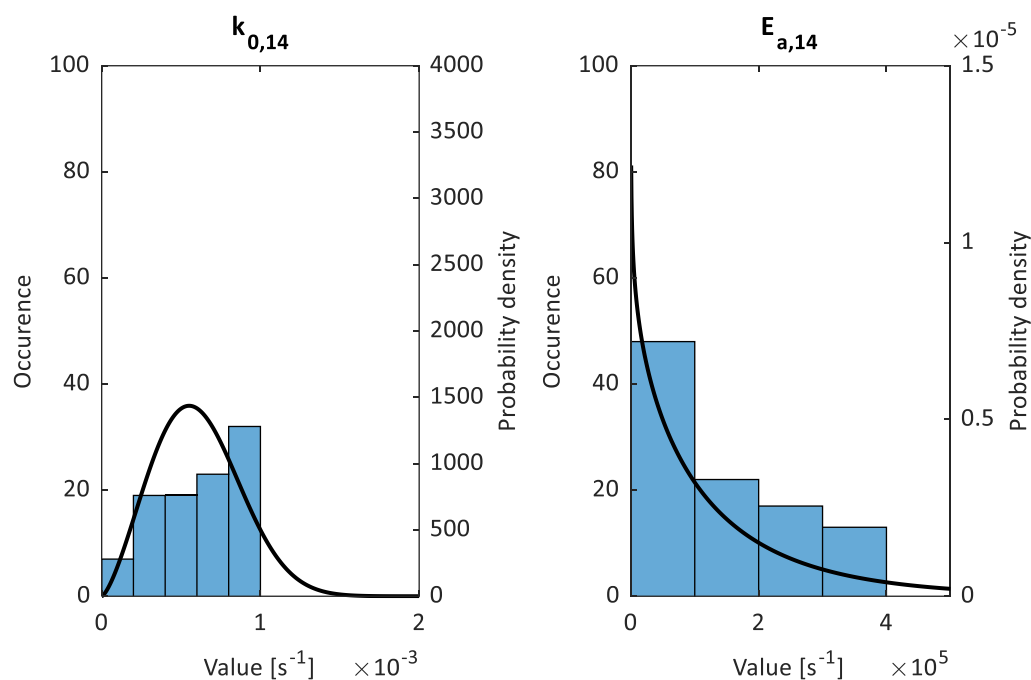


Figure S14. Identified kinetic parameters of the 14<sup>th</sup> reaction for every generated data set using bootstrapping and the fitted Weibull-distribution in case of the complete reaction network for VGO hydrocracking.

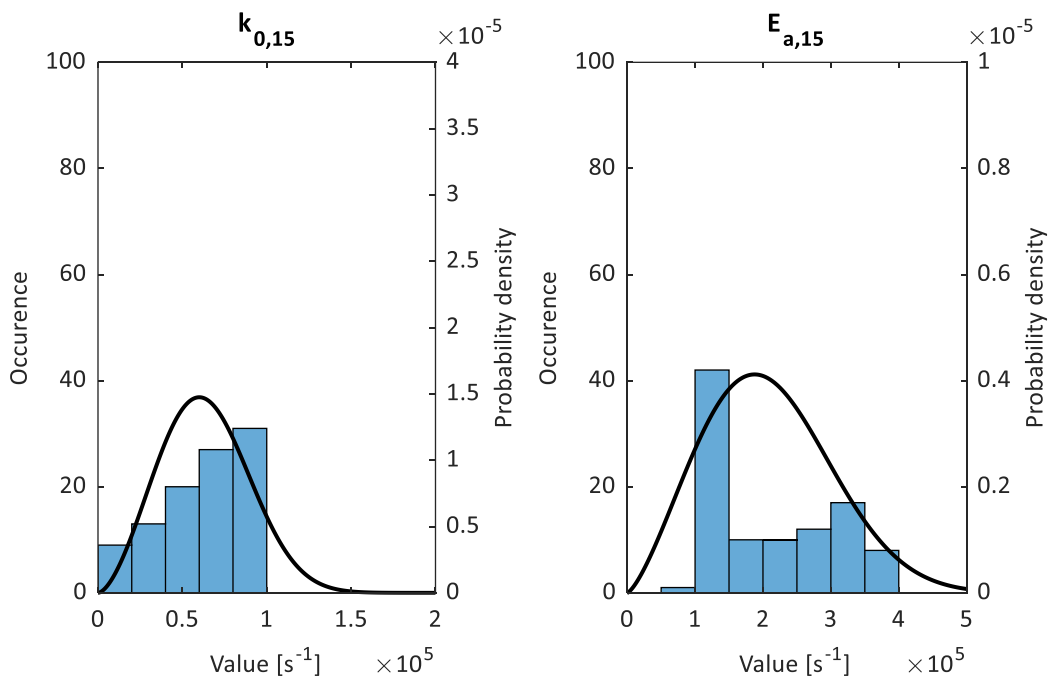


Figure S15. Identified kinetic parameters of the 15<sup>th</sup> reaction for every generated data set using bootstrapping and the fitted Weibull-distribution in case of the complete reaction network for VGO hydrocracking.



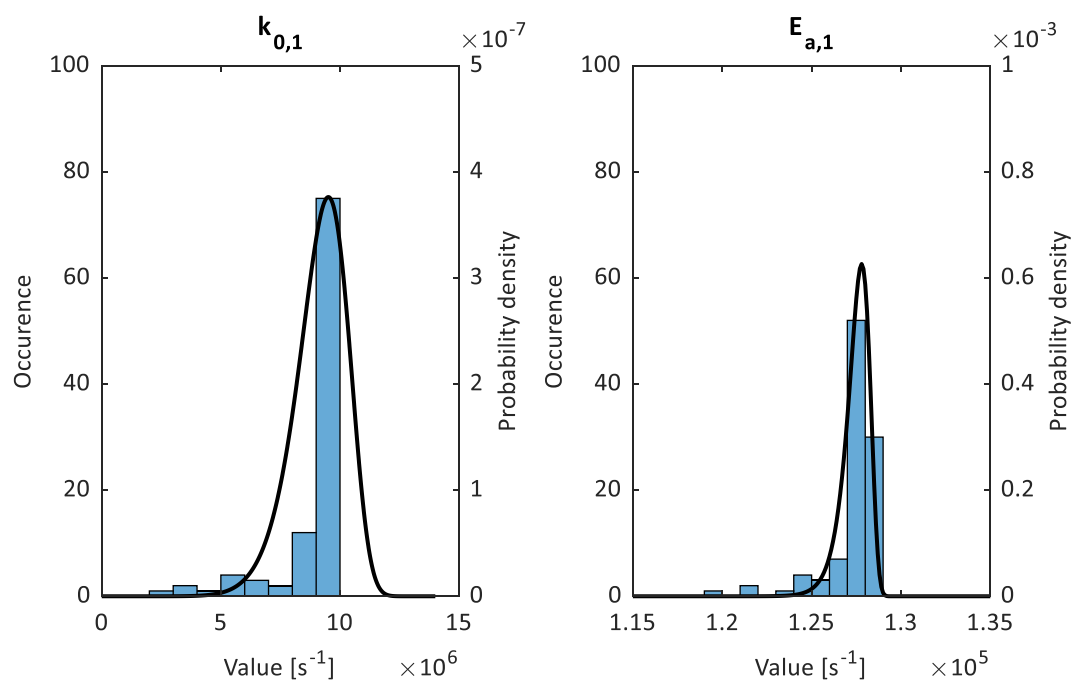


Figure S16. Identified kinetic parameters of the 1<sup>st</sup> reaction for every generated data set using bootstrapping and the fitted Weibull-distribution in case of the reduced reaction network for VGO hydrocracking.

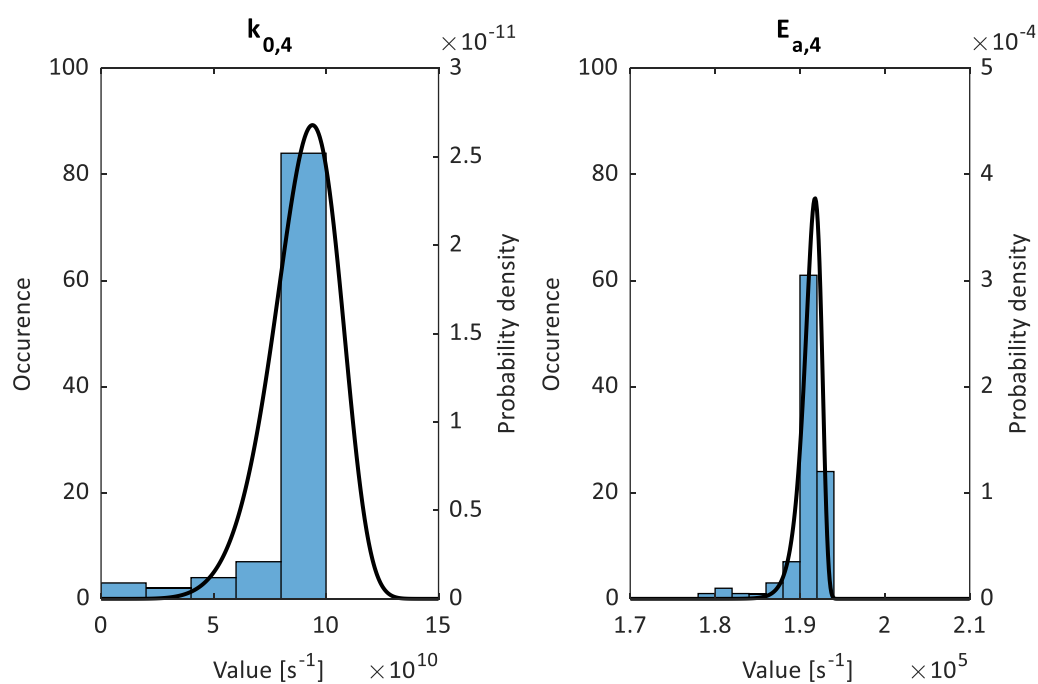


Figure S17. Identified kinetic parameters of the 4<sup>th</sup> reaction for every generated data set using bootstrapping and the fitted Weibull-distribution in case of the reduced reaction network for VGO hydrocracking.

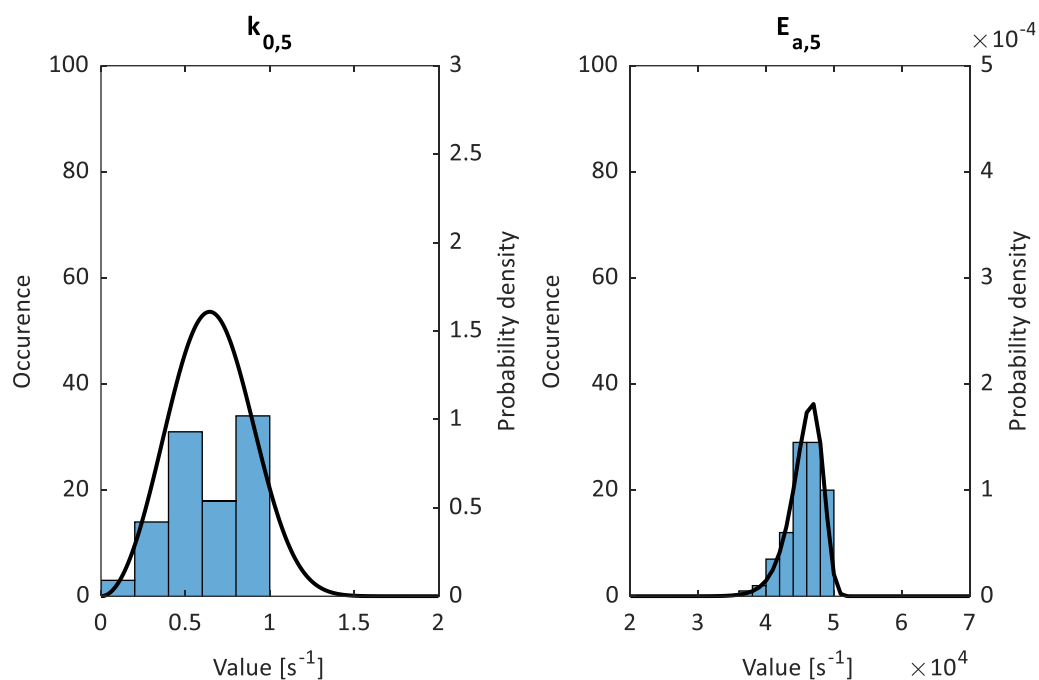


Figure S18. Identified kinetic parameters of the 5<sup>th</sup> reaction for every generated data set using bootstrapping and the fitted Weibull-distribution in case of the reduced reaction network for VGO hydrocracking.

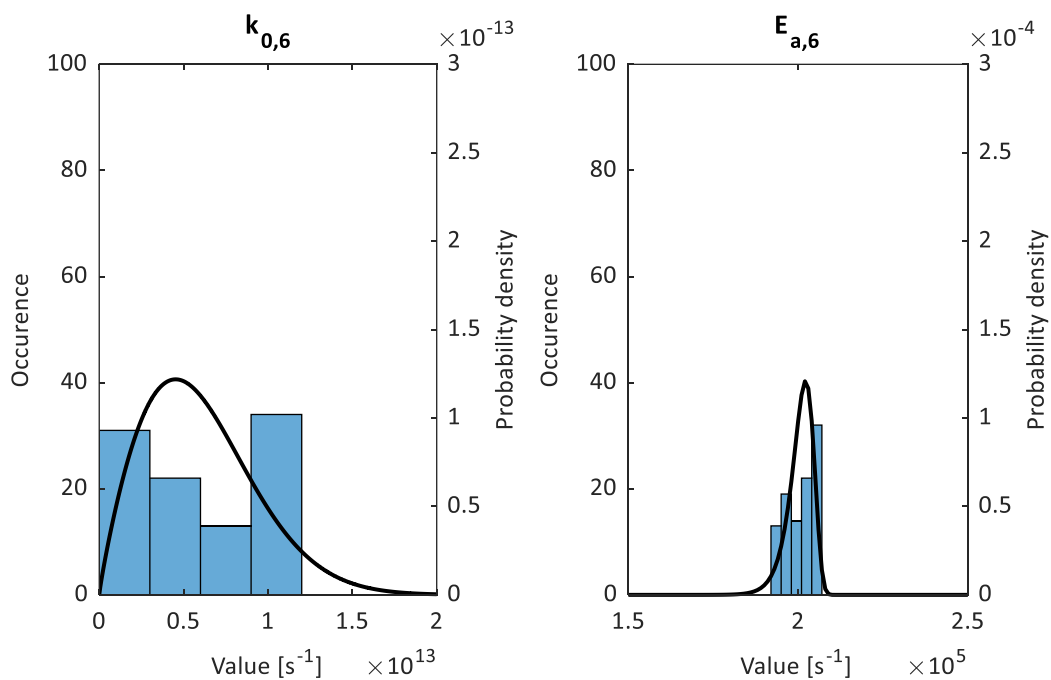


Figure S19. Identified kinetic parameters of the 6<sup>th</sup> reaction for every generated data set using bootstrapping and the fitted Weibull-distribution in case of the reduced reaction network for VGO hydrocracking.

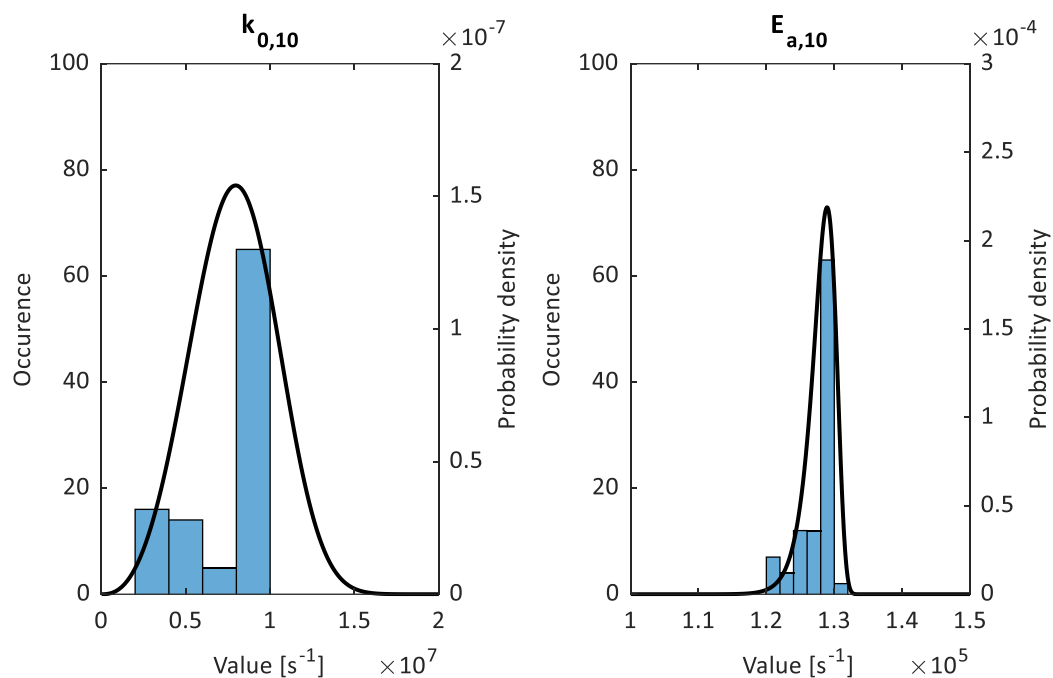


Figure S20. Identified kinetic parameters of the 10<sup>th</sup> reaction for every generated data set using bootstrapping and the fitted Weibull-distribution in case of the reduced reaction network for VGO hydrocracking.

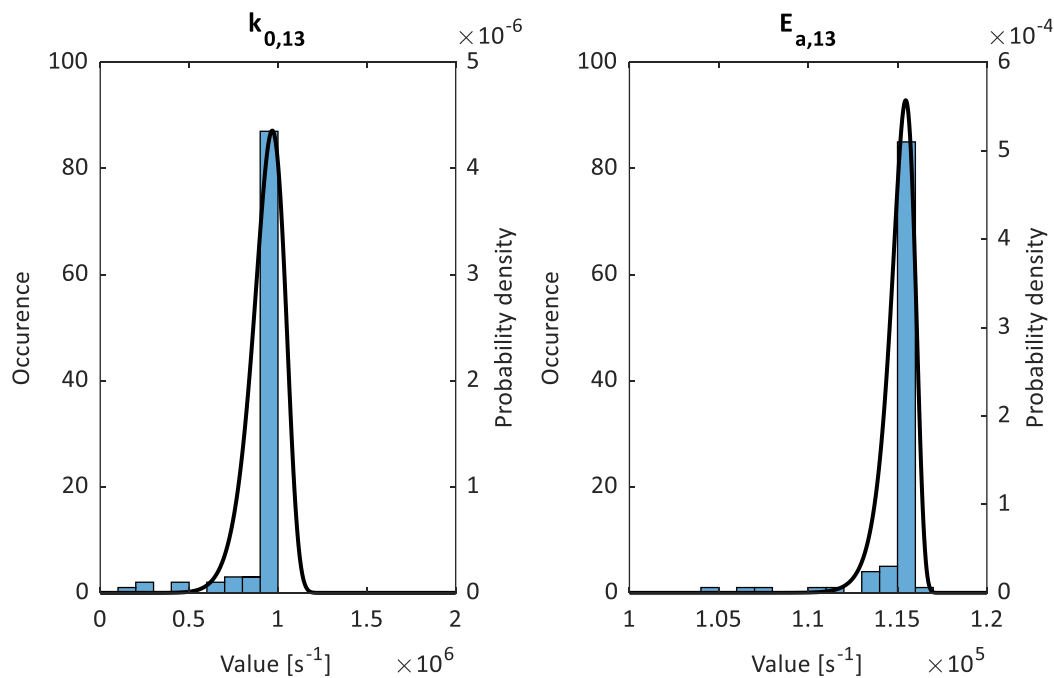


Figure S21. Identified kinetic parameters of the 13<sup>th</sup> reaction for every generated data set using bootstrapping and the fitted Weibull-distribution in case of the reduced reaction network for VGO hydrocracking.

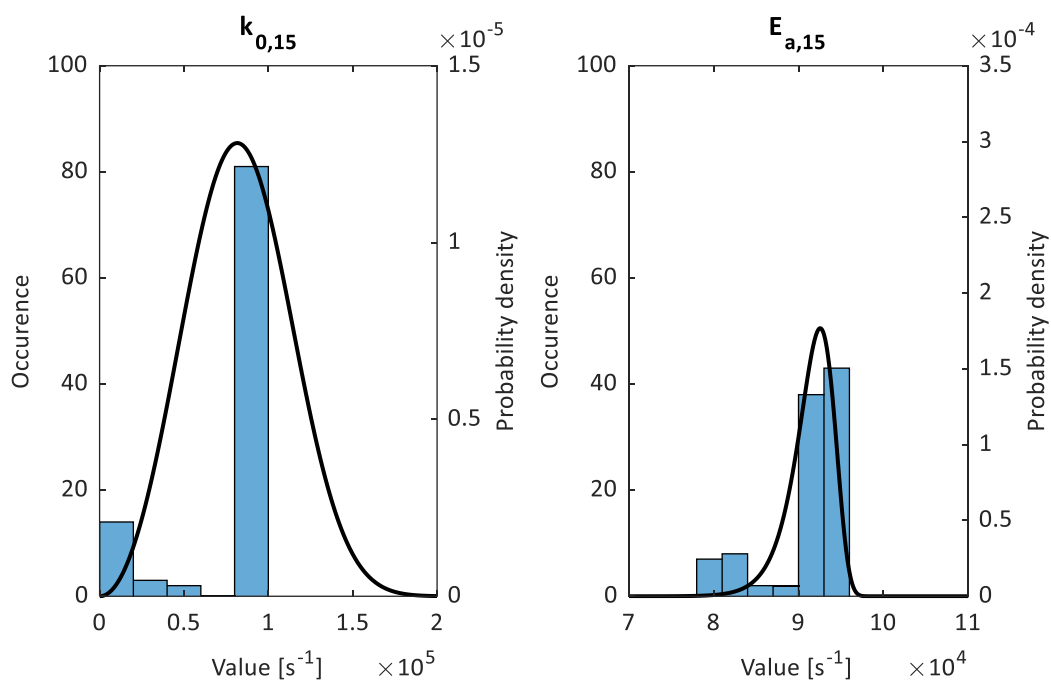


Figure S22. Identified kinetic parameters of the 15<sup>th</sup> reaction for every generated data set using bootstrapping and the fitted Weibull-distribution in case of the reduced reaction network for VGO hydrocracking.

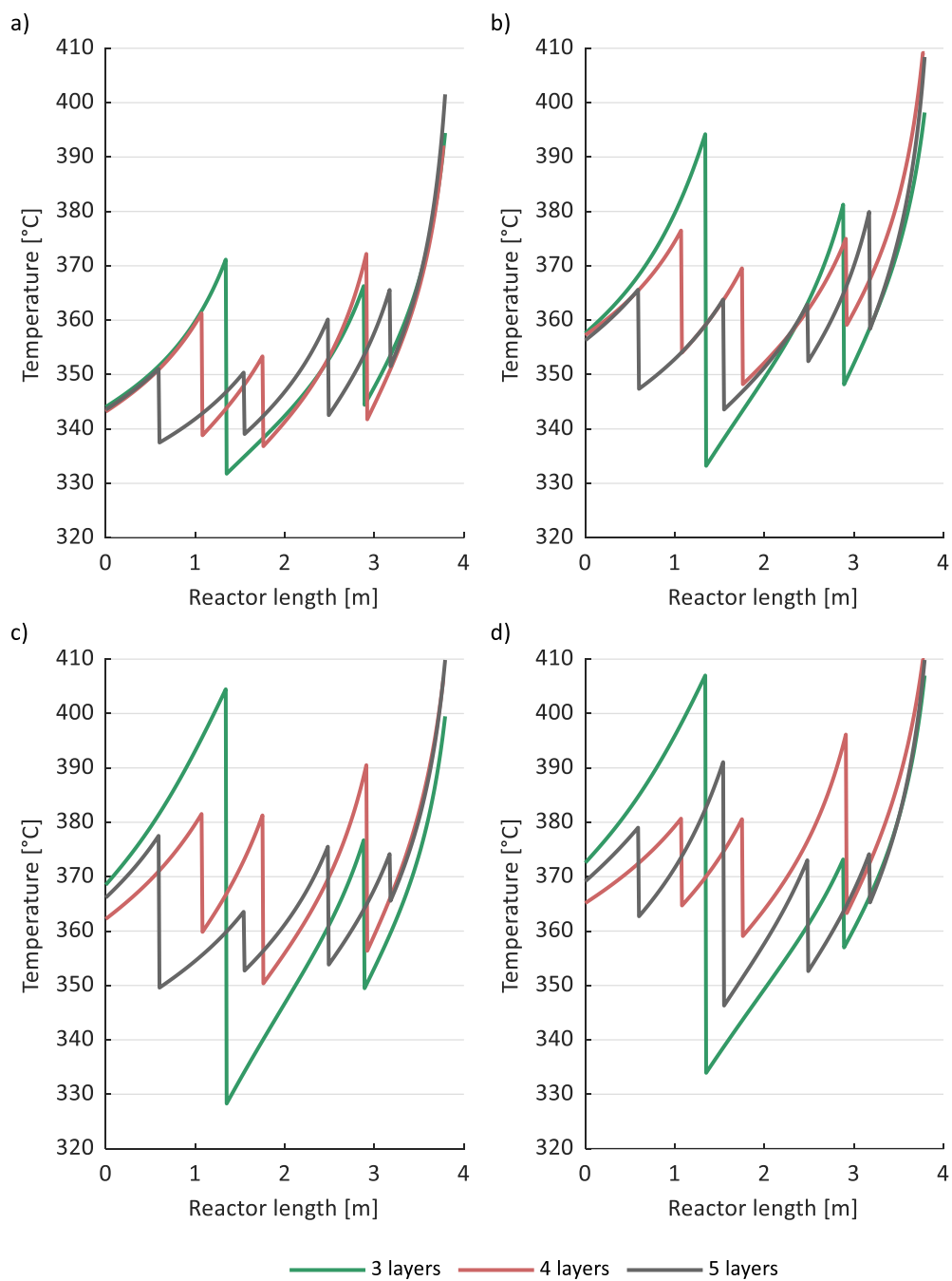


Figure S23. Temperature profiles of the hydrocracking reactor designed using a conventional method in case of different numbers of catalyst layers and different LHSV values – a)  $0.5 \text{ h}^{-1}$ , b)  $1 \text{ h}^{-1}$ , c)  $1.5 \text{ h}^{-1}$ , d)  $2 \text{ h}^{-1}$ .

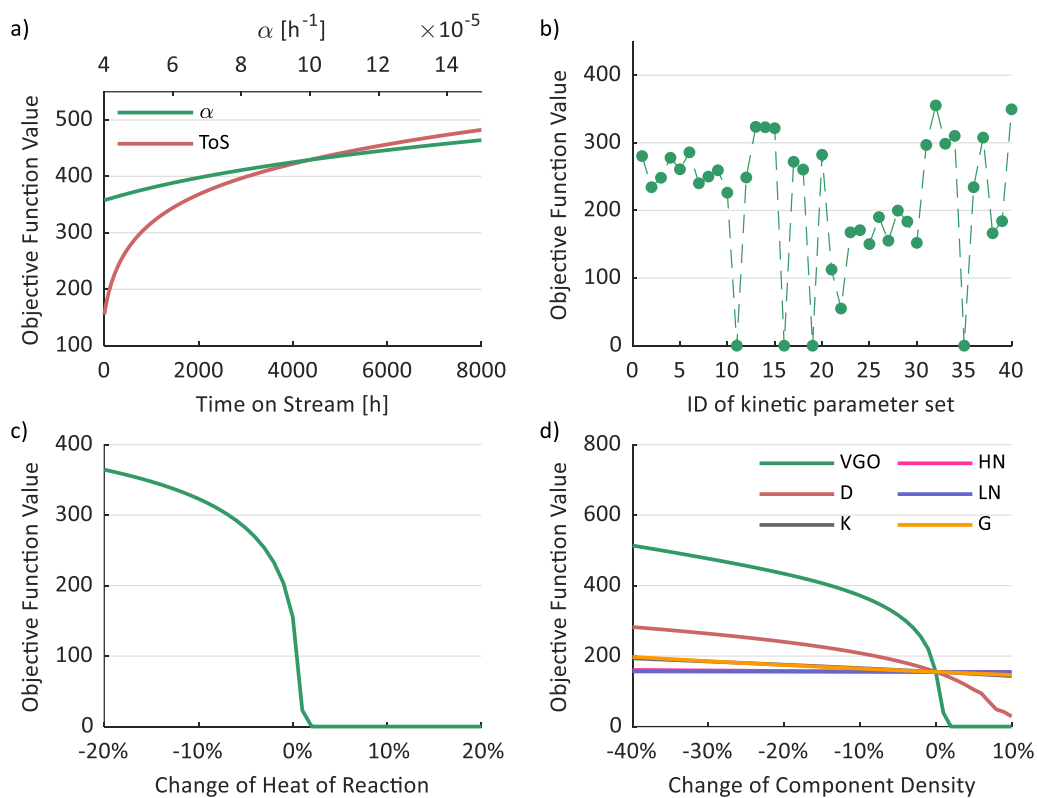


Figure S24. Local sensitivity analysis of the hydrocracking reactor with three catalyst layers to different uncertain parameters designed using the conventional method.

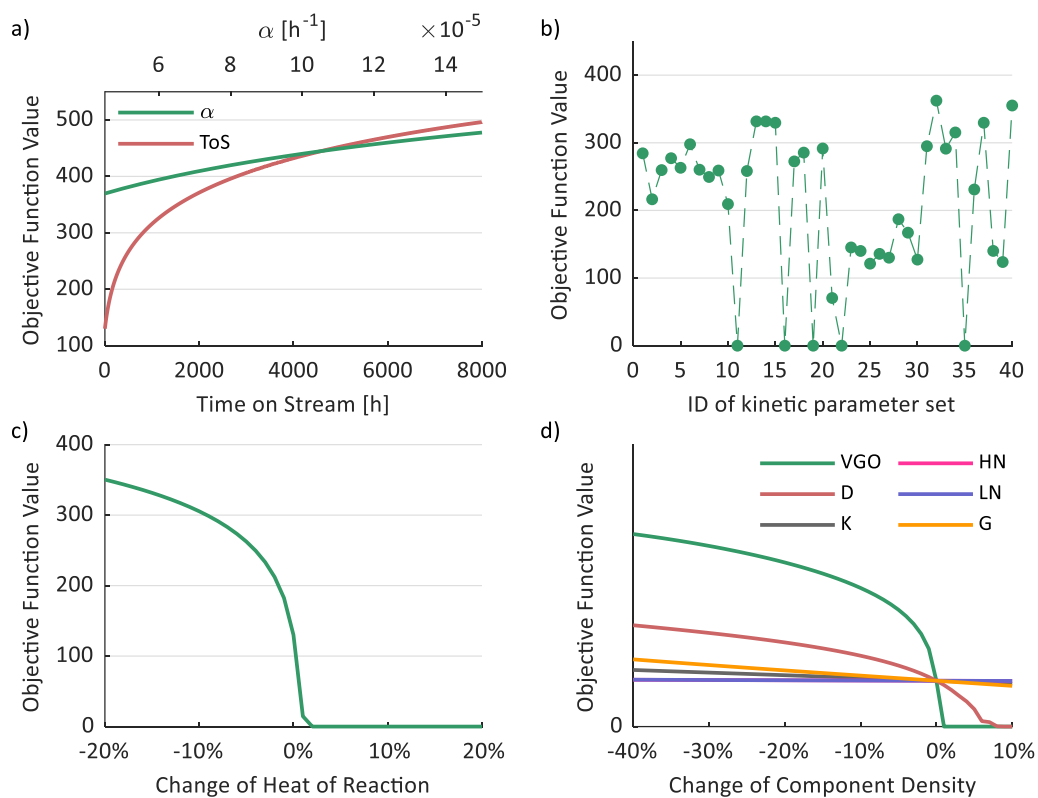


Figure S25. Local sensitivity analysis of the hydrocracking reactor with five catalyst layers to different uncertain parameters designed using the conventional method.

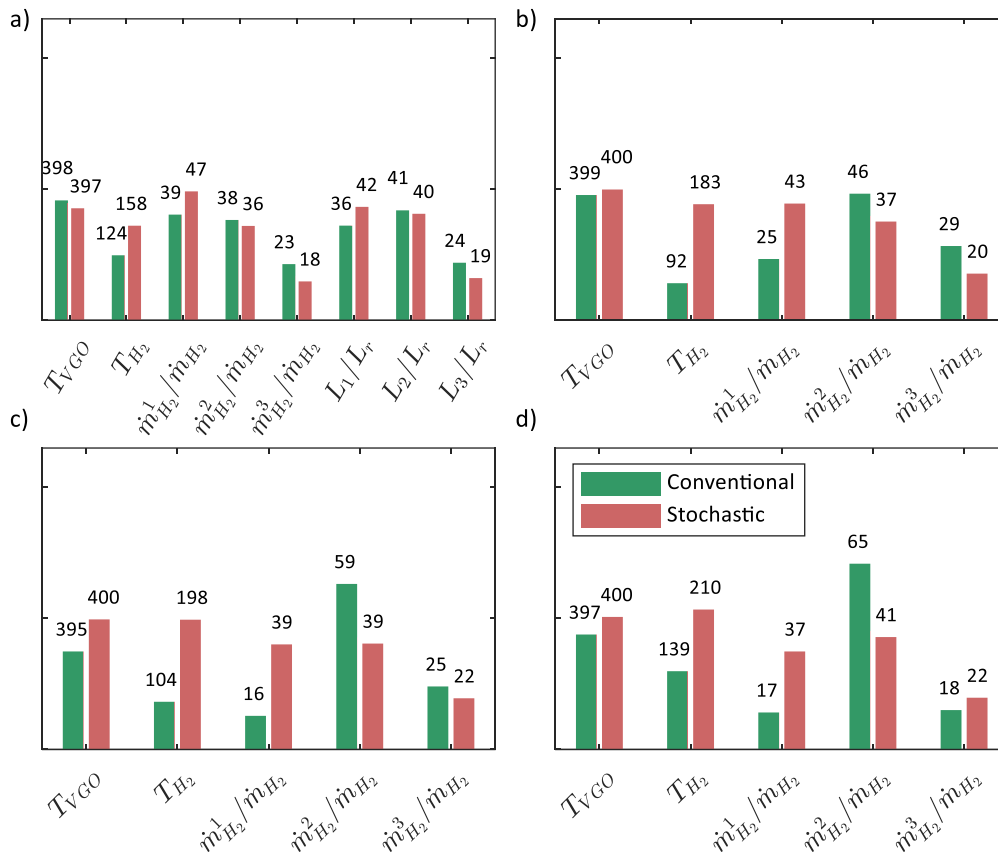


Figure S26. Nominal values of design variables of the hydrocracking reactor with three catalyst layers in case of different LHSV values – a) 0.5 h<sup>-1</sup>, b) 1 h<sup>-1</sup>, c) 1.5 h<sup>-1</sup>, d) 2 h<sup>-1</sup>.



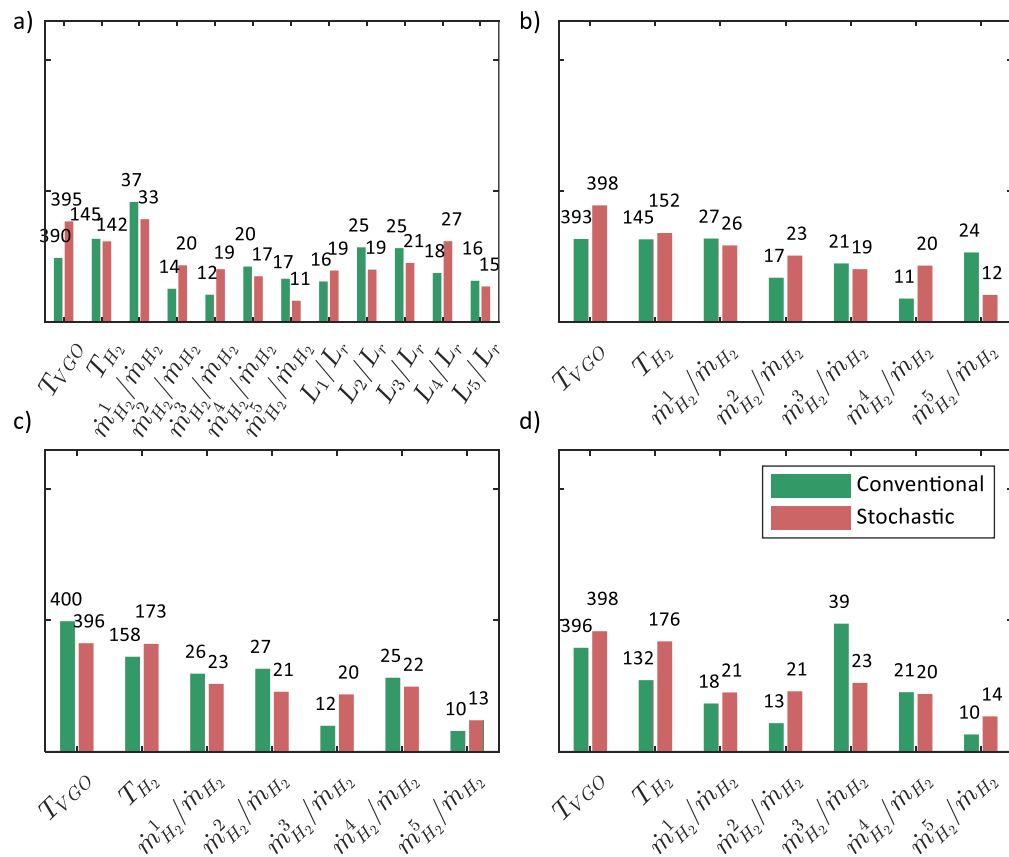


Figure S27. Nominal values of design variables of the hydrocracking reactor with five catalyst layers in case of different LHSV values – a) 0.5 h<sup>-1</sup>, b) 1 h<sup>-1</sup>, c) 1.5 h<sup>-1</sup>, d) 2 h<sup>-1</sup>.

Table S1. Identifiers of the different lumped reaction networks introduced in the thesis.

Number of reactions	Number of components				
	Plastic Waste Pyrolysis			VGO hydrocracking	
	5	6	7	6	7
5	P-N1-R5 Figure 7.2	P-N0-R5 Figure 6.2b		VGO-N0-R5 Figure 5.9	VGO-N1-R5 Figure 3.5
7				VGO-N0-R7 Figure 6.5b	
9			P-N2-R9 Figure 7.5b	VGO-N0-R9 Figure 5.6	
10		P-N0-R10 Figure 3.2 Figure 6.2a			
15				VGO-N0-R15 Figure 3.4 Figure 5.4 Figure 6.5a	

Table S2. Stoichiometric matrix of the reaction network from Figure 3.2.

	r1	r2	r3	r4	r5	r6	r7	r8	r9	r10
<b>P</b>	-1									
<b>P-</b>	1	-1	-1	-1	-1					
<b>L+</b>		1				-1	-1	-1		
<b>L-</b>			1			1			-1	-1
<b>G</b>				1			1		1	
<b>C</b>					1			1		1

Table S3. Physical properties of the components included in the plastic waste pyrolysis reactor model (Section 3.1).

Components	M [kg kmol <sup>-1</sup> ]	$\rho$ [kg m <sup>-3</sup> ]		
		a	b	c
P	200 000	0	0	937.83
P-	100 000	0	0	937.83
L+	312	0	$-9.48 \cdot 10^{-3}$	12.42
L-	157	0	$-4.63 \cdot 10^{-3}$	6.02
G	15	0	$-4 \cdot 10^{-4}$	0.54
C	12	0	0	937.83
N <sub>2</sub>	28	$2.6 \cdot 10^{-6}$	$-4.14 \cdot 10^{-3}$	2.11

Table S4. Physical properties of the components included in the VGO hydrocracking reactor model (Section 3.2 and 3.3).

Components	M [kg kmol <sup>-1</sup> ]	$\rho$ [kg m <sup>-3</sup> ]	$c_p$ [J kg <sup>-1</sup> K <sup>-1</sup> ]
VGO	732.3	942.2	3512.3
D	222.7	835.5	3465.6
K	178.1	812.3	3448.1
HN	130.5	772.7	3435.4
LN	81.69	701.1	3563.7
G	33.48	81.44	3439.6
H <sub>2</sub>	2.02	5.02	14566

Table S5. Stoichiometric matrix of the reaction network from Figure 3.5.

	<b>r1</b>	<b>r2</b>	<b>r3</b>	<b>r4</b>	<b>r5</b>
<b>VGO</b>	-1	-1			
<b>D</b>	3.3		-1		
<b>K</b>			1.3	-1	-1
<b>HN</b>				1.4	
<b>LN</b>		9			
<b>G</b>					5.3
<b>H<sub>2</sub></b>	-6.6	-17.9	-2.5	-2.7	-10.6

Table S6. HCl oxidation reactor model constants and variables (Section 3.1).

Notation	Type	Description	Unit	Value or formula
$A$	constant	reactor tube cross-section	m <sup>2</sup>	$3.52 \cdot 10^{-4}$
$a$	variable	catalyst bed activity	-	optimization variable ( $0 \leq a \leq 1$ )
$c_p$	variable	average heat capacity of gas mixture on molar basis	$\text{kJ kmol}^{-1} \text{K}^{-1}$	$c_p = \frac{\sum_{comp} p_i c_{p,i}}{p}$ Individual heat capacities are calculated as in [221]
$D_i$	constant	reactor diameter	m	0.022

Notation	Type	Description	Unit	Value or formula
$d_p$	constant	average diameter of catalyst pellet	m	0.003
$d_t$	constant	thermowell diameter	m	0.006
$\delta$	constant	change of the total molecular number	-	0.25
$E_a$	constant	activation energy	$\text{kJ mol}^{-1}$	82 100
$f$	constant	friction factor	-	1.75
$F_{HCl,0}$	constant	HCl gas inlet	$\text{kmol s}^{-1}$	$1.75 \cdot 10^{-5}$
$G$	constant	Inlet mass flow	$\text{kg m}^{-2} \text{s}^{-1}$	2.61
$\Delta_r H$	variable	enthalpy of reaction	$\text{kJ kmol}^{-1}$	$-0.996 \cdot T - 28381$ empirical correlation using data from Aspen 8.8
$\Delta_r H^\ominus$	constant	enthalpy of reaction at standard state	$\text{kJ kmol}^{-1}$	-28 560
$k_0$	constant	pre-exponential factor	$\frac{\text{kmol}}{\text{kg}_{\text{cat.}}^{-1} \text{s}^{-1}}$	85 300
$K_{Cl_2,0}$	constant	adsorption equilibrium constant of $\text{Cl}_2$	$\text{kPa}^{-0.5}$	4.79
$K_{HCl,0}$	constant	adsorption equilibrium constant of HCl	$\text{kPa}^{-1}$	3.65
$K_{O_2,0}$	constant	adsorption equilibrium constant of $\text{O}_2$ ,	$\text{kPa}^{-1}$	1.854
$M$	variable	average molar weight of gas mixture	$\text{kg kmol}^{-1}$	$M = \frac{\sum_{\text{comp}} p_i M_i}{p}$
$p$	variable	reactor pressure	kPa	solution of Eq. (3.32)
$Q_{Cl_2}$	constant	adsorption activation energy of $\text{Cl}_2$	$\text{kJ mol}^{-1}$	2 277
$Q_{HCl}$	constant	adsorption activation energy of HCl	$\text{kJ mol}^{-1}$	966

Notation	Type	Description	Unit	Value or formula
$Q_{O_2}$	constant	adsorption activation energy of $O_2$	$\text{kJ mol}^{-1}$	238
$r_{HCl}$	variable	reaction rate of HCl oxidation	$\frac{\text{kmol}}{\text{kg}_{\text{cat.}}^{-1} \text{ s}^{-1}}$	solution of Eq. (3.29)
$R$	constant	gas constant	$\frac{\text{kJ kmol}^{-1}}{\text{K}^{-1}}$	8.314
$T$	variable	reactor temperature	K	solution of Eq. (3.31)
$T_0$	variable	shell temperature	K	optimization variable
$u$	constant	gas velocity	$\text{m s}^{-1}$	1.71
$x_{HCl}$	variable	molar HCl conversion	-	solution of Eq. (3.24)
$z$	variable	reactor axial coordinate	m	independent variable
$\varepsilon$	constant	catalyst bed void fraction	-	0.35
$\eta$	variable	internal effectiveness factor of the shaped catalyst	-	$\eta \approx 3.54$
$\kappa$	constant	overall heat transfer coefficient	$\frac{\text{kW m}^{-2} \text{K}^{-1}}{1}$	0.15
$\rho_B$	constant	density of catalyst bed	$\text{kg m}^{-3}$	780
$\rho_g$	constant	gas density	$\text{kg m}^{-3}$	1.53

Table S7. Physical properties of the components included in the ethane pyrolysis reactor model.

Components	M [kg kmol <sup>-1</sup> ]	$\rho$ [kg m <sup>-3</sup> ]		
		a	b	c
H•	1.01	$1.95 \cdot 10^{-8}$	$-5.74 \cdot 10^{-5}$	0.050
H <sub>2</sub>	2.02	$3.91 \cdot 10^{-8}$	$-1.15 \cdot 10^{-4}$	0.099
CH <sub>3</sub> •	15.03	$2.92 \cdot 10^{-7}$	$-8.57 \cdot 10^{-4}$	0.741
CH <sub>4</sub>	16.04	$3.11 \cdot 10^{-7}$	$-9.14 \cdot 10^{-4}$	0.790
C <sub>2</sub> H <sub>2</sub>	26.04	$5.05 \cdot 10^{-7}$	$-1.48 \cdot 10^{-3}$	1.283
C <sub>2</sub> H <sub>3</sub> •	27.05	$5.25 \cdot 10^{-7}$	$-1.54 \cdot 10^{-3}$	1.332
C <sub>2</sub> H <sub>4</sub>	28.05	$5.44 \cdot 10^{-7}$	$-1.60 \cdot 10^{-3}$	1.382
•C <sub>2</sub> H <sub>4</sub> •	28.05	$5.44 \cdot 10^{-7}$	$-1.60 \cdot 10^{-3}$	1.382
C <sub>2</sub> H <sub>5</sub> •	29.06	$5.64 \cdot 10^{-7}$	$-1.66 \cdot 10^{-3}$	1.432
C <sub>2</sub> H <sub>6</sub>	30.07	$5.83 \cdot 10^{-7}$	$-1.71 \cdot 10^{-3}$	1.481
C <sub>3</sub> H <sub>6</sub>	42.08	$8.16 \cdot 10^{-7}$	$-2.40 \cdot 10^{-3}$	2.073
C <sub>3</sub> H <sub>7</sub> •	43.09	$8.36 \cdot 10^{-7}$	$-2.46 \cdot 10^{-3}$	2.122

Table S8. Identified pre-exponential factors and activation energies for plastic waste pyrolysis (Chapter 4).

	Thermal pyrolysis	Catalytic pyrolysis			
		HZSM-5	NiZSM-5	CuZSM-5	FeZSM-5
$k_{0,1}$	$2.86 \cdot 10^6$	$7.20 \cdot 10^5$	$7.33 \cdot 10^5$	$9.52 \cdot 10^5$	$5.71 \cdot 10^5$
$k_{0,2}$	$4.10 \cdot 10^8$	$3.43 \cdot 10^2$	$1.24 \cdot 10^6$	$9.36 \cdot 10^2$	$1.02 \cdot 10^6$
$k_{0,3}$	$8.93 \cdot 10^5$	$7.67 \cdot 10^2$	$2.17 \cdot 10^5$	$1.35 \cdot 10^1$	$1.47 \cdot 10^6$
$k_{0,4}$	$1.45 \cdot 10^{-3}$	$7.16 \cdot 10^2$	$2.16 \cdot 10^5$	$1.14 \cdot 10^4$	$3.14 \cdot 10^4$
$k_{0,5}$	3.97	$1.13 \cdot 10^1$	$1.60 \cdot 10^4$	5.37	$2.28 \cdot 10^3$
$k_{0,6}$	$9.49 \cdot 10^{-3}$	$5.17 \cdot 10^{22}$	$1.00 \cdot 10^{21}$	$6.41 \cdot 10^{21}$	$6.89 \cdot 10^4$
$k_{0,7}$	$8.10 \cdot 10^{-1}$	$1.05 \cdot 10^{22}$	$4.47 \cdot 10^{21}$	$7.16 \cdot 10^{21}$	$1.22 \cdot 10^{18}$
$k_{0,8}$	$4.17 \cdot 10^{-3}$	$3.06 \cdot 10^{22}$	$9.22 \cdot 10^{21}$	$2.38 \cdot 10^{22}$	$4.88 \cdot 10^{22}$
$k_{0,9}$	$9.51 \cdot 10^{21}$	$1.35 \cdot 10^{22}$	$1.02 \cdot 10^{17}$	$9.04 \cdot 10^{21}$	$1.34 \cdot 10^{15}$
$k_{0,10}$	$2.31 \cdot 10^{-2}$	$1.42 \cdot 10^{21}$	$1.00 \cdot 10^{21}$	$5.49 \cdot 10^6$	$1.45 \cdot 10^{16}$
$E_{a,1}$	$1.23 \cdot 10^5$	$9.69 \cdot 10^4$	$9.83 \cdot 10^4$	$9.98 \cdot 10^4$	$9.57 \cdot 10^4$
$E_{a,2}$	$1.56 \cdot 10^5$	$4.85 \cdot 10^4$	$9.89 \cdot 10^4$	$5.69 \cdot 10^4$	$9.97 \cdot 10^4$
$E_{a,3}$	$1.22 \cdot 10^5$	$5.61 \cdot 10^4$	$9.12 \cdot 10^4$	$3.31 \cdot 10^4$	$1.05 \cdot 10^5$
$E_{a,4}$	$7.27 \cdot 10^3$	$5.64 \cdot 10^4$	$9.11 \cdot 10^4$	$7.20 \cdot 10^4$	$8.21 \cdot 10^4$
$E_{a,5}$	$4.99 \cdot 10^5$	$4.10 \cdot 10^4$	$8.64 \cdot 10^4$	$3.71 \cdot 10^4$	$7.56 \cdot 10^4$
$E_{a,6}$	$3.72 \cdot 10^2$	$3.18 \cdot 10^5$	$5.84 \cdot 10^5$	$7.30 \cdot 10^5$	$6.18 \cdot 10^4$
$E_{a,7}$	$1.82 \cdot 10^4$	$3.05 \cdot 10^5$	$2.97 \cdot 10^5$	$4.01 \cdot 10^5$	$2.56 \cdot 10^5$
$E_{a,8}$	$2.35 \cdot 10^1$	$5.32 \cdot 10^5$	$3.09 \cdot 10^5$	$3.16 \cdot 10^5$	$7.31 \cdot 10^5$
$E_{a,9}$	$5.90 \cdot 10^5$	$5.61 \cdot 10^5$	$9.97 \cdot 10^5$	$9.14 \cdot 10^5$	$7.15 \cdot 10^5$
$E_{a,10}$	8.46	$4.04 \cdot 10^6$	$5.62 \cdot 10^5$	$2.86 \cdot 10^5$	$5.41 \cdot 10^5$



Table S9. Measured mass concentration values for VGO hydrocracking [218].

T [°C]	LHSV [h <sup>-1</sup> ]	Product composition [% (m/m)]					
		VGO	D	K	HN	LN	G
380	0.5	35%	37%	13.5%	2%	1.0%	12%
	1	46%	25.5%	7.5%	1%	0.6%	9.5%
	1.5	57%	28%	6.0%	1.5%	0.4%	7.0%
	2	66%	22.5%	2%	0.6%	0.1%	5%
400	0.5	25%	26%	24.5%	7.2%	2.4%	14.5%
	1	38%	25%	19.5%	5.4%	1.9%	11.0%
	1.5	48%	23%	14%	4%	1.5%	8.5%
	2	61%	25%	10.5%	2.5%	0.5%	6%
410	0.5	8%	22%	25.5%	14.5%	3.1%	26.5%
	1	29%	21%	20%	9%	2.2%	19.5%
	1.5	41%	18%	17.5%	6.5%	1.9%	14%
	2	50%	20%	14.5%	6%	1.6%	7.5%
420	0.5	0%	11%	29.5%	21.5%	3.8%	34%
	1	14%	20%	28.5%	12.5%	2.6%	28%
	1.5	21%	23%	26.5%	9.5%	2.5%	17.5%
	2	24%	31%	24.5%	8%	2.3%	9.5%

Table S10. Pre-exponential factors for reactions in reaction networks identified with Method 1 from Section 5.1.

R.	Pre-exponential factor [ $\text{m}^3 \text{h}^{-1} \text{m}_{\text{cat}}^3$ ]														
	F→D	F→K	F→HN	F→LN	F→G	D→K	D→HN	D→LN	D→G	K→HN	K→LN	K→G	HN→LN	HN→G	LN→G
1		$3.60 \cdot 10^{16}$													
2		$3.60 \cdot 10^{16}$		$2.21 \cdot 10^{14}$											
3		$3.60 \cdot 10^{16}$		$1.28 \cdot 10^{14}$						$2.74 \cdot 10^{10}$					
4		$3.60 \cdot 10^{16}$		$2.08 \cdot 10^{14}$		$4.66 \cdot 10^{15}$				$3.52 \cdot 10^{10}$					
5	$2.88 \cdot 10^{10}$	$6.27 \cdot 10^{16}$		$3.56 \cdot 10^{14}$		$4.29 \cdot 10^{15}$				$2.12 \cdot 10^{10}$					
6	$3.60 \cdot 10^9$	$2.83 \cdot 10^{17}$		$3.45 \cdot 10^{14}$		$3.62 \cdot 10^{16}$				$2.64 \cdot 10^{10}$					$4.08 \cdot 10^7$
7	$2.52 \cdot 10^{10}$	$2.31 \cdot 10^{17}$		$3.52 \cdot 10^{14}$	$3.60 \cdot 10^3$	$3.13 \cdot 10^{16}$				$2.61 \cdot 10^{10}$					$2.07 \cdot 10^8$
8	$3.60 \cdot 10^9$	$1.79 \cdot 10^{17}$	$3.60 \cdot 10^3$	$3.58 \cdot 10^{14}$	$3.60 \cdot 10^3$	$1.92 \cdot 10^{16}$				$3.58 \cdot 10^{10}$					$3.43 \cdot 10^8$
9	$2.43 \cdot 10^{10}$	$3.25 \cdot 10^{17}$	$3.60 \cdot 10^3$	$3.59 \cdot 10^{14}$	$1.97 \cdot 10^3$	$3.50 \cdot 10^{16}$				$1.92 \cdot 10^{10}$		$3.39 \cdot 10^3$			$3.55 \cdot 10^8$
10	$1.63 \cdot 10^{10}$	$3.48 \cdot 10^{17}$	$1.65 \cdot 10^3$	$2.98 \cdot 10^{14}$	$3.60 \cdot 10^3$	$3.09 \cdot 10^{16}$				$3.60 \cdot 10^{10}$	$3.58 \cdot 10^3$	$2.75 \cdot 10^3$			$3.57 \cdot 10^8$
11	$3.60 \cdot 10^9$	$1.44 \cdot 10^{17}$	$1.71 \cdot 10^3$	$3.57 \cdot 10^{14}$	$3.60 \cdot 10^3$	$3.19 \cdot 10^{16}$	126.1			$3.60 \cdot 10^{10}$	$2.91 \cdot 10^3$	$3.60 \cdot 10^3$			$2.76 \cdot 10^8$
12	$3.60 \cdot 10^9$	$3.54 \cdot 10^{17}$	$3.00 \cdot 10^3$	$3.46 \cdot 10^{14}$	$3.60 \cdot 10^3$	$8.79 \cdot 10^{15}$	360.0		29.6	$3.57 \cdot 10^{10}$	$2.39 \cdot 10^3$	$1.23 \cdot 10^3$			$3.48 \cdot 10^8$
13	$3.60 \cdot 10^9$	$3.60 \cdot 10^{17}$	$3.14 \cdot 10^3$	$3.59 \cdot 10^{14}$	$3.32 \cdot 10^3$	$9.27 \cdot 10^{15}$	326.8		19.5	$3.33 \cdot 10^{10}$	$3.53 \cdot 10^3$	$1.50 \cdot 10^3$	$6.77 \cdot 10^8$		$1.97 \cdot 10^8$
14	$3.60 \cdot 10^9$	$3.42 \cdot 10^{17}$	$3.60 \cdot 10^3$	$3.48 \cdot 10^{14}$	$3.44 \cdot 10^3$	$3.33 \cdot 10^{16}$	38.7	33.24	3.6	$3.59 \cdot 10^{10}$	$3.60 \cdot 10^3$	$2.41 \cdot 10^3$	$4.49 \cdot 10^8$		$3.60 \cdot 10^8$
15	$7.27 \cdot 10^9$	$2.53 \cdot 10^{17}$	$2.61 \cdot 10^3$	$1.90 \cdot 10^{14}$	$3.60 \cdot 10^3$	$3.32 \cdot 10^{16}$	360.0	34.17	31.5	$3.47 \cdot 10^{10}$	$3.56 \cdot 10^3$	$3.11 \cdot 10^3$	$3.18 \cdot 10^9$	0.71	$1.19 \cdot 10^8$

R.: Number of reactions present in the subnetwork

Table S11. Activation energies for reactions in reaction networks identified with Method 1 from Section 5.1.

R.	Activation energy [J mol <sup>-1</sup> ]														
	F→D	F→K	F→HN	F→LN	F→G	D→K	D→HN	D→LN	D→G	K→HN	K→LN	K→G	HN→LN	HN→G	LN→G
1		2.14·10 <sup>5</sup>													
2		2.14·10 <sup>5</sup>		2.00·10 <sup>5</sup>											
3		2.12·10 <sup>5</sup>		1.96·10 <sup>5</sup>						1.33·10 <sup>5</sup>					
4		2.12·10 <sup>5</sup>		1.98·10 <sup>5</sup>		2.07·10 <sup>5</sup>				1.34·10 <sup>5</sup>					
5	1.31·10 <sup>5</sup>	2.13·10 <sup>5</sup>		1.99·10 <sup>5</sup>		3.99·10 <sup>5</sup>				1.31·10 <sup>5</sup>					
6	1.17·10 <sup>5</sup>	2.26·10 <sup>5</sup>		1.86·10 <sup>5</sup>		1.96·10 <sup>5</sup>				1.31·10 <sup>5</sup>					7.77·10 <sup>4</sup>
7	1.28·10 <sup>5</sup>	2.24·10 <sup>5</sup>		1.99·10 <sup>5</sup>	4.40·10 <sup>4</sup>	2.10·10 <sup>5</sup>				1.32·10 <sup>5</sup>					3.85·10 <sup>5</sup>
8	1.17·10 <sup>5</sup>	2.23·10 <sup>5</sup>	5.42·10 <sup>4</sup>	1.99·10 <sup>5</sup>	4.40·10 <sup>4</sup>	2.07·10 <sup>5</sup>				1.35·10 <sup>5</sup>					1.21·10 <sup>5</sup>
9	1.27·10 <sup>5</sup>	2.26·10 <sup>5</sup>	5.42·10 <sup>4</sup>	1.99·10 <sup>5</sup>	4.49·10 <sup>4</sup>	2.07·10 <sup>5</sup>				1.31·10 <sup>5</sup>		4.00·10 <sup>4</sup>			3.98·10 <sup>5</sup>
10	1.25·10 <sup>5</sup>	2.26·10 <sup>5</sup>	4.98·10 <sup>4</sup>	1.98·10 <sup>5</sup>	4.81·10 <sup>4</sup>	2.07·10 <sup>5</sup>				1.35·10 <sup>5</sup>	3.96·10 <sup>5</sup>	3.89·10 <sup>4</sup>			3.77·10 <sup>5</sup>
11	1.16·10 <sup>5</sup>	2.21·10 <sup>5</sup>	4.99·10 <sup>4</sup>	2.00·10 <sup>5</sup>	4.79·10 <sup>4</sup>	2.07·10 <sup>5</sup>	3.18·10 <sup>5</sup>			1.35·10 <sup>5</sup>	5.13·10 <sup>4</sup>	4.11·10 <sup>4</sup>			1.06·10 <sup>5</sup>
12	1.16·10 <sup>5</sup>	2.26·10 <sup>5</sup>	5.30·10 <sup>4</sup>	1.99·10 <sup>5</sup>	4.81·10 <sup>4</sup>	2.00·10 <sup>5</sup>	2.96·10 <sup>5</sup>		2.69·10 <sup>5</sup>	1.35·10 <sup>5</sup>	5.86·10 <sup>4</sup>	3.43·10 <sup>4</sup>			3.40·10 <sup>5</sup>
13	1.16·10 <sup>5</sup>	2.26·10 <sup>5</sup>	5.33·10 <sup>4</sup>	1.99·10 <sup>5</sup>	4.77·10 <sup>4</sup>	2.00·10 <sup>5</sup>	3.95·10 <sup>5</sup>		2.70·10 <sup>5</sup>	1.35·10 <sup>5</sup>	3.75·10 <sup>5</sup>	3.54·10 <sup>4</sup>	3.94·10 <sup>5</sup>		3.53·10 <sup>5</sup>
14	1.16·10 <sup>5</sup>	2.26·10 <sup>5</sup>	5.40·10 <sup>4</sup>	1.99·10 <sup>5</sup>	4.78·10 <sup>4</sup>	2.07·10 <sup>5</sup>	2.67·10 <sup>5</sup>	3.93·10 <sup>5</sup>	3.97·10 <sup>5</sup>	1.35·10 <sup>5</sup>	6.11·10 <sup>4</sup>	3.82·10 <sup>4</sup>	3.61·10 <sup>5</sup>		4.00·10 <sup>5</sup>
15	1.20·10 <sup>5</sup>	2.24·10 <sup>5</sup>	2.96·10 <sup>5</sup>	1.89·10 <sup>5</sup>	4.83·10 <sup>4</sup>	2.08·10 <sup>5</sup>	4.02·10 <sup>4</sup>	3.53·10 <sup>4</sup>	3.65·10 <sup>5</sup>	1.30·10 <sup>5</sup>	4.00·10 <sup>5</sup>	3.05·10 <sup>5</sup>	1.15·10 <sup>5</sup>	4.00·10 <sup>5</sup>	8.69·10 <sup>4</sup>

R.: Number of reactions present in the subnetwork

Table S12. Pre-exponential factors for reactions in reaction networks identified with Method 2 from Section 5.1.

R.	Pre-exponential factor [ $\text{m}^3 \text{h}^{-1} \text{m}_{\text{cat}}^{-3}$ ]														
	F→D	F→K	F→HN	F→LN	F→G	D→K	D→HN	D→LN	D→G	K→HN	K→LN	K→G	HN→LN	HN→G	LN→G
1	$6.95 \cdot 10^9$														
2	$6.95 \cdot 10^9$											$3.13 \cdot 10^3$			
3	$6.95 \cdot 10^9$					$1.31 \cdot 10^{16}$						$3.13 \cdot 10^3$			
4	$3.09 \cdot 10^9$			$3.60 \cdot 10^{14}$		$1.44 \cdot 10^{16}$						$1.65 \cdot 10^3$			
5	$1.07 \cdot 10^{10}$			$2.62 \cdot 10^{14}$		$6.14 \cdot 10^{15}$				$3.57 \cdot 10^{10}$		$3.59 \cdot 10^3$			
6	$3.50 \cdot 10^{10}$			$3.54 \cdot 10^{14}$	$5.03 \cdot 10^2$	$3.61 \cdot 10^{15}$				$3.57 \cdot 10^{10}$		$3.60 \cdot 10^3$			
7	$1.04 \cdot 10^{10}$			$3.04 \cdot 10^{14}$	$3.60 \cdot 10^3$	$3.59 \cdot 10^{16}$			22.39	$1.60 \cdot 10^{10}$		$1.99 \cdot 10^3$			
8	$3.59 \cdot 10^{10}$			$3.60 \cdot 10^{14}$	$2.22 \cdot 10^3$	$1.41 \cdot 10^{16}$	351.6		35.85	$3.44 \cdot 10^{10}$		$3.55 \cdot 10^3$			
9	$3.22 \cdot 10^{10}$	$1.45 \cdot 10^7$		$3.25 \cdot 10^{14}$	$4.34 \cdot 10^2$	$2.14 \cdot 10^{16}$	327.1		34.36	$3.59 \cdot 10^{10}$		$3.60 \cdot 10^3$			
10	$9.51 \cdot 10^9$	$2.39 \cdot 10^7$		$3.47 \cdot 10^{14}$	$3.60 \cdot 10^3$	$2.26 \cdot 10^{16}$	360.0		36.00	$2.77 \cdot 10^{10}$		$1.55 \cdot 10^3$			$3.56 \cdot 10^8$
11	$2.59 \cdot 10^{10}$	$3.04 \cdot 10^7$		$3.33 \cdot 10^{14}$	$1.75 \cdot 10^3$	$3.40 \cdot 10^{16}$	358.9		35.88	$3.03 \cdot 10^{10}$	$3.42 \cdot 10^3$	$3.59 \cdot 10^3$			$2.21 \cdot 10^8$
12	$2.70 \cdot 10^{10}$	$3.18 \cdot 10^7$		$8.50 \cdot 10^{13}$	$2.70 \cdot 10^3$	$3.57 \cdot 10^{16}$	347.6		34.01	$3.59 \cdot 10^{10}$	$6.70 \cdot 10^2$	$3.38 \cdot 10^3$		3.60	$1.62 \cdot 10^8$
13	$3.99 \cdot 10^9$	$3.48 \cdot 10^7$	$3.58 \cdot 10^3$	$3.31 \cdot 10^{14}$	$3.60 \cdot 10^3$	$2.56 \cdot 10^{16}$	356.5		35.91	$2.79 \cdot 10^{10}$	$2.79 \cdot 10^3$	$3.08 \cdot 10^3$		3.60	$3.39 \cdot 10^8$
14	$1.05 \cdot 10^{10}$	$1.89 \cdot 10^7$	$2.75 \cdot 10^7$	$3.57 \cdot 10^{14}$	$3.60 \cdot 10^3$	$3.16 \cdot 10^{16}$	360.0	3.80	22.06	$3.04 \cdot 10^{10}$	$2.14 \cdot 10^3$	$3.42 \cdot 10^3$		3.58	$3.58 \cdot 10^8$
15	$2.57 \cdot 10^{10}$	$3.45 \cdot 10^7$	$3.60 \cdot 10^7$	$3.51 \cdot 10^{14}$	$3.60 \cdot 10^3$	$3.12 \cdot 10^{16}$	360.0	34.16	35.95	$2.45 \cdot 10^{10}$	$3.43 \cdot 10^3$	$3.59 \cdot 10^3$	$3.30 \cdot 10^9$	3.52	$3.60 \cdot 10^8$

R.: Number of reactions present in the subnetwork

Table S13. Activation energies for reactions in reaction networks identified with Method 2 from Section 5.1.

R.	Activation energy [J mol <sup>-1</sup> ]														
	F→D	F→K	F→HN	F→LN	F→G	D→K	D→HN	D→LN	D→G	K→HN	K→LN	K→G	HN→LN	HN→G	LN→G
1	0														
2	0														
3	1.19·10 <sup>5</sup>					1.98·10 <sup>5</sup>						3.63·10 <sup>4</sup>			
4	1.27·10 <sup>5</sup>			2.00·10 <sup>5</sup>		1.99·10 <sup>5</sup>						3.26·10 <sup>4</sup>			
5	1.21·10 <sup>5</sup>			1.97·10 <sup>5</sup>		1.93·10 <sup>5</sup>				1.33·10 <sup>5</sup>		3.75·10 <sup>4</sup>			
6	1.28·10 <sup>5</sup>			1.99·10 <sup>5</sup>	3.71·10 <sup>4</sup>	1.91·10 <sup>5</sup>				1.33·10 <sup>5</sup>		3.99·10 <sup>4</sup>			
7	1.21·10 <sup>5</sup>			1.98·10 <sup>5</sup>	4.77·10 <sup>4</sup>	2.04·10 <sup>5</sup>			8.32·10 <sup>4</sup>	1.29·10 <sup>5</sup>		3.69·10 <sup>4</sup>			
8	1.28·10 <sup>5</sup>			1.99·10 <sup>5</sup>	4.50·10 <sup>4</sup>	1.99·10 <sup>5</sup>	3.63·10 <sup>4</sup>		3.94·10 <sup>5</sup>	1.35·10 <sup>5</sup>		4.01·10 <sup>4</sup>			
9	1.28·10 <sup>5</sup>	2.21·10 <sup>5</sup>		1.98·10 <sup>5</sup>	3.67·10 <sup>4</sup>	2.05·10 <sup>5</sup>	3.69·10 <sup>4</sup>		4.00·10 <sup>5</sup>	1.35·10 <sup>5</sup>		4.01·10 <sup>4</sup>			
10	1.21·10 <sup>5</sup>	2.23·10 <sup>5</sup>		1.98·10 <sup>5</sup>	5.28·10 <sup>4</sup>	2.13·10 <sup>5</sup>	3.63·10 <sup>4</sup>		1.42·10 <sup>4</sup>	1.34·10 <sup>5</sup>		3.95·10 <sup>4</sup>			3.79·10 <sup>5</sup>
11	1.27·10 <sup>5</sup>	2.25·10 <sup>5</sup>		1.99·10 <sup>5</sup>	4.43·10 <sup>4</sup>	2.08·10 <sup>5</sup>	3.76·10 <sup>4</sup>		1.04·10 <sup>5</sup>	1.34·10 <sup>5</sup>	6.02·10 <sup>4</sup>	4.03·10 <sup>4</sup>			2.98·10 <sup>5</sup>
12	1.28·10 <sup>5</sup>	2.25·10 <sup>5</sup>		1.90·10 <sup>5</sup>	4.58·10 <sup>4</sup>	2.08·10 <sup>5</sup>	3.18·10 <sup>5</sup>		2.63·10 <sup>5</sup>	1.31·10 <sup>5</sup>	3.92·10 <sup>5</sup>	4.39·10 <sup>4</sup>		0.53	2.77·10 <sup>5</sup>
13	1.17·10 <sup>5</sup>	2.26·10 <sup>5</sup>	4.00·10 <sup>5</sup>	1.99·10 <sup>5</sup>	4.74·10 <sup>4</sup>	2.06·10 <sup>5</sup>	3.91·10 <sup>4</sup>		3.96·10 <sup>5</sup>	1.31·10 <sup>5</sup>	5.95·10 <sup>4</sup>	4.35·10 <sup>4</sup>		0	3.71·10 <sup>5</sup>
14	1.22·10 <sup>5</sup>	2.23·10 <sup>5</sup>	5.20·10 <sup>4</sup>	1.99·10 <sup>5</sup>	4.79·10 <sup>4</sup>	2.07·10 <sup>5</sup>	2.60·10 <sup>5</sup>	3.85·10 <sup>5</sup>	3.72·10 <sup>5</sup>	1.32·10 <sup>5</sup>	5.30·10 <sup>4</sup>	4.29·10 <sup>4</sup>		1.80·10 <sup>3</sup>	1.12·10 <sup>5</sup>
15	1.27·10 <sup>5</sup>	2.26·10 <sup>5</sup>	5.43·10 <sup>4</sup>	1.99·10 <sup>5</sup>	4.81·10 <sup>4</sup>	2.07·10 <sup>5</sup>	3.98·10 <sup>5</sup>	4.14·10 <sup>4</sup>	2.51·10 <sup>5</sup>	1.33·10 <sup>5</sup>	4.00·10 <sup>5</sup>	4.03·10 <sup>4</sup>	1.36·10 <sup>5</sup>	3.89·10 <sup>5</sup>	2.10·10 <sup>5</sup>

R.: Number of reactions present in the subnetwork

Table S14. Pre-exponential factors for reactions in reaction networks identified with Method 3 from Section 5.1.

R.	Pre-exponential factor [ $\text{m}^3 \text{h}^{-1} \text{m}_{\text{cat}}^3$ ]														
	F→D	F→K	F→HN	F→LN	F→G	D→K	D→HN	D→LN	D→G	K→HN	K→LN	K→G	HN→LN	HN→G	LN→G
1	$2.25 \cdot 10^{10}$														
2	$3.39 \cdot 10^{10}$					$7.84 \cdot 10^{15}$									
3	$3.39 \cdot 10^{10}$			$3.23 \cdot 10^{14}$		$7.84 \cdot 10^{15}$									
4	$3.23 \cdot 10^{10}$			$3.60 \cdot 10^{14}$		$2.27 \cdot 10^{16}$									$1.01 \cdot 10^8$
5	$3.55 \cdot 10^{10}$			$3.60 \cdot 10^{14}$		$2.83 \cdot 10^{16}$					360.0				$1.06 \cdot 10^8$
6	$3.57 \cdot 10^{10}$			$3.60 \cdot 10^{14}$	360.8	$2.67 \cdot 10^{16}$					360.0				$1.01 \cdot 10^8$
7	$3.60 \cdot 10^{10}$			$3.60 \cdot 10^{14}$	360.0	$2.75 \cdot 10^{16}$					360.0		$3.60 \cdot 10^8$		$1.01 \cdot 10^8$
8	$3.60 \cdot 10^{10}$			$2.62 \cdot 10^{14}$	412.6	$3.60 \cdot 10^{16}$				$4.13 \cdot 10^9$	517.7		$3.60 \cdot 10^9$		$7.42 \cdot 10^7$
9	$3.60 \cdot 10^{10}$		360.0	$1.65 \cdot 10^{14}$	598.0	$3.60 \cdot 10^{16}$				$7.19 \cdot 10^9$	$3.60 \cdot 10^3$		$2.78 \cdot 10^9$		$8.21 \cdot 10^7$
10	$3.44 \cdot 10^{10}$	$3.60 \cdot 10^{17}$	360.0	$1.49 \cdot 10^{14}$	598.0	$3.24 \cdot 10^{16}$				$7.19 \cdot 10^9$	$3.60 \cdot 10^3$		$2.56 \cdot 10^9$		$8.21 \cdot 10^7$
11	$3.44 \cdot 10^{10}$	$3.60 \cdot 10^{17}$	360.0	$1.53 \cdot 10^{14}$	598.0	$3.24 \cdot 10^{16}$	36.0			$7.19 \cdot 10^9$	$3.60 \cdot 10^3$		$2.56 \cdot 10^9$		$8.21 \cdot 10^7$
12	$3.44 \cdot 10^{10}$	$3.60 \cdot 10^{17}$	360.0	$1.53 \cdot 10^{14}$	598.0	$3.24 \cdot 10^{16}$	36.0			$7.19 \cdot 10^9$	$3.60 \cdot 10^3$		$2.56 \cdot 10^9$	0.36	$8.21 \cdot 10^7$
13	$3.40 \cdot 10^{10}$	$3.60 \cdot 10^{17}$	403.2	$1.53 \cdot 10^{14}$	626.8	$3.26 \cdot 10^{16}$	40.1			$7.18 \cdot 10^9$	$3.60 \cdot 10^3$	441.1	$2.54 \cdot 10^9$	1.14	$8.25 \cdot 10^7$
14	$3.36 \cdot 10^{10}$	$3.59 \cdot 10^{17}$	403.2	$1.56 \cdot 10^{14}$	626.6	$3.26 \cdot 10^{16}$	36.0	3.80		$7.18 \cdot 10^9$	$3.60 \cdot 10^3$	441.3	$2.52 \cdot 10^9$	1.29	$8.25 \cdot 10^7$
15	$3.36 \cdot 10^{10}$	$3.60 \cdot 10^{17}$	405.9	$1.56 \cdot 10^{14}$	625.0	$3.21 \cdot 10^{16}$	36.1	3.82	3.61	$7.19 \cdot 10^9$	$3.60 \cdot 10^3$	752.0	$2.52 \cdot 10^9$	1.29	$8.26 \cdot 10^7$

R.: Number of reactions present in the subnetwork

Table S15. Activation energies for reactions in reaction networks identified with Method 3 from Section 5.1.

R.	Activation energy [J mol <sup>-1</sup> ]														
	F→D	F→K	F→HN	F→LN	F→G	D→K	D→HN	D→LN	D→G	K→HN	K→LN	K→G	HN→LN	HN→G	LN→G
1	1.32·10 <sup>5</sup>														
2	1.30·10 <sup>5</sup>					2.00·10 <sup>5</sup>									
3	1.30·10 <sup>5</sup>			2.00·10 <sup>5</sup>		2.00·10 <sup>5</sup>									
4	1.30·10 <sup>5</sup>			2.00·10 <sup>5</sup>		2.06·10 <sup>5</sup>									1.01·10 <sup>4</sup>
5	1.30·10 <sup>5</sup>			1.87·10 <sup>5</sup>		2.06·10 <sup>5</sup>					4.00·10 <sup>5</sup>				8.29·10 <sup>4</sup>
6	1.30·10 <sup>5</sup>			1.87·10 <sup>5</sup>	2.00·10 <sup>5</sup>	2.06·10 <sup>5</sup>					4.00·10 <sup>5</sup>				8.28·10 <sup>4</sup>
7	1.30·10 <sup>5</sup>			1.87·10 <sup>5</sup>	4.03·10 <sup>4</sup>	2.06·10 <sup>5</sup>					4.00·10 <sup>5</sup>		3.98·10 <sup>5</sup>		8.28·10 <sup>4</sup>
8	1.30·10 <sup>5</sup>			1.87·10 <sup>5</sup>	4.03·10 <sup>4</sup>	2.06·10 <sup>5</sup>				1.21·10 <sup>5</sup>	4.00·10 <sup>5</sup>		1.66·10 <sup>5</sup>		8.28·10 <sup>4</sup>
9	1.28·10 <sup>5</sup>		3.41·10 <sup>5</sup>	1.87·10 <sup>5</sup>	3.86·10 <sup>4</sup>	2.05·10 <sup>5</sup>				1.21·10 <sup>5</sup>	3.80·10 <sup>5</sup>		1.14·10 <sup>5</sup>		8.44·10 <sup>4</sup>
10	1.28·10 <sup>5</sup>	2.30·10 <sup>5</sup>	3.41·10 <sup>5</sup>	1.87·10 <sup>5</sup>	3.86·10 <sup>4</sup>	2.05·10 <sup>5</sup>				1.21·10 <sup>5</sup>	6.02·10 <sup>4</sup>		1.14·10 <sup>5</sup>		8.44·10 <sup>4</sup>
11	1.28·10 <sup>5</sup>	2.30·10 <sup>5</sup>	3.41·10 <sup>5</sup>	1.87·10 <sup>5</sup>	3.86·10 <sup>4</sup>	2.05·10 <sup>5</sup>	2.80·10 <sup>5</sup>			1.21·10 <sup>5</sup>	6.02·10 <sup>4</sup>		1.14E·10 <sup>5</sup>		8.44·10 <sup>4</sup>
12	1.28·10 <sup>5</sup>	2.30·10 <sup>5</sup>	3.41·10 <sup>5</sup>	1.87·10 <sup>5</sup>	3.86·10 <sup>4</sup>	2.05·10 <sup>5</sup>	2.80·10 <sup>5</sup>			1.21·10 <sup>5</sup>	6.02·10 <sup>4</sup>		1.14·10 <sup>5</sup>	2.24·10 <sup>5</sup>	8.44·10 <sup>4</sup>
13	1.28·10 <sup>5</sup>	2.29·10 <sup>5</sup>	3.48·10 <sup>5</sup>	1.88·10 <sup>5</sup>	3.88·10 <sup>4</sup>	2.06·10 <sup>5</sup>	2.80·10 <sup>5</sup>			1.21·10 <sup>5</sup>	5.30·10 <sup>4</sup>	4.00·10 <sup>5</sup>	1.14·10 <sup>5</sup>	2.20·10 <sup>5</sup>	8.43·10 <sup>4</sup>
14	1.28·10 <sup>5</sup>	2.29·10 <sup>5</sup>	3.48·10 <sup>5</sup>	1.88·10 <sup>5</sup>	3.89·10 <sup>4</sup>	2.06·10 <sup>5</sup>	2.80·10 <sup>5</sup>	3.90·10 <sup>5</sup>		1.21·10 <sup>5</sup>	5.30·10 <sup>4</sup>	4.00·10 <sup>5</sup>	1.14·10 <sup>5</sup>	2.21·10 <sup>5</sup>	8.43·10 <sup>4</sup>
15	1.28·10 <sup>5</sup>	2.29·10 <sup>5</sup>	3.45·10 <sup>5</sup>	1.88·10 <sup>5</sup>	3.89·10 <sup>4</sup>	2.06·10 <sup>5</sup>	2.80·10 <sup>5</sup>	3.90·10 <sup>5</sup>	3.04E+05	1.21·10 <sup>5</sup>	5.29·10 <sup>4</sup>	4.00·10 <sup>5</sup>	1.14·10 <sup>5</sup>	2.31·10 <sup>5</sup>	8.44·10 <sup>4</sup>

R.: Number of reactions present in the subnetwork

Table S16. Identified kinetic parameters of the thermo-catalytic pyrolysis reaction networks (from Section 6.2).

Reaction	Pre-exponential factor [ $s^{-1}$ ]		Activation energy [ $J mol^{-1}$ ]	
	Complete network	Reduced network	Complete network	Reduced network
$P \rightarrow P^-$	$5.71 \cdot 10^5$	$7.01 \cdot 10^7$	$9.57 \cdot 10^4$	$1.25 \cdot 10^5$
$P^- \rightarrow L^+$	$1.02 \cdot 10^6$	$2.55 \cdot 10^2$	$9.97 \cdot 10^4$	$4.92 \cdot 10^4$
$P^- \rightarrow L^-$	$1.47 \cdot 10^6$	$3.88 \cdot 10^2$	$1.05 \cdot 10^5$	$5.44 \cdot 10^4$
$P^- \rightarrow G$	$3.14 \cdot 10^4$	$1.44 \cdot 10^1$	$8.21 \cdot 10^4$	$3.50 \cdot 10^4$
$P^- \rightarrow C$	$2.28 \cdot 10^3$	1.04	$7.56 \cdot 10^4$	$2.83 \cdot 10^4$
$L^+ \rightarrow L^-$	$6.89 \cdot 10^4$	n.a.	$6.18 \cdot 10^4$	n.a.
$L^+ \rightarrow G$	$1.22 \cdot 10^{18}$	n.a.	$2.56 \cdot 10^5$	n.a.
$L^+ \rightarrow C$	$4.88 \cdot 10^{22}$	n.a.	$7.31 \cdot 10^5$	n.a.
$L^- \rightarrow G$	$1.34 \cdot 10^{15}$	n.a.	$7.15 \cdot 10^5$	n.a.
$L^- \rightarrow C$	$1.45 \cdot 10^{16}$	n.a.	$5.41 \cdot 10^5$	n.a.



Table S17. Identified kinetic parameters of the vacuum gas oil hydrocracking reaction networks (from Section 6.3).

Reaction	Pre-exponential factor [ $s^{-1}$ ]		Activation energy [ $J mol^{-1}$ ]	
	Complete network	Reduced network	Complete network	Reduced network
VGO $\rightarrow$ D	$7.15 \cdot 10^6$	$4.21 \cdot 10^6$	$1.27 \cdot 10^5$	$1.23 \cdot 10^5$
VGO $\rightarrow$ K	$9.59 \cdot 10^{13}$	n.a.	$2.26 \cdot 10^5$	n.a.
VGO $\rightarrow$ HN	1.00	n.a.	$5.43 \cdot 10^4$	n.a.
VGO $\rightarrow$ LN	$9.75 \cdot 10^{10}$	$9.86 \cdot 10^{10}$	$1.99 \cdot 10^5$	$1.91 \cdot 10^5$
VGO $\rightarrow$ G	$9.99 \cdot 10^{-1}$	$1.25 \cdot 10^{-1}$	$4.81 \cdot 10^4$	$3.75 \cdot 10^4$
D $\rightarrow$ K	$8.68 \cdot 10^{12}$	$1.02 \cdot 10^{12}$	$2.07 \cdot 10^5$	$1.91 \cdot 10^5$
D $\rightarrow$ HN	$1.00 \cdot 10^{-1}$	n.a.	$3.98 \cdot 10^5$	n.a.
D $\rightarrow$ LN	$9.49 \cdot 10^{-3}$	n.a.	$4.14 \cdot 10^4$	n.a.
D $\rightarrow$ G	$9.99 \cdot 10^{-3}$	n.a.	$2.51 \cdot 10^5$	n.a.
K $\rightarrow$ HN	$6.82 \cdot 10^6$	$8.59 \cdot 10^6$	$1.33 \cdot 10^5$	$1.29 \cdot 10^5$
K $\rightarrow$ LN	$9.53 \cdot 10^{-1}$	n.a.	$4.00 \cdot 10^5$	n.a.
K $\rightarrow$ G	$9.97 \cdot 10^{-1}$	n.a.	$4.03 \cdot 10^4$	n.a.
HN $\rightarrow$ LN	$9.17 \cdot 10^5$	$1.02 \cdot 10^5$	$1.36 \cdot 10^5$	$1.02 \cdot 10^5$
HN $\rightarrow$ G	$9.78 \cdot 10^{-4}$	n.a.	$3.89 \cdot 10^5$	n.a.
LN $\rightarrow$ G	$1.00 \cdot 10^5$	$1.20 \cdot 10^4$	$2.10 \cdot 10^5$	$8.06 \cdot 10^4$

Table S18. Identified pre-exponential factors of the reaction network from Figure 3.5.

Set	$k_{0,1}$	$k_{0,2}$	$k_{0,3}$	$k_{0,4}$	$k_{0,5}$	RMSE <sup>6</sup>
1	$3.56 \cdot 10^{13}$	$2.18 \cdot 10^{18}$	$7.97 \cdot 10^{17}$	$9.5 \cdot 10^{13}$	$1.64 \cdot 10^7$	5.61%
2	$1.73 \cdot 10^{13}$	$2.17 \cdot 10^{18}$	$8.13 \cdot 10^{16}$	$8.84 \cdot 10^{13}$	$7.44 \cdot 10^7$	5.52%
3	$4.53 \cdot 10^{13}$	$2.21 \cdot 10^{18}$	$1.21 \cdot 10^{17}$	$9.27 \cdot 10^{13}$	$4.34 \cdot 10^6$	5.50%
4	$3.06 \cdot 10^{13}$	$2.19 \cdot 10^{18}$	$6 \cdot 10^{17}$	$9.06 \cdot 10^{13}$	$4.23 \cdot 10^7$	5.60%
5	$3.46 \cdot 10^{13}$	$2.2 \cdot 10^{18}$	$1.93 \cdot 10^{17}$	$5.86 \cdot 10^{13}$	$1.81 \cdot 10^7$	5.53%
6	$7.63 \cdot 10^{13}$	$7.39 \cdot 10^{17}$	$2.05 \cdot 10^{17}$	$2.36 \cdot 10^{13}$	$1.08 \cdot 10^7$	5.50%
7	$8.44 \cdot 10^{13}$	$2.26 \cdot 10^{18}$	$2.59 \cdot 10^{16}$	$9.74 \cdot 10^{13}$	$4.90 \cdot 10^6$	5.40%
8	$2.62 \cdot 10^{13}$	$2.19 \cdot 10^{18}$	$2.24 \cdot 10^{17}$	$5.58 \cdot 10^{13}$	$1.32 \cdot 10^7$	5.55%
9	$3.43 \cdot 10^{13}$	$2.20 \cdot 10^{18}$	$1.46 \cdot 10^{17}$	$6.7 \cdot 10^{13}$	$3.26 \cdot 10^7$	5.51%
10	$1.25 \cdot 10^{13}$	$2.15 \cdot 10^{18}$	$2.32 \cdot 10^{17}$	$1.53 \cdot 10^{13}$	$3.10 \cdot 10^7$	5.59%
11	$2.31 \cdot 10^{12}$	$2.13 \cdot 10^{18}$	$1.09 \cdot 10^{15}$	$9.97 \cdot 10^{13}$	$1.63 \cdot 10^5$	5.41%
12	$6.8 \cdot 10^{13}$	$2.18 \cdot 10^{18}$	$2.35 \cdot 10^{16}$	$5.2 \cdot 10^{13}$	$1.55 \cdot 10^7$	5.40%
13	$10^{14}$	$2.15 \cdot 10^{18}$	$6.93 \cdot 10^{17}$	$9.99 \cdot 10^{13}$	$9.98 \cdot 10^7$	5.55%
14	$9.95 \cdot 10^{13}$	$1.8 \cdot 10^{18}$	$9.37 \cdot 10^{17}$	$8.84 \cdot 10^{13}$	$8.82 \cdot 10^7$	5.57%
15	$9.51 \cdot 10^{13}$	$7.14 \cdot 10^{17}$	$9.84 \cdot 10^{17}$	$9.77 \cdot 10^{13}$	$10^8$	5.57%
16	$10^{14}$	$2.34 \cdot 10^{18}$	$1.04 \cdot 10^{15}$	$6.11 \cdot 10^{13}$	$6.65 \cdot 10^6$	5.27%
17	$2.61 \cdot 10^{13}$	$1.67 \cdot 10^{18}$	$6.28 \cdot 10^{17}$	$1.72 \cdot 10^{13}$	$1.33 \cdot 10^7$	5.61%
18	$9.91 \cdot 10^{13}$	$1.88 \cdot 10^{18}$	$8.14 \cdot 10^{16}$	$2.45 \cdot 10^{13}$	$1.45 \cdot 10^6$	5.45%
19	$9.39 \cdot 10^{12}$	$2.20 \cdot 10^{18}$	$1.04 \cdot 10^{15}$	$9.26 \cdot 10^{13}$	$1.16 \cdot 10^5$	5.36%
20	$4.65 \cdot 10^{13}$	$2.15 \cdot 10^{18}$	$6.33 \cdot 10^{17}$	$7.67 \cdot 10^{13}$	$5.86 \cdot 10^6$	5.58%
21	$10^{14}$	$2.32 \cdot 10^{18}$	$10^{15}$	$1.3 \cdot 10^{12}$	$10^8$	5.26%
22	$5.11 \cdot 10^{13}$	$10^{17}$	$10^{15}$	$3.47 \cdot 10^{13}$	$6.01 \cdot 10^7$	5.28%
23	$10^{14}$	$2.27 \cdot 10^{18}$	$10^{15}$	$10^{11}$	$10^8$	5.26%
24	$9.22 \cdot 10^{13}$	$10^{17}$	$10^{15}$	$1.83 \cdot 10^{12}$	$9.93 \cdot 10^7$	5.26%
25	$10^{14}$	$2.31 \cdot 10^{18}$	$10^{15}$	$10^{11}$	$10^8$	5.26%
26	$5.9 \cdot 10^{13}$	$10^{17}$	$10^{15}$	$10^{11}$	$9.93 \cdot 10^7$	5.27%
27	$10^{14}$	$2.3 \cdot 10^{18}$	$10^{15}$	$5.04 \cdot 10^{11}$	$10^8$	5.26%
28	$10^{14}$	$10^{17}$	$10^{15}$	$1.11 \cdot 10^{12}$	$7.84 \cdot 10^7$	5.28%

<sup>6</sup> Root of mean squared error between pseudocomponent mass percentages from experimental data and simulation results (aggregated data for all temperatures, pseudocomponents and LHSV values)

Set	$k_{0,1}$	$k_{0,2}$	$k_{0,3}$	$k_{0,4}$	$k_{0,5}$	RMSE <sup>6</sup>
29	$10^{14}$	$2.3 \cdot 10^{18}$	$10^{15}$	$7.44 \cdot 10^{11}$	$9.99 \cdot 10^7$	5.26%
30	$10^{14}$	$2.31 \cdot 10^{18}$	$10^{15}$	$4.03 \cdot 10^{12}$	$9.99 \cdot 10^7$	5.26%
31	$10^{14}$	$10^{18}$	$10^{15}$	$9.96 \cdot 10^{13}$	$7.83 \cdot 10^7$	5.31%
32	$10^{14}$	$1.37 \cdot 10^{18}$	$9.98 \cdot 10^{17}$	$3.12 \cdot 10^{13}$	$9.77 \cdot 10^7$	5.59%
33	$2.19 \cdot 10^{13}$	$10^{17}$	$9.48 \cdot 10^{17}$	$9.89 \cdot 10^{13}$	$10^8$	5.64%
34	$6.76 \cdot 10^{13}$	$1.33 \cdot 10^{18}$	$5.85 \cdot 10^{17}$	$10^{14}$	$9.37 \cdot 10^7$	5.56%
35	$2.75 \cdot 10^{12}$	$2 \cdot 10^{18}$	$10^{15}$	$2.19 \cdot 10^{13}$	$1.21 \cdot 10^6$	5.41%
36	$4.67 \cdot 10^{13}$	$4.25 \cdot 10^{17}$	$1.84 \cdot 10^{16}$	$8.33 \cdot 10^{12}$	$4.27 \cdot 10^7$	5.40%
37	$10^{14}$	$10^{17}$	$9.63 \cdot 10^{17}$	$9.79 \cdot 10^{13}$	$10^5$	5.60%
38	$1.38 \cdot 10^{13}$	$2.17 \cdot 10^{18}$	$7 \cdot 10^{16}$	$6.89 \cdot 10^{13}$	$5.86 \cdot 10^6$	5.52%
39	$2.81 \cdot 10^{12}$	$10^{17}$	$7.1 \cdot 10^{17}$	$8.94 \cdot 10^{13}$	$3.49 \cdot 10^7$	5.75%
40	$10^{14}$	$1.03 \cdot 10^{17}$	$5.14 \cdot 10^{16}$	$9.97 \cdot 10^{13}$	$8.78 \cdot 10^7$	5.50%

Table S19. Identified activation energies of the reaction network from Figure 3.5.

Set	$E_{a,1}$	$E_{a,2}$	$E_{a,3}$	$E_{a,4}$	$E_{a,5}$
1	$1.86 \cdot 10^5$	$3 \cdot 10^5$	$2.3 \cdot 10^5$	$1.86 \cdot 10^5$	$1.08 \cdot 10^5$
2	$1.81 \cdot 10^5$	$3 \cdot 10^5$	$2.17 \cdot 10^5$	$1.86 \cdot 10^5$	$1.17 \cdot 10^5$
3	$1.87 \cdot 10^5$	$3 \cdot 10^5$	$2.19 \cdot 10^5$	$1.86 \cdot 10^5$	$1.01 \cdot 10^5$
4	$1.85 \cdot 10^5$	$3 \cdot 10^5$	$2.28 \cdot 10^5$	$1.86 \cdot 10^5$	$1.14 \cdot 10^5$
5	$1.85 \cdot 10^5$	$3 \cdot 10^5$	$2.22 \cdot 10^5$	$1.83 \cdot 10^5$	$1.09 \cdot 10^5$
6	$1.9 \cdot 10^5$	$2.94 \cdot 10^5$	$2.22 \cdot 10^5$	$1.78 \cdot 10^5$	$1.06 \cdot 10^5$
7	$1.9 \cdot 10^5$	$3 \cdot 10^5$	$2.11 \cdot 10^5$	$1.86 \cdot 10^5$	$1.01 \cdot 10^5$
8	$1.84 \cdot 10^5$	$3 \cdot 10^5$	$2.23 \cdot 10^5$	$1.83 \cdot 10^5$	$1.07 \cdot 10^5$
9	$1.85 \cdot 10^5$	$3 \cdot 10^5$	$2.20 \cdot 10^5$	$1.84 \cdot 10^5$	$1.12 \cdot 10^5$
10	$1.8 \cdot 10^5$	$3 \cdot 10^5$	$2.23 \cdot 10^5$	$1.76 \cdot 10^5$	$1.12 \cdot 10^5$
11	$1.7 \cdot 10^5$	$3 \cdot 10^5$	$1.93 \cdot 10^5$	$1.86 \cdot 10^5$	$8.20 \cdot 10^4$
12	$1.89 \cdot 10^5$	$3 \cdot 10^5$	$2.1 \cdot 10^5$	$1.83 \cdot 10^5$	$1.08 \cdot 10^5$
13	$1.91 \cdot 10^5$	$3 \cdot 10^5$	$2.29 \cdot 10^5$	$1.86 \cdot 10^5$	$1.18 \cdot 10^5$
14	$1.91 \cdot 10^5$	$2.99 \cdot 10^5$	$2.31 \cdot 10^5$	$1.86 \cdot 10^5$	$1.18 \cdot 10^5$
15	$1.91 \cdot 10^5$	$2.94 \cdot 10^5$	$2.31 \cdot 10^5$	$1.86 \cdot 10^5$	$1.18 \cdot 10^5$
16	$1.91 \cdot 10^5$	$3 \cdot 10^5$	$1.92 \cdot 10^5$	$1.83 \cdot 10^5$	$1.02 \cdot 10^5$
17	$1.84 \cdot 10^5$	$2.99 \cdot 10^5$	$2.29 \cdot 10^5$	$1.76 \cdot 10^5$	$1.07 \cdot 10^5$

---

<b>Set</b>	<b>E<sub>a,1</sub></b>	<b>E<sub>a,2</sub></b>	<b>E<sub>a,3</sub></b>	<b>E<sub>a,4</sub></b>	<b>E<sub>a,5</sub></b>
18	$1.91 \cdot 10^5$	$2.99 \cdot 10^5$	$2.17 \cdot 10^5$	$1.78 \cdot 10^5$	$9.41 \cdot 10^4$
19	$1.78 \cdot 10^5$	$3 \cdot 10^5$	$1.92 \cdot 10^5$	$1.86 \cdot 10^5$	$7.97 \cdot 10^4$
20	$1.87 \cdot 10^5$	$3 \cdot 10^5$	$2.29 \cdot 10^5$	$1.85 \cdot 10^5$	$1.02 \cdot 10^5$
21	$1.91 \cdot 10^5$	$3 \cdot 10^5$	$1.92 \cdot 10^5$	$1.61 \cdot 10^5$	$1.18 \cdot 10^5$
22	$1.87 \cdot 10^5$	$2.82 \cdot 10^5$	$1.92 \cdot 10^5$	$1.80 \cdot 10^5$	$1.15 \cdot 10^5$
23	$1.91 \cdot 10^5$	$3 \cdot 10^5$	$1.92 \cdot 10^5$	$1.47 \cdot 10^5$	$1.18 \cdot 10^5$
24	$1.91 \cdot 10^5$	$2.82 \cdot 10^5$	$1.92 \cdot 10^5$	$1.63 \cdot 10^5$	$1.18 \cdot 10^5$
25	$1.91 \cdot 10^5$	$3 \cdot 10^5$	$1.92 \cdot 10^5$	$1.47 \cdot 10^5$	$1.18 \cdot 10^5$
26	$1.88 \cdot 10^5$	$2.82 \cdot 10^5$	$1.92 \cdot 10^5$	$1.47 \cdot 10^5$	$1.18 \cdot 10^5$
27	$1.91 \cdot 10^5$	$3 \cdot 10^5$	$1.92 \cdot 10^5$	$1.56 \cdot 10^5$	$1.18 \cdot 10^5$
28	$1.91 \cdot 10^5$	$2.82 \cdot 10^5$	$1.92 \cdot 10^5$	$1.6 \cdot 10^5$	$1.17 \cdot 10^5$
29	$1.91 \cdot 10^5$	$3 \cdot 10^5$	$1.92 \cdot 10^5$	$1.58 \cdot 10^5$	$1.18 \cdot 10^5$
30	$1.91 \cdot 10^5$	$3 \cdot 10^5$	$1.92 \cdot 10^5$	$1.68 \cdot 10^5$	$1.18 \cdot 10^5$
31	$1.91 \cdot 10^5$	$2.96 \cdot 10^5$	$1.92 \cdot 10^5$	$1.86 \cdot 10^5$	$1.17 \cdot 10^5$
32	$1.92 \cdot 10^5$	$2.98 \cdot 10^5$	$2.32 \cdot 10^5$	$1.8 \cdot 10^5$	$1.19 \cdot 10^5$
33	$1.83 \cdot 10^5$	$2.83 \cdot 10^5$	$2.31 \cdot 10^5$	$1.86 \cdot 10^5$	$1.19 \cdot 10^5$
34	$1.89 \cdot 10^5$	$2.97 \cdot 10^5$	$2.28 \cdot 10^5$	$1.86 \cdot 10^5$	$1.18 \cdot 10^5$
35	$1.71 \cdot 10^5$	$3 \cdot 10^5$	$1.92 \cdot 10^5$	$1.78 \cdot 10^5$	$9.35 \cdot 10^4$
36	$1.87 \cdot 10^5$	$2.91 \cdot 10^5$	$2.09 \cdot 10^5$	$1.72 \cdot 10^5$	$1.13 \cdot 10^5$
37	$1.91 \cdot 10^5$	$2.83 \cdot 10^5$	$2.31 \cdot 10^5$	$1.86 \cdot 10^5$	$7.93 \cdot 10^4$
38	$1.8 \cdot 10^5$	$3 \cdot 10^5$	$2.16 \cdot 10^5$	$1.84 \cdot 10^5$	$1.02 \cdot 10^5$
39	$1.71 \cdot 10^5$	$2.83 \cdot 10^5$	$2.29 \cdot 10^5$	$1.86 \cdot 10^5$	$1.13 \cdot 10^5$
40	$1.92 \cdot 10^5$	$2.83 \cdot 10^5$	$2.15 \cdot 10^5$	$1.86 \cdot 10^5$	$1.18 \cdot 10^5$

---

Table S20. Nominal operating conditions of the hydrocracking reactor designed using a conventional method in case of one catalyst layer.

Operating variable	LHSV = 0.5	LHSV = 1	LHSV = 1.5	LHSV = 2
$T_{VGO}$	412	401	408	395
$T_{H_2}$	228	279	287	321
$\frac{\dot{m}_{H_2}^k}{\dot{m}_{H_2}}$	1	1	1	1
$w_{VGO}$	62.2%	61.3%	61.4%	63.5%
$w_D$	29.5%	29.8%	29.7%	28.6%
$T_{max}$	392	404	410	410
$\Delta T_{max}^k$	50	50	49	44
$f(\underline{x})$	63.84	62.14	62.48	66.64

Table S21. Nominal operating conditions of the hydrocracking reactor designed using a conventional method in case of two catalyst layers.

Operating variable	layer	LHSV = 0.5	LHSV = 1	LHSV = 1.5	LHSV = 2
$T_{VGO}$	all	407	381	412	396
$T_{H_2}$	all	204	224	258	278
$\frac{\dot{m}_{H_2}^k}{\dot{m}_{H_2}}$	1	75.1%	38.2%	80.0%	59.1%
$\frac{\dot{m}_{H_2}^k}{\dot{m}_{H_2}}$	2	24.9%	61.8%	20.0%	40.9%
$\frac{L^k}{L_r}$	1		49.1%		
$\frac{L^k}{L_r}$	2		51.9%		
$w_{VGO}$		56.5%	55.8%	58.0%	57.2%
$w_D$		32.4%	32.0%	31.7%	31.9%
$T_{max}$		394	392	410	410
$\Delta T_{max}^k$		50	50	44	44
$f(\underline{x})$		52.39	51.80	55.29	53.95

Table S22. Nominal operating conditions of the hydrocracking reactor designed using a conventional method in case of two catalyst layers with independent H<sub>2</sub> inlet temperatures.

Operating variable	layer	LHSV = 0.5	LHSV = 1	LHSV = 1.5	LHSV = 2
$T_{VGO}$	all	407	419	417	407
$T_{H_2}$	1	196	172	252	260
	2	233	278	130	172
$\overline{\dot{m}}_{H_2}^k$	1	75.8%	62.7%	81.9%	65.0%
$\overline{\dot{m}}_{H_2}$	2	24.2%	37.3%	18.1%	35.0%
$\overline{L}^k$	1		15.7%		
$\overline{L}_r$	2		84.3%		
$w_{VGO}$		52.2%	53.9%	55.3%	53.9%
$w_D$		33.8%	33.1%	32.9%	32.8%
$T_{max}$		407	410	410	410
$\Delta T_{max}^k$		50	45	34	42
$f(\underline{x})$		44.60	47.73	50.14	47.98

Table S23. Nominal operating conditions of the hydrocracking reactor designed using a conventional method in case of three catalyst layers.

<b>Operating variable</b>	<b>layer</b>	<b>LHSV = 0.5</b>	<b>LHSV = 1</b>	<b>LHSV = 1.5</b>	<b>LHSV = 2</b>
$T_{VGO}$	all	398	399	395	397
$T_{H_2}$	all	124	92	104	139
$\frac{\dot{m}_{H_2}^k}{\dot{m}_{H_2}}$	1	39.3%	24.9%	15.9%	17.0%
	2	37.5%	46.0%	58.7%	65.2%
	3	23.2%	29.1%	25.4%	17.8%
$\frac{L^k}{L_r}$	1		35.7%		
	2		40.7%		
	3		23.7%		
$w_{VGO}$		47.7%	46.1%	47.7%	48.1%
$w_D$		34.3%	32.4%	30.8%	31.6%
$T_{max}$		395	398	405	407
$\Delta T_{max}^k$		50	50	50	50
$f(\underline{x})$		37.32	36.65	40.74	40.48

Table S24. Nominal operating conditions of the hydrocracking reactor designed using a conventional method in case of four catalyst layers.

Operating variable	layer	LHSV = 0.5	LHSV = 1	LHSV = 1.5	LHSV = 2
$T_{VGO}$	all	392	411	401	402
$T_{H_2}$	all	116	140	117	159
	1	34.1%	39.4%	25.2%	28.3%
$\frac{\dot{m}_{H_2}^k}{\dot{m}_{H_2}}$	2	19.5%	20.9%	16.5%	14.6%
	3	15.9%	22.4%	26.5%	21.7%
	4	30.5%	17.4%	31.9%	35.4%
	1		28.6%		
$\frac{L^k}{L_r}$	2		18.1%		
	3		30.8%		
	4		22.6%		
$w_{VGO}$		46.9%	45.8%	44.6%	46.6%
$w_D$		34.4%	35.0%	33.9%	34.2%
$T_{max}$		392	409	407	410
$\Delta T_{max}^k$		50	50	50	47
$f(\underline{x})$		36.03	33.76	32.97	35.62



Table S25. Nominal operating conditions of the hydrocracking reactor designed using a conventional method in case of five catalyst layers.

Operating variable	layer	LHSV = 0.5	LHSV = 1	LHSV = 1.5	LHSV = 2
$T_{VGO}$	all	390	393	400	396
$T_{H_2}$	all	145	145	158	132
$\frac{\dot{m}_{H_2}^k}{\dot{m}_{H_2}}$	1	37.1%	27.4%	25.8%	17.8%
	2	14.0%	16.9%	27.1%	12.6%
	3	12.4%	20.7%	11.9%	39.2%
	4	19.9%	11.3%	24.7%	20.9%
	5	16.6%	23.7%	10.5%	9.6%
$\frac{L^k}{L_r}$	1		15.9%		
	2		25.0%		
	3		24.8%		
	4		18.2%		
	5		16.1%		
$w_{VGO}$		45.7%	44.3%	45.7%	44.1%
$w_D$		35.2%	35.0%	35.2%	34.2%
$T_{max}$		402	409	410	410
$\Delta T_{max}^k$		50	50	44	45
$f(\underline{x})$		33.40	31.41	33.28	31.99

Table S26. Nominal operating conditions of the hydrocracking reactor designed using a conventional method in case of six catalyst layers.

Operating variable	layer	LHSV = 0.5	LHSV = 1	LHSV = 1.5	LHSV = 2
$T_{VGO}$	all	403	390	401	392
$T_{H_2}$	all	100	182	116	125
	1	31.5%	28.6%	23.2%	11.0%
	2	23.6%	21.8%	10.2%	27.6%
$\dot{m}_{H_2}^k$	3	9.7%	19.1%	16.4%	15.4%
$\overline{\dot{m}_{H_2}}$	4	13.2%	9.7%	16.2%	15.5%
	5	7.8%	7.2%	21.1%	17.1%
	6	14.3%	13.6%	12.9%	13.3%
	1		11.8%		
	2		24.5%		
$\frac{L^k}{L_r}$	3		8.4%		
	4		21.8%		
	5		16.7%		
	6		16.8%		
$w_{VGO}$		44.6%	46.2%	42.9%	43.8%
$w_D$		35.3%	35.3%	34.8%	34.8%
$T_{max}$		398	410	410	406
$\Delta T_{max}^k$		50	50	47	50
$f(\underline{x})$		31.59	33.91	29.63	30.85

Table S27. Nominal values of operating variables of the hydrocracking reactor at the base uncertainty level.

Operating variable	Traditional			Stochastic		
	3 layers	4 layers	5 layers	3 layers	4 layers	5 layers
$T_{VGO}^{LHSV=0.5}$ [°C]	398	392	390	403	398	404
$T_{VGO}^{LHSV=1}$ [°C]	399	411	393	396	392	399
$T_{VGO}^{LHSV=1.5}$ [°C]	395	401	400	399	400	400
$T_{VGO}^{LHSV=2}$ [°C]	397	402	396	396	406	390
$T_{H_2}^{LHSV=0.5}$ [°C]	124	116	145	121	143	111
$T_{H_2}^{LHSV=1}$ [°C]	92	140	145	161	82	96
$T_{H_2}^{LHSV=1.5}$ [°C]	104	117	158	161	108	133
$T_{H_2}^{LHSV=2}$ [°C]	139	159	132	188	126	84
$\dot{m}_{H_2}^{1,LHSV=0.5} / \dot{m}_{H_2}$ [% (m/m)]	39%	34%	37%	44%	43%	41%
$\dot{m}_{H_2}^{1,LHSV=1} / \dot{m}_{H_2}$ [% (m/m)]	25%	39%	27%	35%	20%	25%
$\dot{m}_{H_2}^{1,LHSV=1.5} / \dot{m}_{H_2}$ [% (m/m)]	16%	25%	26%	34%	23%	25%
$\dot{m}_{H_2}^{1,LHSV=2} / \dot{m}_{H_2}$ [% (m/m)]	17%	28%	18%	30%	25%	12%
$\dot{m}_{H_2}^{2,LHSV=0.5} / \dot{m}_{H_2}$ [% (m/m)]	38%	20%	14%	30%	26%	10%
$\dot{m}_{H_2}^{2,LHSV=1} / \dot{m}_{H_2}$ [% (m/m)]	46%	21%	17%	38%	34%	12%
$\dot{m}_{H_2}^{2,LHSV=1.5} / \dot{m}_{H_2}$ [% (m/m)]	59%	17%	27%	22%	25%	20%
$\dot{m}_{H_2}^{2,LHSV=2} / \dot{m}_{H_2}$ [% (m/m)]	65%	15%	13%	35%	32%	15%
$\dot{m}_{H_2}^{3,LHSV=0.5} / \dot{m}_{H_2}$ [% (m/m)]	23%	16%	12%	26%	14%	11%
$\dot{m}_{H_2}^{3,LHSV=1} / \dot{m}_{H_2}$ [% (m/m)]	29%	22%	21%	27%	18%	33%

Operating variable	Traditional			Stochastic		
	3 layers	4 layers	5 layers	3 layers	4 layers	5 layers
[% (m/m)]						
$\dot{m}_{H_2}^{3,LHSV=1.5} / \dot{m}_{H_2}$	25%	26%	12%	45%	34%	11%
[% (m/m)]						
$\dot{m}_{H_2}^{3,LHSV=2} / \dot{m}_{H_2}$	18%	22%	39%	35%	15%	12%
[% (m/m)]						
$\dot{m}_{H_2}^{4,LHSV=0.5} / \dot{m}_{H_2}$	n.a	30%	20%	n.a	17%	15%
[% (m/m)]						
$\dot{m}_{H_2}^{4,LHSV=1} / \dot{m}_{H_2}$	n.a	17%	11%	n.a	29%	20%
[% (m/m)]						
$\dot{m}_{H_2}^{4,LHSV=1.5} / \dot{m}_{H_2}$	n.a	32%	25%	n.a	18%	10%
[% (m/m)]						
$\dot{m}_{H_2}^{4,LHSV=2} / \dot{m}_{H_2}$	n.a	35%	21%	n.a	28%	42%
[% (m/m)]						
$\dot{m}_{H_2}^{5,LHSV=0.5} / \dot{m}_{H_2}$	n.a	n.a	17%	n.a	n.a	22%
[% (m/m)]						
$\dot{m}_{H_2}^{5,LHSV=1} / \dot{m}_{H_2}$	n.a	n.a	24%	n.a	n.a	10%
[% (m/m)]						
$\dot{m}_{H_2}^{5,LHSV=1.5} / \dot{m}_{H_2}$	n.a	n.a	10%	n.a	n.a	33%
[% (m/m)]						
$\dot{m}_{H_2}^{5,LHSV=2} / \dot{m}_{H_2}$	n.a	n.a	10%	n.a	n.a	20%
[% (m/m)]						

## List of Figures

Figure 3.1. Pyrolysis process (1–1 <sup>st</sup> reactor, 2–2 <sup>nd</sup> reactor, 3 – heat exchanger, 4 – separator, 5 – gas flow meter, 6 – computer) [224].	41
Figure 3.2. P-N0-R10 reaction network with ten reactions between six lumps....	43
Figure 3.3. Sequential solution of the proposed reactor system model.	46
Figure 3.4. VGO-N0-R15 reaction network consisting of 6 component lumps and 15 lumped reactions, labeled in different colors based on reactants.....	47
Figure 3.5. VGO-N1-R5 reaction network of VGO hydrocracking, consisting of six lumps, H <sub>2</sub> and five reactions.....	50
Figure 4.1. Kinetic parameter identification strategy.....	58
Figure 4.2. Local sensitivity analysis of calculated parameters for thermal pyrolysis. (a) pre-exponential factors; (b) activation energies.....	62
Figure 4.3. Pseudocomponent mass fractions from run nr. 6 at 455 °C – experimental (markers) and simulation (lines).	65
Figure 4.4. Pseudocomponent mass fractions from run nr. 3 (a) and 5 (b) at 455 °C – experimental (markers) and simulation (lines).	66
Figure 4.5. Pseudocomponent mass fractions from run nr. 8 at 425 °C – experimental (markers) and simulation (lines).	67
Figure 4.6. Rate of the P → P– reaction in case of thermal pyrolysis and in the presence of various catalysts at different temperatures.....	68
Figure 5.1. First reaction network identification strategy .....	75
Figure 5.2. Second reaction network identification strategy .....	76
Figure 5.3. Third reaction network identification strategy .....	78
Figure 5.4. VGO-N0-R15 reaction network consisting of 6 component lumps and 15 lumped reactions .....	80
Figure 5.5. Objective function values for reaction subnetworks obtained by different model reduction methods .....	81

Figure 5.6. VGO-N0-R9 reaction networks consisting of 6 lumps and 9 reactions, obtained by (a) Method 1, (b) Method 2, and (c) Method 3. Reactions that are not present in all three networks are marked with dashed lines ..... 83

Figure 5.7. Results of the state-space model linearization at the outlet of the reactor for VGO at 380 °C..... 86

Figure 5.8. Observability of reaction networks consisting of 1-9 reactions, obtained using different methods ..... 87

Figure 5.9. VGO-N0-R5 reaction network consisting of 5 reactions, obtained by Method 2..... 88

Figure 5.10. Pseudocomponent concentrations at the reactor outlet for different LHSV values at 410 °C. Data points represent measured data, dashed lines indicate the 15-reaction system results, and solid lines represent the 5-reaction system results..... 89

Figure 6.1. Convergence of RS-HDMR sensitivity indices in case of a) thermo-catalytic pyrolysis, b) VGO hydrocracking..... 93

Figure 6.2. Identified reaction networks for thermo-catalytic pyrolysis at 455 °C a) P-N0-R10, b) P-N0-R5 (GSA results)..... 96

Figure 6.3. Pseudocomponent mass fractions in case of the reduced network for thermo-catalytic pyrolysis at 455 °C – experimental (markers); P-N0-R10 (dashed lines) and P-N0-R5 (solid lines) ..... 97

Figure 6.4. Root-mean-square-error for reaction subnetworks obtained using the sensitivity order obtained using different GSA methods ..... 99

Figure 6.5. Identified reaction networks for VGO hydrocracking at 410 °C a) VGO-N0-R15, b) VGO-N0-R7 (GSA results)..... 101

Figure 6.6. Pseudocomponent mass fractions in case of the reduced network for VGO hydrocracking at 410 °C – experimental (markers); complete (dashed lines) and reduced (solid lines) model..... 102

Figure 6.7. Occurrence of objective function values calculated using the PDFs of the kinetic parameters for VGO hydrocracking a) complete network, b) reduced network.....	106
Figure 7.1. a) mass ratio of the L+ and L- lumps as a function of reaction time and temperature level b – d) mass distribution of the liquid product at different temperature levels .....	111
Figure 7.2. P-N1-R5 reaction network (N1) with the correlation between the L+ and L- lumps taken into consideration .....	113
Figure 7.3. Pseudocomponent mass fractions at a) 425 °C b) 485 °C using one average liquid composition for all temperature levels (first scenario). Markers: experimental, dashed lines: P-N0-R10 reaction network results, solid lines: P-N1-R5 reaction network results.....	114
Figure 7.4. Pseudocomponent mass fractions at a) 425 °C b) 485 °C using one average liquid composition at each temperature level (second scenario). Markers: experimental, dashed lines: P-N0-R10 reaction network results, solid lines: P-N1-R5 reaction network results.....	115
Figure 7.5. a) time-average liquid composition at 455 °C b) newly constructed reaction network (P-N2-R9) with six pairs of correlated liquid lumps.....	118
Figure 7.6. Pseudocomponent mass fractions at 425 °C for reaction network P-N2-R9 using one average liquid composition at each temperature level (3) and each liquid product type (3) .....	120
Figure 7.7. Pseudocomponent mass fractions at 455 °C for network P-N1-R5 for FeZSM-5 / Ni/Mo-Al <sub>2</sub> O <sub>3</sub> catalysts identified using generated measurement data a) comparison with generated data b) comparison with original GC data.....	123
Figure 8.1. Performance of different algorithms for VGO hydrocracking a) VGO-N0-R15 b) VGO-N0-R5.....	133
Figure 8.2. Performance of different algorithms for ethane pyrolysis.....	134
Figure 8.3: Correlation between the identified parameters in the case of the a) VGO-N0-R15 and b) VGO-N0-R5 model.....	136

Figure 8.4. Standard deviation of mass concentrations calculated using kinetic parameters at different global minima.....	137
Figure 9.1. Original catalyst activity profile of the reactor. Light gray: zero activity (alumina spheres); dark gray: low activity (0.3); black: high activity (1) .....	140
Figure 9.2. Maximum achievable HCl conversion in the reactor by dividing it to $N \in [1, 6]$ zones.....	142
Figure 9.3. Temperature profiles of a three-zoned reactor optimized for maximum conversion.....	143
Figure 9.4. Reactor temperature profiles obtained by minimizing the standard deviation of the overall temperature profile of the reactor with zoning the catalyst bed .....	148
Figure 9.5. Temperature profiles (a) and gradients (b) of reactors resulting temperature profile optimization .....	149
Figure 10.1. Schematics of the VGO hydrocracking reactor with the design variables.....	154
Figure 10.2. Temperature profiles of the hydrocracking reactor designed using a conventional method in case of different numbers of catalyst layers and different LHSV values – a) $0.5 \text{ h}^{-1}$ , b) $2 \text{ h}^{-1}$ .....	159
Figure 10.3. Sensitivity indices of the hydrocracking reactor designed using the conventional method to different uncertain parameters. ....	161
Figure 10.4. Local sensitivity analysis of the hydrocracking reactor with four catalyst layers to different uncertain parameters designed using the conventional method. ....	162
Figure 10.5. Nominal values of design variables of the hydrocracking reactor with four catalyst layers in case of different LHSV values – a) $0.5 \text{ h}^{-1}$ , b) $1 \text{ h}^{-1}$ , c) $1.5 \text{ h}^{-1}$ , d) $2 \text{ h}^{-1}$ .....	163



---

Figure 10.6. Probability density of the optimized objective function values in the space of uncertain parameters in case of the hydrocracking reactor with a) three b) four c) five catalyst layers. ....	166
Figure S1. Identified kinetic parameters of the 1 <sup>st</sup> reaction for every generated data set using bootstrapping and the fitted Weibull-distribution in case of the complete reaction network for VGO hydrocracking. ....	215
Figure S2. Identified kinetic parameters of the 2 <sup>nd</sup> reaction for every generated data set using bootstrapping and the fitted Weibull-distribution in case of the complete reaction network for VGO hydrocracking. ....	216
Figure S3. Identified kinetic parameters of the 3 <sup>rd</sup> reaction for every generated data set using bootstrapping and the fitted Weibull-distribution in case of the complete reaction network for VGO hydrocracking. ....	216
Figure S4. Identified kinetic parameters of the 4 <sup>th</sup> reaction for every generated data set using bootstrapping and the fitted Weibull-distribution in case of the complete reaction network for VGO hydrocracking. ....	217
Figure S5. Identified kinetic parameters of the 5 <sup>th</sup> reaction for every generated data set using bootstrapping and the fitted Weibull-distribution in case of the complete reaction network for VGO hydrocracking. ....	217
Figure S6. Identified kinetic parameters of the 6 <sup>th</sup> reaction for every generated data set using bootstrapping and the fitted Weibull-distribution in case of the complete reaction network for VGO hydrocracking. ....	218
Figure S7. Identified kinetic parameters of the 7 <sup>th</sup> reaction for every generated data set using bootstrapping and the fitted Weibull-distribution in case of the complete reaction network for VGO hydrocracking. ....	218
Figure S8. Identified kinetic parameters of the 8 <sup>th</sup> reaction for every generated data set using bootstrapping and the fitted Weibull-distribution in case of the complete reaction network for VGO hydrocracking. ....	219

Figure S9. Identified kinetic parameters of the 9<sup>th</sup> reaction for every generated data set using bootstrapping and the fitted Weibull-distribution in case of the complete reaction network for VGO hydrocracking. .... 219

Figure S10. Identified kinetic parameters of the 10<sup>th</sup> reaction for every generated data set using bootstrapping and the fitted Weibull-distribution in case of the complete reaction network for VGO hydrocracking. .... 220

Figure S11. Identified kinetic parameters of the 11<sup>th</sup> reaction for every generated data set using bootstrapping and the fitted Weibull-distribution in case of the complete reaction network for VGO hydrocracking. .... 220

Figure S12. Identified kinetic parameters of the 12<sup>th</sup> reaction for every generated data set using bootstrapping and the fitted Weibull-distribution in case of the complete reaction network for VGO hydrocracking. .... 221

Figure S13. Identified kinetic parameters of the 13<sup>th</sup> reaction for every generated data set using bootstrapping and the fitted Weibull-distribution in case of the complete reaction network for VGO hydrocracking. .... 221

Figure S14. Identified kinetic parameters of the 14<sup>th</sup> reaction for every generated data set using bootstrapping and the fitted Weibull-distribution in case of the complete reaction network for VGO hydrocracking. .... 222

Figure S15. Identified kinetic parameters of the 15<sup>th</sup> reaction for every generated data set using bootstrapping and the fitted Weibull-distribution in case of the complete reaction network for VGO hydrocracking. .... 222

Figure S16. Identified kinetic parameters of the 1<sup>st</sup> reaction for every generated data set using bootstrapping and the fitted Weibull-distribution in case of the reduced reaction network for VGO hydrocracking. .... 223

Figure S17. Identified kinetic parameters of the 4<sup>th</sup> reaction for every generated data set using bootstrapping and the fitted Weibull-distribution in case of the reduced reaction network for VGO hydrocracking. .... 223

Figure S18. Identified kinetic parameters of the 5<sup>th</sup> reaction for every generated data set using bootstrapping and the fitted Weibull-distribution in case of the reduced reaction network for VGO hydrocracking. .... 224

Figure S19. Identified kinetic parameters of the 6 <sup>th</sup> reaction for every generated data set using bootstrapping and the fitted Weibull-distribution in case of the reduced reaction network for VGO hydrocracking.....	224
Figure S20. Identified kinetic parameters of the 10 <sup>th</sup> reaction for every generated data set using bootstrapping and the fitted Weibull-distribution in case of the reduced reaction network for VGO hydrocracking.....	225
Figure S21. Identified kinetic parameters of the 13 <sup>th</sup> reaction for every generated data set using bootstrapping and the fitted Weibull-distribution in case of the reduced reaction network for VGO hydrocracking.....	225
Figure S22. Identified kinetic parameters of the 15 <sup>th</sup> reaction for every generated data set using bootstrapping and the fitted Weibull-distribution in case of the reduced reaction network for VGO hydrocracking.....	226
Figure S23. Temperature profiles of the hydrocracking reactor designed using a conventional method in case of different numbers of catalyst layers and different LHSV values – a) 0.5 h <sup>-1</sup> , b) 1 h <sup>-1</sup> , c) 1.5 h <sup>-1</sup> , d) 2 h <sup>-1</sup> . ....	227
Figure S24. Local sensitivity analysis of the hydrocracking reactor with three catalyst layers to different uncertain parameters designed using the conventional method.....	228
Figure S25. Local sensitivity analysis of the hydrocracking reactor with five catalyst layers to different uncertain parameters designed using the conventional method.....	229
Figure S26. Nominal values of design variables of the hydrocracking reactor with three catalyst layers in case of different LHSV values – a) 0.5 h <sup>-1</sup> , b) 1 h <sup>-1</sup> , c) 1.5 h <sup>-1</sup> , d) 2 h <sup>-1</sup> .....	230
Figure S27. Nominal values of design variables of the hydrocracking reactor with five catalyst layers in case of different LHSV values – a) 0.5 h <sup>-1</sup> , b) 1 h <sup>-1</sup> , c) 1.5 h <sup>-1</sup> , d) 2 h <sup>-1</sup> .....	231



**List of Tables**

Table 2.1. Heterocatalytic reactions of industrial importance .....	12
Table 2.2. Hydrotreating and hydrocracking: ranges of H <sub>2</sub> partial pressure and conversion. ....	14
Table 3.1. List of catalysts used in the two reactors during different runs. ....	41
Table 3.2. VGO hydrocracking reactor main dimensions.....	50
Table 3.3. List of reactions and kinetic parameters for the ethane pyrolysis model .....	54
Table 3.4. Ethane pyrolysis reactor main dimensions [223].....	55
Table 4.1. Suggested kinetic parameter identification sequence. ....	61
Table 4.2. Root-mean-square error (RMSE) between experimental and calculated data. ....	64
Table 4.3. Ratio of the rates of P <sup>-</sup> → L <sup>+</sup> and P <sup>-</sup> → L <sup>-</sup> reactions in case of thermal pyrolysis and in the presence of various catalysts at different temperatures .....	69
Table 4.4. Sizing of a pilot-scale pyrolysis reactor .....	70
Table 4.5. Maximizing the feedstock conversion ( $X_P$ ) and the amount of L <sup>-</sup> ( $w_{L^-}$ ) in a tube reactor .....	71
Table 5.1. Lower and upper bounds of kinetic parameters of the specified reactions used in every identification strategy .....	79
Table 5.2. Pearson correlations between measured and calculated data.....	82
Table 6.1. Sample sizes chosen for different GSA methods and case studies. ....	93
Table 6.2. Different GSA indices for thermo-catalytic pyrolysis. ....	95
Table 6.3. Root-mean-square error (RMSE) between experimental and calculated weight percentages of the component lumps. ....	96
Table 6.4. Different GSA indices for VGO hydrocracking. ....	98
Table 6.5. Root-mean-square error (RMSE) between experimental and calculated mass fractions.....	100

Table 6.6. Confidence intervals for the identified parameters for VGO hydrocracking. ....	105
Table 7.1. Estimated fractions of the L+ and L- lumps in the liquid product in the N1 network .....	114
Table 7.2. Root-mean-square error (RMSE) between experimental and calculated data .....	117
Table 7.3. Identified kinetic parameters for plastic waste pyrolysis on CuZSM-5 / Ni/Mo-Al <sub>2</sub> O <sub>3</sub> catalysts for reaction network (N1).....	117
Table 7.4. Identified kinetic parameters for plastic waste pyrolysis on CuZSM-5 / Ni/Mo-Al <sub>2</sub> O <sub>3</sub> catalysts for reaction network P-N2-R9.....	120
Table 7.5. Identified kinetic parameters for plastic waste pyrolysis on FeZSM-5 / Ni/Mo-Al <sub>2</sub> O <sub>3</sub> catalysts for reaction network P-N1-R5.....	122
Table 8.1. Lower and upper bounds of kinetic parameters of the reactions in the VGO-N0-R15 model. ....	128
Table 8.2. Lower and upper bounds of kinetic parameters of the reactions in the VGO-N0-R5 model .....	128
Table 8.3. Lower and upper bounds of kinetic parameters of the reactions in the ETP model.....	129
Table 8.4. List of nonlinear optimization algorithms considered for comparison. ....	131
Table 9.1. Developed objective functions for the optimization of the reactor temperature profile. ....	144
Table 9.2. Minimized values of objective functions for the optimization of the reactor temperature profile. ....	145
Table 9.3. Maximum values of temperatures and gradients in case of optimized temperature profiles in the reactor.....	147
Table 9.4. Optimized reactor configuration of reactors resulting temperature profile optimization .....	150

---

Table 10.1. Lower and upper bounds of search variables for constrained optimization. ....	155
Table 10.2. Lower and upper bounds of uncertain parameters of the reactor model. ....	158
Table 10.3. Nominal operating conditions of the hydrocracking reactor designed using a conventional method in case of different numbers of catalyst layers and averaged over LHSV values.....	159
Table 10.4. Maps of the uncertain parameter space for the tests or robustness..	164
Table 12.1. Relations between major topics, reactor models and theses. ....	173
Table S1. Identifiers of the different lumped reaction networks introduced in the thesis.....	232
Table S2. Stoichiometric matrix of the reaction network from Figure 3.2.....	232
Table S3. Physical properties of the components included in the plastic waste pyrolysis reactor model (Section 3.1). ....	233
Table S4. Physical properties of the components included in the VGO hydrocracking reactor model (Section 3.2 and 3.3). ....	234
Table S5. Stoichiometric matrix of the reaction network from Figure 3.5.....	234
Table S6. HCl oxidation reactor model constants and variables (Section 3.1)...	234
Table S7. Physical properties of the components included in the ethane pyrolysis reactor model.....	237
Table S8. Identified pre-exponential factors and activation energies for plastic waste pyrolysis (Chapter 4).....	238
Table S9. Measured mass concentration values for VGO hydrocracking [218].	239
Table S10. Pre-exponential factors for reactions in reaction networks identified with Method 1 from Section 5.1. ....	240
Table S11. Activation energies for reactions in reaction networks identified with Method 1 from Section 5.1.....	241

Table S12. Pre-exponential factors for reactions in reaction networks identified with Method 2 from Section 5.1.....	242
Table S13. Activation energies for reactions in reaction networks identified with Method 2 from Section 5.1.....	243
Table S14. Pre-exponential factors for reactions in reaction networks identified with Method 3 from Section 5.1.....	244
Table S15. Activation energies for reactions in reaction networks identified with Method 3 from Section 5.1.....	245
Table S16. Identified kinetic parameters of the thermo-catalytic pyrolysis reaction networks (from Section 6.2). .....	246
Table S17. Identified kinetic parameters of the vacuum gas oil hydrocracking reaction networks (from Section 6.3). .....	247
Table S18. Identified pre-exponential factors of the reaction network from Figure 3.5. ....	248
Table S19. Identified activation energies of the reaction network from Figure 3.5. ....	249
Table S20. Nominal operating conditions of the hydrocracking reactor designed using a conventional method in case of one catalyst layer.....	251
Table S21. Nominal operating conditions of the hydrocracking reactor designed using a conventional method in case of two catalyst layers.....	251
Table S22. Nominal operating conditions of the hydrocracking reactor designed using a conventional method in case of two catalyst layers with independent H <sub>2</sub> inlet temperatures. ....	252
Table S23. Nominal operating conditions of the hydrocracking reactor designed using a conventional method in case of three catalyst layers.....	253
Table S24. Nominal operating conditions of the hydrocracking reactor designed using a conventional method in case of four catalyst layers. ....	254
Table S25. Nominal operating conditions of the hydrocracking reactor designed using a conventional method in case of five catalyst layers.....	255



Table S26. Nominal operating conditions of the hydrocracking reactor designed using a conventional method in case of six catalyst layers..... 256

Table S27. Nominal values of operating variables of the hydrocracking reactor at the base uncertainty level. .... 257



**Acknowledgement**

Takács-Bárkányi Ágnes  
Németh Sándor  
Ruppert Tamás Miskolczi Norbert  
Gyurik Livia Kummer Alex  
Módis Márton  
Abonyi János Dörgő Gyula  
Nagy Lajos Honti Gergely  
Chován Tibor Ulbert Zsolt  
Varga Tamás  
Egedy Attila Klein Mónika  
Tóth-Gyóllai Dániel  
Hamadi Omar Sója János  
Lakatos Béla  
Szeifert Ferenc